Effective Field Theory for Halo Nuclei

Dissertation

zur

Erlangung des Doktorgrades (Dr. rer. nat.)

der

Mathematisch-Naturwissenschaftlichen Fakultät

der

Rheinischen Friedrich-Wilhelms-Universität Bonn

vorgelegt von

Philipp Robert Hagen

aus

Troisdorf

Bonn 2013

Angefertigt mit der Genehmigung der Mathmatisch-Naturwissenschaftlichen Fakultät der Rheinischen Friedrich-Wilhelms-Universität Bonn

1. Gutachter: Prof. Dr. Hans-Werner Hammer

2. Gutachter: Prof. Dr. Bastian Kubis

Tag der Promotion: 19.02.2014

Erscheinungsjahr: 2014

Abstract

We investigate properties of two- and three-body halo systems using effective field theory. If the two-particle scattering length a in such a system is large compared to the typical range of the interaction R, low-energy observables in the strong and the electromagnetic sector can be calculated in halo EFT in a controlled expansion in $R/|a|$. Here we will focus on universal properties and stay at leading order in the expansion.

Motivated by the existence of the P-wave halo nucleus ^{6}He, we first set up an EFT framework for a general three-body system with resonant two-particle P-wave interactions. Based on a Lagrangian description, we identify the area in the effective range parameter space where the two-particle sector of our model is renormalizable. However, we argue that for such parameters, there are two two-body bound states: a physical one and an additional deeper-bound and non-normalizable state that limits the range of applicability of our theory. With regard to the three-body sector, we then classify all angular-momentum and parity channels that display asymptotic discrete scale invariance and thus require renormalization via a cut-off dependent three-body force. In the unitary limit an Efimov effect occurs. However, this effect is purely mathematical, since, due to causality bounds, the unitary limit for P-wave interactions can not be realized in nature. Away from the unitary limit, the three-body binding energy spectrum displays an approximate Efimov effect but lies below the unphysical, deep two-body bound state and is thus unphysical. Finally, we discuss possible modifications in our halo EFT approach with P-wave interactions that might provide a suitable way to describe physical three-body bound states.

We then set up a halo EFT formalism for two-neutron halo nuclei with resonant two-particle S-wave interactions. Introducing external currents via minimal coupling, we calculate observables and universal correlations for such systems. We apply our model to some known and suspected halo nuclei, namely the light isotopes ^{11}Li, ^{14}Be and ^{22}C and the hypothetical heavy atomic nucleus ^{62}Ca. In particular, we calculate charge form factors, relative electric charge radii and dipole strengths as well as general dependencies of these observables on masses and one- and two-neutron separation energies. Our analysis of the ^{62}Ca system provides evidence of Efimov physics along the Calcium isotope chain. Experimental key observables that facilitate a test of our findings are discussed.

Parts of this thesis have been published in:

- E. Braaten, P. Hagen, H.-W. Hammer and L. Platter. Renormalization in the Three-body Problem with Resonant P-wave Interactions. *Phys. Rev. A*, **86**:012711, (2012), arXiv:1110.6829v4 [cond-mat.quant-gas].
- P. Hagen, H.-W. Hammer and L. Platter. Charge form factors of two-neutron halo nuclei in halo EFT. *Eur. Phys. J. A*, **49**:118, (2013), arXiv:1304.6516v2 [nucl-th].
- G. Hagen, P. Hagen, H.-W. Hammer and L. Platter. Efimov Physics around the neutron rich Calcium-60 isotope. *Phys. Rev. Lett.*, **111**:132501, (2013), arXiv:1306.3661 [nucl-th].

Contents

Chapter 1

Introduction

1.1 From the standard model to halo effective field theory

A vast amount of physical phenomena in nature can be described within the so-called *standard model* (SM). Its fundamental degrees of freedom, the elementary particles, are ordered in three generations of quarks and leptons and a set of exchange particles, describing their interactions. The interactions are commonly divided into the electromagnetic, the weak, and the strong sector, where the first two were successfully unified to the electroweak force. Furthermore, within this picture, all elementary particles are point-like and their inertial masses are generated by the Higgs mechanism, which introduces at least one additional bosonic field. This mechanism was already proposed in 1964 by, among others, Higgs and Englert [1–3]. Recent experiments at CERN confirmed the existence of such a so-called Higgs field, awarding both authors the 2013 Nobel prize in physics.

The theory of strong interactions is usually referred to as *quantum chromodynamics* (QCD). It describes how quark fields q interact with each other through gauge bosons G called *gluons*. Since gluons carry color charge, they can interact with each other. The fundamental object, the theory is mathematically based on, is the QCD-Lagrangian

$$\begin{aligned} \mathcal{L}_{\mathrm{QCD}}(q,G) &= q_f^\dagger \gamma^0 \Big(i\gamma^\mu \big[\partial_\mu - i g_s \frac{\lambda_a}{2} G^a_\mu\big] - m_f \Big) q_f - \frac{1}{4} F^a_{\mu\nu} F^{\mu\nu}_a \quad , \\ F^a_{\mu\nu} &= \partial_\mu G^a_\nu - \partial_\nu G^a_\mu + g_s f^{abc} G^b_\mu G^c_\nu \quad , \end{aligned} \tag{1.1}$$

where we implicitly sum over all double indices. Thereby, the ranges for flavor indices (f), color indices (a, b, c) and Lorentz indices (μ, ν) are $\{1, \ldots 6\}$, $\{1, \ldots 8\}$ and $\{0, \ldots, 3\}$, respectively. γ^μ are the four Dirac matrices and λ_a are the eight Gell-Mann matrices with structure constants f^{abc}. m_f is the bare mass parameter for a quark of flavor f and g_s is the strong coupling constant.

In the course of the great progress in the understanding of nature, provided by the SM, various new questions and problems came up. On the one hand, there are in a way fundamental problems to the SM. For example, satisfying explanations for phenomena related to the gravitational sector, such as gravitation itself or dark matter and dark energy, are still missing. In addition to that, the unification of all forces remains a major task in theoretical physics. In order to solve these problems, the SM has to be extended in a hitherto unknown way. However, on the other hand, there is another category of problems which has to do with the complexity of the interactions that are already included in the SM. In particular, QCD, which, in principle, is described by eq. (1.1), is not fully understood yet. The main problem comes from its running coupling constant g_s. At large energies g_s becomes small such that perturbation theory is applicable. The quarks then behave as free particles whose scattering processes can be calculated analytically and order by order in terms of Feynman diagrams. This phenomenon is called *asymptotic freedom* and was discovered in 1973 by Gross, Wilczek and Politzer [4, 5]. Calculated predictions in this high-energy sector match very well with experimental data. However, in the low-energy regime the situation is the exact opposite. Since g_s becomes large, perturbation theory can no longer be applied. Instead, the attractive force between quarks rises with increasing distance. As a consequence, they can not be isolated and are confined into color neutral objects. This confinement provides the basis for the existence of all hadrons but is nether fully understood nor mathematically proven yet.

There are different approaches to this unresolved problem. One, for instance, is to use a discretized version of eq. (1.1) and perform computer-based calculations [6, 7]. Thereby, the continuous space time is replaced by a discrete lattice with less symmetries. Although current results of this so-called *lattice QCD* look promising, limited computing power is a major drawback. In order to get physical results, one namely has to consider the limit of vanishing lattice spacing and physical masses, rapidly stretching state-of-the-art supercomputers to their limits. Thus, first principle lattice QCD calculations for nuclear systems with many constituents such as the atomic nuclei of ^{22}C or ^{62}Ca, which are discussed in this thesis, will stay out of reach in the foreseeable future.

Another approach that proved itself in practice is to use *effective field theory* (EFT). Generally speaking, an EFT, such as chiral perturbation theory (ChPT) [8–10], is an approximation to an underlying more fundamental theory. Ideally, it shares the same symmetries and well describes observed phenomena within a certain parameter region. The complex substructure and the number of the degrees of freedom in the original theory typically are reduced within an EFT framework. Eventually, even the current SM will be seen as an EFT as soon as the underlying, more fundamental theory is discovered.

The aim of this work is to set up a non-relativistic EFT for large scattering length and apply it to a specific class of three-body systems called halo nuclei. The corresponding effective field theory is called halo EFT. With respect to such systems, we first consider a more general theoretical issue that came up recently, namely the question if and how such halo systems can be generated through P-wave interactions. After that, we derive and calculate concrete physical observables for S-wave halo nuclei with an emphasis on the electromagnetic sector.

1.1.1 Overview

The outline of this work is as follows: In sec. 1.2 we first give a brief introduction on EFTs with large scattering length. Thereby, sec. 1.2.1 begins with a repetition of basic aspects of scattering theory including the effective range expansion. Sec. 1.2.2 then proceeds with a short review of the concept of large scattering length, universality, the phenomenon of discrete scale invariance and the Efimov effect. An introduction to halo nuclei and halo effective field theory with hitherto results in this area of research is presented in sec. 1.2.3. In sec. 1.3 we specify the notational conventions that are used throughout this work.

In chapter 2 we investigate the question if and how halo nuclei or general two- and three-body systems with large scattering length can be realized through two-particle P-wave interactions. Therefore, in sec. 2.1 we first repeat fundamental properties of non-relativistic EFTs with contact interactions on the Lagrangian level. Especially, we analyze how possible contributions to the Lagrangian are constraint by the requirement of Galilean invariance. Furthermore, equivalent ways of introducing auxiliary fields to our theory are explained. Sec. 2.2 discusses already existing results for three-body systems with resonant S-wave interactions. In particular, examples for systems exhibiting the Efimov effect are given. The central question of chapter 2 then is how these results transfer to halo systems with resonant P-wave interactions. In sec. 2.3 we address this issue in a more general framework, by setting up an effective Lagrangian for a general three-body system with such interactions. Solving the two- and the three-body problem in this system, we then classify all channels that display discrete scale invariance. Finally, we discuss the possibility of three-body bound states and the Efimov effect.

In chapter 3 we apply non-relativistic halo EFT with resonant S-wave interactions to two-neutron halo nuclei. We proceed analogously to sec. 2.3, meaning that in sec. 3.1 we first lay out the field theoretical formalism required for all subsequent calculations. The introduced effective Lagrangian for a two-neutron halo system is then used in order to solve the corresponding two- and three-body problem. In sec. 3.2 we extend our model by allowing the charged core to couple to external currents via minimal coupling. Based on the corresponding Lagrangian we then derive and calculate different electromagnetic observables of two-neutron halo nuclei at leading order including form factors and electric charge radii in sec. 3.2.2. Moreover, we also investigate general correlations between different observables (see sec. 3.2.3). Finally, in sec. 3.2.4 we present first results for photodisintegration processes of halo nuclei. The methods are applied to some known and suspected two-neutron halo nuclei candidates. Results are compared to experimental data where available.

Chapter 4 encapsulates all the main results presented in this work. In addition, we give a brief outlook to possible future theoretical as well as experimental work in halo EFT that is related to the considered range of subjects.

All extended calculations are included in the appendix. Sec. A discusses the relevant analytic properties of the appearing integral kernels. Applied numerical methods are presented in sec. B. For the case of resonant two-particle P-wave interactions, explicit calculations for the coupling of angular momenta in the three-particle sector can be found in sec. C. Furthermore, sec. D contains detailed calculations of required nontrivial Feynman diagrams.

1.2 EFT with large scattering length

1.2.1 Scattering theory concepts

Before we start with our EFT analysis, we first briefly discuss some basic scattering theory concepts [11] that will be applied throughout this work. In particular, we consider properties and relations between the *scattering amplitude*, the *S-matrix* and the *T-matrix*. These quantities represent fundamental objects of scattering theory and are related to various physical observables. The scattering amplitude e.g. completely determines the asymptotic behavior of the stationary wave function and its absolute value squared yields the differential cross section.

We now assume that two distinguishable particles with reduced mass μ elastically scatter off each other in on-shell center-of-mass kinematics. Then, for incoming and outgoing relative three-momenta $\mathbf{p}$ and $\mathbf{k}$, respectively, the relation $p = |\mathbf{p}| = |\mathbf{k}|$ holds. If, furthermore, the potential has spherical symmetry, as it is the case for all the contact interactions presented in this work, the scattering amplitude f can effectively be written as a function that only depends on p and $\cos\theta$, where $\theta := \sphericalangle(\mathbf{p}, \mathbf{k})$ is the scattering angle. f is related to the T-matrix of the scattering process according to:

$$f(p, \cos\theta) \;=\; \frac{\mu}{2\pi}\, T(p, \cos\theta) \quad . \tag{1.2}$$

Since $\cos\theta \in [-1, 1]$ holds and the Legendre-polynomials P_ℓ form a complete set of functions on the interval $[-1, 1]$, a decomposition into *partial waves*

$$f(p, \cos\theta) \;=\; \sum_\ell (2\ell + 1)\, f^{[\ell]}(p)\, P_\ell(\cos\theta) \tag{1.3}$$

can be performed, where $\ell \in \{0, 1, 2, \dots\}$. A completely analogous equation holds for the T-matrix. The relation between the partial wave coefficient $f^{[\ell]}$ and the corresponding S-matrix element reads $S^{[\ell]}(p) = 1 + 2ipf^{[\ell]}(p)$. The unitarity of the S-matrix combined with angular momentum conservation in each partial wave then implies $|S^{[\ell]}(p)| = 1$. Without loss of generality, we can thus write $S^{[\ell]}(p) = \exp(2i\delta^{[\ell]}(p))$, where the real angle $\delta^{[\ell]}(p)$ is called the *phase shift*. This leads to the well known relation:

$$f^{[\ell]}(p) \;=\; \frac{1}{p\cot\delta^{[\ell]}(p) - ip} \quad . \tag{1.4}$$

If the energy lies above any inelastic threshold, the phase shift becomes complex.

For exponentially bound potentials, such as the contact interactions used in this work, one can show that the term $p^{2\ell+1}\cot\delta^{[\ell]}(p)$ is analytic in p^2 (see e.g. [12,13]). Consequently, it can be written in terms of a Taylor series in p^2:

$$p^{2\ell+1}\cot\delta^{[\ell]}(p) \;=\; -\frac{1}{a^{[\ell]}} + \frac{r^{[\ell]}}{2}\,p^2 + \mathcal{O}(p^4) \quad . \tag{1.5}$$

Eq. (1.5) is called the *effective range expansion.* Of course, it can only be a good approximation in the low-energy regime. The first appearing low-energy constants $a^{[\ell]}$ and $r^{[\ell]}$ are called *scattering length* and *effective range*, respectively. In order to match with the left-hand side of eq. (1.5), their dimensions have to be $[a^{[\ell]}] = -2\ell - 1$ and $[r^{[\ell]}] = 2\ell - 1$. Higher order coefficients in the expansion (1.5), which are called *shape parameters*, will not be considered in this work. In case of P-waves, the quantity $a^{[1]}$ is usually also referred to as the *scattering volume.* Combining eq. (1.4) and eq. (1.5) leads to:

$$f^{[\ell]}(p) \;=\; \frac{p^{2\ell}}{-\frac{1}{a^{[\ell]}} + \frac{r^{[\ell]}}{2}\,p^2 - ip^{2\ell+1} + \mathcal{O}(p^4)} \quad . \tag{1.6}$$

This relation will be used in order to determine effective range parameters from the T-matrix. Inserting eq. (1.2) into eq. (1.6), for example, yields:

$$-\frac{\mu}{2\pi}\lim_{p\to 0} p^{-2\ell}\,T^{[\ell]}(p) \;=\; a^{[\ell]} \quad . \tag{1.7}$$

1.2.2 Universality, discrete scale invariance and the Efimov effect

As outlined in the previous sec. 1.2.1, the scattering of two particles can be described by a few low-energy constants, the effective range parameters, given that the mentioned requirements are met. Naively, one would expect that, with regard to their dimension, these parameters should all be of the same order. Such a behavior would imply the existence a natural low-energy length scale l such that e.g. for the S-wave case $|a^{[0]}| \sim l$ and $|r^{[0]}| \sim l$ should hold. For P-waves, the corresponding conditions would be $|a^{[1]}| \sim l^3$ and $|r^{[1]}| \sim l^{-1}$. Many physical systems indeed exhibit this kind of natural scaling.

However, there also exist diverse systems, where the scattering length is large compared to the natural length scale. Such systems represent ideal candidates for a description within a non-relativistic EFT framework with contact interactions. The required parameter fine-tuning can either (i) simply occur by nature or (ii) be generated artificially by experimental means:

(i) Systems with accidental parameter fine-tuning can e.g. be found in nuclear physics. For example, the scattering length for two-neutron spin-singlet scattering was measured to be $a^{[0]}_{nn} = -18.7(6)$ fm [14], whereas the corresponding effective range $r^{[0]}_{nn} = 2.75(11)$ fm [15] is approximately one order of magnitude smaller. Also hypothetical hadronic molecules such as $X(3872)$ and $Y(4660)$, which were recently discovered by the Belle collaboration [16, 17], are candidates for systems with accidentally large scattering lengths [18, 19]. Another even more prominent example are halo nulcei, which are the main topic of this work and will be introduced in sec. 1.2.3.

(ii) A class of systems that belongs to the second category are ultracold atomic or molecular gases. Thereby, experimental tuning of the scattering length is achieved by varying an external magnetic field, generating a so-called *Feshbach resonance* [20]. The basis for this mechanism is the existence of both an open and a closed channel in the scattering of two particles. Modulating the external field, the depth of the closed channel is tuned such that one of its bound-state energy levels moves as close as possible to the threshold in the open channel. This way, a large scattering length and an enhancement in the cross section is produced. Feshbach resonances have first been observed in Bose–Einstein condensates of alkali atoms [21, 22].

The interesting observation for all those systems with large scattering length is that they display *universal* features [23]. This means that observables, in terms of the low-energy scattering parameters, only depend on the scattering length. For resonant S-wave scattering, the simplest manifestation of universality is the existence of a shallow two-body bound state. This can be understood as follows: Assuming that $f^{[0]}$ is the dominant contribution to the scattering amplitude (1.3) and that $|a^{[0]}| \gg |r^{[0]}|$ holds, the existence of a two-body bound state requires $f^{[0]}$ to have a pole at imaginary binding momentum $p = i\gamma$. Consequently, the denominator in eq. (1.6) has to vanish according to:

$$0 \;=\; -\frac{1}{a^{[0]}} + \frac{r^{[0]}}{2}\,(i\gamma)^2 - i(i\gamma) \;=\; -\frac{r^{[0]}}{2}\left[\gamma^2 - \frac{2}{r^{[0]}}\,\gamma + \frac{2}{a^{[0]}r^{[0]}}\right] \quad . \tag{1.8}$$

The two possible solutions are:

$$\gamma_{\pm} \;=\; \frac{1}{r^{[0]}} \pm \sqrt{\frac{1}{(r^{[0]})^2}\left(1 - 2\,\frac{r^{[0]}}{a^{[0]}}\right)} \;\approx\; \frac{1}{r^{[0]}}\left[1 \mp 1 \pm \frac{r^{[0]}}{a^{[0]}}\right] \;=\; \begin{cases} +\frac{1}{a^{[0]}} \\ -\frac{1}{a^{[0]}} + \frac{2}{r^{[0]}} \end{cases} \quad . \tag{1.9}$$

Consequently, there exists a bound state near the two-body threshold with binding energy $E^{(2)} = (i\gamma_+)^2/(2\mu) = -1/(2\mu(a^{[0]})^2)$. Except for the reduced mass, $E^{(2)}$ indeed only depends on the scattering length. So far, universal features predominantly have been investigated in the two- and three-particle sector.

Closely related to universality is the so-called *unitary limit*. It is characterized by vanishing effective range parameters: $1/a^{[\ell]} \to 0$, $r^{[\ell]}/2 \to 0$, etc. Thus, in terms of parameter space, the regime of universality can be seen as the neighborhood of the unitary limit. The word "unitary" comes from the fact that, in the unitary limit, the only remaining term in the expansion (1.6) is $-ip^{2\ell+1}$, which itself guarantees the unitarity of the S-matrix.

The three-particle sector of a theory can exhibit another interesting phenomenon called *discrete scale invariance*. First of all, of course, there exists a trivial continuous scale invariance: For any $\lambda > 0$, the rescaling of every kinematic variable (momenta, cut-offs, energies, etc.), scattering parameter (scattering length, effective range, etc.) and mass by powers of λ simply results in rescaling amplitudes and observables by powers of λ. By the corresponding powers of λ we mean that if a quantity has dimension m, it is rescaled by a factor of λ^m. This continuous scale invariance also holds if only all kinematic variables and scattering parameters are rescaled. In the unitary limit, where all effective range parameters vanish, this in turn effectively reduces to a continuous scale invariance in the kinematic variables. However, for some configurations in the three-particle sector, there exists an additional discrete scale invariance in the unitary limit. Thereby, quantities such as the scattering amplitude are scale-invariant for some specific number $\lambda_0 > 0$, even if only an appropriate subset of kinematic variables (for instance, take only the ultraviolet momentum cut-off Λ) is rescaled. λ_0 is called the *discrete scaling factor*. In terms of a dimensionless three-body coupling H that depends on the cut-off, discrete scale invariance is directly connected to an ultraviolet (UV) *limit cycle* in the *renormalization group* (RG) [24]. If the UV cut-off runs through a λ_0-cycle, the three-body coupling returns to its original value: $H(\lambda_0\Lambda) = H(\Lambda)$. Only in the unitary limit discrete scale invariance is exact. In the region of universality around this unique point it is only approximately valid.

Assuming that a three-body system exhibits discrete scale invariance and, in addition, has a three-body bound state at the energy $E = E^{(3)} < 0$, the existence of further bound states at $E^{(z)} = \lambda_0^{2z} E^{(3)}$ with $z \in \mathbb{Z}$ directly follows. Hence, there is a whole tower of countably infinitely many three-body bound states forming a geometric spectrum which is unbound from below and has an accumulation point at $E = 0$. This remarkable phenomenon is known as the *Efimov effect* and was already predicted in 1970 [25]. Counterintuitively, it can even occur for so-called *Borromean* three-particle systems, where none of the two-particle subsystems is bound. Phenomena in nature that are closely related to the Efimov effect are often referred to as *Efimov physics* [26]. Details about the connection between the Efimov effect and RG methods can e.g. be found in [27]. With the help of the afore-mentioned Feshbach resonances in ultracold gases, the Efimov effect eventually became experimentally accessible as it exhibits typical signatures in recombination rates. The first Efimov three-body bound state was discovered 2005 in a ^{133}Cs ensemble [28]. Subsequent experiments with ^{39}K and ^{7}Li gases then also confirmed the existence of an Efimov spectrum with discrete scale invariance [29, 30]. Also for mixtures of atoms, such as ^{87}Rb-^{41}K [31], the Efimov effect was found [32]. As a natural consequence of discrete scale invariance, an exact Efimov effect is only present in the unitary limit. Of course, this individual point in parameter space can not exactly be reached experimentally such that at best an approximate accumulation point is observed. Moreover, any real Efimov spectrum will be bound from below, since the entire theory is a low-energy approximation and can not be extended to infinitely large binding momenta. Thus, a real experiment within the universal regime will always at best detect an approximate Efimov effect with a finite number of three-body Efimov states that are connected through an approximate discrete scale invariance.

1.2.3 Halo EFT and halo nuclei

A prominent example for an EFT with large scattering length is *halo EFT*. Within a halo EFT framework, a complex many-particle system, such as an atomic nucleus, is effectively treated in terms of only a view degrees of freedom, namely a tightly bound core surrounded by a halo of a few spectator particles. In contrast to ab initio approaches, which try to predict nuclear observables from a fundamental nucleon-nucleon interaction, halo

EFT essentially provides relations between different nuclear low-energy observables. When information on the interaction between the core and the spectator particles is known, it provides a framework that facilitates a consistent calculation of continuum and bound-state properties. On the other side, it can also be used in the opposite direction, where the knowledge of a sufficient number of few-body observables restricts the two-body scattering properties. A technical advantage of halo EFT over a more fundamental theory, of course, is that through the reduction of the number of fundamental fields the overall computational complexity decreases significantly.

For many suspected *halo nuclei*, the spectator particles are simply weakly-attached valence nucleons [33–36]. Usually, such halo nuclei are identified by an extremely large matter radius or a sudden decrease in the one- or two-nucleon separation energy along an isotope chain. Thus, they display a separation of scales which exhibits itself also in low-energy scattering observables through a scattering length a that is large compared to the range R of the core-nucleon interaction. The corresponding small ratio $R/|a|$ can then be used as an expansion parameter of the halo EFT [37–40]. With regard to the chart of nuclides, natural candidates for halo nuclei are located along its proton- and neutron-rich boundaries called *drip lines*. For a recent theoretical determination of those lines, see e.g. ref. [41]. Nuclei along the proton drip line have a proton excess and predominantly decay through proton emission, positron emission or electron capture. Isotopes at the neutron drip line have a neutron excess. Their major decay channels are neutron emission and beta decay. In fig. 1.1 the lightest known halo nuclei or halo nuclei candidates are given. There seem to exist isotopes with one, two and even four spectator nucleons in the halo. The determination of the properties of those isotopes poses one of the major challenges for modern nuclear experiment and theory. The associated observables are an important input to studies of stellar evolution and the formation of elements and provide insight into fundamental aspects of nuclear structure. An up to date overview of the experimental and theoretical state of the art in the field of halo nuclei can be found in the proceedings of a recent Nobel Symposium on physics with radioactive beams [42].

Halo nuclei can also be examined under the aspects of Efimov physics and universal features, which we discussed in sec. 1.2.2. Whether there exists any excited Efimov state in the nuclear landscape is still unclear. The most promising system known so far is ^{22}C, which was found to display an extremely large matter radius [44] and is known to have a significant S-wave component in the ^{20}C-n subsystem [45]. In a previous work, Canham and Hammer [46, 47] explored universal properties and the structure of such two-neutron halo nuclei candidates to NLO in the expansion in $R/|a|$. They described the halo nucleus as an effective three-body system consisting of a core and two loosely bound valence neutrons and discussed the possibility of such three-body systems to display multiple Efimov states. In addition matter density form factors and mean square matter radii were calculated. Using this framework, Acharya et al. recently carried out a detailed analysis of the ^{22}C system [48]. The implications of the large ^{22}C matter radius for the binding energy and the possibility of excited Efimov states were discussed. For a selection of previous studies of the possibility of the Efimov effect in halo nuclei using three-body models, see refs. [49–52]. A recent review can be found in [53]. However, typically only very few observables in these

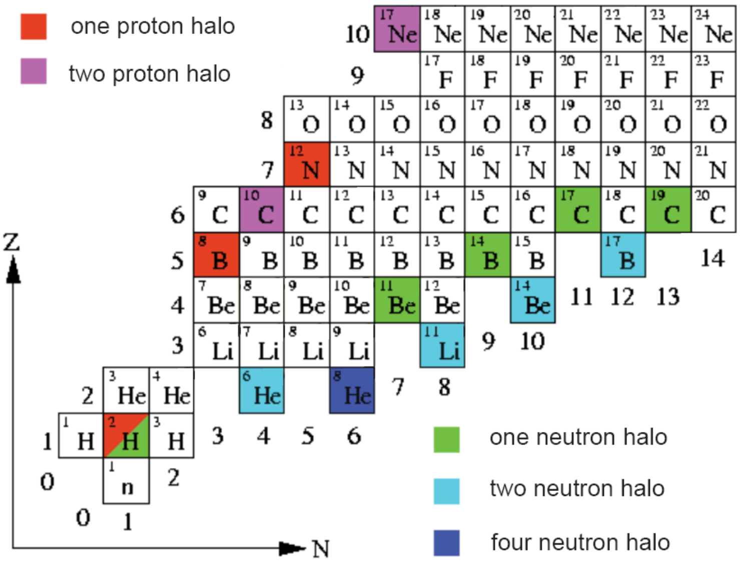

Figure 1.1: The lightest known halo nuclei or halo nuclei candidates. The depicted section ($Z \leq 10$,$N \leq 14$) of the chart of nuclides is extracted from ref. [43]. The proton- and neutron-halo systems are located at the corresponding drip lines. Nuclides in light blue cells qualify for a two-neutron halo EFT analysis.

systems are accessible experimentally such that a definitive proof for an excited Efimov state is yet to come.

1.3 Notation and conventions

The following conventions will be used throughout this work and are valid if not specified otherwise. They will contribute to a convenient and consistent notation.

Particles: In this work, we consider systems of at most three scalar particles. Thereby, two situations occur: the case with three distinguishable particle fields (ψ_0, ψ_1, ψ_2) and the case where two of them are equal (ψ_0, ψ_1, ψ_1). We now present a convenient notation in which both configurations can be treated within the same framework. Therefore, we first define the set of possible scalar field indices I_1 through:

$$I_1 \ := \begin{cases} \{0,1,2\} & : \ (\psi_0, \psi_1, \psi_2) \\ \{0,1,1\} = \{0,1\} & : \ (\psi_0, \psi_1, \psi_1) \end{cases} . \tag{1.10}$$

In our theory, we allow two-particle S- or P-wave interactions between different scalar particles. If all three particles are of different type, there are three possible pairs of two different particles: $(1,2)$, $(2,0)$ and $(0,1)$. They are elements of I_1^2. In the case where two of the three particles are of the same kind, there is only one such possible pair, i.e. $(0,1) \in I_1^2$. For a system of three particles, the specification of one index completely determines the other two. We take advantage of this fact, by identifying a particle pair by the index of the remaining third particle. The corresponding set $I_2 \subset I_1$ is defined through:

$$I_2 \ := \begin{cases} \{0,1,2\} = I_1 & : \ (\psi_0, \psi_1, \psi_2) \\ \{1\} & : \ (\psi_0, \psi_1, \psi_1) \end{cases} . \tag{1.11}$$

The identification can then be formalized via the mapping:

$$\sigma : I_2 \to I_1^2 \quad , \qquad \sigma(i) \;:=\; \begin{cases} (i_1, i_2) \text{ with } i, i_1, i_2 \text{ cyclic} & : \; (\psi_0, \psi_1, \psi_2) \\ (0, 1) & : \; (\psi_0, \psi_1, \psi_1) \quad . \end{cases} \tag{1.12}$$

We use this rather mathematical approach, since it can be applied to a large class of three-body systems. However, for reasons of readability, we will drop the redundant symbol σ and simply use $i_1 = (\sigma(i))_1$ and $i_2 = (\sigma(i))_2$ or $j = (\sigma(i))_1$ and $k = (\sigma(i))_2$ implicitly in subsequent considerations.

Masses: Considering the masses in the three-particle system, we take the mass of ψ_i to be m_i for all $i \in I_1$. Furthermore, we define M_Σ and M_Π as the sum and the product of all three particle masses, respectively:

$$M_\Sigma \;:=\; \begin{cases} m_0 + m_1 + m_2 & : (\psi_0, \psi_1, \psi_2) \\ m_0 + 2m_1 & : (\psi_0, \psi_1, \psi_1) \end{cases} \quad , \quad M_\Pi \;:=\; \begin{cases} m_0 m_1 m_2 & : (\psi_0, \psi_1, \psi_2) \\ m_0 m_1^2 & : (\psi_0, \psi_1, \psi_1) \; . \end{cases} \tag{1.13}$$

Additionally, for all $i \neq j \in I_1$, we define a number of mass-related quantities, namely single- and two-particle masses m_{ij} and M_i, reduced masses μ_i and $\bar{\mu}_i$, a total reduced mass $\bar{M}$, dimensionless mass ratios ω_{ij} and angles ϕ_{ij}. Their definitions read:

$$\begin{aligned} m_{ij} \;&:=\; \frac{M_\Pi}{m_i m_j} \;=\; M_\Sigma - m_i - m_j \quad , \qquad M_i \;:=\; M_\Sigma - m_i \quad , \\ \mu_i \;&:=\; \frac{M_\Pi}{m_i M_i} \quad , \quad \bar{\mu}_i \;:=\; \frac{m_i M_i}{M_\Sigma} \quad , \quad \bar{M} \;:=\; \sqrt{\frac{M_\Pi}{M_\Sigma}} \quad , \\ \omega_{ij} \;&:=\; \frac{m_{ij}}{\sqrt{\mu_i \mu_j}} \;=\; \sqrt{\big(1 + \frac{m_{ij}}{m_i}\big)\big(1 + \frac{m_{ij}}{m_j}\big)} \;>\; 1 \quad , \\ \phi_{ij} \;&:=\; \arcsin(1/\omega_{ij}) \;\in\; (0, \pi/2) \quad . \end{aligned} \tag{1.14}$$

Using these quantities will contribute to a more convenient and compact notation in subsequent calculations, especially within the three-particle sector. The definitions for m_{ij} and ω_{ij} and ϕ_{ij} are restricted to unequal indices $i \neq j \in I_1$. Using the set of remaining third indices (1.11), we can alternatively also label them by according to $m_i = m_{i_1 i_2}$, $\omega_i = \omega_{i_1 i_2}$ and $\phi_i = \phi_{i_1 i_2}$.

Using the definitions (1.14) one can straightforwardly deduce the identity

$$\cot^2 \phi_i \;=\; \omega_i^2 - 1 \;=\; (m_i/\bar{M})^2 \quad , \tag{1.15}$$

which, for the mass angles, implies the relation:

$$\begin{aligned} \cos(\phi_0 + \phi_1 + \phi_1) \;&=\; \cos(\phi_0)\cos(\phi_1)\cos(\phi_2) \;-\; \sin(\phi_0)\sin(\phi_1)\cos(\phi_2) \\ &\quad -\; \sin(\phi_0)\cos(\phi_1)\sin(\phi_2) \;-\; \cos(\phi_0)\sin(\phi_1)\sin(\phi_2) \\ &=\; \frac{\sqrt{\omega_0^2 - 1}\sqrt{\omega_1^2 - 1}\sqrt{\omega_2^2 - 1} - \sqrt{\omega_2^2 - 1} - \sqrt{\omega_1^2 - 1} - \sqrt{\omega_0^2 - 1}}{\omega_0 \omega_1 \omega_2} \\ &=\; \frac{m_0 m_1 m_2 / \bar{M}^3 - (m_0 + m_1 + m_2)/\bar{M}}{\omega_0 \omega_1 \omega_2} \;=\; 0 \quad . \end{aligned} \tag{1.16}$$

Since $\phi_0 + \phi_1 + \phi_2 \in (0, 3\pi/2)$ holds, the only possible configuration for their sum is:

$$\phi_0 + \phi_1 + \phi_2 \;=\; \pi/2 \quad . \tag{1.17}$$

Consequently, the allowed parameter space for the three mass angles ϕ_0, ϕ_1 and ϕ_2 can be represented in a Dalitz-like Plot for the variables ϕ_0, ϕ_1 and ϕ_2, where $m_i = \cot\phi_i\,\bar{M}$ reproduces the original masses. The relations (1.15)-(1.17) are valid for any three numbers $\{m_0, m_1, m_2\}$ and thus, a priori, do not have physical significance. However, it turns out that the quantities ω_i and ϕ_i naturally appear in calculations of systems with three particles such that their use is beneficial.

Energy and momenta: We label all four-momenta by upper bars. For example, a real four-momentum reads $\bar{p} \in \mathbb{R}^4$. It has a zeroth component $p^0 \in \mathbb{R}$ and a three-vector, which is labeled as a bold type letter $\mathbf{p} \in \mathbb{R}^3$. Furthermore, the modulus of such a vector will be denoted as $p := |\mathbf{p}|$. Unit vectors will be labeled by $\mathbf{e}_i$, where, of course, $(\mathbf{e}_i)_j = \delta_{ij}$ holds. In addition, for a given three-vector $\mathbf{p}$ the corresponding unit vector reads $\mathbf{e_p} := \mathbf{p}/p$. The same conventions hold for four-dimensional space-time vectors $\bar{x} \in \mathbb{R}$. In later calculations we will often consider matrix elements that depend on four-momenta. In order to compactify the notation,the following rules are used:

- If for a given function $X(\ldots, \bar{p}, \ldots)$ the four-momentum $\bar{p}$ is put on-shell, we define

  $$X(\ldots, \mathbf{p}, \ldots) \;:=\; X(\ldots, \bar{p}, \ldots)|_{\text{on-shell condition for } \bar{p}} \quad . \tag{1.18}$$

  The concrete form of the on-shell condition for $\bar{p}$ depends on the chosen kinematics. For the calculations in sec. 2.3, where two-particle P-wave interactions are considered, we will use center-of-mass kinematics with the on-shell condition (2.31). With regard to two-neutron halo nuclei EFT with external currents, which is presented in chapter 3, we will use more general kinematics with the condition (3.18).

- If a function $X(\ldots, \mathbf{p}, \ldots)$ effectively only depends on the modulus of the three-vector $p = |\mathbf{p}|$, we will always use the redefinition

  $$X(\ldots, p, \ldots) \;:=\; X(\ldots, p \cdot \mathbf{e}_3, \ldots) \quad , \tag{1.19}$$

  where, of course, $\mathbf{e}_3$ could also be replaced by any other unit vector.

- If a function $X(\bar{P}, \ldots)$, with $\bar{P} = \bar{P}(E)$ being the total four-momentum of the halo system, effectively only depends on the energy variable E, we define:

  $$X(E, \ldots) \;:=\; X(\bar{P}(E), \ldots) \quad . \tag{1.20}$$

- If, furthermore, for a function $X(E, \ldots)$ the energy is fixed to a three-body binding energy $E = E^{(3)}$, we simply drop this variable according to:

  $$X(\ldots) \;:=\; X(E^{(3)}, \ldots) \quad . \tag{1.21}$$

  Two-body binding energies will be labeled by $E^{(2)}$.

Three-body force: For any quantity F that implicitly depends on the three-body force $\bar{H}$, we will use the following convention:

$$^{\bullet}F \;:=\; F\big|_{\bar{H}=0 \text{ in the interaction}} \quad . \tag{1.22}$$

Indices: Considering the indices of function or quantity X, such as $X_{ij}^{[j_1m_1;j_2m_2|j_3m_3;j_4m_4]}$, subscripts always represent particle types or particle channels, whereas superscripts denote spatial components or angular momentum quantum numbers. The latter ones are always written in square brackets $^{[\dots|\dots]}$. The optional line $|$ in the middle separates the angular momentum quantum numbers of the left, incoming state that corresponds to i from those of the right, outgoing state that corresponds to j. If an incoming or outgoing state has not yet been projected to angular momentum eigenstates, the corresponding side in the square brackets is left empty. A Clebsch–Gordan coefficient (CGC) that couples angular momenta j_1 and j_2 to J will be labeled by $C_{j_1m_1;j_2m_2}^{JM}$, where the remaining indices are the magnetic quantum numbers.

With regard to angular momentum, we will use implicit lower and upper bounds in summations over the quantum numbers ℓ and m according to:

$$\sum_{\ell}(\dots) := \sum_{\ell=0}^{\infty}(\dots) \quad , \quad \sum_{m}(\dots) := \sum_{m=-\ell}^{\ell}(\dots) \quad . \tag{1.23}$$

We will use this short notation for total angular momenta (j and m), for orbital angular momenta (ℓ and m) as well as for spin (S and s).

Chapter 2

Three-body halos with P-wave interactions

The lightest two-neutron halo nucleus known so far is ^{6}He [34,36]. As a three-body system it contains the alpha particle ^{4}He as a core, which is surrounded by two spectator neutrons. The subsystem ^{5}He is unstable such that ^{6}He is Borromean. The ^{4}He-n scattering reveals a strong P-wave resonance. An analysis within an EFT framework of the ^{5}He system can be found in [37]. Also the many-body physics of spin-1/2 fermions interacting via resonant P-wave couplings have been studied using mean-field approximations [54–58]. However, such approximations fail to describe qualitatively new features that might occur if the P-wave interactions are strongly resonant [59]. Thus, the question arises how a halo EFT can be formulated in order to describe a bound three-body halo nucleus containing resonant two-particle P-wave interactions. Furthermore, we want to understand if such a system, in principle, can exhibit discrete scale invariance and the Efimov effect.

In this chapter, we address this question within a slightly modified approach, by dropping the requirement for the three-particle system to be a halo nucleus. More generally, we simply consider a system of three scalar particles with resonant two-particle P-wave interactions and investigate the possibility of bound states and Efimov physics within its three-particle sector. In this way, our ansatz also applies to atomic physics, which appears beneficial, since again ultracold atoms provide a promising laboratory for experimental studies. By modulating an external magnetic field, now the scattering volume $a^{[1]}$ can be tuned to arbitrarily large values with the help of a P-wave Feshbach resonance near threshold. The first experimental studies of such resonances used ultracold ensembles of fermionic ^{40}K atoms [60]. Also fermionic ^{6}Li atoms and fermion-boson mixtures such as ^{40}K-^{87}Rb have been studied in this context [61–63]. Furthermore, binding energies and inelastic collision rates of P-wave dimers have been measured [64,65]. Since P-wave Feshbach resonances in ultracold atoms usually are very narrow, precise experimental studies with fine-tuned $a^{[1]}$ are challenging.

We also want to compare our findings for two-particle P-wave interactions with already known results for the S-wave case. Therefore, in the following, we first shed some light on the structure of the Lagrangian for such EFTs. Especially, we discuss allowed building blocks and explain the introduction of auxiliary fields in a very general manner.

2.1 Fundamentals of non-relativistic EFTs

In this section, we briefly repeat general basic properties of non-relativistic EFTs with contact interactions. Therefore, we assume that the degrees of freedom of our theory are $N \in \mathbb{N}$ distinguishable types of scalar fields $\{\psi_i : \mathbb{R}^4 \to \mathbb{C} | i \in \{0, \dots, N-1\}\}$. Every single field ψ_i can either be bosonic or fermionic. Since we consider three-body halo systems, the number of such fields is limited to $N \leq 3$. The dynamics and interactions between the scalar fields, are then described in terms of a Lagrangian $\mathcal{L}$.

2.1.1 Galilean invariance

For a relativistic field theory, invariance under Lorentz-transformations is a fundamental requirement. These transformations form the so-called *Lorentz group*. Since in this work all appearing velocities are small compared to the speed of light, we only demand invariance under the non-relativistic limit of the Lorentz group, the so-called *Galilean group* [66]. This way, it is guaranteed that the physics in two inertial frames, connected through a Galilean transformation, are the same.

2.1.1.1 Galilean group

First, we briefly recall the structure of the Galilean group. It is defined as the set $\mathcal{G}$ with an operation $\circ : \mathcal{G} \times \mathcal{G} \to \mathcal{G}$ given through:

$$\begin{aligned} \mathcal{G} \;&=\; \left\{ \; (R, \mathbf{v}, \bar{a}) \;\in\; SO(3) \times \mathbb{R}^3 \times \mathbb{R}^4 \; \right\} \quad , \\ (R, \mathbf{v}, \bar{a}) \;\circ\; (S, \mathbf{w}, \bar{b}) \;&=\; \left(RS,\; \mathbf{v} + R\mathbf{w},\; \left(\begin{smallmatrix} 1 & 0 \\ \mathbf{v} & R \end{smallmatrix}\right) \bar{b} + \bar{a}\right) \quad . \end{aligned} \tag{2.1}$$

This composition is closed, associative, its identity element is $(\mathbb{1}, \mathbf{0}, 0) \in \mathcal{G}$ and the inverse of an element is: $(R, \mathbf{v}, \bar{a})^{-1} = \left(R^{\mathrm{T}}, -R^{\mathrm{T}}\mathbf{v}, -\left(\begin{smallmatrix} 1 & 0 \\ -R^{\mathrm{T}}\mathbf{v} & R^{\mathrm{T}} \end{smallmatrix}\right) \bar{a}\right) \in \mathcal{G}$.

2.1.1.2 Galilean invariants

Before performing a field quantization, our theory is formulated in terms of a fundamental Lagrangian $\mathcal{L}$ and an action functional $\mathcal{S}[\psi_0, \dots, \psi_{N-1}] = \int_{\mathbb{R}^4} \mathrm{d}x^4 \mathcal{L}(\psi_0, \dots, \psi_{N-1})(\bar{x})$, which is the space-time integral over the Lagrangian. The stationary points of this action are the physical field configurations that are realized in nature. Using Hamilton's principle then yields the Euler–Lagrange equations, which are the equations of motion for the fields. Thus, requiring Galilean invariance directly translates to the invariance of the action $\mathcal{S}[h\psi_0, \dots, h\psi_{N-1}] = \mathcal{S}[\psi_0, \dots, \psi_{N-1}]$ under a general element $h = (R, \mathbf{v}, \bar{a})$ of the Galilean group. h acts on space-time vectors $\bar{x} \in \mathbb{R}^4$ according to $(R, \mathbf{v}, \bar{a})\bar{x} = \left(\begin{smallmatrix} 1 & 0 \\ \mathbf{v} & R \end{smallmatrix}\right) \cdot \bar{x} + \bar{a}$. Consequently, substituting $\bar{x} \mapsto h\bar{x}$ within a space-time integral $\int_{\mathbb{R}^4} \mathrm{d}x$ for any Galilean transformation simply leads to an additional factor $|1 \cdot \det(R)| = 1$ from the corresponding

Jacobian. In order to ensure the invariance of the action integral, we thus require the Lagrangian to be invariant under $\mathcal{G}$ according to $\mathcal{L}(h\psi_0, \ldots, h\psi_{N-1}) = \mathcal{L}(\psi_0, \ldots, \psi_{N-1}) \circ h^{-1}$. Hence, for setting up a general non-relativistic EFT framework, our task is to construct the corresponding Lagrangian from Galilean-invariant building blocks that contain the scalar fields.

We begin this procedure by analyzing how a scalar field ψ_i transforms under the elements of the Galilean group (2.1). The transformation rule reads:

$$\psi_i \;\mapsto\; h\psi_i \;=\; e^{im_i f_h} \cdot (\psi_i \circ h^{-1}) \quad , \qquad f_h(\bar{x}) \;=\; -\frac{1}{2}\mathbf{v}^2(x_0 - a_0) + \mathbf{v}^{\mathrm{T}}(\mathbf{x} - \mathbf{a}) \quad . \tag{2.2}$$

The unobservable phase factor contains the particle mass m_i and the real function $f_h : \mathbb{R}^4 \to \mathbb{R}$, whose specific form is determined by combining the following two constraints: First, it is required that the transformation (2.2) leaves the non-relativistic free propagation part $\mathcal{L}_i^{(\mathrm{free})}(\psi_i) = \psi_i^\dagger (i\partial_0 + \nabla^2/(2m_i))\psi_i$ of the Lagrangian invariant. Second, eq. (2.2) also has to give a representation of the Galilean group. In short, field transformations according to (2.2) are a local $U(1)$ symmetry of the free Lagrangian.

From eq. (2.2) we directly calculate the transformation behavior for derivatives of the scalar fields:

$$\begin{aligned}
\partial_\mu \psi_i \;&\mapsto\; \partial_\mu(h\psi_i) \\
&= \; e^{im_i f_h} \begin{cases} \left[\left(-i\frac{m_i \mathbf{v}^2}{2} + \partial_0 - \mathbf{v}^{\mathrm{T}} R\nabla\right)\psi_i\right] \circ h^{-1} & : \mu = 0 \\ \left[(im_i \mathbf{v} + R\nabla)_j \, \psi_i\right] \circ h^{-1} & : \mu = j \in \{1,2,3\} \end{cases} \quad , \\
\nabla^2 \psi_i \;&\mapsto\; \nabla^2(h\psi_i) \;=\; e^{im_i f_h} \; \left[\left(-m_i^2 \mathbf{v}^2 + 2im_i \mathbf{v}^{\mathrm{T}} R\nabla + \nabla^2\right)\psi_i\right] \circ h^{-1} \quad .
\end{aligned} \tag{2.3}$$

Using these transformation rules (2.2) and (2.3) one can demonstrate the invariance of the free Lagrangian via:

$$\begin{aligned}
\mathcal{L}_i^{(\mathrm{free})}(\psi_i) \;&\mapsto\; \mathcal{L}_i^{(\mathrm{free})}(h\psi_i) \;=\; (h\psi_i)^\dagger \left(i\partial_0 + \frac{\nabla^2}{2m_i}\right)(h\psi_i) \\
&= \; \left[\psi_i^\dagger \left(\frac{m_i \mathbf{v}^2}{2} + i\partial_0 - i\mathbf{v}^{\mathrm{T}} R\nabla - \frac{m_i \mathbf{v}^2}{2} + i\mathbf{v}^{\mathrm{T}} R\nabla + \frac{\nabla^2}{2m_i}\right)\psi_i\right] \circ h^{-1} \\
&= \; \mathcal{L}_i^{(\mathrm{free})}(\psi_i) \circ h^{-1} \quad .
\end{aligned} \tag{2.4}$$

Furthermore, the transformation rules (2.3) can be used in order to construct potential Galilean invariants that contribute to the interaction part of the full Lagrangian. Clearly any product of pairs of scalar fields $\psi_i^\dagger \psi_i$ is manifestly Galilean-invariant. If derivatives of the fields are included, Galilean invariance is less obvious. For example, the scalar $(i\nabla\psi_i)^\dagger(i\nabla\psi_i)$ is not Galilean-invariant, since eq. (2.3) leads to extra terms from $im_i\mathbf{v} \neq \mathbf{0}$. In order to subtract these interfering terms, we first define a mass operator $\hat{m}$ through $\hat{m}\psi_i = m_i\psi_i$. In addition, for any operator τ we define $\psi_i \overleftrightarrow{\tau} \psi_j = (\tau\psi_i)\psi_j - (\tau\psi_j)\psi_i$. Therewith we construct an invariant scalar that includes spatial derivatives:

$$(\psi_i \overleftrightarrow{\left(\frac{i\nabla}{\hat{m}}\right)} \psi_j)^\dagger (\psi_i \overleftrightarrow{\left(\frac{i\nabla}{\hat{m}}\right)} \psi_j) \quad . \tag{2.5}$$

Evidently, the expression (2.5) vanishes for $i = j$. Hence, from (2.5) one can only construct P-wave interactions between distinguishable particles. However, this will suffice for the systems that are considered in this work.

2.1.2 Auxiliary fields

We now consider a general non-relativistic theory for scalar particles $\{\psi_0, \dots \psi_{N-1}\}$ interacting via contact coupling terms. The Lagrangian for such a theory can be written very compactly in the way:

$$\mathcal{L} \;=\; \mathcal{L}^{(\mathrm{free})} \;+\; \mathcal{L}^{(\mathrm{int})} \quad , \qquad \mathcal{L}^{(\mathrm{int})} \;=\; -\Psi^\dagger G\, \Psi \;=\; -\sum_{\alpha,\beta} \Psi^\dagger_\alpha G_{\alpha\beta} \Psi_\beta \quad , \tag{2.6}$$

$\mathcal{L}^{(\mathrm{free})} = \sum_{i=0}^{N-1} \mathcal{L}_i^{(\mathrm{free})}$ describes the free propagation of the scalar fields. The vector Ψ in the interaction part $\mathcal{L}^{(\mathrm{int})}$ has components Ψ_α that are linear combinations of field products. Their specific form is determined by the multi-index alpha. Note that this very general notation (2.6) covers possible interactions between two fields $\propto (\psi_i\psi_j)^\dagger(\psi_i\psi_j)$, three fields $\propto (\psi_i\psi_j\psi_k)^\dagger(\psi_i\psi_j\psi_k)$, etc. In addition, also coupling terms with derivatives according to (2.5) are allowed. The appearing hermitian matrix G with multi-indices α and β then specifies how these different channels are coupled together in a Galilean-invariant manner. Of course, G can be diagonal, as it will be the case in our later considerations. For this section, we define the order of a field product Ψ_α to be the number of scalar field factors it is composed of. In addition, we define the order $|\alpha|$ of a multi-index α as the order of the corresponding field product Ψ_α. For instance, the P-wave interaction (2.5) consists of two field products of order two.

For the calculation of matrix elements, it is often functional to introduce auxiliary fields, which represent specific products of the scalar fields. An auxiliary field of this type is called a *dimer* or a *trimer* if it represents a field product of order two or three, respectively. As in this work we consider systems of at most three particles, only these two cases will be relevant to us. However, since the effort will be the same, at this point we proceed with a more general analysis including also higher order products, such as tetramers, pentamers, etc. For instance, tetramers have been studied in the past for the case of four identical bosons [67]. The crucial requirement for a modified Lagrangian with general auxiliary fields is that after eliminating these fields via Euler–Lagrange equations, the initial theory described by the Lagrangian (2.6) has to be reproduced. Consequently, both theories will then describe the same physical dynamics for the fundamental degrees of freedom $\{\psi_0, \dots, \psi_{N-1}\}$.

2.1.2.1 Equivalent Lagrangians

Our method of equivalently rewriting the Lagrangian is based on Hubbard–Stratanovich transformations. For each field product Ψ_α we introduce an auxiliary fields d_α. We will denote the vector of all these auxiliary fields by d and couple it to Ψ via an arbitrary invertible matrix A in the way:

$$\mathcal{L}_d^{(\mathrm{int})} = \mathcal{L}^{(\mathrm{int})} + \big(\Psi - Ad\big)^\dagger G\big(\Psi - Ad\big) = d^\dagger A^\dagger G A\, d - d^\dagger A^\dagger G\, \Psi - \Psi^\dagger\, G A\, d \quad . \tag{2.7}$$

The Euler–Lagrange equations for the auxiliary fields then read:

$$0 = \frac{\partial \mathcal{L}_d^{(\mathrm{int})}}{\partial d^\dagger} = -A^\dagger G\big(\Psi - A\, d\big) \qquad \Leftrightarrow \qquad G\big(\Psi - A\, d\big) = 0 \quad . \tag{2.8}$$

Integrating out d by inserting the equation of motion (2.8) into the Lagrangian (2.7), the equivalence to the fundamental theory for the scalar fields (2.6) becomes obvious:

$$\mathcal{L}_d^{(\mathrm{int})} = \mathcal{L}^{(\mathrm{int})} + \big(\Psi - Ad\big)^\dagger 0 = \mathcal{L}^{(\mathrm{int})} \quad . \tag{2.9}$$

Using this method, there are as many equivalent Lagrangians as there are invertible matrices A. In this sense there exists a whole class of equivalent theories.

2.1.2.2 Equivalence up to higher orders

Using the Lagrangian (2.7), field products of arbitrary high order are coupled to auxiliary fields. For later purposes, we only want to introduce auxiliary fields up to certain order, in our case dimers and trimers, which are of order two and three, respectively. Thus, the general task is to construct an equivalent Lagrangian in which only field products of order $|\alpha| \leq n$ are coupled to auxiliary fields d. One way to formalize this in a compact way is to define a projection operator P which projects all quantities onto this subset of field products via:

$$\begin{aligned} &P_{\alpha\beta} := \Theta(n - |\alpha|)\, \delta_{\alpha\beta} \;\Rightarrow\; P^2 = P \quad , \qquad \Psi' := P\Psi \quad , \quad d' := Pd \quad , \\ &G' := PGP \quad , \qquad A' := PAP \quad , \qquad H := G - G' \quad . \end{aligned} \tag{2.10}$$

The symbol $'$ labels the projected quantities. The matrix H exactly contains all higher order couplings. Θ is the Heaviside step function with the convention $\Theta(0) = 1$. We now construct the Lagrangian for the projected quantities very analogous to eq. (2.7):

$$\begin{aligned} \mathcal{L}_{d'}^{(\mathrm{int})} &= -\,\Psi'^\dagger\, G'\, \Psi' + \big(\Psi' - A'\, d'\big)^\dagger G'\big(\Psi' - A'\, d'\big) \\ &\quad - \big(C(\Psi)\, A'\, d'\big)^\dagger\, H\, \big(C(\Psi)\, A'\, d'\big) \\ &= d'^\dagger\, A'^\dagger G'\, A'\, d' - d'^\dagger\, A'^\dagger G'\, \Psi' - \Psi'^\dagger\, G'\, A'\, d' \\ &\quad - d'^\dagger\, A'^\dagger\, C(\Psi)^\dagger\, H\, C(\Psi)\, A'\, d' \quad . \end{aligned} \tag{2.11}$$

The only additional term in eq. (2.11) contains a field-dependent matrix $C(\Psi)$ with components $C(\Psi)_{\alpha\beta} := c_{\alpha\beta} \Psi_\alpha \Psi_\beta^{-1}$ of order $|\alpha| - |\beta|$ in the fields. The only requirements on the coefficients $c_{\alpha\beta}$ are:

$$\begin{aligned} c_{\alpha\beta} &= 0 \quad \text{if} \quad |\beta| > n \quad \text{or} \quad \Psi_\alpha \neq (\text{ product of } \psi_i\text{'s }) \cdot \Psi_\beta \\ \wedge \quad \sum_{|\beta| \leq n} c_{\alpha\beta} &= 1 \quad . \end{aligned} \tag{2.12}$$

Consequently, there is a big freedom of choice in these coefficients. In later calculations, for convenience, we will always choose $c_{\alpha\beta} = \delta_{\gamma(\alpha),\beta}$ such that the H couplings will only be present in one specific channel $\gamma(\alpha)$. One can show that the Lagrangian (2.11) is again Galilean-invariant.

In order to prove the equivalence of $\mathcal{L}^{(\mathrm{int})}$ and $\mathcal{L}_{d'}^{(\mathrm{int})}$, we first use (2.12) to deduce:

$$\begin{aligned} \big(C(\Psi)\Psi'\big)_\alpha &= \sum_{\beta\gamma} c_{\alpha\beta}\, \Psi_\alpha\, \Psi_\beta^{-1}\, P_{\beta\gamma}\, \Psi_\gamma \;=\; \Psi_\alpha \sum_{|\beta|\le n} c_{\alpha\beta} \;=\; \Psi_\alpha \\ \Rightarrow\quad C(\Psi)\Psi' &= \Psi \quad . \end{aligned} \tag{2.13}$$

We now assume that the matrix resulting from G' after dropping the vanishing rows and columns is invertible. Using the short notation $R'(\Psi) := G'^{-1} C(\Psi)^\dagger\, H\, C(\Psi)$, the Euler–Lagrange equations for the projected auxiliary fields derived from the Lagrangian (2.11) read:

$$\begin{aligned} 0 \;&=\; \frac{\partial \mathcal{L}_{d'}^{(\mathrm{int})}}{\partial d'^\dagger} \;=\; -A'^\dagger G'\big(\Psi' - \big[\mathbb{1} - R'(\Psi)\big] A'\, d'\big) \\ \Rightarrow\qquad A'\, d' \;&=\; \big[\mathbb{1} - R'(\Psi)\big]^{-1}\Psi' \;=\; \sum_{k=0}^{\infty} R'(\Psi)^k\, \Psi' \;=\; \Psi' \;+\; R'(\Psi)\Psi' \;+\; \ldots \end{aligned} \tag{2.14}$$

Thereby, in addition, we assumed that the higher order couplings are small in a way that the geometric series of the matrix $R'(\Psi)$ exists. Integrating out d' by inserting the equation of motion (2.14) into eq. (2.11) and using eq. (2.13) then yields:

$$\begin{aligned} \mathcal{L}_{d'}^{(\mathrm{int})} &= 0 \;-\; \Psi'^\dagger\, G' \left[\Psi' \;+\; R'(\Psi)\Psi' \;+\; \ldots\right] \\ &= \;-\;\Psi'^\dagger\, G'\,\Psi' \;-\; \Psi'^\dagger\, C(\Psi)^\dagger\, H\, C(\Psi)\,\Psi' \;+\; \mathcal{L}^{(\ge n+2)} \\ &= \;-\;\Psi^\dagger\, G'\,\Psi \;-\; \Psi^\dagger\,(G - G')\Psi \;+\; \mathcal{L}^{(\ge n+2)} \\ &= \mathcal{L}^{(\mathrm{int})} \;+\; \mathcal{L}^{(\ge n+2)} \quad . \end{aligned} \tag{2.15}$$

The additional contribution $\mathcal{L}^{(\ge n+2)}$ includes interactions that contain field products of order $\ge n+2$. Thus, the described method leads to additional many-body forces. Later in this work we will introduce dimer fields of order $n = 2$, which consequently lead to extra contributions of order $\ge 2+2 = 4$ in eq. (2.15). Since we will only consider systems of at most three particles, such four-particle interactions will not appear in any calculation and can be dropped. Our method can be seen as a generalization of the diatom field trick that is presented in [23] for three identical particles.

The introduced auxiliary fields d_α can be made dynamical by adding extra terms $\eta_\alpha\, d_\alpha^\dagger(i\partial_0 + \nabla^2/M_\alpha)d_\alpha$, analogous to the free Lagrangian $\mathcal{L}^{(\mathrm{free})}$ for the scalar fields. In this case, M_α is the mass of d_α. A positive prefactor η_α corresponds to an ordinary, normalizable dimer, whereas a negative η_α corresponds to a non-normalizable so-called *ghost field.*

From now on we will use the short notations $\Delta := A'^\dagger G'\, A'$ and $g := G'\, A'$ for the coupling constants and drop all remaining $'$ symbols. Since G' is hermitian, it has real eigenvalues and can be diagonalized by a unitary matrix. Choosing A' to be proportional to this matrix, we can always diagonalize Δ. Further redefining A', even the modulus of these eigenvalues can be equalized. On the contrary, also the matrix g can be diagonalized by choosing $A' \propto G'^{-1}$. In this way, g is even proportional to the unit matrix. In the case where G is already diagonal, this leads to the fact that a theory with auxiliary fields can be formulated in a way where all the differences in the couplings can be absorbed into Δ or g. The entries of the other real diagonal matrix g or Δ then are constant or of constant modulus, respectively. All appearing couplings Δ, g and H are unobservable and, a priori, unknown. In our renormalization scheme, they depend on an ultraviolet cut-off.

Performing a field quantization with commutator and anticommutator relations for bosons and fermions, respectively, then yields the corresponding EFT framework. In the following sections, we will consider theories with S- and P-wave two-particle interactions that are constructed with the presented method.

2.2 S-wave interactions

2.2.1 Effective Lagrangian

Before we investigate possible Efimov physics for two-particle P-wave interactions, we present some results for the S-wave case [23]. As an example we consider a system of three distinguishable, non-relativistic, bosonic spin-0 fields (ψ_0, ψ_1, ψ_2). We assume that each of the three possible two-particle subsystems interacts resonantly via S-wave couplings. We use the notational conventions, presented in sec. 1.3 with one- and two-particle index sets $I_1 = \{0, 1, 2\}$ and $I_2 = I_1$. As explained in sec. 2.1.2, the two-body coupling terms can be rewritten equivalently by introducing S-wave dimers as auxiliary fields. We label these dimer fields by d_i with $i \in I_2$.

The system of three interacting bosons is then described by the Lagrangian:

$$\boxed{\begin{aligned} \mathcal{L} &= \mathcal{L}^{(1)} + \mathcal{L}^{(2)} \quad , \qquad \mathcal{L}^{(1)} = \mathcal{L}^{(\text{free})} = \sum_{i\in I_1} \psi_i^\dagger \Big(i\partial_0 + \frac{\nabla^2}{2m_i} \Big) \psi_i \quad , \\ \mathcal{L}^{(2)} &= \sum_{i \in I_2} \Big\{ \Delta_i \, d_i^\dagger \, d_i \; - \; g_i \, d_i^\dagger \psi_{i_1} \psi_{i_2} \; + \; \text{h.c.} \Big\} \quad . \end{aligned} \qquad (2.16)}$$

Eq. (2.16) includes one- and two-particle contributions. The one-particle Lagrangian $\mathcal{L}^{(1)}$ simply describes the free non-relativistic propagation of the bosonic fields. The S-wave coupling of these fields to auxiliary dimer fields is included in the two-particle contribution $\mathcal{L}^{(2)}$. It is constructed from an equivalent original theory without auxiliary dimer fields, via the method that is explained in sec. 2.1.2.2. The bare coupling parameters Δ_i and g_i are unknown and have to be renormalized. In our renormalization scheme, they depend on the ultraviolet cut-off in the two-particle sector and can be expressed in terms of low-energy

Figure 2.1: Dalitz-like plot for the discrete scaling factor $\lambda_0 = e^{\pi/s_0}$ in a three-boson system as a function of the three rescaled mass angles $\varphi_i := \phi_i/(\pi/2) \in (0,1)$. λ_0 displays a dihedral D_3 symmetry due to invariance under particle permutations. The distances of a point to the edges of the equilateral triangle are φ_0, φ_1 and φ_2. λ_0 is maximal in the center where all three masses are equal.

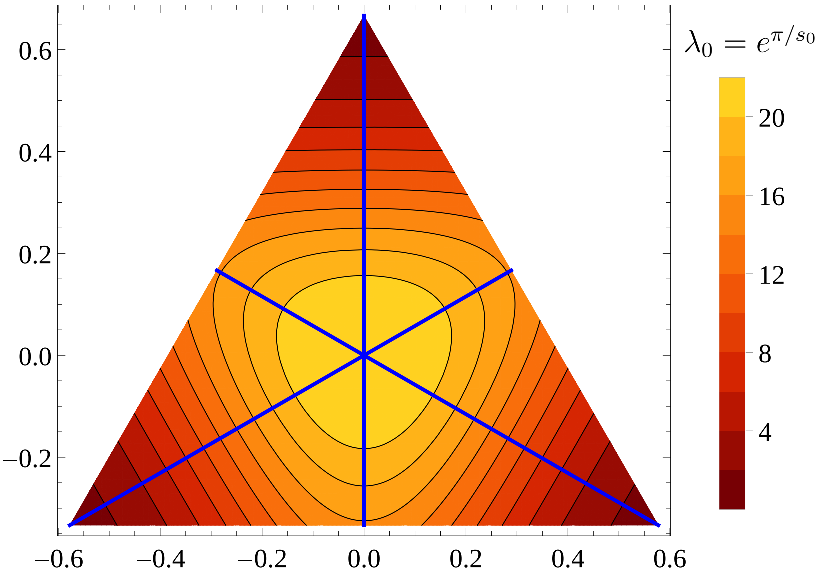

observables from the corresponding effective range expansion. In order to renormalize the three-particle sector of this theory, the introduction of an appropriate three-particle contribution would be required. Such a Lagrangian has also been applied to bosonic three-body systems such as the hypothetical hadronic molecule $Y(4660)$ [19, 68]. However, for the general results that are presented in this section, three-body renormalization is irrelevant and thus three-particle interactions are omitted.

2.2.2 Discrete scale invariance and the Efimov effect

For our considered system of three bosons, it turns out that the channel with total angular momentum $J = 0$ exhibits discrete scale invariance and the Efimov effect [23]. Thereby, the discrete scaling factor λ_0 is given in terms of $\lambda_0 = e^{\pi/s_0}$, where is_0 is a purely imaginary solution of the transcendental equation:

$$\begin{aligned} \mathcal{F}(s) &= 0 \quad \text{with} \quad \mathcal{F}(s) := \left|\det[\mathbb{1} - \mathcal{K}(s)]\right| \quad , \qquad \mathcal{K}(s) \in \mathbb{C}^{3\times 3} \quad , \\ \mathcal{K}_{ij}(s) &= \xi(\phi_{ij})\,\frac{\mathcal{Q}_0(\phi_{ij}, s)}{\sin\phi_{ij}} \quad , \quad \mathcal{Q}_0(\phi, s) \;=\; \pi\phi\,\frac{j_0(\phi s)}{\cos(\frac{\pi}{2}s)} \quad , \quad \xi(\phi) \;:=\; \frac{1}{\pi}\,\frac{1}{\cos\phi} \;. \end{aligned} \tag{2.17}$$

$j_0(x) = \sin(x)/x$ is the zeroth spherical Bessel function. Eq. (2.17) can be derived in a field theoretical approach with contact interactions as well as using Faddeev equations for a short-range potential (see e.g. [69] or eq. (389) in [23]). Details about the function $\mathcal{Q}_0$ can be found in appendix A.2.4. Interestingly, eq. (2.17) does not depend on the three particle masses but only on the mass angles ϕ_0, ϕ_1 and $\phi_2 = \pi/2 - \phi_0 - \phi_1$. Thus, also its imaginary solutions is_0 only depend on these quantities. Furthermore, the equation is invariant under any permutation of the three particles. For two-particle P-wave interactions, we will later give an explicit derivation for the corresponding P-wave analogue of (2.17).

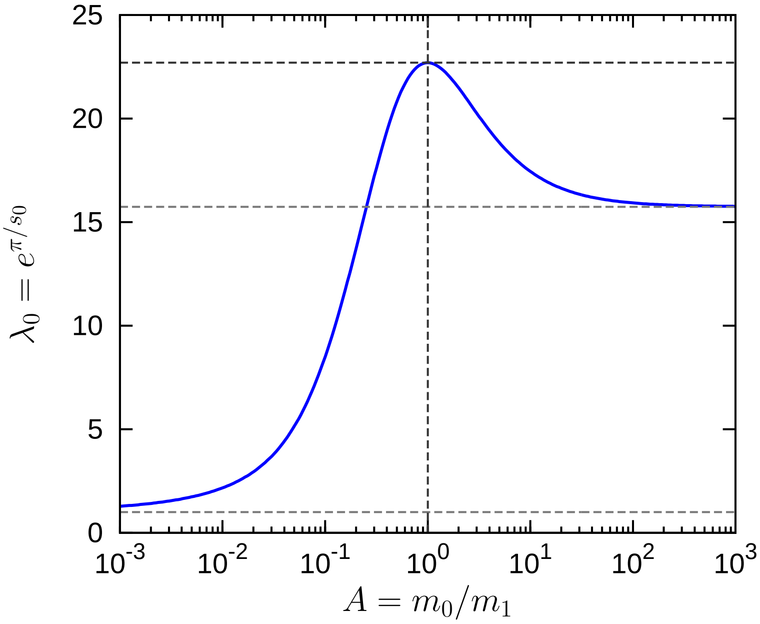

Figure 2.2: The discrete scaling factor $\lambda_0 = e^{\pi/s_0}$ as a function of the mass ratio $A = m_0/m_1$ with two equal masses $m_1 = m_2$. At $A = 1$ all three equal masses are equal and $\lambda_0 = 22.69438$ is maximal. As the mass ratio vanishes λ_0 approaches 1. For diverging A, the discrete scaling factor becomes 15.74250.

Applying a root-finding algorithm to $\mathcal{F}$, the quantities s_0 and $\lambda_0 = e^{\pi/s_0}$ can be determined. In fig. 2.1 the discrete scaling factor λ_0 depending on the three rescaled mass angles $\varphi_i := \phi_i/(\pi/2) \in (0,1)$ is given in terms of a Dalitz-like plot. The invariance under any particle permutations reflects itself in the dihedral $D3$-symmetry of the plot. As usual, the distances of a point in the Dalitz plot to the edges of the equilateral triangle are φ_0, φ_1 and φ_2. The origin in its center represents the equal-mass case $m_0 = m_1 = m_2 \Leftrightarrow \varphi_0 = \varphi_1 = \varphi_2$. At this point, the discrete scaling factor $\lambda_0 = e^{\pi/s_0} = 22.69438$ is maximal with $s_0 = 1.006238$ being very close to unity. As wee see, λ_0 decreases with growing distance to the equal mass point. It is constant on the contour lines. However, their exact shape seems to be nontrivial.

The three blue lines in fig. 2.1 represent the special case in parameter space where two of the masses are equal $m_i = m_j \Leftrightarrow \varphi_i = \varphi_j$, leading to $\varphi_k = [1 - \varphi_i]/2$. They all intersect in the center of the triangle. The center of all three edges represents the limit $m_i = m_j \gg m_k$ where $s_0 = 1.139760$ and $\lambda_0 = 15.74250$ holds. The three corners represent the limit $m_i = m_j \ll m_k$, leading to $s_0 \to \infty$ and $\lambda_0 \to 1$. Assuming that $m_1 = m_2$, λ_0 can effectively only depend on one parameter, for example, the mass ratio $A := m_0/m_1$. In fig. 2.2 λ_0 is given as a function of A. The three mentioned characteristic values $\lambda_0 = 1$, 22.69438, 15.74250 are approached at $A = 0$, 1, ∞, respectively.

Solving a homogeneous coupled channel integral equation for dimer-particle scattering, also the three-body energy spectrum can be determined. In fig. 2.3 we give a typical plot for the trimer energies, revealing an Efimov spectrum. The states are arranged in an infinite geometric series with an accumulation point at threshold and discrete scaling factor $\lambda_0 = 2$. As mentioned in sec. 1.2.2, signatures of these spectra were experimentally observed in several ultracold atomic or molecular systems. Also an approximate discrete scaling factor of $\lambda_0 \approx 22.7$ in the case of three equal bosons was confirmed [29].

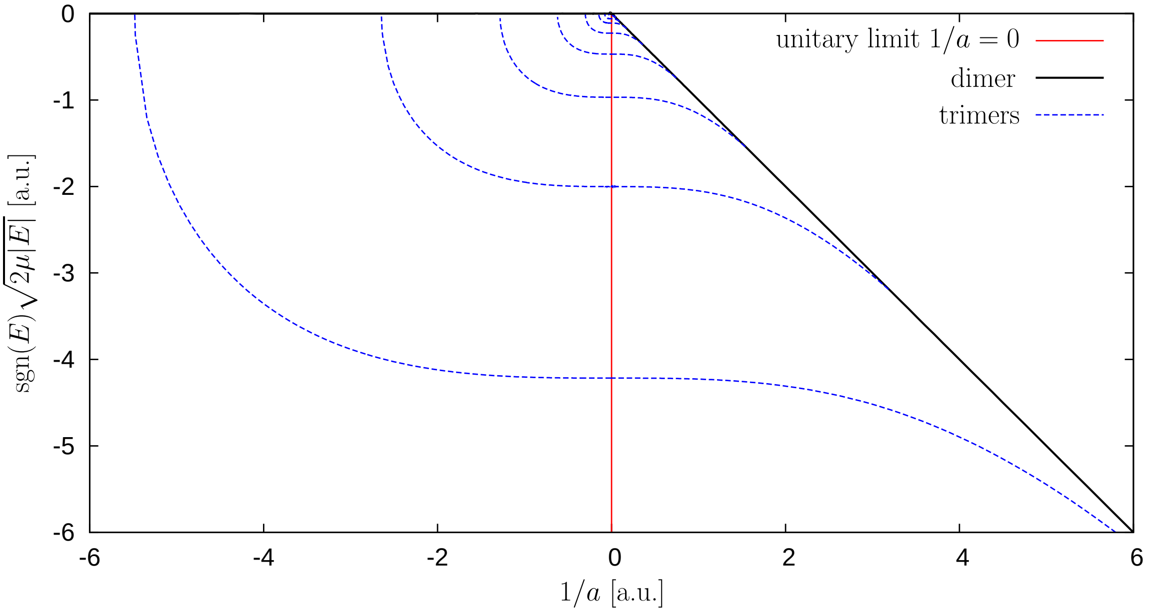

Figure 2.3: Schematic illustration of the bound-state spectrum for three bosons with S-wave interactions. The trimer states display discrete scale invariance with an accumulation point at threshold.

2.3 P-wave interactions

Inspired by the Efimov physics in the S-wave sector, in this section, we now investigate the possibility of similar phenomena for resonant P-wave interactions. A former analysis by Macek and Sternberg for spin-1/2 fermions in zero-range pseudopotentials suggested that there indeed is an Efimov effect in the P-wave sector for $J^P = 1^-$ [70, 71]. The aim of our analysis is to use a field theoretical approach in order to add more clarity to this issue and compare the results with the S-wave case. Furthermore, we also consider the renormalization of the three-body problem for P-wave interactions.

The derivations and results in sec. 2.3 have in parts been published in [72].

2.3.1 Effective Lagrangian

First, we set up an EFT for three non-relativistic scalar spin-0 fields on the Lagrangian level, where each two particles interact resonantly via P-wave couplings if they are distinguishable. Each particle can either be a boson or a fermion and we consider both the case where all three particle types are different (ψ_0, ψ_1, ψ_2) as well as the case where two of them are equal (ψ_0, ψ_1, ψ_1). We neglect P-wave couplings between identical particles, which are possible in case of fermions. In order to apply our model to a wider set of three-body systems, we can also simply assume that the intrinsic spin of a single particle remains inactive in all scattering processes. We use the notational conventions, presented in sec. 1.3 with the corresponding one- and two-particle index sets I_1 and I_2. As explained in sec. 2.1.2, the two-body coupling terms can be rewritten equivalently by introducing spin-1 P-wave dimers as auxiliary fields. Each such dimer $\mathbf{d}_i$ with $i \in I_2$ has three spatial components d_i^a, where $a \in \{1,2,3\}$ is the upper spacial index. The corresponding Lagrangian for our theory then has one-, two- and three-particle contributions:

$$\boxed{\begin{aligned}
\mathcal{L} &= \mathcal{L}^{(1)} + \mathcal{L}^{(2)} + \mathcal{L}^{(3)} \quad , \qquad \mathcal{L}^{(1)} \;=\; \mathcal{L}^{(\text{free})} \;=\; \sum_{i\in I_1} \psi_i^\dagger \Big(i\partial_0 + \frac{\nabla^2}{2m_i} \Big) \psi_i \quad , \\
\mathcal{L}^{(2)} &= \sum_{i\in I_2} \Big\{ \mathbf{d}_i^\dagger \Big[\Delta_i + \eta_i \Big(i\partial_0 + \frac{\nabla^2}{2M_i} \Big) \Big] \mathbf{d}_i \\
&\qquad\qquad - \; g_i\, \mu_i \; \mathbf{d}_i^\dagger \big(\psi_{i_1} \Big(\frac{i\overleftrightarrow{\nabla}}{\hat{m}} \Big) \psi_{i_2} \big) \; + \; \text{h.c.} \Big\} \quad , \\
\mathcal{L}^{(3)} &= -\, H \; \psi_1^\dagger \, \mathbf{d}_1^\dagger \, \mathbf{d}_1 \, \psi_1 \quad .
\end{aligned}} \tag{2.18}$$

The one-particle Lagrangian $\mathcal{L}^{(1)} = \mathcal{L}^{(\text{free})}$ simply describes the free non-relativistic propagation of the scalar fields.

The two-particle Lagrangian $\mathcal{L}^{(2)}$ consists of two contributions. First, there is a term analog to $\mathcal{L}^{(1)}$, representing the free propagation of the dynamical dimer fields $\mathbf{d}_i$. As explained, $\text{sgn}(\eta_i) = \pm 1$ corresponds to a normalizable physical field or a non-normalizable ghost field, respectively. The remaining contribution to $\mathcal{L}^{(2)}$ includes the bare dimer-dimer interaction and the coupling of a dimer to its two corresponding scalar fields. The specific form of these P-wave couplings with spatial derivatives is due to the required Galilean-invariance, which was discussed in sec. 2.1.1.2. It is directly transferred from the term eq. (2.5). As mentioned before, by the choice of I_2 from eq. (1.11), we implicitly neglect all P-wave interactions between identical particles, even if they are possible in case of fermions. The bare coupling parameters Δ_i and g_i are unknown and have to be renormalized. In our renormalization scheme, they depend on the ultraviolet cut-off in the two-particle sector and will be expressed in terms of low-energy observables from the effective range expansion. The reduced mass factors μ_i are conventional and could just as well be absorbed in g_i.

For simplicity, in the three-particle Lagrangian $\mathcal{L}^{(3)}$ we chose the three-body force to be only present in the $\mathbf{d}_1\psi_1$-channel. According to the conditions (2.12), there also exist other equivalent possibilities to introduce such a coupling. As mentioned before, $\mathcal{L}^{(2)}$ and $\mathcal{L}^{(3)}$ are constructed via the methods that are explained in sec. 2.1.2.2.

We now calculate matrix elements in perturbation theory, where we construe the free parts of the Lagrangian eq. (2.18) as the given theory and the remaining couplings as a perturbation. Feynman diagrams are then evaluated in momentum space, where the time-direction in all our diagrams points from the left to the right. Within a Feynman diagram, single and double lines represent scalar particles and dimers, respectively. Propagators are denoted by arrows and couplings by ellipses. White or filled symbols correspond to bare or full quantities, respectively. Detailed calculations of more involved Feynman graphs and their symmetry factors can be found in appendix D.2. Since we consider a non-relativistic theory, the one-body properties are not modified by interactions. Thus, we proceed with the two-body sector.

2.3.2 Two-body problem

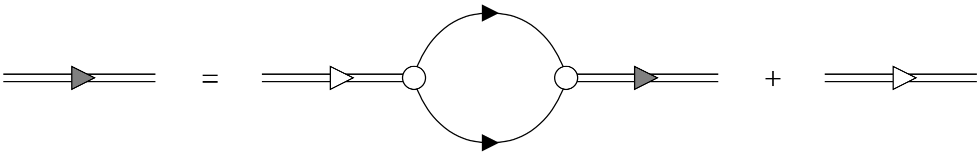

Figure 2.4: Diagrammatic representation of the integral equation for the full P-wave dimer propagator iD. The white arrow represents the bare propagator. The bubble represents the self-energy $-i\Sigma$.

First, we consider the two-particle sector of our theory with P-wave interactions. Since, in terms of Feynman diagrams, a dimer can split up into its two different components and then recombine, we have to include all such possible loops in the calculation of the full dimer propagator iD. A diagrammatic representation is given in fig. 2.4. iD depends on the total four-momentum $\bar{p}$ and, a priori, has components D_{ij}^{ab}, where i and a (j and b) are the particle type and spatial indices of the full dimer in the incoming (outgoing) channel. The corresponding matrix integral equation then reads

$$iD \;=\; i\Omega^{-1}\,(-i\Sigma)\,iD \;+\; i\Omega^{-1} \;=\; i[\Omega-\Sigma]^{-1} \quad . \tag{2.19}$$

The term Ω from the bare propagator and the self-energy Σ depend on the four-momentum $\bar{p}$ according to:

$$\begin{aligned} \Omega_{ij}^{ab}(\bar{p}) &= \delta_{ij}\delta^{ab}\left[\Delta_i + \frac{\eta_i}{2\mu_i} y_i^2(\bar{p})\right] \quad , \qquad y_i(\bar{p}) \;=\; \sqrt{2\mu_i\left(p^0 - \frac{\mathbf{p}^2}{2M_i} + i\varepsilon\right)} \quad , \\ -\Sigma_{ij}^{ab}(\bar{p}) &= \delta_{ij}\delta^{ab}\,\frac{g_i^2\mu_i}{3\pi^2}\left[\frac{\Lambda_i^3}{3} + \Lambda_i y_i^2(\bar{p}) + \frac{\pi}{2}\,i y_i^3(\bar{p})\right] \quad . \end{aligned} \tag{2.20}$$

The function y_i has the dimension of momentum. For a detailed calculation of the bubble diagram Σ, see eq. (D.2) in appendix D.2.1. We note that both Σ and Ω are diagonal in the spatial indices a and b and that the diagonal elements are independent of s, which then directly transfers to the full dimer propagator via $D_{ij} = \delta_{ij}\delta^{ab}D_i$ with diagonal elements:

$$D_i(\bar{p}) \;=\; \frac{1}{\left(\Delta_i + \frac{g_i^2\mu_i}{3\pi^2}\frac{\Lambda_i^3}{3}\right) + \left(\frac{\eta_i}{2\mu_i} + \frac{g_i^2\mu_i}{3\pi^2}\Lambda_i\right) y_i^2(\bar{p}) + \left(\frac{g_i^2\mu_i}{6\pi}\right) i y_i^3(\bar{p})} \quad . \tag{2.21}$$

The couplings Δ_i, g_i and the two-particle cut-offs Λ_i are not observable. Hence, we eliminate them via a renormalization procedure. In the following, we therefore consider the low-energy limit of the two-particle scattering amplitude, which can be written as an effective range expansion. The unknown quantities are then expressed in terms of the low-energy parameters of this expansion.

2.3.2.1 Effective range expansion

Figure 2.5: Feynmangraph for the two-particle scattering matrix element $it_{ij}(\bar{p}_1, \bar{p}_2, \bar{k}_1, \bar{k}_2)$. i and j are the particle-type indices. The sum over the upper spatial indices $a, b \in \{1, 2, 3\}$ is implicit.

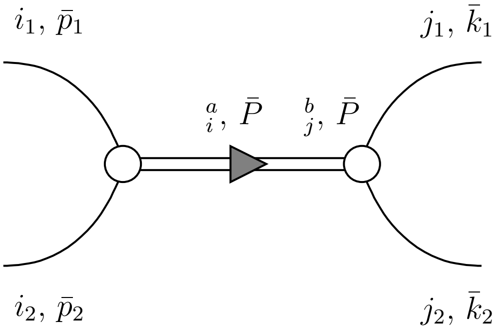

In order to renormalize the full dimer propagator in eq. (2.21), we consider the scattering of two particles, depicted in fig. 2.5. The incoming (outgoing) particles of type i_1 and i_2 (j_1 and j_2) have four-momenta $\bar{p}_1$ and $\bar{p}_2$ ($\bar{k}_1$ and $\bar{k}_2$). The full dimer propagator only allows indices $i, j \in I_2$ and is diagonal. Denoting its total four-momentum by $\bar{P} = \bar{p}_1 + \bar{p}_2 = \bar{k}_1 + \bar{k}_2$, leads to the matrix element:

$$\begin{aligned} & it_{ij}(\bar{p}_1, \bar{p}_2, \bar{k}_1, \bar{k}_2) \\ = & \sum_{a,b=1}^{3} (-ig_i) \left[\mathbf{p}_1 - \frac{m_{i_1}}{M_i}\mathbf{P}\right]^a i\delta_{ij}\delta^{ab} D_i(\bar{p}_1 + \bar{p}_2)\,(-ig_j) \left[\mathbf{k}_1 - \frac{m_{j_1}}{M_j}\mathbf{P}\right]^b \\ = & \ (-ig_i^2)\,\delta_{ij} \left[\mathbf{p}_1 - \frac{m_{i_1}}{M_i}\mathbf{P}\right] \cdot \left[\mathbf{k}_1 - \frac{m_{i_1}}{M_i}\mathbf{P}\right] D_i(\bar{P}) \quad . \end{aligned} \tag{2.22}$$

We now calculate the scattering amplitude in the center-of-mass frame. In these kinematics, the total four-momentum simply reads $P^0 = {\mathbf{p}_1}^2/(2\mu_i) = {\mathbf{k}_1}^2/(2\mu_i)$ and $\mathbf{P} = \mathbf{0}$. Using the relative momentum $\mathbf{p} := \mathbf{p}_1 = -\mathbf{p}_2$, the matrix element effectively only depends on the modulus $p = |\mathbf{p}|$ and the angle $\cos\theta := \frac{\mathbf{p}_1 \cdot \mathbf{k}_1}{|\mathbf{p}_1| \cdot |\mathbf{k}_1|}$. Using eq. (1.2), the scattering amplitude can be written as

$$f_i(p, \cos\theta) \ = \ \frac{\mu_i}{2\pi}\, t_{ii}(p, \cos\theta) \ = \ -\frac{g_i^2\,\mu_i}{2\pi}\, p^2\, D_i\Big(\frac{p^2}{2\mu_i}, \mathbf{0}\Big) \cos\theta \quad . \tag{2.23}$$

Comparing eq. (2.23) with the partial wave expansion (1.3) from $\cos\theta = P_1(\cos\theta)$, we deduce that only P-waves contribute to the scattering amplitude as required:

$$(2\ell + 1)\, f_i^{[\ell]}(p) \ = \ \delta^{1\ell} \left(-\frac{g^2 \mu_i}{2\pi}\right) p^2\, D_i\Big(\frac{p^2}{2\mu_i}, \mathbf{0}\Big) \quad . \tag{2.24}$$

According to eq. (1.6) the scattering amplitude is directly related to the effective range expansion. For simplicity, we will from now on drop the redundant partial wave index $\ell = 1$

in the labeling ${}^{[\ell]}$ of all effective range parameters. Knowing that $y_i\left(p^2/(2\mu_i),\mathbf{0}\right) = p$ we use eq. (2.21), eq. (2.24) and eq. (1.6) in order to renormalize the unobservable couplings and cut-offs in the dimer denominator according to:

$$\begin{aligned} -\frac{1}{a_i} + \frac{r_i}{2}p^2 - ip^3 + \mathcal{O}(p^4) &= -\frac{6\pi}{g^2\mu_i}\,\frac{1}{D_i\left(\frac{p^2}{2\mu_i},\mathbf{0}\right)} \\ = -\frac{6\pi}{g_i^2\mu_i}\Bigg[\left(\Delta_i + \frac{g_i^2\mu_i}{3\pi^2}\frac{\Lambda_i^3}{3}\right) &+ \left(\frac{\eta_i}{2\mu_i} + \frac{g_i^2\mu_i}{3\pi^2}\Lambda_i\right)p^2 + \left(\frac{g_i^2\mu_i}{6\pi}\right)ip^3\Bigg] \quad . \end{aligned} \tag{2.25}$$

Matching the coefficients on both sides of eq. (2.25) then directly yields the renormalization conditions:

$$\Delta_i + \frac{g_i^2\mu_i}{3\pi^2}\frac{\Lambda_i^3}{3} = -\frac{g_i^2\mu_i}{6\pi}\left(-\frac{1}{a_i}\right) \quad , \quad \frac{\eta_i}{2\mu_i} + \frac{g_i^2\mu_i}{3\pi^2}\Lambda_i = -\frac{g_i^2\mu_i}{6\pi}\frac{r_i}{2} \quad . \tag{2.26}$$

Since eq. (2.26) holds for all $\Lambda_i > 0$, it is also valid in the ultraviolet limit $\Lambda_i \to \infty$. From that requirement, we read off the asymptotic behavior of the coupling constants for large cut-offs: Multiplying both equations with $1/g_i^2$ shows that Δ_i/g_i^2 has to scale like $-\Lambda_i^3$ and η_i/g_i^2 has to scale like $-\Lambda_i$ in order to reproduce finite a $1/a_i$ and r_i. $g_i^2 > 0$ then implies $\eta_i < 0$. Due to this negative prefactor, the dimers $\mathbf{d}_i$ in eq. (2.18) must be ghost fields, corresponding to a negative-probability states. Furthermore, even in the hypothetical case $\eta_i = 0$ where the dimers would not be dynamical, the calculation of the P-wave self-energy (see eq. (D.2)) introduces a term $g_i^2\mu_i\Lambda_i/(3\pi^2) \propto \Lambda_i$ that contributes to the effective range. This is different from the case of two-particle S-wave interactions where such terms at leading order do not appear (see eq. (D.9)).

Inserting the renormalization conditions (2.26) into the formula for the full dimer propagator (2.21), we end up with:

$$D_i(\bar{p}) = -\frac{6\pi}{g_i^2\mu_i}\,\frac{1}{-\frac{1}{a_i} + \frac{r_i}{2}\,y_i^2(\bar{p}) - iy_i^3(\bar{p})} \quad . \tag{2.27}$$

If the interacting particles are atoms, one should keep in mind that they interact through a short-range potential combined with a long-range van der Waals tail. In this case, the denominator of the dimer propagator (2.27) would have to be modified by including a term which is linear in y_i. However, the conditions under which (2.27) is still a good approximation have been studied by Zhang, Naidon and Ueda [73]. We will now analyze the pole and residue structure of the full P-wave dimer propagator (2.27) as a function of the scattering volume and the effective range.

2.3.2.2 Pole and residue structure

The geometry of the propagator-poles in eq. (2.27) is more involved then in the S-wave case. Dropping the index i, the propagator has three, in general, complex poles in y, namely $\{y_n | n = 0,1,2\}$. Their positions on the first or second Riemann sheet and their residues

$\{Z_n | n = 0, 1, 2\}$ depend on the effective range parameters a and r. A detailed analysis is performed in sec. A.1.1.2, where the results are summarized in tab. A.4. It turns out that there are always one or two unphysical poles on the first Riemann sheet, but only for negative effective range $r < 0$ and a scattering length

$$r < 0 \qquad \wedge \qquad 1/a \in (0, |r|^3/54) \tag{2.28}$$

a physical pole on the first Riemann sheet exists. By (un-)physical we mean that the pole has (non-)positive residue. In addition to the physical pole, in this parameter region, there also exists one additional spurious pole on the first sheet with negative residue and a deeper binding energy. We will refer to these two poles as the *shallow* and *deep dimer*, respectively. The deep dimer corresponds to an unphysical non-normalizable state and thus its binding energy $E^{(2)} \lesssim -|r|^2/(18\mu)$ sets a scale beyond which our theory can no longer be applied. Hence, (2.27) is only valid for momenta that are much smaller than the effective range, which recently was also pointed out by Nishida [74]. The impact of the unphysical deep dimer on the three-particle sector will be discussed, among other aspects, in sec. 2.3.3.

From a purely mathematical point of view, the emergence of such spurious poles is due to the truncation of the effective range expansion. If the highest power of momentum that appears in this expansion is $N \in \mathbb{N}$, the full dimer propagator automatically has N complex poles. Some of them might be located on the first Riemann sheet $\sqrt{\mathbb{C}}$ and might be unphysical. Hence, taking into account higher and higher orders in the effective range expansion only increases the number of spurious poles and thus even compounds the problem. Moreover, also the ultraviolet behavior of the propagator would be changed. In general, approximating a meromorphic function, such as the scattering amplitude, not by an Laurent series but by an inverse polynomial expansion in its argument (see (1.6)), does not seem to represent a proper treatment of the function with respect to its pole structure and limiting behavior at infinity. In the context of this problem, pure S-wave interactions seem to represent the only exceptional case: For vanishing effective range and negative scattering length, there exists only one pole, which is indeed physical. Details about the S-wave dimer structure can be found in sec. A.1.1.1.

2.3.3 Three-body problem

We proceed with considering the three-particle sector of our Lagrangian (2.18). First, we calculate the amplitude $T_{ij}(\bar{p}_1, \bar{p}_2, \bar{k}_1, \bar{k}_2)$ for a scattering-process between a dimer and a single particle, which is depicted in fig. 2.6. Thereby, the incoming dimer $d_i^{a\dagger}$ and particle $\psi_i^\dagger$ have four-momenta $\bar{p}_1$ and $\bar{p}_2$ and the outgoing dimer d_j^b and particle ψ_j have four-momenta $\bar{k}_1$ and $\bar{k}_2$, respectively.

2.3.3.1 Kinematics

Within this section, it suffices to calculate the T-matrix in the center-of-mass frame with the four-momenta of the single particles being on-shell. Using four-momentum conservation

Figure 2.6: Diagrammatic representation of the T-matrix element $iT_{ij}(\bar{p}_1, \bar{p}_2, \bar{k}_1, \bar{k}_2)$ for dimer-particle scattering with two-particle P-wave interactions.

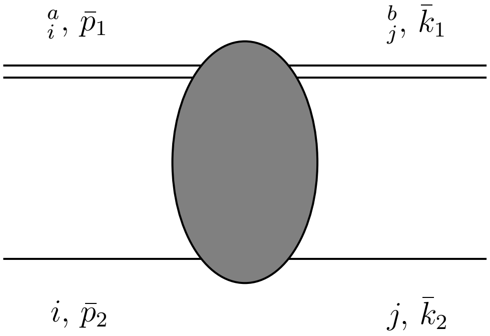

for the incoming and outgoing particles

$$\bar{p}_1 + \bar{p}_2 \;=\; \bar{k}_1 + \bar{k}_2 \;=:\; \bar{P} \;=\; \begin{pmatrix} E \\ \mathbf{0} \end{pmatrix} \quad , \tag{2.29}$$

we define relative four-momenta for the incoming and outgoing channel according to:

$$\bar{p} \;:=\; \bar{P} - \bar{p}_1 \;=\; \bar{p}_2 \quad , \qquad \bar{k} \;=\; \bar{P} - \bar{k}_1 \;=\; \bar{k}_2 \quad . \tag{2.30}$$

The on-shell condition for a single-particle propagator in the i-channel then reads:

$$p^0 \;=\; p_2^0 \;=\; \frac{\mathbf{p}_2^2}{2m_i} - i\varepsilon \;=\; \frac{\mathbf{p}^2}{2m_i} - i\varepsilon \quad . \tag{2.31}$$

The calculation of an off-shell T-matrix in an arbitrary frame is more involved but can also be performed straightforwardly. Its kinematics will be presented in sec. 3.1.3.1 where it is needed for the determination of electromagnetic observables in halo nuclei with two-particle S-wave interactions. In general an arbitrary inertial frame is, of course, related to the center-of-mass frame through a Galilean transformation.

With the definitions (2.29) and (2.30), the T-matrix can be rewritten in terms of only the three quantities, namely the total four-momentum $\bar{P}$ and the two relative four-momenta $\bar{p}$ and $\bar{k}$:

$$\begin{aligned} T_{ij}(\bar{P}, \bar{p}, \bar{k}) \;&:=\; T_{ij}\Big(\bar{P} - \bar{p}, \bar{p}, \bar{P} - \bar{k}, \bar{k}\Big) \\ \Leftrightarrow \quad T_{ij}(\bar{p}_1, \bar{p}_2, \bar{k}_1, \bar{k}_2) \;&=\; T_{ij}\Big(\bar{p}_1 + \bar{p}_2, \bar{p}_2, k_2\Big) \quad . \end{aligned} \tag{2.32}$$

The full dimer propagator in the chosen kinematics reads:

$$\begin{aligned} D_i(\bar{P}, \bar{p}) \;:=\; D_i\Big(\bar{P} - \bar{p}\Big) \;&=\; -\frac{6\pi}{g_i^2 \mu_i} \, \frac{1}{-\frac{1}{a_i} \;+\; \frac{r_i}{2}\, y_i^2(\bar{P}, \bar{p}) \;-\; i y_i^3(\bar{P}, \bar{p})} \quad , \\ y_i(\bar{P}, \bar{p}) \;:=\; y_i\Big(\bar{P} - \bar{p}\Big) \;&=\; \sqrt{2\mu_i\Big(E - p^0 + \frac{\mathbf{p}^2}{2m_i} - \frac{\mathbf{p}^2}{2\tilde{\mu}_i} + i\varepsilon\Big)} \quad . \end{aligned} \tag{2.33}$$

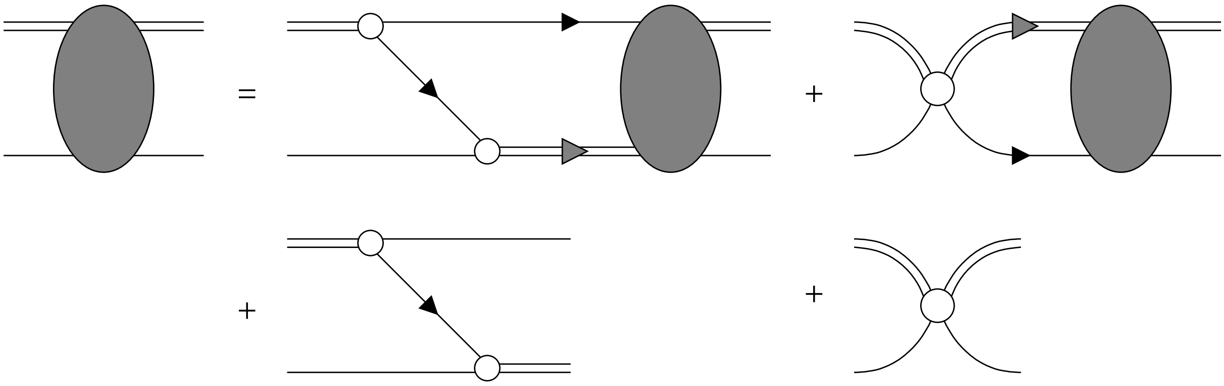

Figure 2.7: Diagrammatic representation of the integral equation for dimer-particle scattering iT, represented by Feynman graphs. The homogenous part includes full dimer propagators iD and integrations over the loop momenta $\int \mathrm{d}^4\bar{q}/(2\pi)^4$.

2.3.3.2 T-matrix integral equation

In fig. 2.7 the integral equation for the T-matrix is illustrated in terms of Feynman diagrams. Using Feynman rules in momentum space, it formally reads:

$$\begin{aligned} iT^{ab}_{ij}(\bar{P},\bar{p},\bar{k}) &= iR^{ab}_{ij}(\bar{P},\bar{p},\bar{k}) \ + \sum_{k\in I_2}\sum_{c=1}^{3}\int \frac{\mathrm{d}^3\mathbf{q}}{(2\pi)^3}\int_{-\infty}^{\infty}\frac{\mathrm{d}q^0}{2\pi}\, iR^{ac}_{ik}(\bar{P},\bar{p},\bar{q}) \\ &\times \frac{i}{q^0-\frac{\mathbf{q}^2}{2m_k}+i\varepsilon}\, iD_k(\bar{P},\bar{q})\; iT^{cb}_{kj}(\bar{P},\bar{q},\bar{k}) \quad , \end{aligned} \tag{2.34}$$

where a detailed derivation of the interaction kernel

$$\begin{aligned} R^{ab}_{ij}(\bar{P},\bar{p},\bar{k}) &= -\Bigg[\nu\,\kappa_{ij}\,(g_i g_j)\,\frac{\left(\mathbf{k}+\frac{m_j}{M_i}\mathbf{p}\right)^a\left(\mathbf{p}+\frac{m_i}{M_j}\mathbf{k}\right)^b}{E-p^0+\frac{\mathbf{p}^2}{2m_i}-k^0+\frac{\mathbf{k}^2}{2m_j}-\frac{\mathbf{p}^2}{2\mu_j}-\frac{\mathbf{k}^2}{2\mu_i}-\frac{\mathbf{p}\cdot\mathbf{k}}{m_{ij}}+i\varepsilon} \\ &\quad + \ \delta_{1i}\delta_{1j}\delta^{ab}\,H\Bigg] \quad , \end{aligned} \tag{2.35}$$

$$\nu = \begin{cases} +1 & : \ \#\text{fermions} \leq 1 \\ -1 & : \ \#\text{fermions} > 1 \end{cases} \quad , \quad \kappa_{ij} := \begin{cases} 1 & : \ 2 \text{ types} \\ (1-\delta_{ij}) & : \ 3 \text{ types} \end{cases} \quad ,$$

is given in appendix D.2.2.

We now utilize the residue theorem in order to perform the q^0-integration. Considering the integrand in eq. (2.34), we note that the appearing single-particle propagator $i/(q^0-\mathbf{q}^2/(2m_k)+i\varepsilon)$ for real three momentum $\mathbf{q}$ has a single pole in the lower complex plane, located at $q^0=\mathbf{q}^2/(2m_k)-i\varepsilon$. The more complicated pole structure of the full P-wave dimer propagator D_k is discussed in detail in appendix A.1.1.2. As explained there, $D_k(\bar{P},\bar{q}) = D_k(\bar{P}-\bar{q})$ has no q^0-poles in the lower complex half-plane if and only if the scattering volume obeys

$$-1/a \in \left(\min\{0,r^3/54\},\infty\right) \setminus \left\{\max\{0,r^3/54\}\right\} \quad . \tag{2.36}$$

The omitted point in parameter space $\max\{0, r^3/54\}$ represents an unphysical configuration with second order poles in the propagator. The condition (2.36) is less strict than (2.28), which was identified as the physically reasonable one. However, for the subsequent analytical calculations in the three-particle sector we only require the validity of (2.36). Assuming that also $T^{cb}_{kj}(\bar{P}, \bar{q}, \bar{k})$ has no q^0-poles in the lower complex half-plane, we apply the formula

$$\int_{-\infty}^{\infty} \frac{\mathrm{d}q^0}{(2\pi)} \frac{i}{q^0 - \frac{\mathbf{q}^2}{2m_k} + i\varepsilon} f(q^0) \;=\; \frac{i}{2\pi}(-2\pi i)\, f\Big(\frac{\mathbf{q}^2}{2m_k} - i\varepsilon\Big) \;=\; f\Big(\frac{\mathbf{q}^2}{2m_k} - i\varepsilon\Big) \quad , \tag{2.37}$$

to eq. (2.34). Thereby, f simply denotes the products of all functions in the integrand except for the single-particle propagator. Formula (2.37) is valid because the q^0 integration contour can be closed through a lower arc. In the limit of infinite arc-radius this are does not contribute to the integral, since the amplitude is assumed to fall of rapidly enough. Using the conventions (1.18) and (1.20) from sec. 1.3 this leads to the on-shell T-matrix integral equation:

$$\begin{aligned} T^{ab}_{ij}(E, \mathbf{p}, \mathbf{k}) \;&=\; R^{ab}_{ij}(E, \mathbf{p}, \mathbf{k}) \;-\; \sum_{k \in I_2} \sum_{c=1}^{3} \int \frac{\mathrm{d}^3\mathbf{q}}{(2\pi)^3}\, R^{ac}_{ik}(E, \mathbf{p}, \mathbf{q}) \\ &\quad \times\; D_k(E, \mathbf{q})\; T^{cb}_{kj}(E, \mathbf{q}, \mathbf{k}) \quad . \end{aligned} \tag{2.38}$$

All appearing functions depend on the total energy E. The dimer only exhibits a dependence on the modulus of the loop three-momentum, whereas the interaction kernel depends on the moduli of the incoming and outgoing three-momenta as well as the polar angle between them.

Although the residue theorem in the form (2.37) is only applicable to eq. (2.34) for scattering parameters fulfilling the condition (2.36), the resulting T-matrix integral equation (2.38) can be analytically continued to the excluded parameter region. Formally, we can thus interpret (2.38) as an integral equation for all scattering parameters, as long as we keep in mind that, strictly speaking, eq. (2.36) is required and that the physically reasonable region is restricted by the even sharper condition (2.28).

2.3.3.3 Angular momentum eigenstates

The matrix integral equation (2.38) only yields a formal solution for the Cartesian components of the T-matrix. Since possible physical three-body bound states need to have good angular quantum numbers, a projection onto total angular momentum eigenstates has to be performed. Thereby, the total angular momentum J results from coupling the intrinsic dimer spin $S = 1$ to the orbital angular momentum ℓ in the dimer-particle system. For our model with P-wave interactions, this spin-orbit coupling is rather elaborate and will be performed in several steps within the following sections, where extended calculations are outsourced to appendix C. For a better readability, we drop particle type indices i, j, k and interpret all equations as matrix equations in terms of the particle types if not otherwise specified.

Intrinsic dimer spin: First, we transform the spatial components of the P-wave dimer field, and thus all other quantities appearing in the integral equation (2.38), into appropriate spin-triplet components for the incoming and outgoing channel. For both quantities $X \in \{T, R\}$, this is achieved by conjugation with a unitary matrix according to:

$$A \;:=\; \begin{pmatrix} \frac{-1}{\sqrt{2}} & \frac{-i}{\sqrt{2}} & 0 \\ 0 & 0 & 1 \\ \frac{1}{\sqrt{2}} & \frac{-i}{\sqrt{2}} & 0 \end{pmatrix} \in U(3) \quad , \qquad X^{[1|1]} \;:=\; AXA^\dagger \quad , \tag{2.39}$$

where the components read: $X^{[1s_1|1s_2]} = (AXA^\dagger)^{s_1 s_2} = \sum_{a,b=1}^{3} (A)^{s_1 a} X^{ab} (A^\dagger)^{b s_2}$. The spin indices s_n can assume the three values -1, 0 and 1, which correspond to the states in the spin triplet. Since the dimer propagator is diagonal in spacial indices, it commutes with A and we can rewrite eq. (2.38) compactly as a matrix integral equation:

$$T^{[1|1]}(E, \mathbf{p}, \mathbf{k}) \;=\; R^{[1|1]}(E, \mathbf{p}, \mathbf{k}) \;-\; \int \frac{\mathrm{d}^3\mathbf{q}}{(2\pi)^3}\, R^{[1|1]}(E, \mathbf{p}, \mathbf{q})\, D(E, \mathbf{q})\, T^{[1|1]}(E, \mathbf{q}, \mathbf{k}) \;. \tag{2.40}$$

Orbital angular momentum: With regard to the orbital angular momentum in the dimer-particle system, we now perform a decomposition of the T-matrix and the interaction kernel into spherical harmonics $Y_{\ell m}$ (see sec. C.2 for more details). We formally expand $X \in \{T, R\}$ in terms of:

$$\begin{aligned} X^{[1s_1|1s_2]}(E, \mathbf{p}, \mathbf{k}) \;&=\; X^{[1s_1|1s_2]}(E, p \cdot \mathbf{e}_p, k \cdot \mathbf{e}_k) \\ &=: \; 4\pi \sum_{\ell_1, m_1} \sum_{\ell_2, m_2} Y^*_{\ell_1 m_1}(\mathbf{e}_p)\; X^{[1s_1;\ell_1 m_1|1s_2;\ell_2 m_2]}(E, p, k)\; Y_{\ell_2 m_2}(\mathbf{e}_k) \\ \Rightarrow \;\; X^{[1s_1;\ell_1 m_1|1s_2;\ell_2 m_2]}&(E, p, k) \\ &= \int \frac{\mathrm{d}\Omega_{\mathbf{p}}}{\sqrt{4\pi}} \int \frac{\mathrm{d}\Omega_{\mathbf{k}}}{\sqrt{4\pi}}\; Y_{\ell_1 m_1}(\mathbf{e}_p)\; X^{[1s_1|1s_2]}(E, p \cdot \mathbf{e}_p, k \cdot \mathbf{e}_k)\; Y^*_{\ell_2, m_2}(\mathbf{e}_k) \quad . \end{aligned} \tag{2.41}$$

In the last line, the orthonormality relation (C.6) was used. The prefactor of 4π is purely conventional. It matches with standard definitions (see e.g. [11]) and is designed to compensates the two $Y_{00} = 1/\sqrt{4\pi}$ factors in the case of pure $\ell_1 = \ell_2 = 0$ orbital angular momentum. Multiplying eq. (2.40) with $Y_{\ell_1 m_1}(\mathbf{e}_p) Y^*_{\ell_2 m_2}(\mathbf{e}_k)$ and integrating over $\mathrm{d}\Omega_{\mathbf{p}} \mathrm{d}\Omega_{\mathbf{k}}/(4\pi)$, projects onto the appropriate contribution:

$$\begin{aligned} T^{[1s_1;\ell_1 m_1|1s_2;\ell_2 m_2]}(E, p, k) \;&=\; R^{[1s_1;\ell_1 m_1|1s_2;\ell_2 m_2]}(E, p, k) \\ -\; \int_0^\infty & \frac{\mathrm{d}q\, q^2\, (4\pi)^2}{(4\pi)(2\pi)^3} \sum_{\ell_3, m_3} \sum_{s_3} \\ \times\;\; R^{[1s_1;\ell_1 m_1|1s_3;\ell_3 m_3]}&(E, p, q)\; D(E, q)\; T^{[1s_3;\ell_3 m_3|1s_2;\ell_2 m_2]}(E, q, k) \quad . \end{aligned} \tag{2.42}$$

The on-shell full dimer propagator $D(E, \mathbf{q})$ appearing in eq. (2.40) effectively does not display any angular dependence. It is a pure S-wave quantity. For notational convenience, we then redefine

$$D^{[0]}(E, p) \;:=\; -\frac{4\pi}{(2\pi)^3}\, p^2\, D(E, p) \quad , \tag{2.43}$$

where the convention (1.19) was used. Note that the prefactor $4\pi/(2\pi)^3 p^2 = p^2/(2\pi^2)$ from the measure of the integration over the loop momentum as well as the relative minus sign have been absorbed in $D^{[0]}$. An explicit expression of the angular-decomposed interaction kernel $R^{[1s_1;\ell_1 m_1|1s_2;\ell_2 m_2]}$ can be found in eq. (C.20) in sec. C.3.

Spin-orbit coupling: We are now in the position to couple the intrinsic dimer spin with the orbital angular momentum to a total angular momentum. As is well known, the coupling of general angular momenta is performed using Clebsch–Gordan coefficients (CGC), which, in principle, are nothing else but the entries of a unitary matrix, describing the change of orthonormal bases in the tensor product of Hilbert-spaces. For two angular momenta j_1 and j_2 coupled to total angular momentum $|j_1 - j_2| \leq J \leq j_1 + j_2$, we label the corresponding CGC by $C^{JM}_{j_1 m_1; j_2 m_2}$, where m_1, m_2 and M are the magnetic quantum numbers. In the following, we will use several symmetries and properties of CGGs. They are collected in appendix C.1. For a detailed discussion of CGCs, see e.g. ref. [75].

For $X \in \{T, R\}$, covering both the T-matrix and the interaction kernel, we define projected quantities $X^{[J_1 M_1;1;\ell_1|J_2 M_2;1;\ell_2]}$ according to eq. (C.4). Multiplying eq. (2.42) with $C^{J_1 M_1}_{1s_1;\ell_1 m_1} C^{J_2 M_2}_{1s_2;\ell_2 m_2}$ and summing over all magnetic quantum numbers, we use the products-formula (C.5) for the homogeneous part and end up with the projected T-matrix equation:

$$\begin{aligned} T^{[J_1 M_1;1;\ell_1|J_2 M_2;1;\ell_2]}(E,p,k) &= R^{[J_1 M_1;1;\ell_1|J_2 M_2;1;\ell_2]}(E,p,k) \\ &+ \int_0^\infty \mathrm{d}q \sum_{\ell_3} \sum_{J_3=|\ell_3-1|}^{\ell_3+1} \sum_{M_3=-J_3}^{J_3} \\ &\times\; R^{[J_1 M_1;1;\ell_1|J_3 M_3;1;\ell_3]}(E,p,q)\, D^{[0]}(E,q)\, T^{[J_3 M_3;1;\ell_3|J_2 M_2;1;\ell_2]}(E,q,k) \quad . \end{aligned} \tag{2.44}$$

The Wigner–Eckart theorem now implies that $X \in \{T, R\}$ is diagonal in the total incoming and outgoing angular momentum quantum numbers according to: $X^{[J_1 M_1;1;\ell_1|J_2 M_2;1;\ell_2]} = \delta^{J_1 J_2} \delta^{M_1 M_2} X^{[J_1][\ell_1|\ell_2]}$. The rather elaborate analytic calculation of $R^{[J_1 M_1;1;\ell_1|J_2 M_2;1;\ell_2]}$, which is performed in appendix C.4, directly displays this diagonality. Insertion into eq. (2.44) leads to:

$$\begin{aligned} T^{[J][\ell_1|\ell_2]}(E,p,k) &= R^{[J][\ell_1|\ell_2]}(E,p,k) \\ &+ \int_0^\infty \mathrm{d}q \sum_{\ell_3=|J-1|}^{J+1} R^{[J][\ell_1|\ell_3]}(E,p,q)\, D^{[0]}(E,q)\, T^{[J][\ell_3|\ell_2]}(E,q,k) \\ \Leftrightarrow\; T^{[J]}(E,p,k) &= R^{[J]}(E,p,k) + \int_0^\infty \mathrm{d}q\, R^{[J]}(E,p,q)\, D^{[0]}(E,q)\, T^{[J]}(E,q,k) \quad . \end{aligned} \tag{2.45}$$

Thus, channels with different total angular momentum J are decoupled and the intermediate orbital angular momentum ℓ_3 is restricted to $|J-1| \leq \ell_3 \leq J+1$. In addition, it becomes apparent (see sec. C.5 for details) that $X \in \{T, R\}$ decomposes into blocks with different parity quantum numbers $P \in \{+, -\}$ according to $X^{[J]} = X^{[J^+]} \oplus X^{[J^-]}$. Hence, we end up with the inhomogeneous one-dimensional matrix integral equation:

$$T^{[J^P]}(E,p,k) = R^{[J^P]}(E,p,k) + \int_0^\infty \mathrm{d}q\, R^{[J^P]}(E,p,q)\, D^{[0]}(E,q)\, T^{[J^P]}(E,q,k) \quad , \tag{2.46}$$

which can be seen as a P-wave analogue of the Skornyakov–Ter-Martirosian (STM) equation in ref. [76]. The full dimer propagator $D^{[0]}$ is given in eqs. (2.43) and (2.27) and the interaction kernels $R^{[J^P]}$ can be found in appendix C.5 in eqs. (C.37) and (C.38).

From the matrix integral equation (2.46), we know that the dimensions of the T-matrix $T^{[J^P]}$ are simply those of the interaction kernel $R^{[J^P]}$. Thereby, in terms of angular momenta, the negative parity component $R^{[J^-]}$ is a scalar function and incoming and outgoing orbital angular momenta are $\ell_1 = \ell_2 = J$. $R^{[J^+]}$ has a more complicated structure. It is a 2×2 matrix. The matrix-elements describe all four possible combinations of incoming and outgoing momenta $\ell_1, \ell_2 \in \{J-1, J+1\}$. However, for the special S-wave case $J = 0$ the only non-vanishing matrix element is the lower right one, which has $\ell_1 = \ell_2 = J + 1$. In this case, the matrix equation effectively is again a scalar one. In all cases, the full matrix dimension d is obtained by a multiplication with the particle-type-related dimension. Summarizing these results yields:

$$\begin{aligned} X^{[J^P]}(E,p,k) \;&\in\; \mathbb{C}^{d\times d} \quad , \qquad d \;:=\; d_d \cdot d_{J^P} \quad , \\ d_d \;:=\; \#I_2 \;&=\; \begin{cases} 1 & : \; 2 \text{ types} \\ 3 & : \; 3 \text{ types} \end{cases} \quad , \qquad d_{J^P} \;:=\; \begin{cases} 1 & J^P \in \{J^-, 0^+\} \\ 2 & \text{otherwise} \quad . \end{cases} \end{aligned} \tag{2.47}$$

Another interesting consequence of eq. (C.37) and eq. (C.38) is that for an EFT with P-wave interactions of type (2.18), the three-particle force H only appears in the 1^+-contribution to the T-matrix. Consequently, this is also the only channel, in which the binding energy of possible three-body bound states can be affected by such a three-body force. The common renormalization procedure for the three-particle sector, in which a momentum cut-off Λ is introduced and a three-body bound-state energy is then fixated to its physical value by fine-tuning H as a function of Λ, can thus only be applied to the 1^+-channel. Renormalization in other J^P-channels would require a modified three-body force, e.g. higher order terms with additional derivatives would have to be included in the $\mathcal{L}^{(3)}$-part of the Lagrangian (2.18). An alternative way to address this problem would be to drop $\mathcal{L}^{(3)}$ in the first place and simply add an effective three-body term to the projected J^P-contributions (C.37) and (C.38). Since for the set of problems tackled in this chapter the exact position of a specific three-body bound state is irrelevant, we will set $H = 0$ in the following.

2.3.3.4 Renormalization

Before we search for possible three-body bound states, we choose a normalization of the T-matrix that eliminates the remaining, unobservable g_i couplings. Since, in the end, pole-positions are invariant under such normalization, we can equivalently solve the bound-state equation for the redefined quantities:

$$\begin{aligned} \forall X \in \{T, R\} : \quad \bar{X}_{ij} \;&:=\; (g_i\sqrt{\mu_i})^{-1}\, X_{ij}\, (g_j\sqrt{\mu_j})^{-1} \quad , \\ \bar{D}_i(E,p) \;&:=\; (g_i\sqrt{\mu_i})^2\, D_i(E,p) \quad . \end{aligned} \tag{2.48}$$

With these definitions, all unobservable g_i-factors in eq. (2.46) cancel and the kernel functions assume a simpler form. Note that for a calculation of physical dimer-particle scattering, the proper physical renormalization would be required, involving the multiplication with appropriate wave function renormalization factors $\sqrt{Z}$, originating from the LSZ theorem [77]. They are given in sec. A.1.1.2. However, for all calculations in the P-wave sector that are presented in this work, using eq. (2.48) suffices and yields simplified equations.

For simplicity, we will from now on only consider the case where two of the three particles are identical. With regard to eq. (2.47), this case has smaller matrix dimensions and the kernel functions are less complex. Anyhow, the qualitative results and conclusions will be the same in both cases. The only appearing channel then is $i = j = k = 1$ such that we can drop these redundant indices. In addition, mass factors $\mu_i/\mu_j = 1$ cancel. The corresponding T-matrix integral equation for a theory of two identical particles ψ_1 interacting with a third one ψ_0 via P-wave contact interactions then altogether reads:

$$\boxed{\begin{aligned}
&\bar{T}^{[J^P]}(E,p,k) \\
&\quad = \bar{R}^{[J^P]}(E,p,k) + \int_0^\infty \mathrm{d}q\, \bar{R}^{[J^P]}(E,p,q)\, \bar{D}^{[0]}(E,q)\, \bar{T}^{[J^P]}(E,q,k) \quad , \\[2ex]
&\bar{D}^{[0]}(E,p) = \frac{3}{\pi} \frac{p^2}{-\frac{1}{a} + \frac{r}{2} y^2(E,p) - i y^3(E,p)} \quad , \\
&y(E,p) = \sqrt{2\mu\Big(E - \frac{p^2}{2\bar{\mu}} + i\varepsilon\Big)} \quad , \\
&\bar{R}^{[J^+]}(E,p,k) = \nu \frac{(-1)^J}{2J+1} \\
&\qquad \times \begin{pmatrix} \Theta_{J-1} & 0 \\ 0 & 1 \end{pmatrix} \begin{pmatrix} \omega\frac{(J-1)(2J+1)}{2J-1} Q_{J-2} - J(\frac{p}{k}+\frac{k}{p}) Q_{J-1} + (\frac{\omega}{2J-1}+\frac{J}{\omega}) Q_J & \sqrt{J(J+1)}[\frac{k}{p} Q_{J-1} - (\omega+\frac{1}{\omega}) Q_J + \frac{p}{k} Q_{J+1}] \\ \sqrt{J(J+1)}[\frac{p}{k} Q_{J-1} - (\omega+\frac{1}{\omega}) Q_J + \frac{k}{p} Q_{J+1}] & (\frac{\omega}{2J+3}+\frac{J+1}{\omega}) Q_J - (J+1)(\frac{p}{k}+\frac{k}{p}) Q_{J+1} + \omega\frac{(J+2)(2J+1)}{2J+3} Q_{J+2} \end{pmatrix} \begin{pmatrix} \Theta_{J-1} & 0 \\ 0 & 1 \end{pmatrix} \quad , \\
&\bar{R}^{[J^-]}(E,p,k) = \nu \frac{(-1)^J}{2J+1}\, \Theta_{J-1} \left(Q_{J+1} - Q_{J-1}\right) \quad , \\
&Q_J = Q_J(c(E,p,k)) \quad , \quad c(E,p,k) = \frac{m_0}{pk}\Big(\frac{p^2}{2\mu} + \frac{k^2}{2\mu} - E - i\varepsilon\Big) \quad , \\
&\nu = \begin{cases} +1 & : \psi_1 \text{ bosons} \\ -1 & : \psi_1 \text{ fermions} \end{cases} \quad , \quad \Theta_J = \begin{cases} 1 & : J \geq 0 \\ 0 & : J < 0 \end{cases} \quad , \\
&\mu = \frac{m_0 m_1}{m_0 + m_1} \quad , \quad \bar{\mu} = \frac{m_1(m_0+m_1)}{m_0 + 2m_1} \quad , \quad \omega = 1 + A \quad , \quad A := \frac{m_0}{m_1} \quad .
\end{aligned}} \tag{2.49}$$

The appearing analytically continued Legendre-functions of second kind Q_J are surveyed in detail in sec. A.2 in the appendix.

2.3.3.5 Bound state equation

We are now in the position to search for possible three-body bound states, which manifest themselves as poles of first order in the T-matrix. Assuming the existence of a three-body bound state with negative binding energy $E = E^{(3)} < 0$ and quantum number J^P, the T-matrix has a pole of first order at this position. The corresponding residue factorizes into momentum dependent functions B according to:

$$\bar{T}^{[J^P]}(E,p,k) \;=\; -\frac{B^{[J^P]}(p)\cdot B^{[J^P]}(k)^{\dagger}}{E-E^{(3)}} + \text{reg.} \quad . \tag{2.50}$$

The term reg. represents an unspecified regular function in the energy. Also in the case where $\bar{T}^{[J^P]}$ has no such pole, eq. (2.50) is still trivially fulfilled with $B^{[J^P]} = 0$. Inserting eq. (2.50) into eq. (2.49), multiplying with $E - E^{(3)}$ and taking the limit $E \to E^{(3)}$, directly yields the bound-state equation

$$B^{[J^P]}(p) \;=\; \int_0^\infty \mathrm{d}q\, \bar{R}^{[J^P]}(p,q)\, \bar{D}^{[0]}(q)\, B^{[J^P]}(q) \tag{2.51}$$

emerges. Its kernel functions are those of eq. (2.49). Note that, in accordance with our convention (1.21), we dropped the energy variables $E = E^{(3)}$. In sec. B we discuss how eq. (2.49) and eq. (2.51) can be solved numerically.

2.3.4 Discrete scale invariance and the Efimov effect

Introducing an ultraviolet momentum cut-off Λ, the bound-state equation (2.51) can be discretized and solved numerically. This will be performed in sec. 2.3.4.2. However, in the limit of large momenta its solutions $B^{[J^P]}$ can even be addressed in a semi-analytic approach, which will be considered in the following sec. 2.3.4.1.

2.3.4.1 Discrete scale invariance

The asymptotic behavior of the solutions of the bound-state equation (2.51) can be used in order to identify J^P-channels which display discrete scale invariance. Discrete scale invariance is a necessary condition for the occurrence of a hypothetical Efimov effect. In order to determine all such channels, we first assume that the momentum p in eq. (2.51) is much larger than any other physical scale, meaning

$$p \;\gg\; \max\{1/|\sqrt[3]{a}|, |r/2|, m_0, m_1, E^{(3)}\} \quad . \tag{2.52}$$

From the expansion (A.46) in appendix A.2.3, we see that for $|c(p,q)| > 1$, the Q_J functions that appear in the integral kernel fall of like $1/c^{J+1}$. Thus, the dominant contributions from $\bar{R}^{[J^P]}(p,q)$ to the q-integration in eq. (2.51) are those with $|c(p,q)| \lesssim 1$. This condition holds for $q \approx p \gg \max\{m_0, m_1, 1/|\sqrt[3]{a}|, |r/2|, E^{(3)}\}$. Hence, we can assume that also q is much larger than any other scale in the problem. In this limit, the functional expressions in eq. (2.51) assume simpler forms. We can write $y(q) \approx i\sqrt{\mu/\bar{\mu}}\,q$ and, since $\sqrt{\mu/\bar{\mu}} = \sqrt{(\omega-1)(\omega+1)/\omega^2} = \cos\phi$ holds, the full dimer propagator reads $\bar{D}^{[0]}(q) \approx -3/(\pi\cos^3\phi\; q)$. Furthermore, in this limit, the argument of the Legendre functions of second kind assumes the form $c(p,q) \approx (p/q + q/p - i\varepsilon)/(2\sin\phi)$. Consequently, c and hence also the kernel function $\bar{R}^{[J^P]}$ effectively only depend on the ratio $x = p/q$ of the momenta. This leads to the asymptotic equation:

$$
\begin{aligned}
B^{[J^P]}(p) \;&=\; \int_0^\infty \frac{\mathrm{d}q}{q}\, \bar{K}^{[J^P]}\Big(\frac{p}{q}\Big)\, B^{[J^P]}(q) \quad , \\
\bar{K}^{[J^+]} \;&=\; \xi^{[J^P]} \left(\begin{smallmatrix} \Theta_{J-1} & 0 \\ 0 & 1 \end{smallmatrix}\right) \begin{pmatrix} \frac{(J-1)(2J+1)}{(2J-1)\sin\phi} Q_{J-2} - J(x+\frac{1}{x})Q_{J-1} + (\frac{1}{(2J-1)\sin\phi} + J\sin\phi)Q_J & \sqrt{J(J+1)}[\frac{1}{x}Q_{J-1} - (\frac{1}{\sin\phi}+\sin\phi)Q_J + xQ_{J+1}] \\ \sqrt{J(J+1)}[xQ_{J-1} - (\frac{1}{\sin\phi}+\sin\phi)Q_J + \frac{1}{x}Q_{J+1}] & (\frac{1}{(2J+3)\sin\phi} + (J+1)\sin\phi)Q_J - (J+1)(x+\frac{1}{x})Q_{J+1} + \frac{(J+2)(2J+1)}{(2J+3)\sin\phi}Q_{J+2} \end{pmatrix} \left(\begin{smallmatrix} \Theta_{J-1} & 0 \\ 0 & 1 \end{smallmatrix}\right) \quad , \qquad (2.53) \\
\bar{K}^{[J^-]} \;&=\; \xi^{[J^P]}\,\Theta_{J-1}\,(Q_{J+1} - Q_{J-1}) \quad , \qquad \xi^{[J^P]} \;:=\; \nu\,\frac{(-1)^{J+1}}{2J+1}\,\frac{1}{\pi}\,\frac{3}{\cos^3\phi} \quad , \\
Q_J \;&=\; (Q_J \circ c)(x) \quad , \qquad c(x) \;=\; \frac{x+1/x}{2\sin\phi} \quad , \qquad \phi = \arcsin(1/\omega) \quad .
\end{aligned}
$$

Of course, we can now also interpret eq. (2.53) as an integral equation for all momenta p, but, as we know, their solutions will only match with those of the physical one (2.51) if the condition (2.52) is fulfilled. We note that eq. (2.53) does no longer depend on m_0 and m_1 individually but only on the mass ratio $A = m_0/m_1$ or equivalently $\omega = 1 + A$ or the angle ϕ.

Another big advantage of eq. (2.53) is that the integration over the kernel can be disentangled with the help of a Mellin-transformation:

$$
\mathcal{M}[f](s) \;:=\; \int_0^\infty \mathrm{d}x\, x^{s-1} f(x) \quad , \qquad (2.54)
$$

which is linear in the function f. The region $\langle a,b\rangle := \{s \in \mathbb{C} \,|\, a < \mathrm{Re}(s) < b\}$ where the integral (2.54) converges and where the resulting Mellin-transform $\mathcal{M}[f]$ is analytic is called the *fundamental strip*. Applying eq. (2.54) on both sides of eq. (2.53), a substitution $x := p/q$ yields $\mathrm{d}p/q = \mathrm{d}x/x$ and thus we end up with the ordinary homogeneous linear equation:

$$
\mathcal{B}^{[J^P]}(s) \;=\; \mathcal{K}^{[J^P]}(s)\,\mathcal{B}^{[J^P]}(s) \quad\Leftrightarrow\quad \big[\mathbb{1} \,-\, \mathcal{K}^{[J^P]}(s)\big]\,\mathcal{B}^{[J^P]}(s) \;=\; 0 \quad . \qquad (2.55)
$$

The functions $\mathcal{B}^{[J^P]} := \mathcal{M}[B^{[J^P]}]$ and $\mathcal{K}^{[J^P]} := \mathcal{M}[\bar{K}^{[J^P]}]$ are the Mellin transforms of the wave function and the kernel, respectively. Using eq. (2.53) and the definition (A.56) of the translation operator $\hat{T}$ with the property (A.62), the formal expression for the transformed kernel in eq. (2.55) reads:

$$\begin{aligned}
\mathcal{K}^{[J^+]} &= \xi^{[J^+]} \left(\begin{smallmatrix} \Theta_{J-1} & 0 \\ 0 & 1 \end{smallmatrix}\right) \begin{pmatrix} \frac{(J-1)(2J+1)}{(2J-1)\sin\phi}\mathcal{Q}_{J-2} - J(\hat{T}_{-1}+\hat{T}_1)\mathcal{Q}_{J-1} + (\frac{1}{(2J-1)\sin\phi}+J\sin\phi)\mathcal{Q}_J & \sqrt{J(J+1)}[\hat{T}_1\mathcal{Q}_{J-1} - (\frac{1}{\sin\phi}+\sin\phi)\mathcal{Q}_J + \hat{T}_{-1}\mathcal{Q}_{J+1}] \\ \sqrt{J(J+1)}[\hat{T}_{-1}\mathcal{Q}_{J-1} - (\frac{1}{\sin\phi}+\sin\phi)\mathcal{Q}_J + \hat{T}_1\mathcal{Q}_{J+1}] & (\frac{\omega}{2J+3}+\frac{J+1}{\omega})\mathcal{Q}_J - (J+1)(\hat{T}_{-1}+\hat{T}_1)\mathcal{Q}_{J+1} + \omega\frac{(J+2)(2J+1)}{2J+3}\mathcal{Q}_{J+2} \end{pmatrix} \left(\begin{smallmatrix} \Theta_{J-1} & 0 \\ 0 & 1 \end{smallmatrix}\right) \quad , \\
\mathcal{K}^{[J^-]} &= \xi^{[J^-]}\,\Theta_{J-1}\,(\mathcal{Q}_{J+1} - \mathcal{Q}_{J-1}) \quad , \qquad \mathcal{Q}_J(s) \;=\; \mathcal{M}[Q_J \circ c](s) \quad .
\end{aligned} \tag{2.56}$$

Of course, the equations (2.55) and (2.56) are only valid in the corresponding fundamental strips. Explicit formulas for the Mellin transforms $\mathcal{Q}_J$, in terms of hypergeometric series or equivalent transcendental expressions, can be found in appendix A.2.4 in eq. (A.54) and eq. (A.57), respectively.

With regard to the asymptotic bound-state equation (2.53), one can show that its solutions can be written as:

$$B^{[J^P]}(p) \;=\; \frac{1}{2\pi i}\oint_\Gamma \mathrm{d}s\,\left[\mathbb{1} \,-\, \mathcal{K}^{[J^P]}(s)\right]^{-1}\mathcal{C}^{[J^P]}(s)\,p^{-s} \quad , \tag{2.57}$$

where the closed integration contour $\oint_\Gamma \mathrm{d}s = \int_{a+\varepsilon+i\infty}^{a+\varepsilon-i\infty}\mathrm{d}s + \int_{b-\varepsilon-i\infty}^{b-\varepsilon+i\infty}\mathrm{d}s$ lies within the fundamental strip $\langle a, b\rangle$. The missing upper and lower connecting line integrals in the contour are infinitely far away and do not contribute, since the integrand falls off rapidly enough. The basic methods used for the derivation of eq. (2.57) can e.g. be found up in [78], especially see eqs. (8.5.19) and (8.5.43) therein. For $J \geq 1$, the J^+-channel has matrix dimension 2×2 such that in this case eq. (2.57) can be seen as the higher dimensional generalization of the original homogeneous one-dimensional case that is considered in [78]. The terms $\mathcal{C}^{[J^P]}$ and $B^{[J^P]}$ have the same matrix dimension. Furthermore, $\mathcal{C}^{[J^P]}(s)$ is also analytic in $\langle a, b\rangle$, though its specific functional dependence on s is irrelevant for our purposes.

Assuming that the inverse matrix $\left[\mathbb{1} - \mathcal{K}^{[J^P]}(s)\right]^{-1}$ has at most countable many poles s_n in the fundamental strip $\langle a+\varepsilon, b-\varepsilon\rangle$ which are all of first order, the residue theorem implies:

$$B^{[J^P]}(p) \;=\; \sum_{n\in\mathbb{N}} C_n^{[J^P]}\,p^{-s_n} \quad , \tag{2.58}$$

with some complex vectors $C_n^{[J^P]}$. For large momenta, the exponent s_n with the smallest real part then dominates the asymptotic behavior of the $B^{[J^P]}$-function. These exponents can simply be determined as the roots of the transcendental function:

$$\mathcal{F}_0^{[J^P]} \;=\{s\in\langle a+\varepsilon, b-\varepsilon\rangle\,|\,\mathcal{F}^{[J^P]}(s) = 0\} \quad , \quad \mathcal{F}^{[J^P]}(s) \;:=\; \left|\det\left[\mathbb{1} - \mathcal{K}^{[J^P]}(s)\right]\right| \;, \tag{2.59}$$

which together with eq. (2.56) is the P-wave analogue of the bosonic S-wave case in eq. (2.17).

Since the interaction kernel $K^{[J^P]}$ in eq. (2.53) is real-valued and obeys the symmetry $\bar{K}^{[J^P]}(1/x) = (\bar{K}^{[J^P]}(x))^{\mathrm{T}}$, its Mellin-transform fulfills:

$$\begin{aligned} \mathcal{K}^{[J^P]}(s^*) &= \int_0^\infty \mathrm{d}x\, x^{s^*-1}\, \bar{K}^{[J^P]}(x) = \left(\mathcal{K}^{[J^P]}(s)\right)^* \quad , \\ \mathcal{K}^{[J^P]}(-s) &= \int_0^\infty \mathrm{d}x\, x^{-s-1}\, \bar{K}^{[J^P]}(x) = \int_0^\infty \frac{\mathrm{d}y}{y^2}\, y^{s+1}\, \bar{K}^{[J^P]}(1/y) \\ &= \int_0^\infty \mathrm{d}y\, y^{s-1}\, (\bar{K}^{[J^P]}(y))^{\mathrm{T}} = \left(\mathcal{K}^{[J^P]}(s)\right)^{\mathrm{T}} \\ \Rightarrow \quad \mathcal{F}^{[J^P]}(s) &= \mathcal{F}^{[J^P]}(s^*) = \mathcal{F}^{[J^P]}(-s) = \mathcal{F}^{[J^P]}(-s^*) \quad . \end{aligned} \tag{2.60}$$

Consequently, the fundamental strip of $\mathcal{K}^{[J^P]}$ is symmetric with respect to the imaginary axis. Considering the root equation (2.59), we additionally conclude that $s_n \in \mathcal{F}_0^{[J^P]}$ also implies $\{\pm s_n, \pm s_n^*\} \subset \mathcal{F}_0^{[J^P]}$, meaning that the set of exponents in (2.58) is symmetric with respect to the real and the imaginary axis. Thus, if a root $s_n \in \mathcal{F}_0^{[J^P]}$ has non-vanishing real part, then either $s_n \in \mathcal{F}_0^{[J^P]}$ or $-s_n \in \mathcal{F}_0^{[J^P]}$ has negative real part, leading to divergent asymptotic solutions (2.58). Hence, discrete scale invariance can only exist for configurations where there are only purely imaginary roots $s_n \in \mathcal{F}_0^{[J^P]}$. More precisely it emerges if and only if $\mathcal{F}_0^{[J^P]} = \{\pm i s_0\}$, where s_0 is real.

terms	Mellin transform	fundamental strip	poles
(1)	$\mathcal{Q}_{J-2}$	$\langle -J+1, J-1\rangle$	$\pm(2\mathbb{N}_0 + J - 1)$
(2)	$\hat{T}_{-1}\mathcal{Q}_{J-1}$	$\langle -J-1, J-1\rangle$	$\pm(2\mathbb{N}_0 + J) - 1$
(3)	$\hat{T}_{1}\mathcal{Q}_{J-1}$	$\langle -J+1, J+1\rangle$	$\pm(2\mathbb{N}_0 + J) + 1$
(4)	$\mathcal{Q}_{J}$	$\langle -J-1, J+1\rangle$	$\pm(2\mathbb{N}_0 + J + 1)$
(5)	$\hat{T}_{-1}\mathcal{Q}_{J+1}$	$\langle -J-3, J+1\rangle$	$\pm(2\mathbb{N}_0 + J + 2) - 1$
(6)	$\hat{T}_{1}\mathcal{Q}_{J+1}$	$\langle -J-1, J+3\rangle$	$\pm(2\mathbb{N}_0 + J + 2) + 1$
(7)	$\mathcal{Q}_{J+2}$	$\langle -J-3, J+3\rangle$	$\pm(2\mathbb{N}_0 + J + 3)$
(8)	$\mathcal{Q}_{J-1}$	$\langle -J, J\rangle$	$\pm(2\mathbb{N}_0 + J)$
(9)	$\mathcal{Q}_{J+1}$	$\langle -J-2, J+2\rangle$	$\pm(2\mathbb{N}_0 + J + 2)$
$(4-7)$	$\mathcal{K}^{[(J=0)^+]}$	$\langle -J-1, J+1\rangle = \langle -1, 1\rangle$	$\pm(2\mathbb{N}_0 + 1)$
$(2-7)$	$\mathcal{K}^{[(J=1)^+]}$	$\langle -J+1, J-1\rangle = \langle 0, 0\rangle$	$\pm(2\mathbb{N}_0)$
$(1-7)$	$\mathcal{K}^{[(J\geq 2)^+]}$	$\langle -J+1, J-1\rangle$	$\pm(2\mathbb{N}_0 + J - 1)$
$(8-9)$	$\mathcal{K}^{[(J\geq 1)^-]}$	$\langle -J, J\rangle$	$\pm(2\mathbb{N}_0 + J)$

Table 2.1: Fundamental strips and poles of terms appearing in the Mellin-transformed kernels (2.56). Due to the off-diagonal terms $\hat{T}_{-1}\mathcal{Q}_0$ and $\hat{T}_1\mathcal{Q}_0$ the channel with quantum numbers $J^P = 1^+$ naively would have $\langle 0, 0\rangle = \emptyset$ and thus no Mellin transform would exist.

In order to identify all channels with $\mathcal{F}_0^{[J^P]} = \{\pm i s_0\}$, we first have to determine the symmetric fundamental strips of analyticity of the transformed kernel. As explained in appendix A.2.4, the Mellin transform $\mathcal{Q}_J = \mathcal{M}[Q_J \circ c]$ of a Legendre functions of second kind is analytic in the strip $\langle -J-1, J+1 \rangle$. More precisely it is even meromorphic in $\mathbb{C}$ with countably infinitely many poles of first order, located on the real axis at the values $\pm(2\mathbb{N}_0 + \ell + 1)$. From that, we can easily derive fundamental strips and singularities for all the Mellin-transformed terms, appearing in eq. (2.56). In tab. 2.1 we summarize our finding and also give combined results for the Mellin-transformed kernels $\mathcal{K}^{[J^P]}$. The case $J^P = 1^+$ is special, since, a priori, the fundamental strips $\langle -2, 0 \rangle$ and $\langle 0, 2 \rangle$ of the separately appearing off-diagonal expressions $\hat{T}_{-1}\mathcal{Q}_0$ and $\hat{T}_1\mathcal{Q}_0$ are disjoint. However, analytically continuing the two expressions, both strips can be brought to an overlap at the imaginary axis, where the only remaining undefined point is a singularity at the origin $s = 0$.

Initially, another promising idea in order to deal with this problem was to search for a specific similarity transformation of the kernel $\bar{R}^{[J^+]} \mapsto O\bar{R}^{[J^+]}O^{-1}$ in eq. (2.56) such that all critical terms $x\, Q_0(c(x))$ and $1/x\, Q_0(c(x))$ either cancel or only appear in the combination $(x + 1/x)Q_0(c(x)) = 2\sin\phi\, c(x)\, Q_0(c(x))$, whose Mellin transform, as shown in eq. (A.63) in sec. A.2.4, is uncritical at $s = 0$ and has a non-empty fundamental strip $\langle -1, 1 \rangle$. As we will see in the following paragraph, such a transformation can not exist. However, using e.g. the orthogonal transformation-matrix $O = 1/\sqrt{2J+1} \left(\begin{smallmatrix} \sqrt{J+1} & \sqrt{J} \\ -\sqrt{J} & \sqrt{J+1} \end{smallmatrix} \right)$ and the recursion relation (A.35) leads to an interesting cancellation of many terms in the upper left matrix component of $O\bar{R}^{[J^+]}O^{\mathrm{T}}$, though it complicates the structure of the off-diagonal elements.

In figs. 2.2 and 2.3, the function $\mathcal{F}^{[J^P]}$ from eq. (2.59) is plotted for complex arguments s. Thereby, contour-plots for ψ_1 being either bosons or fermions and for several J^P-channels are given. The mass ratio is fixed to $A = m_0/m_1 = 1/4$, as for such relatively small values, the structure of the functions is easier to illustrate. Since the precise values of $\mathcal{F}^{[J^P]}(s)$ are irrelevant for our purposes, we only have to understand the functional behavior by tendency. It is encoded in the coloring via the rule: the brighter the shading, the larger $\mathcal{F}^{[J^P]}(s)$. In particular, the dark and bright spots represent roots $\mathcal{F}^{[J^P]}(s) = 0$ and poles $\mathcal{F}^{[J^P]}(s) \to \infty$, respectively. Comparing the positions of the poles with the predictions from tab. 2.1, in all cases, we find perfect agreement. Due to the properties of the determinant, the function $\mathcal{F}^{[J^P]}$ is invariant under similarity transformations of $\bar{R}^{[J^P]}$. This also holds for the pole positions. Consequently, the mentioned agreement reveals that the existence of any similarity transformation that would lead to a cancellation of pole contributions, and hence would helpfully enlarge fundamental strips, is excluded. The vertical red lines bound the fundamental strips and are always fixed to those singularities closest to the origin. In the channel $J^P = 1^+$ this, a priori, leads to a vanishing fundamental strip, since $s = 0$ is singular. Furthermore, the symmetries (2.60) directly become apparent in the plots, as they exhibit mirror-symmetry with respect to the real and imaginary axis.

We can now directly read off the cases in which the roots in the fundamental strip are purely imaginary $\pm is_0$. For bosonic fields ψ_1, $J^P = 1^+$ is the only such channel, whereas for ψ_1 being fermions, imaginary roots appear for $J^P \in \{0^+, 1^+, 1^-, 2^+\}$. This classification of the channels remains stable if the mass ratio A is varied, whereas quantitatively, the purely imaginary roots move towards the origin for increasing A. By contrast, the positions

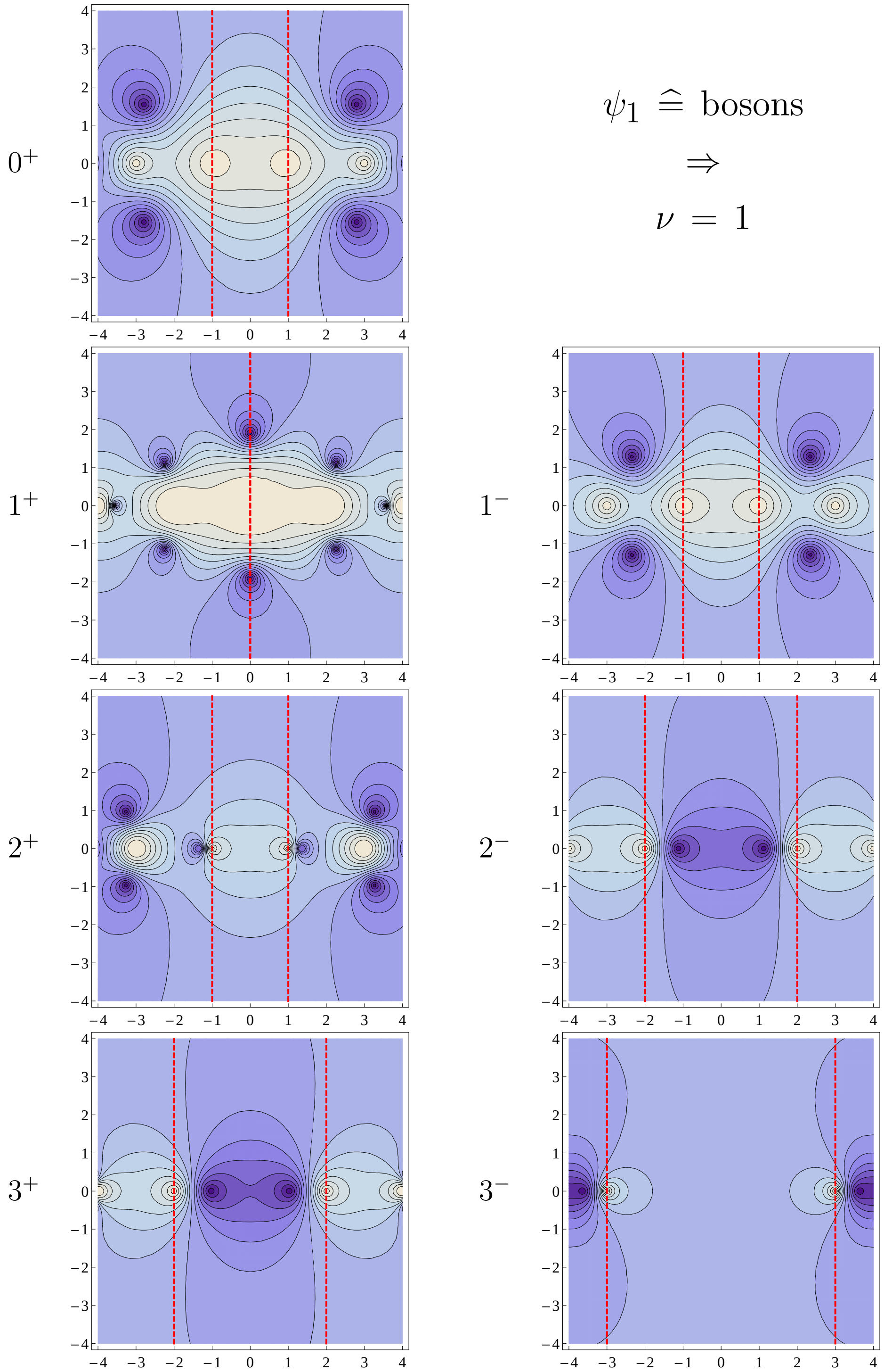

Table 2.2: Contour-plots of $\mathcal{F}^{[J^P]} : \mathbb{C} \to [0, \infty)$ from eq. (2.59) for bosonic fields ψ_1 and different J^P-channels. The mass ratio is fixed to $A = 1/4$. The vertical red lines bound the fundamental strips and dark and bright spots represent roots and poles, respectively. The only channel with purely imaginary roots is $J^P = 1^+$.

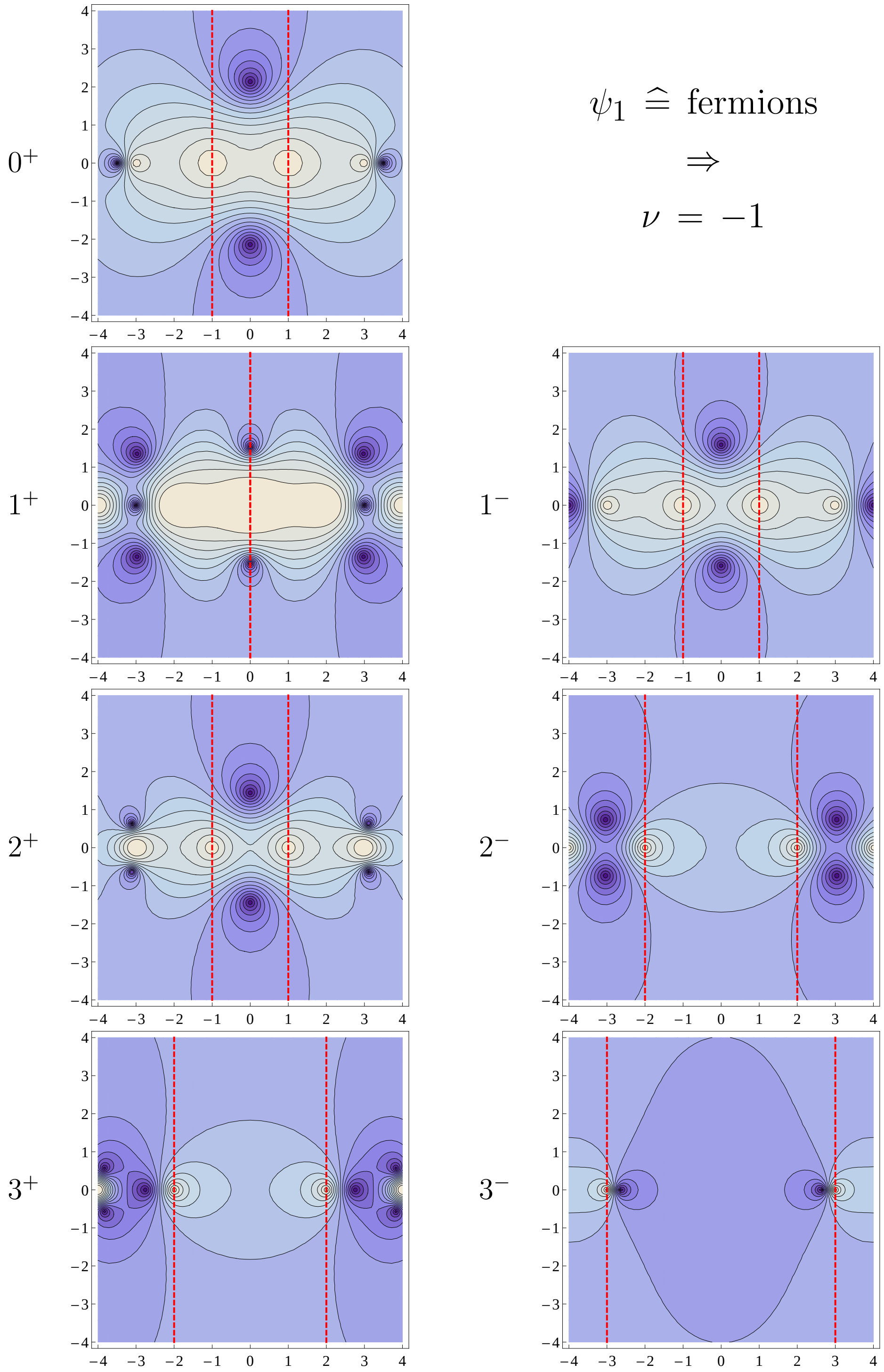

Table 2.3: Contour-plots of $\mathcal{F}^{[J^P]} : \mathbb{C} \to [0, \infty)$ from eq. (2.59) for fermionic fields ψ_1 and different J^P-channels. The mass ratio is fixed to $A = 1/4$. The vertical red lines bound the fundamental strips and dark and bright spots represent roots and poles, respectively. The only channels with purely imaginary roots are $J^P \in \{0^+, 1^+, 1^-, 2^+\}$.

of the singularities are fixed to integer values and are independent of A. Figs. 2.2 and 2.3 only include plots for total angular momenta $J \leq 3$. However, up to very high $J \geq 4$, we did not observe any further channel with roots on the imaginary axis. Although this approach, of course, is not able to strictly prove the non-existence of such roots for all $J \geq 4$, we assume that cases listed above are the only ones. Thus, we end up with five different channels, in which the asymptotic behavior of the solution to the bound-state equation (2.51) is dominated by a purely imaginary exponent. Consequently, these are also exactly the channels that display a discrete scale invariance and are qualified for the possible emergence of an Efimov effect.

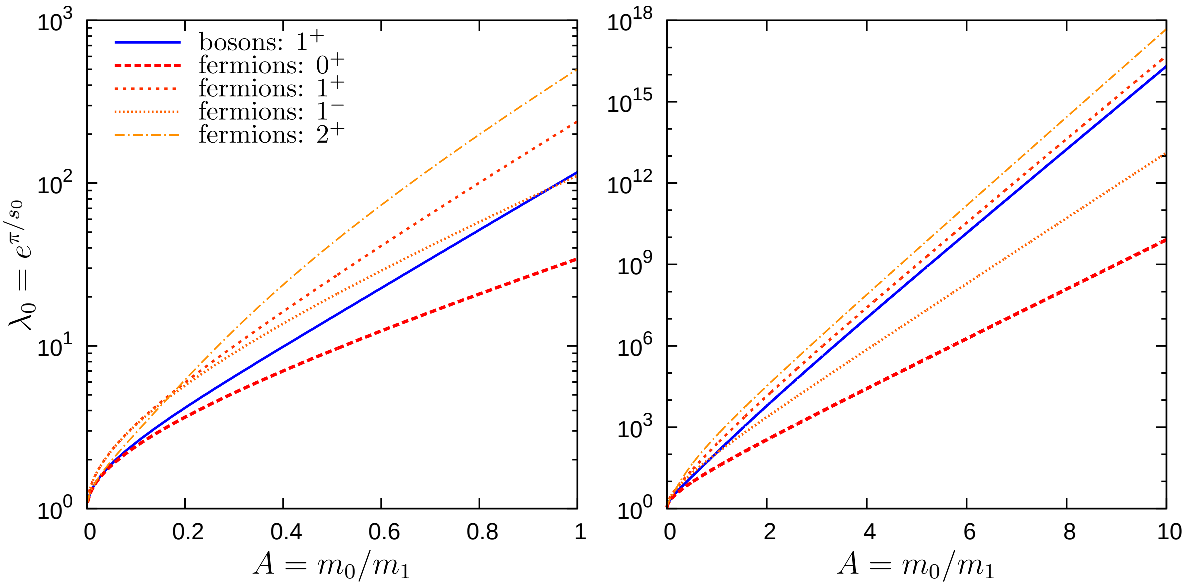

Figure 2.8: Discrete scaling factor $\lambda_0 = e^{\pi/s_0}$ as a function of the mass ratio $A = m_0/m_1$ for all five cases. If the two identical particles ψ_1 are bosons, discrete scale invariance only shows up in the channel $J^P = 1^+$. For ψ_1 being fermions, the allowed channels are $J^P \in \{0^+, 1^+, 1^-, 2^+\}$.

For all five sectors that display imaginary zeros is_0, we can determine the numerical value of s_0 via a root-finding algorithm. The corresponding discrete scaling factor then reads $\lambda_0 = e^{\pi/s_0}$. In fig. 2.8 it is plotted as a function of the mass ratio $A = m_0/m_1$ for all identified channels. The exact functional dependencies seem to be nontrivial, however, λ_0 vanishes for $A \to 0$ and grows exponentially for $A > 1$. Unlike in the S-wave case in fig. 2.2 λ_0 has no maximum. Possible experimental evidence for discrete scale invariance, such as the existence of multiple Efimov states, is most likely to be observed for a small discrete scaling factors. We see that such values are approached if the third particle is much lighter than the two identical ones. Comparing all five channels, we also note that the discrete scaling factor is smallest if the two ψ_1 are fermions and the J^P-quantum numbers are 0^+. In tab. 2.4, numerical values for s_0 and λ_0 for exemplary mass ratios are given.

$A = m_0/m_1$		1/8		1/4		1/2		1		2	
ψ_1	J^P	s_0	λ_0	s_0	λ_0	s_0	λ_0	s_0	λ_0	s_0	λ_0
bosons	1^+	2.951	2.90	1.905	5.20	1.161	14.97	0.660	116.7	0.360	6132
fermions	0^+	3.162	2.70	2.138	4.35	1.404	9.37	0.889	34.2	0.538	345
fermions	1^+	2.323	3.87	1.535	7.74	0.965	25.98	0.574	239.3	0.329	13978
fermions	1^-	2.348	3.81	1.588	7.23	1.047	20.09	0.667	111.2	0.405	2338
fermions	2^+	2.491	3.53	1.441	8.85	0.837	42.56	0.505	501.9	0.302	32919

Table 2.4: Imaginary roots is_0 of eq. (2.59) and the corresponding the discrete scaling factors λ_0 for exemplary mass ratios $A = m_0/m_1 \in \{1/8, 1/4, 1/2, 1, 2\}$. The green-shaded case with $\lambda_0 = 2.70$ will exemplarily be considered for the numerical determination of the bound-state spectrum in sec. 2.3.4.2

2.3.4.2 Bound-state spectrum

As mentioned before, the bound-state equation (2.51) can also be solved numerically by introducing a loop momentum cut-off Λ. A detailed description of our method is given in appendix B. For most J^P-channels, the resulting unphysical cut-off dependence vanishes in the limit $\Lambda \to 0$, since the wave function falls of rapidly enough. By contrast, this limit does not exist for the five previously identified channels that display an asymptotic discrete scale invariance. In these cases, three-body observables log-periodically depend on Λ. In order to eliminate this dependence, renormalization can be performed by adding an appropriate three-body force $H(\Lambda)$. As demonstrated in eq. (C.37) in appendix C.3, our a priori ansatz (2.18) for the three-body interactions $\mathcal{L}^{(3)}$ can only renormalize the 1^+ channel of the three-body sector. In order to renormalize the other channels, couplings with higher order derivatives would have to be included in $\mathcal{L}^{(3)}$. For a given cut-off Λ and a three-body binding energy $E^{(3)}$, the three-body term H is then fixed such that the corresponding bound-state equation has a solution at exactly this desired energy $E = E^{(3)}$. However, in this work, exact values of three-body bound-state energies $E^{(3)}$ are irrelevant, since we only focus on general features of the spectrum, such as energy ratios and the existence of an Efimov effect. Consequently, an inclusion of the three-body renormalization procedure is not needed, which is why we neglect H.

In fig. 2.9 the numerically determined spectrum is given for ψ_1 being bosons, quantum numbers $J^P = 0^+$, a mass ratio $A = m_0/m_1 = 1/8$ and vanishing effective range $r = 0$. As explained in sec. 2.3.3.2 the red-shaded area $1/a > 0$ originates from analytically continuing the P-wave bound-state integral equation from the blue-shaded area $1/a < 0$ that is included in (2.36). A full classification of the parameter regions can be found in tab. A.4 in sec. A.1.1.2. From a mathematical viewpoint, the plot displays a characteristic Efimov spectrum, which looks similar to the S-wave case, depicted in fig. 2.3. In the unitary limit, there is an infinite tower of trimer states with an accumulation point at threshold and with exact discrete scale invariance. Calculating the energy ratios yields a discrete scaling factor $\lambda_0 \approx 2.70$, which is in perfect agreement with the semi-analytic prediction from tab. 2.4 from the previous section. Similar analyses in other channels revealed that

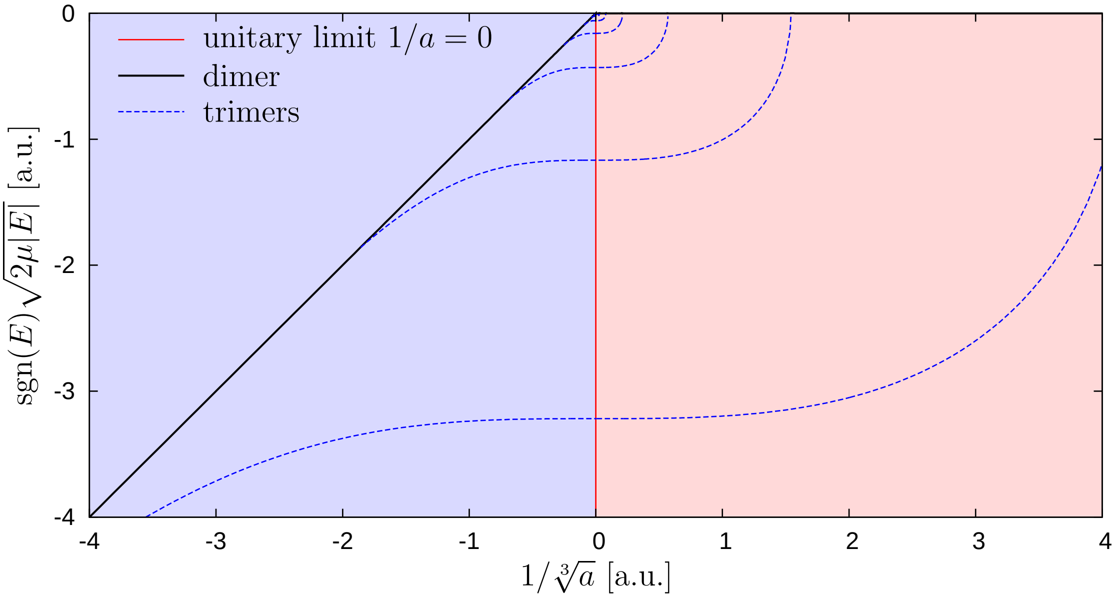

Figure 2.9: Bound state spectrum for $\psi_1 \mathrel{\widehat{=}}$ bosons, $J^P = 0^+$, $A = 1/8$ and vanishing effective range $r = 0$. The energies are expressed in terms of a rescaled parameter $\mathrm{sgn}(E)\sqrt{2\mu|E|}$ in arbitrary units [a.u]. Trimers energies lie below dimer energies and are ordered in a geometric series with discrete scale invariance and an accumulation point at the origin. In the red region, the dimer-particle scattering integral equation can not be derived straightforwardly via the residue theorem and is obtained from an analytic continuation. In the red region, there are unphysical dimer poles on the first Riemann sheet. For all scattering volumes, there are no dimer poles with positive residues on the physical sheet.

the Efimov effect only occurs for ψ_1 being bosons and $J^P \in \{0^+, 1^+, 1^-, 2^+\}$ or for ψ_1 being fermions and $J^P = 1^+$. In addition, also the determined energy ratios perfectly match with the predictions for $\lambda_0(A)$ in fig. 2.8. These complete agreements provide a positive consistency check for the semi-analytic approach chosen in sec. 2.3.4.1.

However, for P-wave interactions, the case of vanishing effective range seems to be unphysical due to the so-called *Wigner bound* [79]. Thereby, the requirement of causality leads to an upper bound on the effective range:

$$\forall \rho \geq R: \quad r \ \leq \ b(\rho) \quad , \qquad b(\rho) \ := \ -\frac{2}{\rho}\left[1 + \frac{\rho^3}{3a} - \frac{1}{5}\left(\frac{\rho^3}{3a}\right)^2\right] \quad , \tag{2.61}$$

where R is the range of the short-range potential. Since $b'(\rho) = 2(3a - \rho^3)^2/(\rho^2(3a)^2) \geq 0$ holds, the function b is monotonically nondecreasing with an absolute minimum at $b(R)$. For large scattering volumes $3a \gg R$, the effective range is then bound from above according to $r \leq -2/R < 0$. Hence, for two-particle P-wave interactions, the unitary limit is excluded by causality. Moreover, the dimer structure analysis in sec. A.1.1.2 shows that the limit $r = 0$ always generates spurious dimer poles with complex or negative residues on the physical Riemann sheet, whereas physical poles with positive residue do not occur. For these reasons, we now assume a negative effective range.

In fig. 2.10, the bound-state spectrum is plotted for ψ_1 being bosons, quantum numbers $J^P = 0^+$, a mass ratio $A = m_0/m_1 = 1/8$ and $r < 0$. The plot displays an approximate Efimov spectrum with approximate discrete scaling factor $\lambda_0 \approx 2.70$. There is an infinite tower of trimer states, which is again unbound from below but has no accumulation point at threshold. Comparing figs. 2.9 and 2.10, now a window in parameter space $1/a \in (0, |r|^3/54)$ exists where there is a physical pole with positive residue. We will refer to this pole as the *shallow dimer*. However, from tab. A.4 we know that there is also a deeper-bound dimer with negative residue on the physical sheet. Such a negative residue corresponds to a non-normalizable solution that can not represent a physical state. Hence, our theory can only be a good approximation above this *deep dimer*. Varying the scattering volume towards $1/a \to |r|^3/54$, both the shallow and the deep dimer meet at the rescaled energy $\mathrm{sgn}(E)\sqrt{2\mu|E|/(|r|/2)^2} = -2/3$ or equivalently $E = -|r|^2/(18\mu)$. This energy can be interpreted as the maximal range of applicability of our model with P-wave interactions. Unfortunately, also for $r < 0$ all trimer states can only be found below the unphysical deep dimer. Consequently, they do not represent physical three-body states and can not be used for a proper physical renormalization of the three-body sector. We now present several approaches we took into consideration in order to deal with the problems caused by the spurious, unphysical deep dimer.

As it was recently shown for a system of three identical bosons interacting through S-wave two-particle contact terms, a proper way to deal with spurious poles is to include effective range corrections only order by order [80, 81]. For this purpose, the original full dimer propagator is effectively written as an expansion in $r^{[0]}$, where each contribution does not have any spurious poles. N^{n}LO calculations in the three-particle sector then only require the inclusion of N$^{\leq n}$LO contributions of this dimer expansion as building blocks for Feynman diagrams. However, the essential difference in our P-wave case is that, due to the form of the interaction, effective range corrections already appear at leading order [37]. In our calculation, this can also be seen from the quadratic term $\sim \Lambda_i y_i^2$ in the dimer self-energy calculation (D.2) in sec. D.2.1, which requires a renormalization with the effective range. Hypothetically setting $r = 0$ and interpreting this as in some way a leading order, anyhow, would not lead to a better behavior of the full P-wave dimer propagator, since already in this case, the propagator (2.27) has poles with complex residue on the physical Riemann sheet. A detailed analysis of this case $r = 0$ is given in appendix A.1.1.2.

As another idea in order to get rid of the spurious poles, one can also treat the unitarity term $-iy^3$ in the denominator of eq. (2.27) as a perturbation. This method was recently applied to ^{6}He [82]. Assuming that the three-body cut-off Λ is sufficiently small, $-iy^3$ is negligible. In this approximation, indeed only the physical shallow dimer state remains. However, such a propagator no longer obeys $D(q \to \infty) \sim 1/q$, which was crucial for the derivation of discrete scale invariance in sec. 2.3.4.1. Correspondingly also the three-body spectrum, obtained from solving the bound-state equation, does not display discrete scale invariance. In particular, the trimer spectrum has no accumulation point at threshold. Furthermore, for commensurable particle masses, the binding momentum of the first ap-

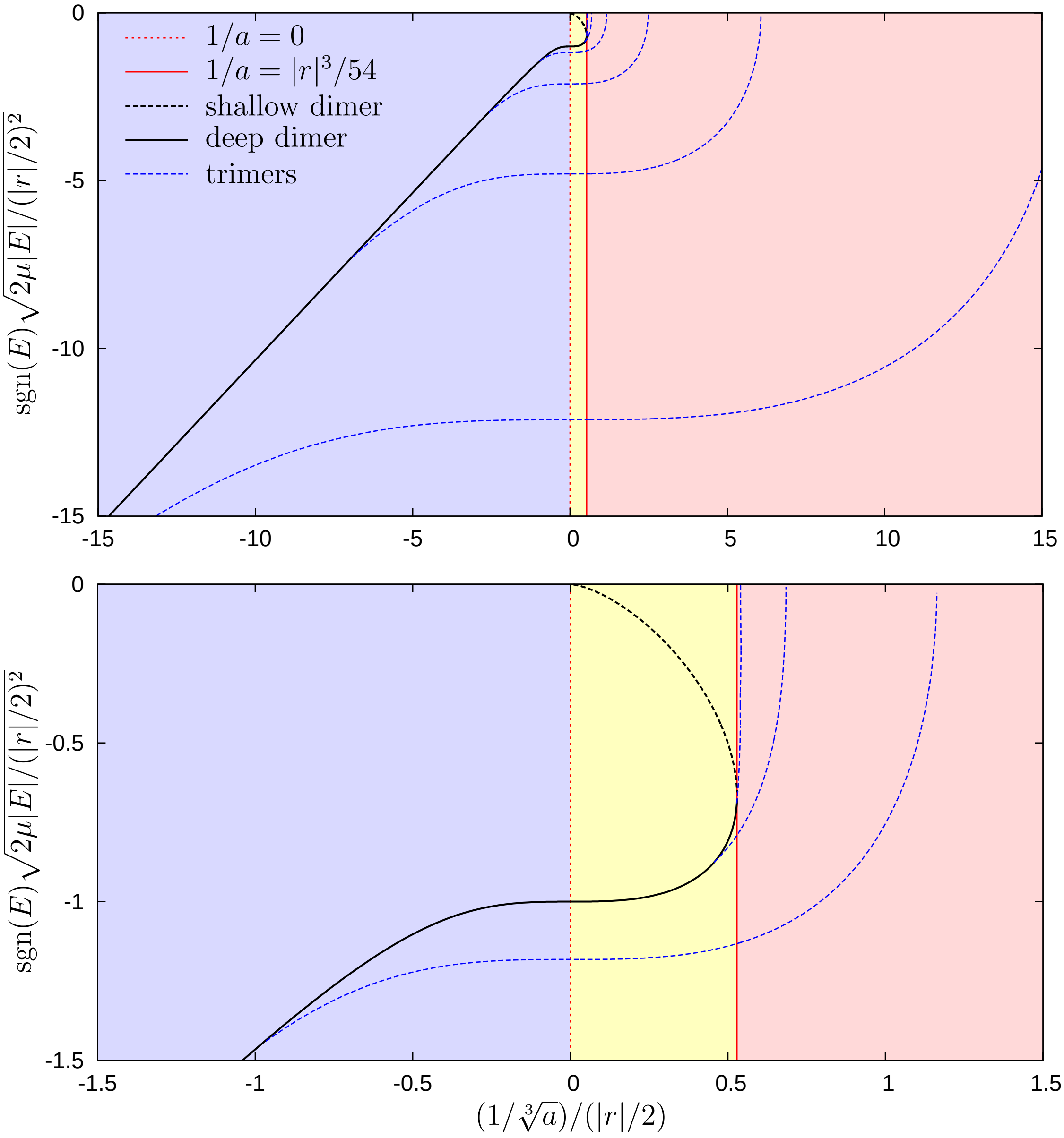

Figure 2.10: Bound state spectrum for $\psi_1 \mathrel{\widehat{=}}$ bosons, $J^P = 0^+$, $A = 1/8$ and negative effective range $r = 0$. The scattering volume and the energies are expressed in terms of rescaled parameters $(1/\sqrt[3]{a})/(|r|/2)$ and $\mathrm{sgn}(E)\sqrt{2\mu|E|/(|r|/2)^2}$. The trimers lie below the dimers and are ordered in an approximate geometric series with approximate discrete scale invariance. There is no accumulation point at threshold. In the red region, the dimer-particle scattering integral equation can not be derived straightforwardly via the residue theorem and is obtained from an analytic continuation. In the blue region there are unphysical poles on the first Riemann sheet. In the red region, there is a shallow dimer state with positive residue and a second deep dimer state with negative residue on the physical sheet.

pearing trimer state already exceeds the momentum cut-off, discarding it as unphysical. Another fundamental drawback of this method is that unitarity is lost, which is actually a requirement for the form (1.4) that was chosen for the scattering amplitude.

Considering the partial fraction decomposition (A.3), alternatively, one could also try to cancel the unphysical residue contributions by adding suitable S-wave counter-terms. However, such terms would have to be designed in a way that for small momenta, spurious poles are exactly eliminated but for large momenta the original dimer propagator is reproduced in order to maintain the required asymptotic $1/q$-dependence. In addition, the interaction term iR from eq. (2.35), should not be changed. The existence of a corresponding counter-term on the Lagrangian level that accomplishes all these requirements, seems to be very unlikely.

In our model, the trimer states represent stable particles. Allowing the trimer to decay, also complex binding-energy solutions of the bound-state equation (2.51) that lie above the unphysical deep dimer, in principle, are possible. The imaginary part of the energy can then be interpreted as the width of the trimer state. With respect to the spectrum in fig. 2.10, trimers whose energies hit the deep dimer threshold could possibly survive as trimer resonances in the region between the deep and the shallow dimer. Such resonances could then also be used in order to renormalize the three-body sector. However, a priori, we can not expect such resonances to exhibit discrete scale invariance or an accumulation point at zero, since the considered limit (2.52) in sec. 2.3.4.1 is not applicable. Furthermore, such resonances could decay into the unphysical deep dimers. On the technical side, the required generalization of all calculations to complex E and the search for complex binding energies represents a major extension to the formalism as well as to computational costs. At first one would have to find an appropriate numerical approximation for the Q_J-functions with complex arguments, analogous to the finite expansion presented in sec. A.2.3.1 that holds for real arguments. Furthermore, an intricate problem would then be to find the complex binding energies in a reliable way. With regard to the numerical determination, as it is discussed in appendix B, they can be expressed as the complex roots of eq. (B.3). Since the mentioned bisection method fails as a complex root-finding algorithm, one natural alternative would be the Newton method. This method begins with one starting value E_0 and then calculates proceeding energies according to $E_{n+1} = E_n - f^{[J^P]}(E_n)/\partial f^{[J^P]}(E_n)$. However, the determination of the derivative $\partial f^{[J^P]}$ would involve the numerical calculation of an inverse kernel matrix. Since, for our purposes, this is too expensive in terms of computation time, an approximation through the secant method seems favorable. It reads $\partial f^{[J^P]}(E_n) = (f^{[J^P]}(E_n) - f^{[J^P]}(E_{n-1}))/(E_n - E_{n-1})$ and needs two initial values E_0 and E_1. Since $f^{[J^P]}$ is roughly an oscillating log-periodic function, both methods are only good in the direct neighborhood of a complex root. Otherwise even its convergence is not guaranteed. This requires a relatively precise guess for the initial values, further aggravating the numerical challenges. If the imaginary parts of the complex binding energies are small, the roots of $\mathrm{Re} \circ f^{[J^P]}$ could already be a good approximation for the roots of $f^{[J^P]}$. Therefore, $\mathrm{Re} \circ f^{[J^P]}$ and $\mathrm{Im} \circ f^{[J^P]}$ should have comparable magnitudes. Comparisons between both functions on the real axis, nevertheless, indicated that this is not the case. Thus, the determination of possible complex binding energies is involved and not part of this work.

Another idea would be to analyze if the spurious non-normalizable deep dimer state is in a way decoupled from the remaining spectrum. For many quantum mechanical potentials, such as the harmonic oscillator or the potential well, there exist discrete solutions to the Schrödinger equation, which are non-normalizable. They are discarded, since normalizability is required and the spectrum of normalizable states already forms a complete set in the corresponding Hilbert space. As demonstrated in sec. A.1.1.2, the shallow dimer has positive residue. For resonant two-particle S-wave interactions, also the trimer states have positive residue, what can be seen from eq. (3.52) in the following chapter. Thus, it would be interesting to investigate if this also holds for resonant two-particle P-wave interactions and if the continuum states together with all discrete positive-residue dimer and trimer bound states already form a complete set in our field theoretical approach. Discarding all remaining states with unphysical residue might then provide a method that restores the physical applicability of our model in the trimer regime. The fact that in figs. 2.9 and 2.10 the trimer energies vanish as they hit the unphysical deep dimer energy, however, indicates that the states can not be separated in this manner.

All obtained results and considerations for the two- and three-particle systems also hold for corresponding halo systems as long as resonant two-particle P-wave interactions are involved and our power counting scheme combined with the effective range expansion is used. Thus, without extensive modifications, our method fails to describe bound three-particle P-wave halo nuclei, while two-particle P-wave halo nuclei, in principle, are accessible. A summary of our results will be given in chapter 4.

Chapter 3

Halo EFT with external currents

In this chapter, we consider non-relativistic halo EFT with resonant two-particle S-wave interactions. With respect to electromagnetic properties of halo nuclei, halo EFT has also been extended to include Coulomb effects [83] and electromagnetic currents [84–87]. Furthermore, also coupled channel effects have been considered for two-body halo nuclei [88]. In the following sections, we extend these studies to two-neutron halo nuclei, where in our model all three fields interact through resonant S-wave contact terms. We derive and calculate form factors and charge radii relative to the core to leading order. In addition, we calculate the dipole strength distribution for the photodisintegration of a two-neutron halo. Moreover, we investigate general dependencies between physical observables in these systems, yielding universal correlations. Our formalism is applied to current light as well as heavy halo nuclei candidates.

The derivations and formulas appearing in secs. 3.1 and 3.2 have in parts been published in [89]. This also includes the calculations of form factors and electric charge radii for the light halo nuclei ^{11}Li, ^{14}Be and ^{22}C in sec. 3.2.2.2 as well as the universal correlations in sec. 3.2.3. The application of our two-neutron halo EFT with external currents to ^{62}Ca in sec. 3.2.3.1 represents the authors' contribution to ref. [90], where the required input parameters for this system were calculated by the coauthors via coupled-cluster methods.

3.1 Two-neutron halo EFT formalism

3.1.1 Effective Lagrangian

First, we set up a non-relativistic effective field theory in the strong sector for a core (c) with spin 0 interacting with two neutrons (n) with spin 1/2. The core is described by a scalar field ψ_0 and the neutrons are described by a two-component spinor field $\vec{\psi}_1 = \binom{\psi_1}{\psi_2} = \binom{n_\uparrow}{n_\downarrow}$. Formally, these are again three fundamental degrees of freedom (ψ_0, ψ_1, ψ_2).

We assume that all two-particle interactions are short-ranged and dominated by S-wave resonances. If they are non-resonant, higher-partial wave interactions are suppressed by three powers of $R/|a|$. An EFT formalism for the treatment of resonant interactions in higher partial waves in the two-body problem was developed in [37, 38]. With regard to the three-body problem, this ansatz was combined with the Gamov shell model and applied to ^{6}He [82, 91]. However, as our analysis in sec. 2.3.4.2 indicated that P-wave interaction without further modifications in the EFT framework are unable to generate physical three-body bound states, we will not consider higher partial waves for our halo nuclei analysis.

The interaction of the two neutrons is described by an auxiliary spin-0 dimer field d_0 and the core-neutron interaction is rewritten in terms of an auxiliary spin-1/2 dimer field $\vec{d}_1 = \left(\begin{smallmatrix} d_1 \\ d_2 \end{smallmatrix}\right) \mathrel{\widehat{=}} \left(\begin{smallmatrix} c\leftrightarrow n_\uparrow \\ c\leftrightarrow n_\downarrow \end{smallmatrix}\right)$. The labeling and indices are chosen to simplify the notation for the three-body equations derived below in sec. 3.1.3. Moreover, we allow for a three-body contact interaction between the core and the two neutrons, which is mediated by a spin-0 trimer auxiliary field t. Note that our choice to introduce auxiliary fields does not necessarily imply bound states in the corresponding channels and merely is a convenient way to introduce interactions.

We use the mass conventions (1.13), presented in sec. 1.3, where, of course, the two distinguishable neutrons ψ_1 and ψ_2 have equal masses $m_1 = m_2$, leading to $M_\Sigma = m_0 + 2m_1$ and $M_\Pi = m_0 m_1^2$.

The effective Lagrangian can then be written as the sum of one-, two- and three-body contributions:

$$
\boxed{
\begin{aligned}
\mathcal{L} &= \mathcal{L}^{(1)} + \mathcal{L}^{(2)} + \mathcal{L}^{(3)} \quad , \qquad \mathcal{L}^{(1)} = \mathcal{L}^{(\text{free})} \quad , \\
\mathcal{L}^{(\text{free})} &= \sum_{i\in I_1} \psi_i^\dagger \Big(i\partial_0 + \frac{\nabla^2}{2m_i} \Big) \psi_i = \psi_0^\dagger \Big(i\partial_0 + \frac{\nabla^2}{2m_0} \Big) \psi_0 + \vec{\psi}_1^\dagger \Big(i\partial_0 + \frac{\nabla^2}{2m_1} \Big) \vec{\psi}_1 \quad , \\
\mathcal{L}^{(2)} &= \Delta_0\, d_0^\dagger d_0 - \frac{g_0}{2} \Big[d_0^\dagger \, (\vec{\psi}_1^{\,\mathrm{T}} P\, \vec{\psi}_1) + (\vec{\psi}_1^{\,\mathrm{T}} P\, \vec{\psi}_1)^\dagger \, d_0 \Big] \\
&\quad + \Delta_1\, \vec{d}_1^{\,\dagger} \vec{d}_1 - g_1 \Big[\vec{d}_1^{\,\dagger} \vec{\psi}_1 \, \psi_0 + \psi_0^\dagger \, \vec{\psi}_1^{\,\dagger} \vec{d}_1 \Big] \quad , \\
\mathcal{L}^{(3)} &= \Xi\, t^\dagger\, t - h \left[t^\dagger \, \psi_0 \, d_0 + (\psi_0 \, d_0)^\dagger t \right] \quad .
\end{aligned}
}
\tag{3.1}
$$

The matrix P projects the two neutrons on the spin-singlet. Its components are the corresponding Clebsch-Gordon coefficients:

$$
\begin{aligned}
P^{s_1 s_2} &= C^{00}_{\frac{1}{2}s_1;\frac{1}{2}s_2} \qquad \Rightarrow \qquad P = \frac{1}{\sqrt{2}} \left(\begin{smallmatrix} 0 & 1 \\ -1 & 0 \end{smallmatrix}\right) = -P^\dagger \quad , \\
PP^\dagger &= \mathbb{1}_2/2 \qquad \Rightarrow \qquad \mathrm{Tr}[PP^\dagger] = 1 \quad , \\
\vec{\psi}_1^{\,\mathrm{T}} P \vec{\psi}_1 &= \frac{1}{\sqrt{2}} (\psi_1 \psi_2 - \psi_2 \psi_1) = \frac{1}{\sqrt{2}} (n_\uparrow n_\downarrow - n_\downarrow n_\uparrow) \quad .
\end{aligned}
\tag{3.2}
$$

The one-particle Lagrangian $\mathcal{L}^{(1)} = \mathcal{L}^{(\text{free})}$, simply describes the free non-relativistic propagation of the scalar fields.

The two-body contribution $\mathcal{L}^{(2)}$ includes the bare dimer propagators and the coupling of a dimer to two single particles. The bare parameters Δ_0, g_0, Δ_1 and g_1 depend on the ultraviolet cut-off in the two-particle sector. Theses couplings have to be renormalized. Additional dynamical dimer terms of the form $\eta_i\, d_i^\dagger\big(i\partial_0 + \frac{\nabla^2}{2M_i}\big)d_i$ would contribute to effective range corrections but will not be considered in the following. The notation is chosen in a way that the lower indices $i = 0, 1$ correspond to the nn and cn channel, respectively.

Finally, $\mathcal{L}^{(3)}$ represents the three-body interaction, written in terms of a trimer auxiliary field (see also [92]). It includes the bare trimer propagator and the coupling of the trimer t to the d_0-dimer and the core field ψ_0. The bare parameters Ξ and h also depend on an ultraviolet cut-off in the three-particle sector.

Writing the three-body interaction in this way will be convenient for the calculation of deduced physical quantities such as the form factor. However, as mentioned before there exists a whole class of equivalent theories in the three-particle sector. Integrating out all auxiliary fields, one can demonstrate that different choices of $\mathcal{L}^{(2)}$ and $\mathcal{L}^{(3)}$ can be transformed into the same theory without dimer and trimer fields up to four- and higher-body interactions. Therefore, we first eliminate the trimer field t using the method described in sec. 2.1.2.1. The classical equation of motion then yields:

$$\mathcal{L}^{(3)} \;\mapsto\; -H(\psi_0 d_0)^\dagger(\psi_0 d_0) \quad , \tag{3.3}$$

where $H = h^2/\Xi$. Applying the equivalence principle described in sec. 2.1.2.2 for the dimer fields $\vec{d}_1$ and d_0 then finally leads to

$$\begin{aligned}\mathcal{L}^{(2)} &\mapsto - C_0^1(\psi_0\vec{\psi}_1)^\dagger(\psi_0\vec{\psi}_1) - C_0^0(\vec{\psi}_1^{\,\mathrm{T}} P\,\vec{\psi}_1)^\dagger(\vec{\psi}_1^{\,\mathrm{T}} P\vec{\psi}_1) \quad , \\ \mathcal{L}^{(3)} &\mapsto - H_0\,\Big(\psi_0\,(\vec{\psi}_1^{\,\mathrm{T}} P\vec{\psi}_1)\Big)^\dagger\,\Big(\psi_0\,(\vec{\psi}_1^{\,\mathrm{T}} P\vec{\psi}_1)\Big) \;+\; \mathcal{L}^{(\geq 4)} \quad ,\end{aligned} \tag{3.4}$$

where $C_0^1 = g_1^2/\Delta_1$, $C_0^0 = 1/4\, g_0^2/\Delta_0$, and $H_0 = C_0^0 H/\Delta_0$. Thus, at LO, physical observables can only depend on these products of coupling constants. Therefore, they are not independent. From the equivalence principle we furthermore know that g_i and h can always be chosen positive. Without loss of generality we thus assume $g_i > 0$ and $h > 0$ in all subsequent calculations. The extra term $\mathcal{L}^{(\geq 4)}$ includes all interactions of four or more particles. Since in this work we only consider processes with at most three particles, we can simply neglect $\mathcal{L}^{(\geq 4)}$. Due to the equivalence principle, the trimer field could also have been introduced in another channel, such as

$$\tilde{\mathcal{L}}^{(3)} = \Xi\, t^\dagger\, t \;-\; h\,\Big[t^\dagger\,(\vec{\psi}_1^{\,\mathrm{T}} P\vec{d}_1) + (\vec{\psi}_1^{\,\mathrm{T}} P\vec{d}_1)^\dagger t\Big] \quad , \tag{3.5}$$

without changing any three-body observable. Moreover, the two-neutron halo Lagrangian (3.1) could also have been formulated completely analogous to eq. (2.16) without any operator P. However, using the form (3.1) the spin-singlet projection is already implemented on the Lagrangian level, simplifying some of the subsequent calculations.

In the following, we use Feynman rules in momentum space to calculate the properties of the two-body systems cn, nn and the three-body system cnn. In all Feynman diagrams, particles, dimers and trimers are denoted by single, double and triple lines, respectively.

Whenever relevant, the core field will be represented by a dashed line. Propagators are represented by arrows and couplings between particles, dimers and trimers by ellipses. These symbols are empty if they correspond to bare and filled if they correspond to full, interacting quantities. Detailed calculations of more involved Feynman graphs and their symmetry factors can be found in appendix D.3. Since we consider a non-relativistic theory, the one-body properties are not modified by interactions. Thus, we proceed with the two-body sector.

3.1.2 Two-body problem

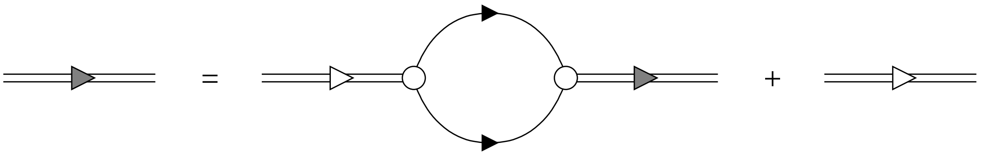

Figure 3.1: Diagrammatic representation of the integral equation for the full dimer propagator iD. The white arrow represents the bare propagator. The bubble represents the self-energy $-i\Sigma$.

Analogue to the considerations in the P-wave sector, we again start with an analysis of the two-body problem. Therefore, we calculate the full dimer propagator $iD_{ij}^{[S_is_1|S_js_2]}$. As mentioned before an index $i,j=0$ corresponds to the nn-channel with $S_{i,j=0}=0$ in spin-singlet configuration and an index $i,j=1$ corresponds to the cn-channel with $S_{i,j=1}=1/2$ in spin-doublet configuration. The corresponding magnetic quantum numbers are labeled by s_1 and s_2. In fig. 3.1, the iterative ansatz for iD is depicted in terms of Feynman diagrams. The corresponding equation reads:

$$iD \;=\; i\Delta^{-1}\,(-i\Sigma)\,iD \;+\; i\Xi^{-1} \;=\; i[\Delta-\Sigma]^{-1} \quad . \tag{3.6}$$

The self-energy Σ depends on the four-momentum $\bar{p}$ according to:

$$\begin{aligned} -\Sigma_{ij}^{[S_is_1|S_js_2]}(\bar{p}) \;&=\delta_{ij}\,\delta^{S_iS_j}\,\delta^{s_1s_2}\,\frac{\tau_i g_i^2\mu_i}{\pi^2}\left[\Lambda_i+\frac{\pi}{2}\,iy_i(\bar{p})\right] \quad , \quad \tau_i \;:=\;\begin{cases}1/2 & : i=0\\ 1 & : i=1\end{cases} \quad , \\ y_i(\bar{p}) \;&=\sqrt{2\mu_i\Big(p^0-\frac{\mathbf{p}^2}{2M_i}+i\varepsilon\Big)}\;. \end{aligned} \tag{3.7}$$

The function y_i has the dimension of momentum. A detailed calculation of $\Sigma_{ij}^{[S_is_1|S_js_2]}$ is given in appendix D.3.1. It is diagonal both in the particle and in the spin indices. The full dimer propagator then reads $D_{ij}^{[S_is_1|S_js_2]}=\delta_{ij}\delta^{s_1s_2}D_i$ with diagonal elements:

$$D_i(\bar{p}) \;=\; \frac{1}{\big(\Delta_i+\frac{\tau_i g_i^2\mu_i}{\pi^2}\Lambda_i\big)\;+\;\big(\frac{\tau_i g_i^2\mu_i}{2\pi}\big)\,iy_i(\bar{p})} \quad . \tag{3.8}$$

Note that the two spin components in the cn-channel are equal, which is due to the $\mathcal{L}^{(2)}$-part of the Lagrangian (3.4). The couplings Δ_i, g_i and the two-particle cut-offs Λ_i are not observable. We eliminate them via a renormalization procedure. In the following, we therefore consider the low-energy limit of the two-particle scattering amplitude, which can be written as an effective range expansion. Unknown quantities are then expressed in terms of the scattering length.

3.1.2.1 Effective range expansion

In order to renormalize the full dimer propagator in eq. (3.8), we consider the scattering of two particles. The corresponding Feynmandiagram fig. D.4 and its calculation can be found in appendix D.3.2. If the incoming (outgoing) particles of type i_1 and i_2 (j_1 and j_2) have four-momenta $\bar{p}_1$ and $\bar{p}_2$ ($\bar{k}_1$ and $\bar{k}_2$) and the total four-momentum is $\bar{P} = \bar{p}_1 + \bar{p}_2 = \bar{k}_1 + \bar{k}_2$, then the matrix elements it_{ij} reads:

$$it_{ij}(\bar{p}_1, \bar{p}_2, \bar{k}_1, \bar{k}_2) \;=\; (-ig_i^2)\,\delta_{ij}\,D_i(\bar{p}) \quad . \tag{3.9}$$

We now calculate the scattering amplitude in the center-of-mass frame. In these kinematics, the total four-momentum $\bar{P}$ has $P^0 = \mathbf{p}_1{}^2/(2\mu_i) = \mathbf{k}_1{}^2/(2\mu_i)$ and $\mathbf{P} = \mathbf{0}$. Using the relative momentum $\mathbf{p} := \mathbf{p}_1 = -\mathbf{p}_2$ the matrix element now effectively only depends on the modulus $p = |\mathbf{p}|$. Using eq. (1.2), it can be written as

$$f_i(p, \cos\theta) \;=\; \frac{\tau_i \mu_i}{2\pi}\, t_{ii}(p) \;=\; -\frac{g_i^2\,\mu_i}{2\pi} D_i\Big(\frac{p^2}{2\mu_i}, \mathbf{0}\Big) \quad . \tag{3.10}$$

Comparing eq. (3.10) with the partial wave expansion (1.3), we check that only S-waves contribute to the scattering amplitude:

$$(2\ell + 1)\, f_i^{[\ell]}(p) \;=\; \delta^{0\ell}\,\Big(-\frac{\tau_i g^2 \mu_i}{2\pi}\Big)\; D_i\Big(\frac{p^2}{2\mu_i}, \mathbf{0}\Big) \quad . \tag{3.11}$$

According to eq. (1.6), the scattering amplitude is directly related to the effective range expansion. For simplicity, we will from now on drop the redundant partial wave index $\ell = 0$ in the labeling ${}^{[\ell]}$ of all effective range parameters. Knowing that $y_i\,(p^2/(2\mu_i), \mathbf{0}) = p$ holds, we use eqs. (3.8), (3.11) and (1.6) in order to renormalize the unobservable couplings and cut-offs in the dimer denominator according to:

$$\begin{aligned} -\frac{1}{a_i} \,-\, ip \,+\, \mathcal{O}(p^2) \;&=\; -\frac{2\pi}{\tau_i g_i^2 \mu_i}\, \frac{1}{D_i\left(\frac{p^2}{2\mu_i}, \mathbf{0}\right)} \\ =\; -\,\frac{2\pi}{\tau_i g^2 \mu_i} &\left[\Big(\Delta_i + \frac{\tau_i g_i^2 \mu_i}{\pi^2}\Lambda_i\Big) + \Big(\frac{\tau_i g_i^2 \mu_i}{2\pi}\Big) ip\right] \quad . \end{aligned} \tag{3.12}$$

Matching the coefficients on both sides of eq. (3.12) directly yields the renormalization condition:

$$\Delta_i + \frac{\tau_i g_i^2 \mu_i}{\pi^2}\,\Lambda_i \;=\; -\frac{\tau_i g_i^2 \mu_i}{2\pi}\,\Big(-\frac{1}{a_i}\Big) \quad . \tag{3.13}$$

Furthermore, we see that the symmetry factor τ_i in the definition (3.10) of the scattering amplitude is crucial for preserving unitarity. Since eq. (3.13) holds for all $\Lambda_i > 0$, it is also valid in the ultraviolet limit $\Lambda_i \to \infty$. From that requirement, we read off the asymptotic behavior of the coupling constants for large cut-off: Multiplying with $1/g_i^2$ shows that Δ_i/g_i^2, which is the coupling constant of the equivalent theory without dimers, has to scale like $-\Lambda_i$ in order to reproduce a finite $1/a_i$.

Inserting the renormalization condition (3.13) into the formula (3.8), we end up with the renormalized full dimer propagator:

$$D_i(\bar{p}) \;=\; -\frac{2\pi}{\tau_i g_i^2 \mu_i} \, \frac{1}{-\frac{1}{a_i} - i y_i(\bar{p})} \quad . \tag{3.14}$$

The leading correction to the propagator (3.14) is due to the effective range. As mentioned before, it could be included by making the dimer fields dynamical. Such theories were e.g. discussed in refs. [80, 93–95]. Here, we stay at leading order in the EFT expansion and neglect effective range corrections.

The geometry of the propagator-poles in eq. (3.14) can be understood straightforwardly. Their location on the first or second Riemann sheet and whose residue depend on the scattering length a_i. A detailed analysis is performed in sec. A.1.1.1, where, for reasons of completeness, also the case of non-vanishing effective range is considered. The results are summarized in tab. A.2. It turns out that for $a_i > 0$, a pole on the first sheet with positive residue

$$Z_i \;=\; \frac{2\pi}{\tau_i g_i^2 \mu_i^2} \frac{1}{a_i} \tag{3.15}$$

exists. For $a_i < 0$, there is no dimer-pole on the physical sheet.

3.1.3 Three-body problem

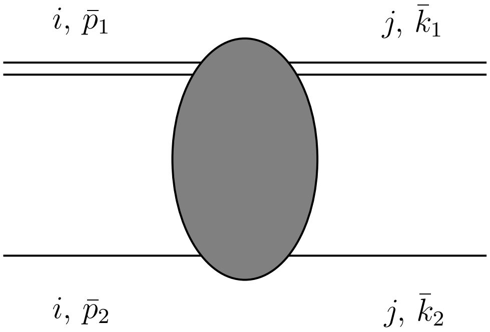

Figure 3.2: Diagrammatic representation of the T-matrix element $iT_{ij}(\bar{p}_1, \bar{p}_2, \bar{k}_1, \bar{k}_2)$ for dimer-particle scattering within a two-neutron halo system.

We proceed with considering the three-particle sector of our two-neutron halo EFT, beginning with the calculation of the amplitude $T_{ij}^{[S_i s_1; S_i s_2 | S_j s_3; S_j s_4]}(\bar{p}_1, \bar{p}_2, \bar{k}_1, \bar{k}_2)$ for dimer-particle scattering. The corresponding Feynman diagram for is depicted in fig. 3.2. The incoming dimer $d_i^\dagger$ and particle $\psi_i^\dagger$ have four-momenta $\bar{p}_1$ and $\bar{p}_2$, respectively. The outgoing dimer d_j and particle ψ_j have four-momenta $\bar{k}_1$ and $\bar{k}_2$, respectively. The lower particle-type indices $i, j \in \{0, 1\}$ are those of the dimer fields. The upper indices $s_1, s_2 \in \{-S, \ldots, S\}$ label the spin structure of the T-matrix. Within the two upper quartets, the left (right) pair denotes the spin quantum numbers of the particle (dimer). For the incoming channel, $i = 0$ represents the *c*-*nn* case where the core c and the nn-dimer are in spin-singlet configuration $S_0 = 0$. $i = 1$ corresponds to the *n*-*cn* configuration, in which both the neutron n and the cn-dimer are spin doublets with $S_1 = 1/2$. The index conventions in the outgoing channel are completely analogous.

3.1.3.1 Kinematics

For later purposes, such as for the form factor calculation, we need to determine the full T-matrix in arbitrary kinematics. In order to calculate it, we first use four-momentum conservation

$$\bar{p}_1 + \bar{p}_2 = \bar{k}_1 + \bar{k}_2 =: \bar{P} = \begin{pmatrix} P^0 \\ \mathbf{P} \end{pmatrix} = \begin{pmatrix} E(\bar{P}) + \frac{\mathbf{P}^2}{2M_\Sigma} \\ \mathbf{P} \end{pmatrix} \quad , \quad E(\bar{P}) := P^0 - \frac{\mathbf{P}^2}{2M_\Sigma} \quad , \tag{3.16}$$

where the kinetic energy $\mathbf{P}^2/(2M_\Sigma)$ of the center of mass is subtracted in the definition of $E(\bar{P})$. Furthermore, we define shifted relative four-momenta

$$\begin{aligned} \bar{p} &:= \bar{p}_1 - \frac{M_i}{M_\Sigma}\bar{P} \quad \Rightarrow \quad \bar{p}_1 = \frac{M_i}{M_\Sigma}\bar{P} + \bar{p} \quad , \quad \bar{p}_2 = \frac{m_i}{M_\Sigma}\bar{P} - \bar{p} \quad , \\ \bar{k} &:= \bar{k}_1 - \frac{M_j}{M_\Sigma}\bar{P} \quad \Rightarrow \quad \bar{k}_1 = \frac{M_j}{M_\Sigma}\bar{P} + \bar{k} \quad , \quad \bar{k}_2 = \frac{m_j}{M_\Sigma}\bar{P} - \bar{k} \quad , \end{aligned} \tag{3.17}$$

which correspond to a Galilean transformation of a general frame into the center-of-mass frame. Using eq. (3.17), the on-shell conditions of a single-particle propagator in the i-channel reads:

$$\begin{aligned} \frac{m_i}{M_\Sigma}P^0 - p^0 = p_2^0 &= \frac{\mathbf{p}_2^2}{2m_i} - i\varepsilon = \frac{\left(\frac{m_i}{M_\Sigma}\mathbf{P} - \mathbf{p}\right)^2}{2m_i} - i\varepsilon \\ \Rightarrow \quad p^0 &= \epsilon_i(\bar{P}, \mathbf{p}) + i\varepsilon \quad , \end{aligned} \tag{3.18}$$

with the real part of the pole position being:

$$\epsilon_i(\bar{P}, \mathbf{p}) := \frac{m_i}{M_\Sigma}P^0 - \frac{\left(\frac{m_i}{M_\Sigma}\mathbf{P} - \mathbf{p}\right)^2}{2m_i} \quad . \tag{3.19}$$

Since in most of the calculations in the following sections the total four-momentum of the system $\bar{P}$ remains invariant, we will simply write $E = E(\bar{P})$ and $\epsilon_{i,\mathbf{p}} = \epsilon_i(\bar{P}, \mathbf{p})$ in order to avoid overlong notations. Deviations from this rule will be mentioned explicitly.

With the definitions (3.16) and (3.17), the T-matrix can be rewritten in terms of only three quantities, namely the total four-momentum $\bar{P}$ and the two relative four-momenta $\bar{p}$ and $\bar{k}$:

$$\begin{aligned} T_{ij}(\bar{P}, \bar{p}, \bar{k}) &:= T_{ij}\Big(\frac{M_i}{M_\Sigma}\bar{P} + \bar{p}, \frac{m_i}{M_\Sigma}\bar{P} - \bar{p}, \frac{M_j}{M_\Sigma}\bar{P} + \bar{k}, \frac{m_j}{M_\Sigma}\bar{P} - \bar{k}\Big) \\ \Leftrightarrow \quad T_{ij}(\bar{p}_1, \bar{p}_2, \bar{k}_1, \bar{k}_2) &= T_{ij}\Big(\bar{p}_1 + \bar{p}_2, \frac{m_i\bar{p}_1 - M_i\bar{p}_2}{M_\Sigma}, \frac{m_j\bar{k}_1 - M_j\bar{k}_2}{M_\Sigma}\Big) \quad . \end{aligned} \tag{3.20}$$

The full dimer propagator in the chosen kinematics reads:

$$\begin{aligned} D_i(\bar{P},\bar{p}) &:= D_i\Big(\frac{M_i}{M_\Sigma}\bar{P}+\bar{p}\Big) &=& -\frac{2\pi}{\tau_i g_i^2 \mu_i}\,\frac{1}{-\frac{1}{a_i}-iy_i(\bar{P},\bar{p})} \quad , \\ y_i(\bar{P},\bar{p}) &:= y_i\Big(\frac{M_i}{M_\Sigma}\bar{P}+\bar{p}\Big) &=& \sqrt{2\mu_i\Big(E+p^0-\epsilon_{i,\mathbf{p}}-\frac{\mathbf{p}^2}{2\tilde{\mu}_i}+i\varepsilon\Big)} \quad . \end{aligned} \tag{3.21}$$

Using the conventions (1.18)-(1.20), the full propagator can be related to its on-shell version $D_i(E,\mathbf{p}) = D_i(E,p)$ through:

$$D_i(\bar{P},\bar{p}) \;=\; D_i(E+p^0-\epsilon_{i,\mathbf{p}},p) \quad . \tag{3.22}$$

3.1.3.2 T-matrix integral equation

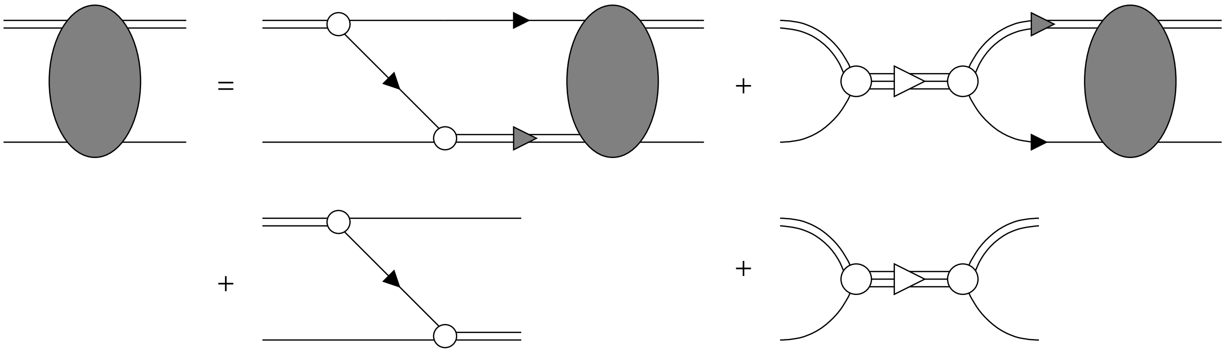

Figure 3.3: Diagrammatic representation of the integral equation for dimer-particle scattering iT, represented by Feynman graphs. The homogenous part includes full dimer propagators iD and integrations over the loop momenta $\int \mathrm{d}^4\bar{q}/(2\pi)^4$. The three-particle interaction is constructed using bare trimer propagators.

In terms of Feynman diagrams, the T-matrix integral equation has the form given in figure 3.3. The corresponding equation reads:

$$\begin{aligned} iT_{ij}^{[S_is_1;S_is_2|S_js_3;S_js_4]}(\bar{P},\bar{p},\bar{k}) \;=&\; iR_{ij}^{[S_is_1;S_is_2|S_js_3;S_js_4]}(\bar{P},\bar{p},\bar{k}) \\ &+\sum_{k=0}^{1}\sum_{s_5,s_6}\int\frac{\mathrm{d}^3\mathbf{q}}{(2\pi)^3}\int_{-\infty}^{\infty}\frac{\mathrm{d}q^0}{2\pi}\; iR_{ik}^{[S_is_1;S_is_2|S_ks_5;S_ks_6]}(\bar{P},\bar{p},\bar{q}) \\ &\times\;\frac{i}{\epsilon_{k,\mathbf{q}}-q^0+i\varepsilon}\; iD_k(\bar{P},\bar{q})\; iT_{kj}^{[S_ks_5;S_ks_6|S_js_3;S_js_4]}(\bar{P},\bar{q},\bar{k}) \quad . \end{aligned} \tag{3.23}$$

A detailed derivation of the interaction kernel

$$\begin{aligned} &R_{ij}^{[S_is_1;S_is_2|S_js_3;S_js_4]}(\bar{P},\bar{p},\bar{k}) \\ &\quad= -\left[\frac{\sigma_{ij}^{[S_is_1;S_is_2|S_js_3;S_js_4]}\; g_ig_j}{E+p^0-\epsilon_{i,\mathbf{p}}+k^0-\epsilon_{j,\mathbf{k}}-\frac{\mathbf{p}^2}{2\mu_j}-\frac{\mathbf{k}^2}{2\mu_i}-\frac{\mathbf{p}\cdot\mathbf{k}}{m_{ij}}+i\varepsilon} \;+\; \delta_{0i}\delta_{0j}H\right] \end{aligned} \tag{3.24}$$

is given in appendix D.3.3. Thereby, the three-body coupling is rewritten in terms of $H = \frac{h^2}{\Xi}$. From eq. (3.24) we see that for on-shell momenta, R effectively only depends on $E = E(\bar{P})$ and the three-momenta $\mathbf{p}$ and $\mathbf{k}$. The spin structure of R is given in terms of the factors:

$$\begin{pmatrix} \sigma_{00}^{[00;00|00;00]} & \sigma_{01}^{[00;00|\frac{1}{2}s_3;\frac{1}{2}s_4]} \\ \sigma_{10}^{[\frac{1}{2}s_1;\frac{1}{2}s_2|00;00]} & \sigma_{11}^{[\frac{1}{2}s_1;\frac{1}{2}s_2|\frac{1}{2}s_3;\frac{1}{2}s_4]} \end{pmatrix} = \begin{pmatrix} 0 & C^{00}_{\frac{1}{2}s_3;\frac{1}{2}s_4} \\ C^{00}_{\frac{1}{2}s_1;\frac{1}{2}s_2} & -\delta^{s_2 s_3}\delta^{s_4 s_1} \end{pmatrix} \quad . \tag{3.25}$$

We now utilize the residue theorem in order to perform the q^0-integration in eq. (3.23). Considering the integrand, we note that the single-particle propagator $i/(\epsilon_{k,\mathbf{q}} + i\varepsilon - q^0)$ for real momenta has a single pole in the upper complex plane. It is located at $q^0 = \epsilon_{k,\mathbf{q}} + i\varepsilon$. As explained in appendix A.1.1.1, the full dimer propagator $D_k(\bar{P}, \bar{q})$ has no q^0-poles in the upper complex half-plane. Assuming that also $T_{kj}(\bar{P}, \bar{q}, \bar{k})$ obeys this condition, we apply the formula

$$\int_{-\infty}^{\infty} \frac{\mathrm{d}q^0}{(2\pi)}\, f(q^0)\, \frac{i}{\epsilon_{k,\mathbf{q}} - q^0 + i\varepsilon} = \frac{(2\pi i)}{(2\pi)}\, f(\epsilon_{k,\mathbf{q}} + i\varepsilon)\, \frac{i}{(-1)} = f(\epsilon_{k,\mathbf{q}} + i\varepsilon) \tag{3.26}$$

to eq. (3.23). The term f simply denotes the products of all functions in the integrand except for the single-particle propagator. Formula (3.26) is valid because the q^0 integration contour can be closed through an upper arc, which in the limit of infinite arc-radius does not contribute to the integral. The reason for this is that the amplitude is assumed to fall of rapidly enough. We thus end up with the T-matrix integral equation:

$$\begin{aligned} T_{ij}^{[S_i s_1;S_i s_2|S_j s_3;S_j s_4]}(\bar{P}, \bar{p}, \bar{k}) \; &= \; R_{ij}^{[S_i s_1;S_i s_2|S_j s_3;S_j s_4]}(\bar{P}, \bar{p}, \bar{k}) \; - \; \sum_{k=0}^{1} \sum_{s_5,s_6} \int \frac{\mathrm{d}^3\mathbf{q}}{(2\pi)^3} \\ \times \; R_{ik}^{[S_i s_1;S_i s_2|S_k s_5;S_k s_6]}(\bar{P}, \bar{p}, \mathbf{q})\; D_k(E, q)\; &T_{kj}^{[S_k s_5;S_k s_6|S_j s_3;S_j s_4]}(\bar{P}, \mathbf{q}, \bar{k}) \quad . \end{aligned} \tag{3.27}$$

3.1.3.3 Angular momentum eigenstates

In order to calculate matrix elements for dimer-particle scattering with specific total angular momentum quantum numbers, we have to project the T-matrix in eq. (3.27) onto total angular momentum eigenstates. This will be performed in several steps.

Spin-singlet coupling: Considering the intrinsic spins of the single particle and the dimer field, we first project the incoming and outgoing states of the T-matrix (3.27) onto the spin-singlet. An alternative coupling to the spin triplet will not be considered in this work. For all three quantities the T-matrix, the interaction kernel and the spin-structure matrix $X \in \{T, R, \sigma\}$, we thus use CGCs in order to define projected quantities $X_{ij}^{[00;S_i;S_i|00;S_j;S_j]}$ via eq. (C.4). Note that for the channel $i = 0$, which represents the c-nn configuration, both spins are $S_0 = 0$, which leads to a trivial projection with $C^{00}_{00;00} = 1$. The same statement holds for the trivial outgoing channel $j = 0$. Multiplying eq. (3.27) with $C^{00}_{S_i s_1;S_i s_2} C^{00}_{S_j s_3;S_j s_4}$

and summing over all magnetic quantum numbers, we use the product identity (C.5) for the homogeneous part and end up with the projected spin-singlet T-matrix equation:

$$\begin{aligned} T_{ij}^{[00;S_i;S_i|00;S_j;S_j]}(\bar{P},\bar{p},\bar{k}) \;&=\; R_{ij}^{[00;S_i;S_i|00;S_j;S_j]}(\bar{P},\bar{p},\bar{k}) \;-\; \sum_{k=0}^{1}\int \frac{\mathrm{d}^3\mathbf{q}}{(2\pi)^3} \\ &\times\; R_{ik}^{[00;S_i;S_i|00;S_k;S_k]}(\bar{P},\bar{p},\mathbf{q})\; D_k(E,\mathbf{q})\; T_{kj}^{[00;S_k;S_k|00;S_j;S_j]}(\bar{P},\mathbf{q},\bar{k}) \quad . \end{aligned} \tag{3.28}$$

Furthermore, using eq. (C.1) and eq. (C.3), one can directly deduce that $\sigma_{ij}^{[00;S_i;S_i|00;S_j;S_j]} = 1-\delta_{0i}\delta_{0j}$ holds.

Orbital angular momentum: Since the particle spin is now coupled to the spin-singlet, the upper particle indices are redundant. In the following, we will drop them and by identifying $X_{ij} := X_{ij}^{[00;S_i;S_i|00;S_j;S_j]}$ for $X \in \{T,R\}$. The total angular momentum in the dimer-particle scattering process is then nothing else but the orbital angular momentum. We now perform a decomposition of the T-matrix and the interaction kernel into spherical harmonics $Y_{\ell m}$, whose properties are described in appendix C.2. In contrast to the P-wave case (2.41), this time we also need more general angular decompositions, where one of the incoming or outgoing relative momenta remains off-shell. For instance, putting only $\bar{p}$ on-shell, yields:

$$\begin{aligned} X(\bar{P},\mathbf{p},\bar{k}) \;&=\; X(\bar{P},p\cdot\mathbf{e_p},\bar{k}) \;=:\; \sqrt{4\pi}\sum_{\ell_1,m_1} Y^*_{\ell_1 m_1}(\mathbf{e_p})\; X^{[\ell_1 m_1|]}(\bar{P},p,\bar{k}) \\ \Rightarrow\quad X^{[\ell_1 m_1|]}(\bar{P},p,\bar{k}) \;&=\; \int \frac{\mathrm{d}\Omega_{\mathbf{p}}}{\sqrt{4\pi}}\; Y_{\ell_1 m_1}(\mathbf{e_p})\; X(\bar{P},p\cdot\mathbf{e_p},\bar{k}) \quad . \end{aligned} \tag{3.29}$$

Due to symmetry reasons, the decomposition for an outgoing on-shell momentum $\mathbf{k}$ is completely analogous. Assuming on-shell kinematics for both momenta, leads to the known complete decomposition:

$$\begin{aligned} X(E,\mathbf{p},\mathbf{k}) \;&=\; X(E,p\cdot\mathbf{e_p},k\cdot\mathbf{e_k}) \\ &=:\; 4\pi\sum_{\ell_1,m_1}\sum_{\ell_2,m_2} Y^*_{\ell_1 m_1}(\mathbf{e_p})\; X^{[\ell_1 m_1|\ell_2 m_2]}(E,p,k)\; Y_{\ell_2 m_2}(\mathbf{e_k}) \\ \Rightarrow\quad & X^{[\ell_1 m_1|\ell_2 m_2]}(E,p,k) \\ &=\; \int \frac{\mathrm{d}\Omega_{\mathbf{p}}}{\sqrt{4\pi}} \int \frac{\mathrm{d}\Omega_{\mathbf{k}}}{\sqrt{4\pi}}\; Y_{\ell_1 m_1}(\mathbf{e_p})\; X(E,p\cdot\mathbf{e_p},k\cdot\mathbf{e_k})\; Y^*_{\ell_2,m_2}(\mathbf{e_k}) \quad . \end{aligned} \tag{3.30}$$

Analogue to the calculations in the P-wave sector, the on-shell full dimer propagator D appearing in eq. (3.28) again does not display any angular dependence and is a pure S-wave quantity. For notational convenience, we redefine

$$D^{[0]}(E,q) \;:=\; -\frac{4\pi}{(2\pi)^3}\, p^2\, D_i(E,q) \quad , \tag{3.31}$$

where the convention (1.19) was used. Note that the prefactor $4\pi/(2\pi)^3p^2 = p^2/(2\pi^2)$ from the measure of the integration over the loop momentum and also the relative minus sign have been absorbed in $D^{[0]}$.

The angular-decomposed interaction kernel R can be determined using the decompositions (C.11), (C.12) and (C.13) that were already performed for the P-wave case. For the off-shell interaction kernel, we write:

$$\begin{aligned} R_{ij}(\bar{P},\bar{p},\bar{k}) &= -\frac{(1-\delta_{0i}\delta_{0j})\; g_i g_j}{[E+p^0-\epsilon_{i,\mathbf{p}}+k^0-\epsilon_{j,\mathbf{k}}]-\frac{p^2}{2\mu_j}-\frac{k^2}{2\mu_i}-\frac{pk\,\mathbf{e_p}\cdot\mathbf{e_k}}{m_{ij}}+i\varepsilon} \;-\; \delta_{0i}\delta_{0j}H \\ &= \sum_{\ell_1,m_1}\sum_{\ell_2,m_2}\sqrt{4\pi}\,Y^*_{\ell_1 m_1}(\mathbf{e_p})\;\sqrt{4\pi}\,Y_{\ell_2 m_2}(\mathbf{e_k}) \\ &\quad\times\;\delta^{\ell_1\ell_2}\delta^{m_1m_2}\Big[(1-\delta_{0i}\delta_{0j})\; g_i g_j\,\frac{m_{ij}}{pk}\,(-1)^{\ell_1}Q_{\ell_1}(c_{ij}(\bar{P},\bar{p},\bar{k}))-\delta_{0i}\delta_{0j}\,H\,\delta^{0\ell_1}\Big] \\ &= \sum_{\ell,m}\sqrt{4\pi}\,Y^*_{\ell m}(\mathbf{e_p})\;\sqrt{4\pi}\,Y_{\ell m}(\mathbf{e_k}) \\ &\quad\times\;\Big[(1-\delta_{0i}\delta_{0j})\; g_i g_j\,\frac{m_{ij}}{pk}\,(-1)^{\ell}Q_{\ell}(c_{ij}(\bar{P},\bar{p},\bar{k}))-\delta_{0i}\delta_{0j}\,H\,\delta^{0\ell}\Big] \quad . \end{aligned} \tag{3.32}$$

The appearing analytically continued Legendre functions of second kind Q_ℓ and their properties and symmetries are discussed in detail in appendix A.2. Their arguments read:

$$c_{ij}(\bar{P},\bar{p},\bar{k}) \;:=\; \frac{m_{ij}}{pk}\Big(\frac{p^2}{2\mu_j}+\frac{k^2}{2\mu_i}-[E+p^0-\epsilon_{i,\mathbf{p}}+k^0-\epsilon_{j,\mathbf{k}}]-i\varepsilon\Big) \quad . \tag{3.33}$$

Using the notational conventions (1.18)-(1.20), this quantity can be related to its own on-shell version $c_{ij}(E,p,k)$ through:

$$c_{ij}(\bar{P},\bar{p},\bar{k}) \;=\; c_{ij}(E+p^0-\epsilon_{i,\mathbf{p}}+k^0-\epsilon_{j,\mathbf{k}},p,k) \quad . \tag{3.34}$$

Only for on-shell momenta $p^0 = \epsilon_{i,\mathbf{p}}+i\varepsilon$ and $k^0 = \epsilon_{j,\mathbf{k}}+i\varepsilon$, eq. (3.32) represents a complete decomposition into spherical harmonics. However, assuming that only $\bar{p}$ is on-shell, we use the orthogonality relation (C.6) and write:

$$\begin{aligned} R^{[\ell m|]}_{ij}(\bar{P},p,\bar{k}) &= \sqrt{4\pi}\,Y_{\ell m}(\mathbf{e_k}) \\ &\quad\times\Big[(1-\delta_{0i}\delta_{0j})\; g_i g_j\,\frac{m_{ij}}{pk}\,(-1)^{\ell}Q_{\ell}(c_{ij}(\bar{P},p,\bar{k}))\;-\delta_{0i}\delta_{0j}\,\delta^{0\ell}\,H\Big] \quad . \end{aligned} \tag{3.35}$$

Recalling that $Y_{00} = 1/\sqrt{4\pi}$ holds, the contribution with $\ell = m = 0$ reads:

$$R^{[00|]}_{ij}(\bar{P},p,\bar{k}) \;=(1-\delta_{0i}\delta_{0j})\; g_i g_j\,\frac{m_{ij}}{pk}\;Q_0(c_{ij}(\bar{P},p,\bar{k}))\;-\delta_{0i}\delta_{0j}\,H \quad . \tag{3.36}$$

Again, an analogous equation holds for the outgoing momentum. If both $\bar{p}$ and $\bar{k}$ are on-shell, we can either use eq. (3.35) with a further projection $\int\frac{\mathrm{d}\Omega_{\mathbf{k}}}{\sqrt{4\pi}}\,Y^*_{\ell m}(\mathbf{e_k})$ or simply directly read of the coefficients $R^{[\ell_1 m_1|\ell_2 m_2]} = \delta^{\ell_1\ell_2}\delta^{m_1 m_2} R^{[\ell_1]}$ from eq. (3.32). Both methods yield the same result:

$$R^{[\ell]}_{ij}(E,p,k) \;=\; (1-\delta_{0i}\delta_{0j})\; g_i g_j\, \frac{m_{ij}}{pk}(-1)^\ell Q_\ell(c_{ij}(E,p,k)) \;-\; \delta_{0i}\delta_{0j}\,\delta^{0\ell}\, H \quad . \tag{3.37}$$

Assuming $\ell = 0$ and inserting eq. (3.34) into eq. (3.36), from eq. (3.37) we thus derive the useful relation:

$$R^{[00|]}_{ij}(\bar P, p, \bar k) \;=\; R^{[0]}_{ij}(E + k^0 - \epsilon_{j,\mathbf{k}}, p, k) \quad . \tag{3.38}$$

As we see, $X \in \{T, R\}$ is diagonal in the total incoming and outgoing angular momentum quantum numbers $X^{[\ell_1 m_1|\ell_2 m_2]} = \delta^{\ell_1\ell_2}\delta^{m_1 m_2} X^{[\ell_1]}$ in agreement with the Wigner–Eckhart theorem. From eq. (3.37) we furthermore know that the three-body force only contributes to the ($\ell = 0$)-component of the T-matrix. With regard to the integral equation (3.28), we now put $\bar p$ and $\bar k$ on-shell, integrate over $\int \mathrm{d}\Omega_{\mathbf{p}}/\sqrt{4\pi} Y_{\ell m}(\mathbf{e_p})$ and $\int \mathrm{d}\Omega_{\mathbf{k}}/\sqrt{4\pi} Y^*_{\ell m}(\mathbf{e_k})$ and use the orthogonality relation (C.6) to derive the set of projected equations:

$$\begin{aligned} T(\bar P, \bar p, \bar k) \;&=\; R(\bar P, \bar p, \bar k) + \sum_{\ell,m}\int_0^\infty \mathrm{d}q\, R^{[|\ell m]}(\bar P, \bar p, q)\, D^{[0]}(E,q)\, T^{[\ell m|]}(\bar P, q, \bar k) \quad , \\ T^{[|\ell m]}(\bar P, \bar p, k) \;&=\; R^{[|\ell m]}(\bar P, \bar p, \bar k) + \int_0^\infty \mathrm{d}q\, R^{[|\ell m]}(\bar P, \bar p, q)\, D^{[0]}(E,q)\, T^{[\ell]}(E, q, k) \quad , \\ T^{[\ell]}(E,p,k) \;&=\; R^{[\ell]}(E,p,k) + \int_0^\infty \mathrm{d}q\, R^{[\ell]}(E,p,q)\, D^{[0]}(E,q)\, T^{[\ell]}(E,q,k) \quad . \end{aligned} \tag{3.39}$$

Note that in all equations, the conventions (1.18)-(1.20) were used.

3.1.3.4 Renormalization

As we know from the LSZ-theorem (see e.g. ref. [77] for more details), the T-matrix has to be renormalized with appropriate $\sqrt{Z}$-factors in order to determine the physical solutions of the dimer-particle scattering process. The calculation of the corresponding dimer wave function renormalization factors (3.15) can be found in appendix A.1.1.1. The renormalized quantities then read:

$$\begin{aligned} &\forall X \in \{T, R\} : \quad \bar X_{ij} \;:=\; |Z_i|^{\frac12}\, X_{ij}\, |Z_j|^{\frac12} \quad , \qquad \bar H \;:=\; |Z_0| H \quad , \\ &\bar D_i(E,p) \;:=\; |Z_i|^{-1}\, D_i(E,p) \quad , \\ &z_i \;:=\; \frac{2\pi}{\mu_i^2}\frac{1}{|a_i|} \qquad \Rightarrow \qquad |Z_i| \;=\; \frac{z_i}{\tau_i g_i^2} \quad . \end{aligned} \tag{3.40}$$

With these definitions all unobservable g_i-factors in eq. (3.39) either cancel or are absorbed in the yet unknown three-body force $\bar H$. Absolute values $|Z_i|$ are only required in the $i = 0$ channel because $a_0 < 0$ and thus $Z_0 < 0$. This channel corresponds to the neutron-neutron auxiliary dimer, which is unbound and thus actually requires no renormalization factor. In this case eq. (3.40) simply provides a convenient redefinition of the amplitude but has no physical significance. The reduced residue factors z_i will contribute to a more compact notation. The resulting renormalized 2×2 matrix integral equation then altogether reads:

$$\boxed{\begin{aligned}
\bar{T}^{[\ell]}(E,p,k) \;&=\; \bar{R}^{[\ell]}(E,p,k) + \int_0^\infty \mathrm{d}q\, \bar{R}^{[\ell]}(E,p,q)\, \bar{D}^{[0]}(E,q)\, \bar{T}^{[\ell]}(E,q,k) \quad ,\\[2ex]
\bar{D}^{[0]}_i(E,p) \;&=\; \frac{1}{\pi\,\mu_i\, z_i}\, \frac{p^2}{-\frac{1}{a_i} - i y_i(E,p)} \quad , \quad y_i(E,p) \;=\; \sqrt{2\mu_i\Big(E - \frac{p^2}{2\bar{\mu}_i} + i\varepsilon\Big)} \quad ,\\
\bar{R}^{[\ell]}_{ij}(E,p,k) \;&=\; (1-\delta_{0i}\delta_{0j})\,\sqrt{\frac{z_i z_j}{\tau_i\tau_j}}\,\frac{m_{ij}}{pk}(-1)^\ell Q_\ell(c_{ij}(E,p,k)) \;-\; \delta_{0i}\delta_{0j}\,\delta^{0\ell}\,\bar{H} \quad ,\\
c_{ij}(E,p,k) \;&=\; \frac{m_{ij}}{pk}\Big(\frac{p^2}{2\mu_j} + \frac{k^2}{2\mu_i} - E - i\varepsilon\Big) \quad ,\\
z_i \;&=\; \frac{2\pi}{\mu_i^2}\frac{1}{|a_i|} \quad , \qquad \tau_i \;=\; \begin{cases} 1/2 & : i = 0\\ 1 & : i = 1 \quad . \end{cases}
\end{aligned}} \tag{3.41}$$

As mentioned before, the only physically relevant element is $\bar{T}_{11}$, since all other matrix elements would lead to an external $\bar{D}^{[0]}_0$ dimer. Such as dimer would represent an external bound two-neutron spin-singlet state that does not exist. $\bar{T}_{11}$ describes the spin-singlet scattering of a neutron from a *cn* bound state. The *cn*-dimer has binding energy $E^{(2)}_1 = -1/(2\mu_1 a_1^2)$. We use the relations (1.2)-(1.7) in order to calculate the scattering amplitude $\bar{f}^{[\ell]}_1$ and the scattering length $\bar{a}^{[\ell]}_1$ in the ℓ-th partial wave. They read:

$$\begin{aligned}
\bar{f}^{[\ell]}_1(p) \;&=\; \frac{1}{p\cot\delta^{[\ell]}_{11}(p) - ip} \;=\; \frac{\bar{\mu}_1}{2\pi}\,\bar{T}^{[\ell]}_{11}\Big(\frac{p^2}{2\bar{\mu}_1} + E^{(2)}_1, p, p\Big) \quad ,\\
\bar{a}^{[\ell]}_1 \;&=\; -\frac{\bar{\mu}_1}{2\pi}\lim_{p\to 0}\; p^{-2\ell}\,\bar{T}^{[\ell]}_{11}\Big(\frac{p^2}{2\bar{\mu}_1} + E^{(2)}_1, p, p\Big) \quad .
\end{aligned} \tag{3.42}$$

In sec. B we explain how eq. (3.41) and eq. (3.42) can be solved numerically.

3.1.3.5 Bound state equation

We are now in the position to search for possible three-body bound states, which manifest themselves as poles of first order in the T-matrix. Assuming that a three-body bound state with negative binding energy $E = E^{(3)} < 0$ and total angular momentum ℓ exists, the T-matrix has a pole of first order at this position and the corresponding residue factorizes into momentum dependent functions B according to:

$$\bar{T}^{[\ell]}(E,p,k) \;=\; -\frac{B^{[\ell]}(p)\cdot B^{[\ell]}(k)^\dagger}{E - E^{(3)}} + \text{reg.} \quad . \tag{3.43}$$

The term reg. represents an unspecified regular function in the energy. Also in the case where $\bar{T}^{[\ell]}$ has no such pole, eq. (3.43) is still trivially fulfilled with $B^{[\ell]} = 0$. Inserting eq. (3.43) into eq. (3.41), multiplying with $E - E^{(3)}$ and taking the limit $E \to E^{(3)}$ then yields the bound-state equation:

$$B^{[\ell]}(p) \;=\; \int_0^\infty \mathrm{d}q\, \bar{R}^{[\ell]}(p,q)\, \bar{D}^{[0]}(q)\, B^{[\ell]}(q) \quad . \tag{3.44}$$

Its kernel functions are those of eq. (3.41). Note that we used the convention (1.21). The solution $B^{[0]}$ we call the wave function. Their numerical determination is discussed in sec. B.

The generalized eigenvalue problem (3.44) can be solved, by introducing a loop momentum cut-off Λ. It turns out that for $\ell \neq 0$, the resulting unphysical cut-off dependence vanishes in the limit $\Lambda \to \infty$, since the wave function falls of rapidly enough. By contrast, this limit does not exist for $\ell = 0$, where the wave function displays an asymptotic discrete scale invariance associated with a renormalization group limit cycle. In this case, three-body observables log-periodically depend on Λ and an Efimov spectrum of three-body bound-state energies exists. In other channels, there are now bound states. Since for $\ell = 0$ the unknown three-body force $\bar{H}$ appears in $\bar{R}$, we interpret it as a function of the cut-off and use it to renormalize the channel. Thereby, for a given cut-off Λ and a three-body binding energy $E^{(3)}$, the three-body term $\bar{H}$ is fixed such that the bound-state equation (3.44) has a solution at exactly this desired energy value $E = E^{(3)}$ (see again sec. B). However, since the equation is homogenous, it can not provide the proper renormalization of the wave function.

Another quantity that will be of use in subsequent calculations is the dimer-integral over the wave-function:

$$\beta \;:=\; \int_0^\Lambda \mathrm{d}q\, \bar{D}^{[0]}_0(q)\, B^{[0]}_0(q) \quad . \tag{3.45}$$

This cut-off dependent quantity is fixed up to a complex phase, since its modulus can be determined from the decomposition (3.43) of the renormalized T-matrix according to:

$$|\beta| \;=\; \lim_{E \to E^{(3)}} \left[-(E - E^{(3)}) \int_0^\Lambda \mathrm{d}q \int_0^\Lambda \mathrm{d}q'\, \bar{D}^{[0]}_0(E,q)\, \bar{T}^{[0]}_{00}(E,q,q')\, \bar{D}^{[0]}_0(E,q') \right]^{\frac{1}{2}} \quad . \tag{3.46}$$

With regard to the bound-state equation (3.44), we then choose $\ell = 0$, introduce the momentum cut-off Λ and insert the trivial identity $\bar{R}^{[0]} = {}^{\bullet}\bar{R}^{[0]} - \bar{H}\,\mathbf{e}_0 \cdot \mathbf{e}_0^\dagger$ yielding:

$$B^{[0]}(p) \;=\; \int_0^\Lambda \mathrm{d}q\, {}^{\bullet}\bar{R}^{[0]}(p,q)\, \bar{D}^{[0]}(q)\, B^{[0]}(q) \;-\; (\beta \bar{H})\, \mathbf{e}_0 \quad . \tag{3.47}$$

Note that according to our convention (1.22), the symbol $^\bullet$ indicates that the three-body force $\bar{H}$ is set to zero within the interaction term $\bar{R}$.

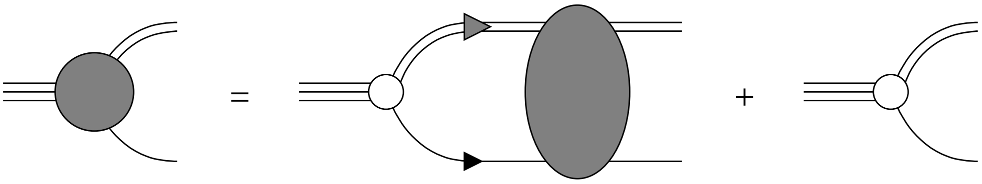

Figure 3.4: Diagrammatic representation of the full trimer-dimer-particle coupling iG. The right side of the equation contains the bare coupling and a part where a loop integral over the T-matrix appears. The later contribution contains all diagrams where the intermediate particles interact before they split up into the outgoing dimer and the particle. The irreducible trimer-dimer-particle coupling can be obtained from iG by simply neglecting the three-body force in the interaction kernel.

3.1.4 Trimer couplings

As building blocks for later calculations of electromagnetic observables we also need to determine the irreducible matrix element of a trimer-state coupling to a dimer-particle state or a three-particle state. By irreducibility we always mean that a corresponding Feynman diagram can not be split up into a trimer propagator and a remaining part by cutting only one trimer line. Before we determine these matrix elements, we first calculate the full coupling $G_i(\bar{P}, \bar{p}_1, \bar{p}_2)$ of an incoming trimer with total four-momentum $\bar{P}$ to an outgoing dimer and a single particle with four-momenta $\bar{p}_1$ and $\bar{p}_2$, respectively. Thereby, analogous to the particle type indices of the T-matrix, $i = 0$ and $i = 1$ again corresponds to the *c-nn* and *n-cn* spin-singlet configuration, respectively. The Feynman diagram belonging to the described full coupling is depicted in fig. 3.4 as a sum of the bare coupling and a contribution that contains all intermediate interactions of the particles. Note that due to our specific choice of the three-particle interaction $\mathcal{L}^{(3)}$ in eq. (3.1), the bare coupling only appears in the channel $i = 0$.

Using four-momentum conservation and the general kinematics (3.16)-(3.19), the full coupling can be re-expressed in terms of only two four-momenta, namely the total four-momentum $\bar{P}$ and the relative four-momentum $\bar{p}$:

$$\begin{aligned} & G_i(\bar{P}, \bar{p}) &:=& \ G_i\Big(\bar{P}, \frac{M_i}{M_\Sigma}\bar{P} + \bar{p}, \frac{m_i}{M_\Sigma}\bar{P} - \bar{p}\Big) \\ \Leftrightarrow \quad & G_i(\bar{P}, \bar{p}_1, \bar{p}_2) &=& \ G_i\Big(\bar{P}, \frac{m_i\bar{p}_1 - M_i\bar{p}_2}{M_\Sigma}\Big) \quad . \end{aligned} \tag{3.48}$$

In these kinematics, the formal expression for the equation depicted in fig. 3.4 reads:

$$\begin{aligned} iG_i(\bar{P},\bar{p}) &= \delta_{0i}(-ih) + \sum_{k=0}^{1}\int\frac{\mathrm{d}^3\mathbf{q}}{(2\pi)^3}\int_{-\infty}^{\infty}\frac{\mathrm{d}q^0}{2\pi}\,\delta_{0k}\,(-ih) \\ &\quad\times\frac{i}{\epsilon_{k,\mathbf{q}}-q^0+i\varepsilon}\,iD_k(\bar{P},\bar{q})\,iT_{ki}(\bar{P},\bar{q},\bar{p}) \\ &= -ih\left[\delta_{0i}-\int\frac{\mathrm{d}^3\mathbf{q}}{(2\pi)^3}\,D_0(E,\mathbf{q})\,T_{0i}(\bar{P},\mathbf{q},\bar{p})\right] \qquad (3.49) \\ &= -ih\left[\delta_{0i}+\int_0^{\Lambda}\mathrm{d}q\,D_0^{[0]}(E,q)\sum_{\ell,m}\int\mathrm{d}\Omega_{\mathbf{q}}\,Y_{00}^*(\mathbf{e_q})Y_{\ell m}(\mathbf{e_q})\,T_{0i}^{[\ell m|]}(\bar{P},q,\bar{p})\right] \\ &= -ih|Z_0|^{\frac{1}{2}}\left[\delta_{0i}+\int_0^{\Lambda}\mathrm{d}q\,\bar{D}_0^{[0]}(E,q)\,\bar{T}_{0i}^{[00|]}(\bar{P},q,\bar{p})\right]|Z_i|^{-\frac{1}{2}} \quad . \end{aligned}$$

Thereby, the integration over q^0 was again performed using closed-contour integration and the residue theorem. In addition, the angular decomposition of the T-matrix was used. All possible dimer-particle loops and interaction as well as intermediate bare trimer propagators are thus included in $\bar{T}$ as it represents all the diagrams given in fig. 3.3. Imposing the on-shell condition $p^0 = \epsilon_{i,\mathbf{p}} + i\varepsilon$ and using $\bar{X}_{0i}^{[00|]}(\bar{P},q,\mathbf{p}) = \bar{X}_{0i}^{[0]}(E,q,p)$ eq. (3.49) assumes the form:

$$G_i(E,\mathbf{p}) = -h|Z_0|^{\frac{1}{2}}\left[\delta_{0i}+\int_0^{\Lambda}\mathrm{d}q\,\bar{D}_0^{[0]}(E,q)\,\bar{T}_{0i}^{[0]}(E,q,p)\right]|Z_i|^{-\frac{1}{2}} = G_i(E,p) \quad . \qquad (3.50)$$

Note that again the conventions (1.18)-(1.20) were used. From eq. (3.50) we see that for on-shell conditions, the full coupling effectively is a pure S-wave coupling and does not display any angular dependence.

3.1.4.1 Trimer residue

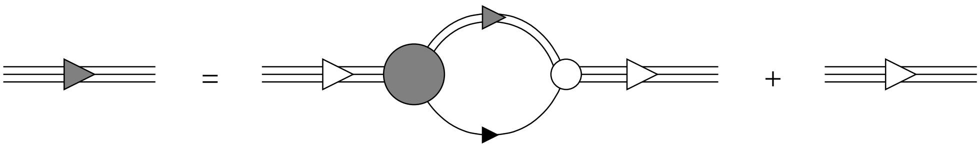

Figure 3.5: Diagrammatic representation of the full trimer propagator *it*. The right side of the equation contains the bare coupling and a part where a loop integral over the full trimer-dimer-particle coupling appears. The later contribution contains all diagrams where the trimer splits up and the intermediate particles interact.

In order to renormalize external trimer legs, as they appear as incoming or outgoing states within Feynman diagrams, we calculate the residue of the full trimer propagator.

This propagator $it(\bar{P})$, with $\bar{P}$ being the total four-momentum, can be determined analogous to the calculation of the full dimer propagator presented in sec. 3.1.2. The corresponding equation is depicted in fig. 3.5 in terms of Feynman diagrams and formally reads:

$$\begin{aligned} it(\bar{P}) &= \frac{i}{\Xi} + \frac{i}{\Xi} \sum_{k=0}^{1} \int \frac{\mathrm{d}^3\mathbf{q}}{(2\pi)^3} \int_{-\infty}^{\infty} \frac{\mathrm{d}q^0}{2\pi}\, iG_k(\bar{P},\bar{q}) \\ &\quad \times \frac{i}{\epsilon_{k,\mathbf{q}} - q^0 + i\varepsilon}\, iD_k(\bar{P},\bar{q})\, \delta_{0k}(-ih)\, \frac{i}{\Xi} \\ &= \frac{i}{\Xi}\Big[1 \;-\; |Z_0|\, \frac{h}{\Xi} \int_0^\Lambda \frac{\mathrm{d}q\; q^2(4\pi)}{(2\pi)^3}\; G_0(E,q)\; |Z_0|^{-1}\, D_0(E,q)\Big] \\ &= \frac{i}{\Xi}\Big[1 \;-\; |Z_0|\, \frac{h^2}{\Xi} \int_0^\Lambda \mathrm{d}q\; \bar{D}_0^{[0]}(E,q) \\ &\qquad \;-\; |Z_0|\, \frac{h^2}{\Xi} \int_0^\Lambda \mathrm{d}q \int_0^\Lambda \mathrm{d}q'\; \bar{D}_0^{[0]}(E,q)\; \bar{T}_{00}^{[0]}(E,q,p)\; \bar{D}_0^{[0]}(E,q')\Big] \quad . \end{aligned} \tag{3.51}$$

Thus, also the full trimer propagator $t(\bar{P}) = t(E)$ is a pure S-wave quantity. Only the last summand in eq. (3.51) has energy-poles, namely those of the S-wave part of the T-matrix. The other two summands are regular functions in E. Consequently, we can multiply both sides with $E - E^{(3)}$, take the limit $E \to E^{(3)}$ and use eq. (3.46) in order to extract the positive trimer residue:

$$Z_{\text{trimer}} \;=\; \lim_{E \to E^{(3)}} (E - E^{(3)})\, t(E) \;=\; |Z_0|\, \frac{h^2}{\Xi^2}\, |\beta|^2 \;>\; 0 \quad . \tag{3.52}$$

3.1.4.2 Irreducible trimer-dimer-particle coupling

We now have all essential ingredients that are needed in order to calculate the irreducible renormalized trimer-dimer-particle coupling $i\bar{G}(\bar{P},\bar{p})$. It will serve as a basic building block in the calculation of form factors and photodisintegration observables of a *cnn* halo system. Fig. 3.4 again gives a representation in terms of Feynman diagrams, where now forbidden internal trimer propagators can be omitted by simply setting $\bar{H} = 0$ in the T-matrix. The remaining trimer-irreducible diagrams exactly cover all contributing topologies. Furthermore, from the LSZ theorem we know that all external legs have to be renormalized with appropriate factors of $\sqrt{Z}$. Since in the channel i there is an external trimer as well as an external dimer, we define

$$\begin{aligned} \bar{G}_i(\bar{P},\bar{p}) &:= Z_{\text{trimer}}^{\frac{1}{2}}\; {}^{\bullet}G_i(\bar{P},\bar{p})\; |Z_i|^{\frac{1}{2}} \\ &= -\,|\beta\bar{H}| \left[\delta_{0i} + \int_0^\Lambda \mathrm{d}q\, \bar{D}_0^{[0]}(E,q)\, {}^{\bullet}\bar{T}_{0i}^{[00l]}(\bar{P},q,\bar{p})\right] \\ \Rightarrow \quad \bar{G}_i(E,\mathbf{p}) &= -\,|\beta\bar{H}| \left[\delta_{0i} + \int_0^\Lambda \mathrm{d}q\, \bar{D}_0^{[0]}(E,q)\, {}^{\bullet}\bar{T}_{0i}^{[0]}(E,q,p)\right] \;=\; \bar{G}_i(E,p) \quad , \end{aligned} \tag{3.53}$$

where we used eqs. (3.49) and (3.52). Inserting eq. (3.39) into eq. (3.53), the off-shell coupling is related to its on-shell version through the useful integral equation:

$$\begin{aligned}
\bar{G}_i(\bar{P},\bar{p}) \;&=\; -|\beta\bar{H}|\left[\delta_{0i} + \int_0^\Lambda \mathrm{d}q\, \bar{D}_0^{[0]}(E,q)\, {}^{\bullet}\bar{R}_{0i}^{[00|]}(\bar{P},q,\bar{p})\right. \\
&\quad \left. + \sum_{j=0}^{1}\int_0^\Lambda \mathrm{d}q\, \bar{D}_0^{[0]}(E,q) \int_0^\Lambda \mathrm{d}q'\, {}^{\bullet}\bar{T}_{0j}^{[0]}(E,q,q')\, \bar{D}_j^{[0]}(E,q')\, {}^{\bullet}\bar{R}_{ji}^{[00|]}(E,q',\bar{p})\right] \\
&=\; \left[\sum_{j=0}^{1}\int_0^\Lambda \mathrm{d}q\, (-|\bar{H}|\,|\beta|)\left(\delta_{0j} + \int_0^\Lambda \mathrm{d}q'\, \bar{D}_0^{[0]}(E,q')\, {}^{\bullet}\bar{T}_{0j}^{[0]}(E,q',q)\right)\right. \qquad (3.54) \\
&\quad \left. \times\; \bar{D}_j^{[0]}(E,q)\, {}^{\bullet}\bar{R}_{ji}^{[00|]}(\bar{P},q,\bar{p})\right] \;-\; |\beta\bar{H}|\,\delta_{0i} \\
&=\; \sum_{j=0}^{1}\int_0^\Lambda \mathrm{d}q\, \bar{G}_j(E,q)\, \bar{D}_j^{[0]}(E,q)\, {}^{\bullet}\bar{R}_{ji}^{[0]}(E+p^0-\epsilon_{i,\mathbf{p}},q,p) \;-\; |\beta\bar{H}|\,\delta_{0i} \quad .
\end{aligned}$$

In the last line we also applied the identity (3.38). If, in addition, $\bar{p}$ is on-shell, eq. (3.54) assumes matrix-form:

$$\bar{G}(E,p) \;=\; \int_0^\Lambda \mathrm{d}q\, {}^{\bullet}\bar{R}^{[0]}(E,p,q)\, \bar{D}^{[0]}(E,q)\, \bar{G}(E,q) \;-\; |\beta\bar{H}|\,\mathbf{e}_0 \quad . \qquad (3.55)$$

For a trimer state with energy $E = E^{(3)}$, this is equivalent to the bound-state equation (3.47). Thus, the renormalized, trimer-irreducible on-shell coupling $\bar{G}(p)$ is basically nothing else but the already known wave function $B^{[0]}(p)$. However, the big advantage of using the coupling (3.53) with eq. (3.46) over the wave function equation (3.47) is that the coupling is directly determined from the T-matrix, and as such, is automatically normalized correctly. For the following two-neutron halo systems, we numerically determined both $\bar{G}_i(p)$ and $B_i^{[0]}(p)$. Calculating their ratio $\alpha_i(p) := \bar{G}_i(p)/B_i^{[0]}(p)$, in all considered cases revealed that relative deviations $|\alpha_i(p)/\alpha_0(0) - 1|$ from a perfect proportionality of both quantities were less than $\sim 10^{-7}$. In addition, for cut-offs Λ that are larger than any other momentum scale in the system, $\bar{G}(p)$ turned out to be cut-off independent, as it should. Both results provide a positive consistency check for our method.

3.1.4.3 Irreducible trimer-three-particle coupling

Based on the results of the previous sec. 3.1.4.2, we now also calculate the irreducible trimer-three-particle coupling $i\bar{M}(\bar{P},\bar{p}_0,\bar{p}_1,\bar{p}_2)$. This matrix element plays a crucial role in the calculation of photodisintegration processes $(cnn) + \gamma \to c + n + n$. Topologically, it can be written as a sum of three contributions $i\bar{M} = \sum_{i=0}^{2} i\bar{M}_i$. The corresponding representation in terms of Feynman diagrams is depicted in fig. 3.6. The incoming trimer has four-momentum $\bar{P}$ and the outgoing core and the two neutrons have $\bar{p}_0$ and $\bar{p}_1$, $\bar{p}_2$,

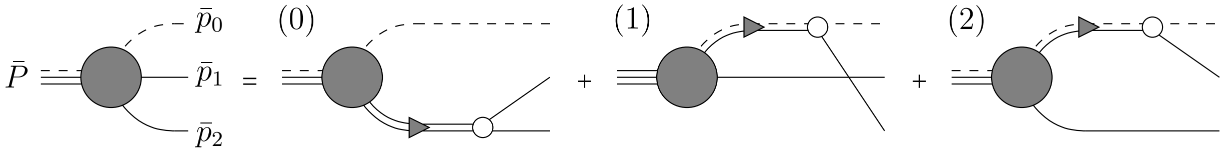

Figure 3.6: Diagrammatic representation of the irreducible trimer-three-particle coupling $i\bar{M}$. The right side of the equation is the sum of three contributions $i\bar{M} = \sum_{i=0}^{2} i\bar{M}_i$, where $i\bar{M}_2$ is the crossed version of $i\bar{M}_1$ and originates from the interchange $\bar{p}_1 \leftrightarrow \bar{p}_2$. The dashed line represents the core field

respectively. With regard to the contribution $i\bar{M}_i$, four-momentum conservation

$$\bar{P} \;=\; \sum_{i=0}^{2} \bar{p}_i \qquad \Rightarrow \qquad \bar{p}_2 \;=\; \bar{P} - (\bar{p}_0 + \bar{p}_1) \tag{3.56}$$

implies that the external single-particle leg and the opposite full dimer propagator, originating from the irreducible trimer-dimer-particle coupling, have four momenta $\bar{p}_i$ and $\bar{P} - \bar{p}_i$, respectively. Thus, we can write $i\bar{M}$ in terms of only three four-momenta $\bar{P}$, $\bar{p}_0$ and $\bar{p}_1$. For the remaining four-momentum $\bar{p}_2$, we use eq. (3.56) implicitly. In addition, if not specified otherwise, from now on, for any quantity X_i with allowed lower indices $i \in \{0, 1\}$, we define a third one via $X_2 := X_1$. This will also contribute to short notation. Recalling the kinematics (3.17), the contribution $\bar{M}_i$ then reads:

$$\begin{aligned} i\bar{M}_i(\bar{P}, \bar{p}_0, \bar{p}_1) \;&=\; i\bar{G}_i\Big(\bar{P}, (\bar{P} - \bar{p}_i) - \frac{M_i}{M_\Sigma}\bar{P}\Big)\, |Z_i|^{-\frac{1}{2}} \\ &\qquad \times\; iD_i\Big(\bar{P}, (\bar{P} - \bar{p}_i) - \frac{M_i}{M_\Sigma}\bar{P}\Big)\, (-ig_i) \\ &=\; i\bar{G}_i\Big(\bar{P}, \frac{m_i}{M_\Sigma}\bar{P} - \bar{p}_i\Big)\; \bar{D}_i\Big(\bar{P}, \frac{m_i}{M_\Sigma}\bar{P} - \bar{p}_i\Big)\, \sqrt{\frac{z_i}{\tau_i}} \quad . \end{aligned} \tag{3.57}$$

Note that in the first line, $|Z_i|^{-\frac{1}{2}}$ compensates the dimer renormalization factors in the definition (3.53), since these legs are now internal full dimer propagators. Additionally, in the channel $i = 0$, there is no factor 1/2 in front of $(-ig_0)$, since performing the contractions, the diagram comes with an overall factor of $(-ig_0/2)\,(2\mathrm{Tr}\left[PP^\dagger\right]) = -ig_0$. This can directly be seen from the contractions that are performed in eq. (D.10) for the outgoing particles in neutron-neutron scattering. Inserting the integral equation (3.54) into eq. (3.57) yields:

$$\begin{aligned} \bar{M}(\bar{P}, \bar{p}_0, \bar{p}_1) \;&=\; \sum_{i=0}^{2} \bar{M}_i(\bar{P}, \bar{p}_0, \bar{p}_1) \quad , \\ \bar{M}_i(\bar{P}, \bar{p}_0, \bar{p}_1) \;&=\; \Big[\sum_{j=0}^{1} \int_0^\Lambda \mathrm{d}q\, \bar{G}_j(E, q)\, \bar{D}_j^{[0]}(E, q) \bullet \bar{R}_{ji}^{[00|]}\Big(\bar{P}, q, \frac{m_i}{M_\Sigma}\bar{P} - \bar{p}_i\Big) \\ &\qquad -\; |\beta\bar{H}|\, \delta_{0i}\Big]\; \bar{D}_i\Big(\bar{P}, \frac{m_i}{M_\Sigma}\bar{P} - \bar{p}_i\Big)\, \sqrt{z_i/\tau_i} \quad . \end{aligned} \tag{3.58}$$

Applying the identities (3.22) and (3.38) with

$$E + \frac{m_i}{M_\Sigma} P^0 - p_i^0 - \epsilon_i(\bar{P}, \frac{m_i}{M_\Sigma}\mathbf{P} - \mathbf{p}_i) \;=\; E + \frac{\mathbf{p}_i^2}{2m_i} - p_i^0 \quad , \tag{3.59}$$

the irreducible trimer-three-particle coupling (3.58) assumes the form:

$$\begin{aligned} \bar{M}_i(\bar{P}, \bar{p}_0, \bar{p}_1) \;=\; & \Big[\sum_{j=0}^{1} \int_0^\Lambda \mathrm{d}q \, \bar{G}_j(E,q) \, \bar{D}_j^{[0]}(E,q) \\ & \times \; {}^\bullet\bar{R}_{ji}^{[0]}\Big(E + \frac{\mathbf{p}_i^2}{2m_i} - p_i^0, q, \big|\frac{m_i}{M_\Sigma}\mathbf{P} - \mathbf{p}_i\big|\Big) \;-\; |\beta \bar{H}| \, \delta_{0i}\Big] \\ & \times \; \bar{D}_i\Big(E + \frac{\mathbf{p}_i^2}{2m_i} - p_i^0, \big|\frac{m_i}{M_\Sigma}\mathbf{P} - \mathbf{p}_i\big|\Big) \, \sqrt{z_i/\tau_i} \quad . \end{aligned} \tag{3.60}$$

3.2 External currents

3.2.1 Effective Lagrangian via minimal coupling

In addition to the strong interactions between the neutrons and the core, we now extend our model by including couplings to external electromagnetic currents. Therefore, we assume that the charge of the core field ψ_0 is $\mathcal{Z}e$, whereas the two neutrons are, of course, uncharged. Electromagnetic interactions are then included via a vector potential A_μ, where the interaction terms are obtained by performing a minimal coupling

$$\begin{aligned} i\partial_\mu \;&\mapsto i\partial_\mu - \hat{Q}A_\mu \qquad \Rightarrow \qquad i\partial_0 \;\mapsto\; i\partial_0 - \hat{Q}A_0 \quad , \\ \nabla^2 \;&\mapsto (\nabla - i\hat{Q}\mathbf{A})^2 \;=\; \nabla^2 \;-\; i\hat{Q}(\nabla \cdot \mathbf{A}) \;-\; i2\hat{Q}\,\mathbf{A}\cdot\nabla \;-\; \hat{Q}^2\mathbf{A}^2 \end{aligned} \tag{3.61}$$

in the Lagrangian (3.1). This transformation insures gauge invariance. The quantity $\hat{Q}$ is the charge operator. Since in our case only the core has non-vanishing charge, $\hat{Q}\psi_0 = \mathcal{Z}e\psi_0$ and $\hat{Q}\vec{\psi}_1 = \vec{0}$ hold. For convenience, we choose Coulomb gauge $(\nabla \cdot \mathbf{A}) = 0$, canceling the second term $-i\hat{Q}(\nabla \cdot \mathbf{A})$ in the last line. Applying the minimal coupling rule (3.61), the resulting effective Lagrangian assumes the form:

$$
\boxed{
\begin{aligned}
\mathcal{L} &= \mathcal{L}^{(1)} + \mathcal{L}^{(2)} + \mathcal{L}^{(3)} \quad , \qquad \mathcal{L}^{(1)} = \mathcal{L}^{(\text{free})} + \mathcal{L}^{(\text{em})} \quad , \\
\mathcal{L}^{(\text{free})} &= \psi_0^\dagger\Big(i\partial_0 + \frac{\nabla^2}{2m_0}\Big)\psi_0 \;+\; \vec{\psi}_1^\dagger\Big(i\partial_0 + \frac{\nabla^2}{2m_1}\Big)\vec{\psi}_1 \quad , \\
\mathcal{L}^{(\text{em})} &= -\,\mathcal{Z}e\;\psi_0^\dagger A_0\,\psi_0 \;-\; \frac{\mathcal{Z}e}{m_0}\,\psi_0^\dagger\,\mathbf{A}\cdot i\nabla\psi_0 \;-\; \frac{(\mathcal{Z}e)^2}{2m_0}\,\psi_0^\dagger\,\mathbf{A}^2\,\psi_0 \quad , \\
\mathcal{L}^{(2)} &= \Delta_0\,d_0^\dagger d_0 \;-\; \frac{g_0}{2}\Big[d_0^\dagger\,(\vec{\psi}_1^{\,\mathrm{T}} P\,\vec{\psi}_1) + (\vec{\psi}_1^{\,\mathrm{T}} P\,\vec{\psi}_1)^\dagger\,d_0\Big] \\
&\quad + \;\Delta_1\,\vec{d}_1^\dagger\vec{d}_1 \;-\; g_1\Big[\vec{d}_1^\dagger\vec{\psi}_1\,\psi_0 + \psi_0^\dagger\,\vec{\psi}_1^\dagger\vec{d}_1\Big] \quad , \\
\mathcal{L}^{(3)} &= \Xi\,t^\dagger t \;-\; h\left[t^\dagger\,\psi_0\,d_0 + (\psi_0\,d_0)^\dagger t\right] \quad .
\end{aligned}
}
\tag{3.62}
$$

Because we consider resonant S-wave interactions, only the scalar fields ψ_i are dynamical and thus electromagnetic couplings do only appear in $\mathcal{L}^{(1)} = \mathcal{L}^{(\text{free})} + \mathcal{L}^{(\text{em})}$. $\mathcal{L}^{(\text{em})}$ contains all electromagnetic interaction terms and originates from the transformed $\mathcal{L}^{(\text{free})}$. Non-minimal coupling terms would only contribute at higher orders and thus are not considered in our LO calculation.

Comparing the Lagrangians (3.1) and (3.62), we note that they only differ in the electromagnetic interaction term $\mathcal{L}^{(\text{em})}$. Thus, all momentum-space Feynman rules used in the previous sections are valid further on and all derived calculations and quantities can be reused. With regard to Feynman diagrams, we will keep to the conventions explained in the end of sec. 3.1.1. Additional photon couplings will be represented by rectangles.

3.2.2 Electric form factor and charge radius

3.2.2.1 Formalism

Figure 3.7: Feynman diagram representing the irreducible coupling $i\bar{\Gamma}$ of an external electric source to a trimer. The incoming and outgoing four-momenta of the trimer are $\bar{P}$ and $\bar{K}$ respectively. The photon has four-momentum transfer $\bar{Q} = \bar{K} - \bar{P}$.

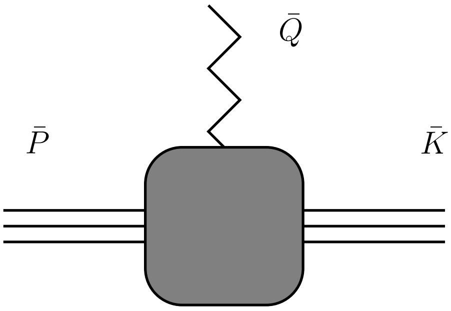

We have now all necessary tools to calculate the charge form factor $\mathcal{F}_\mathrm{E}$ and the electric charge radius $\langle r_\mathrm{E}^2\rangle$ of a *cnn*-system with resonant S-wave interactions. In this section, we first give a derivation for $\mathcal{F}_\mathrm{E}$. In general, the electromagnetic form factor can be extracted from the matrix element of the electromagnetic current between an incoming and an outgoing trimer state. On the Lagrangian level, the associated interaction term in eq. (3.62) is $\mathcal{L}^{(\text{em})}$, where for the electric form factor, the only relevant contribution is

$-\mathcal{Z}e\,\psi_0^\dagger A_0\psi_0$. With regard to Feynman graphs, it simply results in an additional factor $(-i\mathcal{Z}e)$. The term $\sim \mathbf{A}\cdot\nabla$ would only contribute to the magnetic form factor and, since we just consider the coupling to a single external source, also the term $\sim \mathbf{A}^2$, which is of order e^2, is neglected. Internal photons, which would contribute to Coulomb corrections and would significantly complex the derivation of the T-matrix, are not included in our model. The electric charge form factor is then related to $i\bar{\Gamma}$, which is defined as the trimer-irreducible coupling of a trimer to the zeroth component of the electromagnetic current, through:

$$\mathcal{F}_{\mathrm{E}} = (-i\mathcal{Z}e)^{-1}\, i\bar{\Gamma} \quad . \tag{3.63}$$

The coupling is depicted in fig. 3.7, where the incoming and outgoing trimer four-momenta are $\bar{P}$ and $\bar{K}$, respectively. Four-momentum conservation, of course, implies $\bar{Q} = \bar{K} - \bar{P}$ for the momentum transfer of the photon such that, in the first instance, $i\bar{\Gamma}$ effectively only depends on the two four-momenta $\bar{P}$ and $\bar{K}$. In the following, we determine $i\bar{\Gamma}$ via the LSZ reduction formula as it is presented in ref. [77]. That is, we sum all trimer-irreducible diagrams, and renormalize the external trimer legs with factors $\sqrt{Z_{\text{trimer}}}$. We choose this procedure in order to maintain consistency with all the other calculations presented in this work. Note that there also exist alternative approaches. For instance, Kaplan, Savage and Wise used an ansatz based on two- and three-point functions without explicitly introducing trimer fields in order to determine the electromagnetic form-factor of the deuteron [96]. However, both methods are equivalent and yield the same results. Other analog calculations for the charge form factor of the triton system (corresponding to a spin-1/2 core) also previously have been carried out in a wave function based formalism [97, 98].

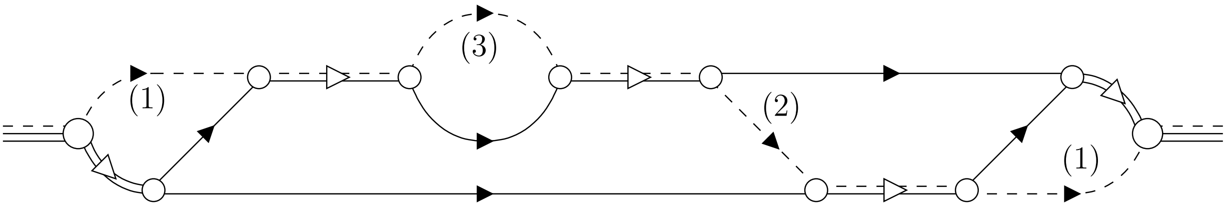

Figure 3.8: Exemplary irreducible graph contributing to the trimer form factor. The dashed line represents the core field which either (1) propagates parallel to the d_0-dimer, (2) is exchanged between d_1-dimers or (3) appears within a d_1-dimer loop.

In order to collect all the different topologies that contribute to $i\bar{\Gamma}$, we consider the typical irreducible graph shown in fig. 3.8. The photon can only couple to the core field c indicated by dashed lines, but for the moment we suppress the photon-core coupling. The d_1-dimer also carries charge, but the photon coupling to d_1 appears only at NLO where the dimers are dynamical. Within the exemplary diagram, there are three positions for a single core propagator to appear: c either

(0) propagates parallel to the d_0-dimer,

(1) is exchanged between between two d_1-dimers or

(2) appears within a d_1-dimer loop.

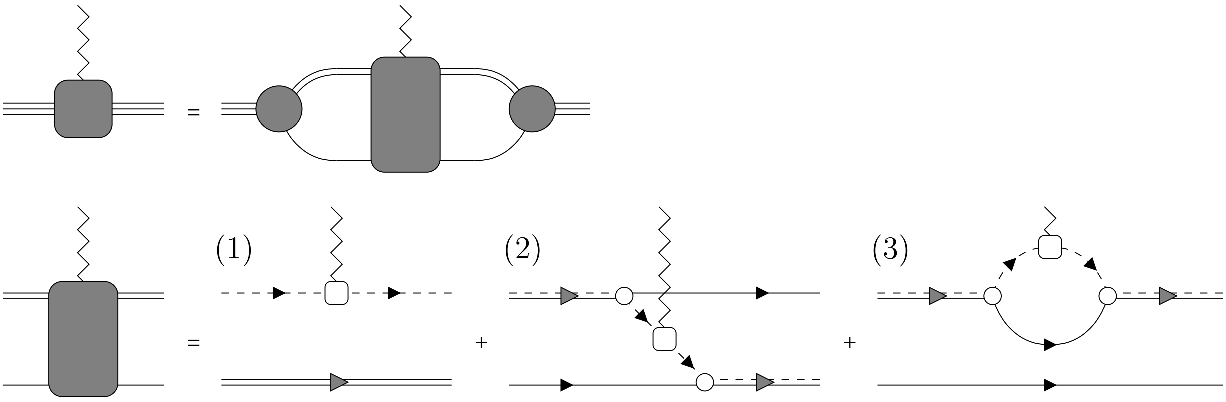

Figure 3.9: Diagrammatic representation of the three contributions to the irreducible coupling $i\bar{\Gamma} = \sum_{i=0}^{2} i\bar{\Gamma}_i$ of a trimer to an external electric source. (1), (2) and (3) labels the parallel-, exchange- and loop-term, respectively.

In fact, these three cases are the only possibilities for a single core propagator to appear in an arbitrary irreducible trimer graph. Thus, including the photon-core coupling and summing over all such diagrams, the form factor can be written as the sum of three contributions

$$\begin{aligned}
\mathcal{F}_{\mathrm{E}} &= \sum_{i=0}^{2} \mathcal{F}_{\mathrm{E},i} \quad , \qquad \mathcal{F}_{\mathrm{E},i} \;=\; (-i\mathcal{Z}e)^{-1}\, i\bar{\Gamma}_i \quad , \\
i\bar{\Gamma}_i(\bar{P},\bar{K}) &= \int \frac{\mathrm{d}^4\bar{p}}{(2\pi)^4} \int \frac{\mathrm{d}^4\bar{k}}{(2\pi)^4} \\
&\qquad \times\; i\bar{G}_i(\bar{P},\bar{p})\; |Z_i|^{-\frac{1}{2}}\; i\Gamma_i^{\mathrm{red}}(\bar{P},\bar{K},\bar{p},\bar{k})\; |Z_i|^{-\frac{1}{2}}\; i\bar{G}_i(\bar{K},\bar{k}) \\
&= (-i\mathcal{Z}e) \int \frac{\mathrm{d}^4\bar{p}}{(2\pi)^4} \int \frac{\mathrm{d}^4\bar{k}}{(2\pi)^4}\; \bar{G}_i(\bar{P},\bar{p})\; \bar{\Gamma}_i^{\mathrm{red}}(\bar{P},\bar{K},\bar{p},\bar{k})\; \bar{G}_i(\bar{K},\bar{k})
\end{aligned} \tag{3.64}$$

corresponding to the cases (0), (1), and (2). In fig. 3.9 this decomposition of the trimer-irreducible matrix element into three classes of diagrams is illustrated pictorially. A similar classification of contributing Feynman diagrams has also been used for the calculation of the electric form factor of the triton [98]. In all three contributions in fig. 3.9 the irreducible trimer-dimer-particle coupling $i\bar{G}$ from eq. (3.53) appears naturally and is again represented by the filled circles. This can be seen as the motivation behind the considerations we performed in sec. 3.1.4 and especially in sec. 3.1.4.2. The factors $|Z_i|^{-\frac{1}{2}}$ compensate the renormalization of the external dimer legs in the definition (3.53). Those legs are now, of course, internal full dimer propagators. The remaining terms $i\Gamma_i^{\mathrm{red}}$ represent the three reduced graphs in the lower right in fig. 3.9. Their renormalized versions are defined as usual, through:

$$\bar{\Gamma}_i^{\mathrm{red}} \;:=\; (\mathcal{Z}e)^{-1}\, |Z_i|^{-\frac{1}{2}}\; \Gamma_i^{\mathrm{red}}\; |Z_i|^{-\frac{1}{2}} \quad . \tag{3.65}$$

Detailed derivations for all three contributions to the form factor can be found in appendix D.3.4, where we refer to $\mathcal{F}_{\mathrm{E},0}$, $\mathcal{F}_{\mathrm{E},1}$ and $\mathcal{F}_{\mathrm{E},2}$ as the *parallel term*, *exchange term* and *loop term*, respectively. Assuming Breit frame kinematics, no energy is transferred by the photon, i.e. $P^0 = K^0$ and $\mathbf{P}^2 = \mathbf{K}^2$. Performing shifts in the loop four-momenta, all three contributions are expressed through symmetric integrals that are even functions in $Q = |\mathbf{Q}| = |\mathbf{K} - \mathbf{P}|$. $\mathbf{Q}$ is the three-momentum transfer. As an even function, the charge form factor in eq. (3.64) then effectively can only depend on Q^2. Explicit expressions for $\mathcal{F}_{\mathrm{E},0}$, $\mathcal{F}_{\mathrm{E},1}$ and $\mathcal{F}_{\mathrm{E},2}$ are given in eqs. (D.38), (D.52) and (D.69), respectively. The numerical calculation of $\mathcal{F}_{\mathrm{E}}(Q^2)$ is explained in sec. B.

At $Q^2 = 0$, the charge form factor is normalized to one. As demonstrated in the following section, this normalization is automatically reproduced in our formalism. For small momentum transfer, the form factor can be expanded in powers of Q^2 as:

$$\mathcal{F}_{\mathrm{E}}(Q^2) \;=\; 1 - \frac{\langle r_{\mathrm{E}}^2 \rangle}{3!} Q^2 \;+\; \mathcal{O}(Q^4) \quad , \tag{3.66}$$

where $\langle r_{\mathrm{E}}^2 \rangle$ is the electric charge radius. In practice, we calculate the form factors for finite momentum transfer and extract the charge radius $\langle r_{\mathrm{E}}^2 \rangle$ by numerically taking the limit

$$\left\langle r_{\mathrm{E}}^2 \right\rangle \;=\; -6 \lim_{Q^2 \to 0^+} (\partial \mathcal{F}_{\mathrm{E}})(Q^2) \quad . \tag{3.67}$$

Here, we have to keep in mind that in our effective theory the core and the neutrons are treated as point-like. Their size enters only in counter terms that appear at higher orders. In typical halo nuclei, however, the charge radius of the core can not be neglected. In this work, we thus interpret the calculated radius as the charge radius of the *cnn* halo nucleus relative to the charge radius of the core. In order to underline this interpretation, we relabel it by $\delta \langle r_{\mathrm{E}}^2 \rangle := \langle r_{\mathrm{E}}^2 \rangle$. Neglecting the relatively small charge radius of the neutron $\langle r_{\mathrm{E}}^2 \rangle_n = -0.115(4)\ \mathrm{fm}^2$, which we extracted from ref. [99], the full charge radius $\langle r_{\mathrm{E}}^2 \rangle_{cnn}$ of the *cnn* halo nucleus, then reads:

$$\left\langle r_{\mathrm{E}}^2 \right\rangle_{cnn} \;=\; \left\langle r_{\mathrm{E}}^2 \right\rangle_c \;+\; \delta \left\langle r_{\mathrm{E}}^2 \right\rangle \quad , \tag{3.68}$$

where we quadratically added our result to the charge radius of the core $\langle r_{\mathrm{E}}^2 \rangle_c$. Thus, $\delta \langle r_{\mathrm{E}}^2 \rangle = \langle r_{\mathrm{E}}^2 \rangle_{cnn} - \langle r_{\mathrm{E}}^2 \rangle_c$ holds. This prescription follows directly if the total charge distribution is a convolution of the charge distributions of the halo and the core.

3.2.2.2 Results

In this section, we apply our two-neutron halo EFT formalism to concrete physical systems and calculate form factors and relative charge radii $\delta \langle r_{\mathrm{E}}^2 \rangle$. Such differences of nuclear charge radii $\delta \langle r_{\mathrm{E}}^2 \rangle$ were measured for a whole range of isotopes, see e.g. [100–104]. We compare these results with our theory where it is applicable.

Our theory applies directly to two-neutron halo systems with $J^P = 0^+$ and with a $J^P = 0^+$ core. Assuming that the spin of the core is inert due to the large mass of the core compared to the neutrons, we can also consider more general systems with quantum numbers J^P, $(J \pm 1/2)^P$, and J^P of the *c*-, *cn*-, and *cnn*-systems, respectively. The lightest known isotopes that would fall into this category are ^{10}He, ^{11}Li, ^{12}Be, ^{14}Be, ^{16}C, ^{20}C, ^{21}C, ^{22}C and ^{24}O, where we used J^P values from the National Nuclear Data Center (NNDC) [105]. On the other hand, from sec. 1.2.3 we know that the lightest isotopes for which there is either experimental evidence for their two-neutron-halo nature or which are good candidates for such a system, are ^{6}He, ^{11}Li, ^{14}Be, ^{17}B and ^{22}C. We apply our EFT framework to the isotopes in the intersection of both sets, namely ^{11}Li, ^{14}Be and ^{22}C. For ^{6}He and ^{17}B, the J^P-quantum numbers indicate that P-wave contributions are dominant.

With regard to the input data for our model, the particle masses read $m_0 = m_c$ and $m_1 = m_n$, where m_c and m_n are the masses of the core and the neutron, respectively. Furthermore, for a general isotope with atomic number Z, mass number A and mass $m_{Z,A}$, the energy $S^{Z,A}_{k\cdot n}$ that is needed in order to separate $k < A - Z$ neutrons form the isotope is given through:

$$S^{Z,A}_{kn} \;=\; m_{Z,A-k} \,+\, k \cdot m_n \,-\, m_{Z,A} \quad . \tag{3.69}$$

In our halo model with three point-like particles, the two-neutron separation energy equals the total binding energy of the three-body system. Thus, for a bound or virtual cn-dimer and a bound cnn-trimer the one- and two-neutron separation energies have to obey $S^{cnn}_{2n} > \max(S^{cn}_{1n}, 0)$. We then use $E^{(2)}_1 = -S^{cn}_{1n}$ and $E^{(3)} = -S^{cnn}_{2n}$ as input for the binding energies in our model. We fix the values of all masses, and energies by taking data from NNDC [105] unless noted otherwise. Furthermore, the cn-scattering length is determined from the relation $a_1 = a_{cn} = \mathrm{sgn}(S^{cn}_{1n})/(2\mu_{cn}|S^{cn}_{1n}|)^{1/2}$, with $\mu_{cn} = m_c m_n/(m_c + m_n)$. Thus, cn-states with negative S^{cn}_{1n} are treated as virtual two-body states with negative scattering length a_1. This approximation corresponds to neglecting the imaginary part of the binding momentum for resonances. For the nn-scattering length, we take the value $a_0 = a_{nn} = -18.7(6)$ fm from Gonzales Trotter et al. [14].

Errors: Before we present results for ^{11}Li, ^{14}Be and ^{22}C, we first discuss the different types of errors in our calculation. There are three types of errors:

(i) Numerical errors: They are negligible.

(ii) Errors in the input variables: Experimentally determined input variables, such as nuclear masses and separation energies, are used to fix our effective field theory parameters. Their uncertainties can be propagated to the final results. The uncertainties in the nuclear masses are relatively small and can be neglected. Uncertainties in the separation energies are only quoted if they are larger than 1%. In the ^{22}C system, those separation energies are only poorly known such that errors of type (ii) dominate.

(iii) Errors from higher orders: They come from operators that contribute at higher orders in the EFT expansion. We note that errors of this type can never be provided in model calculations, since no expansion scheme exists. In this sense, model calculations are uncontrolled. Short of an explicit higher order calculation, one must use dimensional analysis and naturalness to estimate their size. The expansion parameter of our theory $R_{\text{core}}/R_{\text{halo}}$ is roughly $R/|a|$. In order to obtain better estimates, we compare the typical energy scales E_{halo} and E_{core} of the neutron halo and the core, respectively. To estimate E_{halo}, we choose the one- or two-neutron separation energy S_{1n}^{cn} or S_{2n}^{cnn}. The energy scale of the core is estimated by its excitation energy E_*^c or its one-neutron separation energy S_{1n}^c. The square root of the energy ratio $R_{\text{core}}/R_{\text{halo}} \approx \sqrt{|E_{\text{halo}}/E_{\text{core}}|}$ then yields an estimate for the expansion parameter of the effective theory. In particular, if R_{halo} is estimated from E_*^c or S_{1n}^c, this ratio quantifies the quality of the structureless core approximation. For our error estimates, we then take the largest value for $R_{\text{core}}/R_{\text{halo}}$ that can be obtained this way. For ^{11}Li and ^{14}Be, these errors constitute the dominant error contribution, since the expansion parameter $R_{\text{core}}/R_{\text{halo}}$ is typically not much smaller than 1.

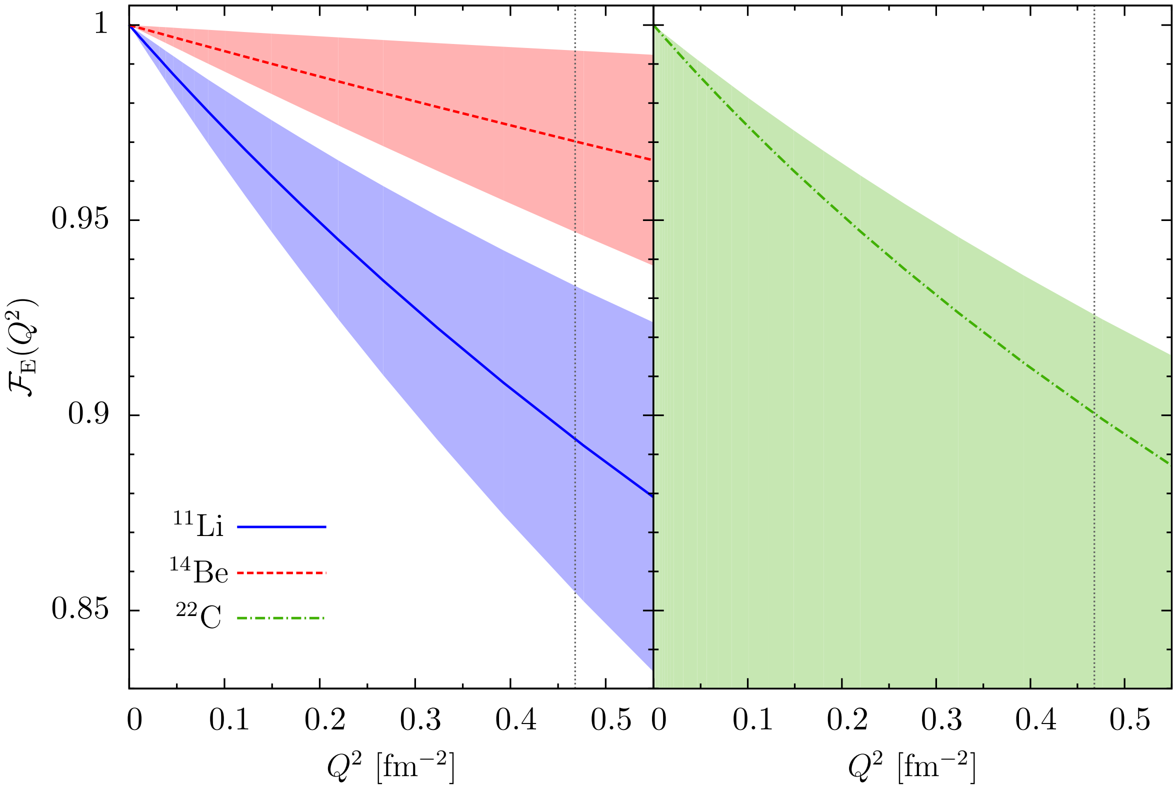

Figure 3.10: The charge form factor $\mathcal{F}_{\text{E}}(Q^2)$ for the halo nuclei ^{11}Li (left plot, blue solid line), ^{14}Be (left plot, red long-dashed line) and ^{22}C (right plot, green dash dotted line) relative to the core in leading order halo EFT. The estimated theory error for ^{11}Li and ^{14}Be is given by the shaded bands. For ^{22}C, varying the separation energies within their errors gives the shaded region. The vertical dashed lines indicate the breakdown scale from explicit pion exchange.

Charge from factors: In fig. 3.10, the charge form factors calculated from eq. (3.64) are depicted as a function of the momentum transfer Q^2. For $Q^2 \to \infty$, the form factors vanish.

c	J^P_c	m_c [MeV]	E^c_* [MeV]	S^c_{1n} [MeV]	$\delta\langle r^2_{\mathrm{E}}\rangle$ [fm^2]
cn	J^P_{cn}	S^{cn}_{1n} [MeV]	S^{cn}_{1n}/E^c_*	S^{cn}_{1n}/S^c_{1n}	$\delta\langle r^2_{\mathrm{E}}\rangle_{\mathrm{exp}}$ [fm^2]
cnn	J^P_{cnn}	S^{cnn}_{2n} [MeV]	S^{cnn}_{2n}/E^c_*	S^{cnn}_{2n}/S^c_{1n}	
^{9}Li	$\frac{3}{2}^-$	8406	2.69	4.06	1.7(6)
^{10}Li	$(2^-, 1^-)$	−0.026(13)	-0.10^2	-0.08^2	1.171(120) [100]
^{11}Li	$\frac{3}{2}^-$	0.37	0.37^2	0.30^2	
^{12}Be	0^+	11201	2.10	3.17	0.4(3)
^{13}Be	$(\frac{1}{2}^-)$	−0.51(1)	-0.49^2	-0.40^2	−−
^{14}Be	0^+	1.27(13)	0.78^2	0.63^2	
^{20}C	0^+	18664	1.59 [106]	2.9(3)	$1.7^{+\infty}_{-0.5}$
^{21}C	$\frac{1}{2}^+$	−0.014(467)	-0.09^2	-0.07^2	−−
^{22}C	0^+	0.11(6)	0.26^2	0.20^2	

Table 3.1: Effective theory parameters, estimates of the expansion parameter, and predicted electric charge radii relative to the core $\delta\langle r^2_{\mathrm{E}}\rangle$ from eq. (3.67) for the halo nuclei ^{11}Li, ^{14}Be and ^{22}C. Further explanations are given in the text.

At small momentum transfers, they approach unity as required by current conservation. Numerical deviations from unity at vanishing Q^2 are less than 10^{-5}. This provides a consistency-check for our calculation. For ^{11}Li and ^{14}Be, the estimated errors from higher orders in the effective theory expansion dominate and are given by the shaded bands. For ^{22}C, the shaded region originates from varying the binding energies within their errors. Our effective theory does neither include explicit pion dynamics nor does it include the structure of the core. Thus, it breaks breaks down for momentum transfers of the order of the pion mass $m^2_\pi \approx 0.5$ fm^{-2} as indicated by the vertical dashed lines in fig. 3.10.

Electric charge radii: In tab. 3.1, we summarize the effective theory parameters and give predictions for the charge radii relative to the core in ^{11}Li, ^{14}Be and ^{22}C. Below, we discuss our analysis for each halo nucleus in detail:

^{11}Li: The ^{11}Li halo nucleus and the ^{9}Li core have both the quantum numbers $J^P = \frac{3}{2}^-$ while ^{10}Li appears to have either $J^P = 2^-$ or 1^-. There is some evidence that both S- and P-wave components contribute to the neutron halo [34]. However, we analyze ^{11}Li under the assumption that only the S-wave contributes in LO and test the consistency of our assumption with the data. P-wave contributions then enter in higher orders. The two-neutron separation energy of ^{11}Li is 0.37 MeV and ^{10}Li is 26(13) keV above the n-^{9}Li threshold. Although the corresponding relative error of $\sim 50\%$ on S^{cn}_{1n} appears large, it does not dominate the overall error, since observables are sensitive to variations in $S^{cnn}_{2n} - S^{cn}_{1n}$, which has only a $\sim 3\%$ error. The first excitation energy of the ^{9}Li ground state is 2.69 MeV and its one-neutron separation energy is 4.06 MeV. Thus, the expansion parameter and the error can be estimated as $R_{\mathrm{core}}/R_{\mathrm{halo}} \approx \sqrt{S^{cnn}_{2n}/E^c_*} \approx 0.37$. Calculating the charge radius relative to ^{9}Li via eq. (3.67) gives $\delta\langle r_\mathrm{E}^2\rangle = 1.68(62)$ fm^2, where the $\sim$ 40% uncertainty comes from the expansion parameter. In ref. [100], the charge radius was measured with the help of high precision laser spectroscopy. The experimental value of $\delta\langle r_\mathrm{E}^2\rangle_\mathrm{exp} = 1.171(120)$ fm^2 is thus compatible with our calculation within the error bars.

^{14}Be: The halo nucleus ^{14}Be and its core ^{12}Be are both in a $J^P = 0^+$ configuration, while the quantum numbers of ^{13}Be are less clear although there is some evidence for $J^P = \frac{1}{2}^-$. For our study, we assume that the ^{13}Be dimer has also positive parity. The binding energy of the ^{14}Be trimer is $S_{2n}^{cnn} = 1.27(13)$ MeV and the virtual ^{13}Be has $S_{1n}^{cn} = -510(10)$ keV. The excitation energy of the ^{12}Be core is $E_*^c = 2.10$ MeV and its one-neutron separation energy is 3.17 MeV. Thus, the resulting expansion parameter $R_\mathrm{core}/R_\mathrm{halo} \approx \sqrt{S_{2n}^{cnn}/E_*^c} \approx 0.78$ is relatively large. Using eq. (3.67), our effective theory then predicts a charge radius relative to ^{12}Be of $\delta\langle r_\mathrm{E}^2\rangle = 0.41(32)$ fm^2 with an $\sim$ 80% error.

^{22}C: There is some theoretical and experimental evidence that ^{22}C is a pure S-wave halo nucleus [44,45]. ^{22}C and the ^{20}C core both have $J^P = 0^+$, while ^{21}C is in $J^P = \frac{1}{2}^+$ configuration. The two-neutron separation energy $S_{2n}^{cnn} = 0.11(6)$ MeV has a relatively large error. Furthermore, ^{21}C seems to be unbound, but $S_{1n}^{cn} = -0.014(467)$ keV is only poorly known. In ref. [106], a 2^+ excited state at 1.588(20) MeV above the ground state was observed. The one-neutron separation energy of ^{20}C is 2.9(3) MeV. We take the central values for S_{2n}^{cnn} and S_{1n}^{cn}, which are also roughly in accord with the allowed parameter region predicted from a recent analysis of the matter radius measurement [44] in the framework of the halo EFT [48]. Calculating the charge radius relative to ^{20}C via eq. (3.67) gives $\delta\langle r_\mathrm{E}^2\rangle = 1.66^{+\infty}_{-0.49}$ fm^2, where the uncertainty now comes from varying the separation energies within their errors. Due to the poorly known input data, $S_{1n}^{cn} = S_{2n}^{cnn}$ is not excluded. Since for such values the charge radius diverges towards positive infinity, the predicted value for $\delta\langle r_\mathrm{E}^2\rangle$ can only be bound from below, where the lower limit is 1.17 fm^2. For the halo nuclei ^{14}Be and ^{22}C, our results are true predictions and can be compared with measurements as soon as the corresponding experimental data is available.

3.2.3 Universal correlations

Another interesting aspect of our two-neutron halo EFT with external currents is that it can also be used in order to determine general correlations between different low-energy observables. If the two-particle scattering lengths are large, such correlations are universal and their corrections are again of order of $R/|a|$. With respect to masses and separation energies, a general two-neutron halo nucleus has three free parameters in our model: the core mass m_c and the one- and two-neutron separation energies S_{1n}^{cn} and S_{2n}^{cnn}. By fixing these three, all other three-particle observables, such as matter and charge radii, are uniquely determined. We will now investigate the general functional dependencies of the relative charge radius $\delta\langle r_\mathrm{E}^2\rangle$ from eq. (3.67) on m_c, S_{1n}^{cn} and S_{2n}^{cnn}.

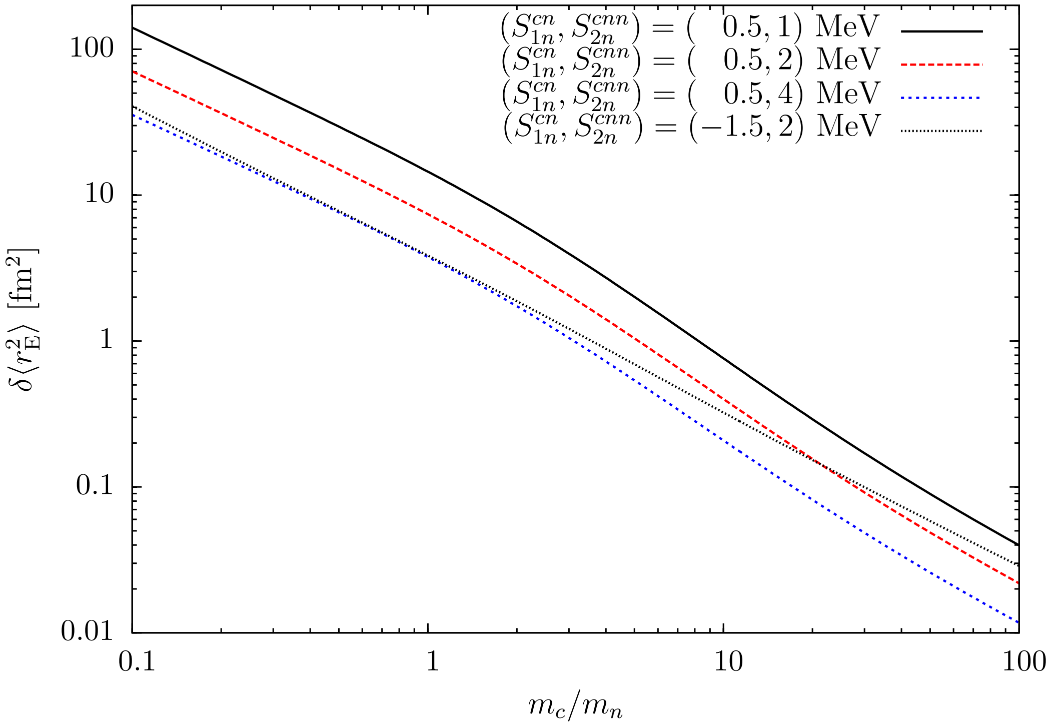

Figure 3.11: The electric charge radius relative to the core $\delta\langle r_{\mathrm{E}}^2\rangle$ as a function of mass ratio m_c/m_n for different binding energies S_{1n}^{cn} and S_{2n}^{cnn}.

In fig. 3.11, $\delta\langle r_{\mathrm{E}}^2\rangle$ is given as a function of the mass ratio m_c/m_n for fixed energy values S_{1n}^{cn} and S_{2n}^{cnn}. The charge radius is always positive and decreases for growing core mass m_c. This reflects that $\delta\langle r_{\mathrm{E}}^2\rangle$, for the two-neutron halo system, originates from the recoil effect of the charged core. For core masses below $2m_n$, the radius roughly falls of like $\sim 1/m_c$. Around $m_c \approx 2m_n$, the slope changes and the charge radii drop even faster as m_c/m_n increases.

In fig. 3.12, the dependence of the charge radius relative to the core on the separation energies S_{2n}^{cnn} and $1 - S_{1n}^{cn}/S_{2n}^{cnn}$ is shown for a fixed mass ratio $m_c/m_n = 10$. The region $1 - S_{1n}^{cn}/S_{2n}^{cnn} < 1$ corresponds to a bound *cn*-system, while $1 - S_{1n}^{cn}/S_{2n}^{cnn} > 1$ implies that the *cn*-system is unbound. In this region the *cnn*-system is Borromean. If $1 - S_{1n}^{cn}/S_{2n}^{cnn} \ll 1$ holds, the *cn*-system is deeply bound and the three-body problem effectively reduces to a two-body problem of *cn* and another neutron. As one would also naively expect, $\delta\langle r_{\mathrm{E}}^2\rangle$ grows as both the binding energy for the three-body system S_{2n}^{cnn} and the binding energy of the dimer-particle system $S_{2n}^{cnn} - S_{1n}^{cn}$ decrease. However, the exact functional dependencies on the 3 quantities m_c, S_{2n}^{cnn} and S_{1n}^{cn} are more complicated. Also note that there is a sudden increase in $\delta\langle r_{\mathrm{E}}^2\rangle$ along the line $1 - S_{1n}^{cn}/S_{2n}^{cnn} = 1$ where the *cnn*-system becomes Borromean. This leads to a ridge along $(S_{2n}^{cnn} - S_{1n}^{cn})/S_{2n}^{cnn} = 1$ that is most easily seen in the contour lines. We summarize our results in chapter 4.

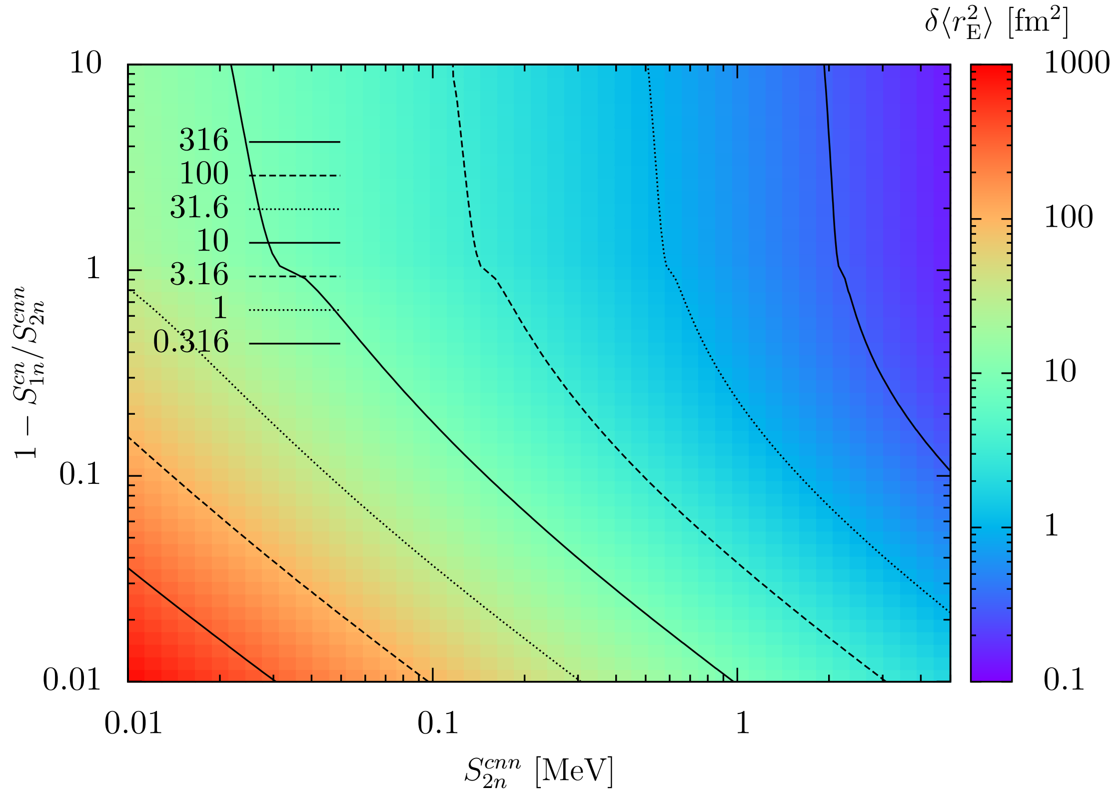

Figure 3.12: The electric charge radius relative to the core $\delta\langle r_E^2\rangle$ as a function of the two-neutron separation energy S_{2n}^{cnn} and the energy ratio $1 - S_{1n}^{cn}/S_{2n}^{cnn}$ for fixed mass ratio $m_c/m_n = 10$.

3.2.3.1 Calcium halo nuclei

We now calculate universal correlations for a concrete physical system, namely the hypothetical neutron-rich calcium isotope ^{62}Ca, consisting out of a ^{60}Ca core and a two-neutron halo. Both ^{60}Ca and ^{62}Ca are assumed to be in 0^+ configuration. We will refer to ^{60}Ca, ^{61}Ca and ^{62}Ca as the c-, cn- and cnn-system, respectively. In contrast to the light two-neutron halo nuclei candidates ^{11}Li, ^{14}Be and ^{22}C considered in sec. 3.2.2.2, it is still an open question whether heavy two-neutron halos exist at all. Recently, there has been much interest, both experimentally [107, 108] and theoretically [109–111], in determining precise values for masses, understanding shell evolution and locating the drip line in the neutron rich calcium isotopes. Coupled-cluster calculations of neutron rich calcium isotopes that included coupling to the scattering continuum and schematic three-nucleon forces, suggested that there is an inversion of shell-model orbitals in ^{53,55,61}Ca. In particular, it was suggested that a large S-wave scattering length might occur in ^{60}Ca-n scattering with interesting implications for ^{62}Ca.

In ref. [90] such coupled-cluster methods, combined with modern ab initio interactions derived from chiral effective theory, were used in order calculate the phase shift $\delta_{cn}(p)$, where p is the momentum in the center-of-mass frame of the cn-subsystem. Effects of three-nucleon forces were included schematically as density dependent nucleon-nucleon interactions. The elastic scattering length a_{cn} and also the effective range r_{cn} were extracted by fitting a polynomial in p^2 to the effective range expansion $p \cot \delta_{cn}(p) = -1/a_{cn} + r_{cn}/p^2 + \mathcal{O}(p^4)$, yielding $a_{cn} = 54(1)$ fm and $r_{cn} = 9.0(2)$ fm. Thereby, the errors originate from variations in the frequencies of spherical harmonic oscillator shells that are contained in the Hartree–Fock basis used to solve the coupled-cluster equations. Details about this method can e.g. be found in ref. [112]. The errors on the effective range from the degree of the fitted polynomials are negligible to the given accuracy. Since a_{cn} is positive, the subsystem ^{61}Ca is bound and we do not considered the case of ^{62}Ca being a Borromean. However, the following results for ^{62}Ca observables, also in this case, would qualitatively remain the same. In addition, the coupled-cluster analysis strongly supports the ground-state of ^{61}Ca having $J^P = 1/2^+$, as required. The scattering length is enhanced by about a factor of six compared to the effective range. Thus, all two-body scattering lengths in the system are large and we expect the three-body sector to display universal features associated with Efimov physics. Assuming $R \sim r_{cn}$, the error from higher order corrections in $R/|a|$ can be estimated to be of order $(r_{cn}/a_{cn})^2 \sim 3\%$. Furthermore, the inverse effective range can be used to estimate the breakdown scale $S_{\text{deep}} = 1/(\mu_{cn} r_{cn}^2) = 0.52(2)$ MeV beyond which the halo EFT with S-wave cannot be applied anymore. The obtained result for $a_{cn} = 54(1)$ fm and the core mass $m_c = 55901$ MeV provide required input parameters for our halo EFT analysis of the cnn-system. Three-body observables are then correlated to the two-neutron separation energy S_{2n}^{cnn}, which is the only remaining free parameter in our model.

Regarding strong interactions, in fig. 3.13, we display the correlation between the two-neutron separation energy S_{2n}^{cnn} of ^{62}Ca and the ^{61}Ca-n scattering length a_{cn-n}. Thereby, a_{cn-n} is extracted from eq. (3.42) with the T-matrix calculated as the solution of the integral equation (3.41). In our case, the whole energy region between $S_{1n}^{cn} \approx 5 - 8$ keV and the breakdown scale $S_{\text{deep}} \approx 520$ keV is available for Efimov states in ^{62}Ca. As we see in fig. 3.13 (a), within this region, the scattering length can take any value between $-\infty$ and ∞. When the binding energy of the halo state ^{62}Ca relative to the ^{61}Ca-n threshold vanishes, the scattering length becomes infinite. The additional divergence around ~ 230 keV indicates the appearance of an additional state in the ^{62}Ca spectrum. This signature of Efimov physics is a consequence of the large scattering length in the cn- and nn-subsystems. It is thus conceivable that ^{62}Ca would display an excited Efimov state and unlikely that it would not display any Efimov states. In fig. 3.13 (b), the rescaled scattering length a_{cn-n}/a_{cn} is given for unphysically large energies. The asymptotic discrete scale invariance is clearly recognizable. The approximate scaling factor of ~ 256 is also in agreement with the energy ratio of neighboring deep trimer energies obtained from solving the corresponding bound-state equation (3.44).

As an example for universal correlations in the electromagnetic sector of the ^{62}Ca system, in fig. 3.14 the relative charge radius $\sqrt{\delta\langle r_{\text{E}}^2\rangle}$ is depicted as function of S_{2n}^{cnn}. $\delta\langle r_{\text{E}}^2\rangle$ is determined from eq. (3.67) and diverges for vanishing two-neutron separation energy, as expected. The function is monotonically nonincreasing and diverges for vanishing separation energy. For a deeply bound three-body system, the total charge radius of ^{62}Ca given through eq. (3.68) is expected to be completely dominated by the ^{60}Ca charge radius,

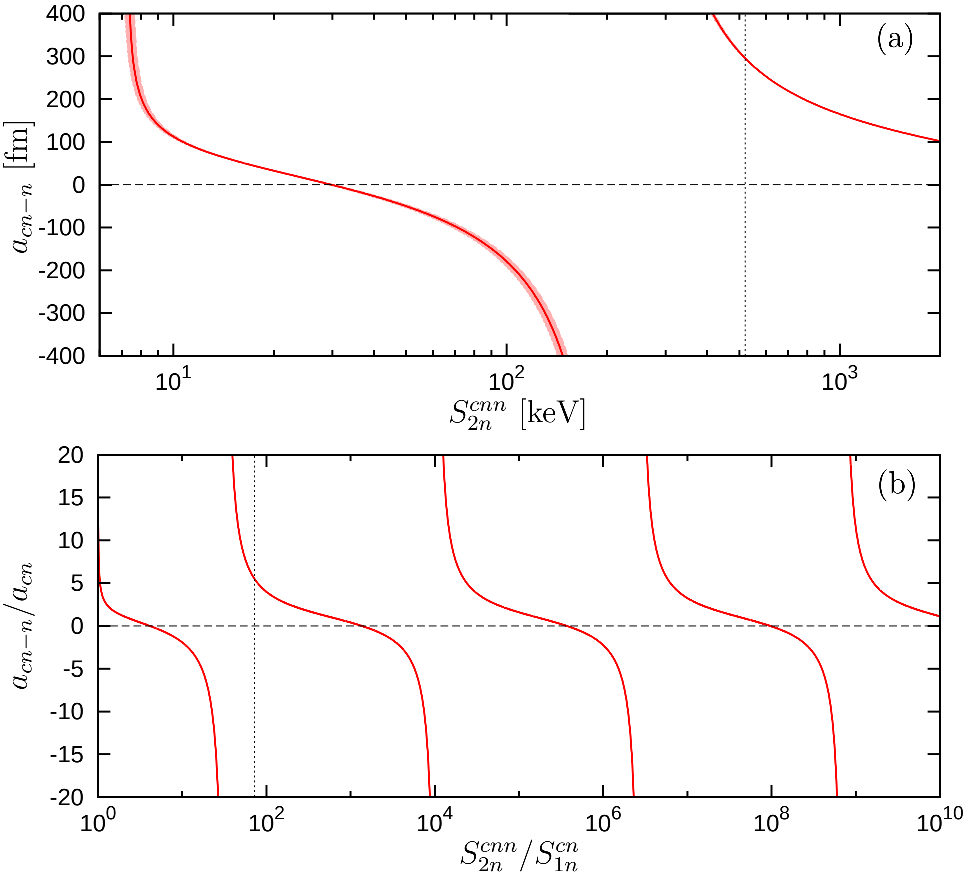

Figure 3.13: The ^{61}Ca-n scattering length a_{cn-n} in the two-neutron halo system ^{62}Ca, with $a_{cn} = 54(1)$ fm. (a) displays a_{cn-n} as a function of the two-neutron separation energy S_{2n}^{cnn} with error bands (shaded regions) (b) gives a dimensionless rescaled version up to unphysically large energies. It displays asymptotic discrete scale invariance with a factors of ~ 256. The breakdown scale $S_{\text{deep}} \approx 520$ keV of theory is represented by the vertical lines.

since at leading order the photon does not couple to the neutrons and $\delta\langle r_{\text{E}}^2\rangle$ vanishes for such binding energies. A summary of the presented results will be given in chapter 4.

3.2.4 Photodisintegration

3.2.4.1 Formalism

In this section, we calculate the photodisintegration amplitude $i\bar{M}^{\gamma}$ of a two-neutron halo nucleus breaking up into its three constituents: the core and the two neutrons. The corresponding Feynman diagram is given in fig. 3.15. We choose the four-momenta for the incoming trimer, the photon, the outgoing core and the two outgoing neutrons to be $\bar{P}$, $\bar{Q}$, $\bar{k}_0$ and $\bar{k}_1$, $\bar{k}_2$, respectively. Four-momentum conservation for those five quantities then

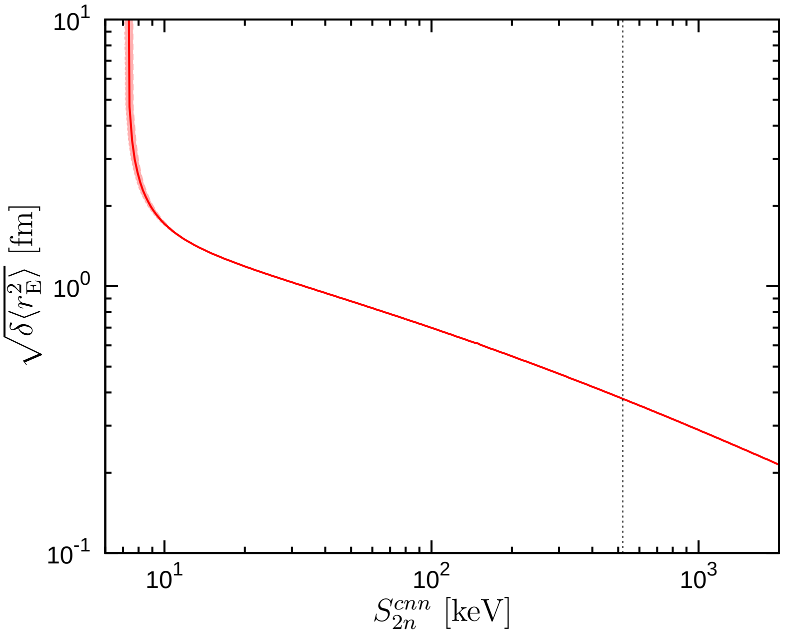

Figure 3.14: The relative charge radius $\sqrt{\delta\langle r_\mathrm{E}^2\rangle}$ of the two-neutron halo system ^{62}Ca as a function of the two-neutron separation energy S_{2n}^{cnn}, with core-neutron scattering length $a_{cn} = 54(1)$ fm. $\sqrt{\delta\langle r_\mathrm{E}^2\rangle}$ diverges as S_{2n}^{cnn} vanishes. The shaded regions are the error bands. The breakdown scale $S_\mathrm{deep} \approx 520$ keV of theory is represented by the vertical line.

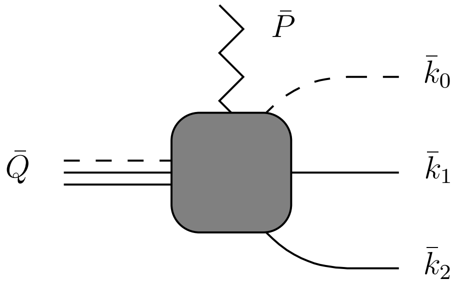

Figure 3.15: Feynman diagram representing the amplitude $i\bar{M}^\gamma$ for a photoinduced breakup of a two-neutron halo system. The incoming and outgoing four-momenta of the trimer and the core and two neutrons are $\bar{P}$ and $\bar{k}_0$ and $\bar{k}_1$, $\bar{k}_2$, respectively. The photon carries four-momentum transfer $\bar{Q} = \bar{K} - \bar{P}$.

yields the relation:

$$\bar{P} + \bar{Q} \;=\; \sum_{i=0}^{2} \bar{k}_i \quad . \tag{3.70}$$

Thus, $i\bar{M}^\gamma$ can effectively be written in terms of only four of the momenta. We choose $\bar{P}$, $\bar{Q}$, $\bar{k}_0$ and $\bar{k}_1$ and use express $\bar{k}_2$ through $\bar{k}_2 = \bar{P} + \bar{Q} - (\bar{k}_0 + \bar{k}_1)$. Furthermore, imposing on-shell conditions for all external particle legs leads to:

$$P^0 \;=\; \frac{\mathbf{P}^2}{2M_\Sigma} + E^{(3)} \quad , \qquad k_i^0 \;=\; \frac{\mathbf{k}_i^2}{2m_i} \quad . \tag{3.71}$$

The total energy in the breakup process then reads:

$$E_\Sigma \;:=\; P^0 + Q^0 \;=\; \sum_{i=0}^{2} \frac{\mathbf{k}_i^2}{2m_i} \qquad \Rightarrow \qquad Q^0 \;=\; E_\Sigma - E^{(3)} - \frac{\mathbf{P}^2}{2M_\Sigma} \quad . \tag{3.72}$$

In order to split up the initial trimer-state, the energy of the photon has to be positive. Thus, in contrast to the form factor calculation in sec. 3.2.2.1, we can not assume Breit-frame kinematics where, by definition, no energy is transferred. Instead, we calculate the process in the center-of-mass frame of the three fragments, which is also the center-of-mass frame of the trimer and the photon:

$$\mathbf{P} + \mathbf{Q} \;=\; 0 \;=\; \sum_{i=0}^{2} \mathbf{k}_i \quad . \tag{3.73}$$

Without loss of generality we furthermore assume that $\mathbf{Q}$ points in 3-direction, implying $\mathbf{Q} = Q\mathbf{e}_3$. We can thus write $\bar{M}^\gamma = \bar{M}^\gamma(E_\Sigma, Q, \mathbf{k}_0, \mathbf{k}_1)$.

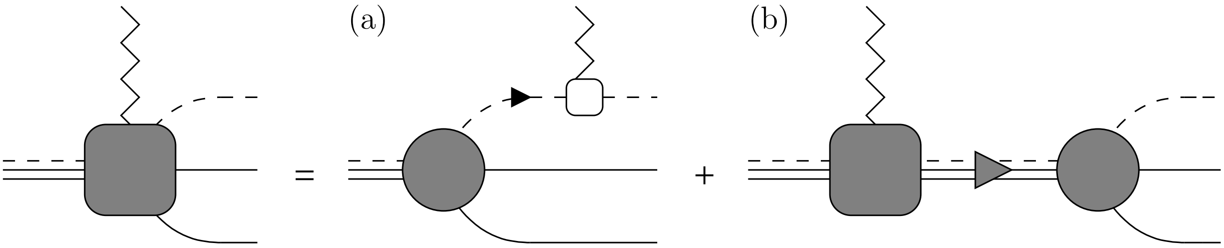

Figure 3.16: Diagrammatic representation of the amplitude $i\bar{M}^\gamma$ for a Coulomb breakup of a two-neutron halo system. The matrix element can be written as the sum of two contributions $i\bar{M}^\gamma = i\bar{M}^{(\mathrm{a})} + i\bar{M}^{(\mathrm{b})}$, where $i\bar{M}^{(\mathrm{a})}$ and $i\bar{M}^{(\mathrm{b})}$ exactly include all Feynman diagrams without and with c-n FSI, respectively. In both contributions the trimer-irreducible trimer-three-particle coupling $i\bar{M}$ appears, which is depicted in fig. 3.6. $i\bar{M}^{(\mathrm{b})}$ also contains the trimer-irreducible coupling of a trimer field to an external electric source as well as a full trimer propagator. They are given in figs. 3.9 and 3.5, respectively

Based on the appearing couplings in the Lagrangian (3.62), the photodisintegration process can be expressed in terms of the Feynman diagrams in fig. 3.16. All the graphs that contribute to the full amplitude $i\bar{M}^\gamma$ can be arranged into two classes. The first one $i\bar{M}^{(\mathrm{a})}$ represents the sum of all diagrams without *c-n final state interactions* (FSI), whereas the second one $i\bar{M}^{(\mathrm{b})}$ collects all graphs with those interactions. Note that the appearance of the irreducible trimer-three-particle coupling $i\bar{M}$ from fig. 3.6 leads to the fact that both $i\bar{M}^{(\mathrm{a})}$ as well as $i\bar{M}^{(\mathrm{b})}$ include diagrams with n-n FSI. As we see, in addition, $i\bar{M}^{(\mathrm{b})}$ contains the full trimer propagator from fig. 3.5 as well as the irreducible coupling of a trimer field to an external electric source. An equation for the latter object in terms of Feynman graphs was already given in fig. 3.9 where it was decomposed into three classes of terms. However, the corresponding calculations presented in sec. 3.2.2.1 (and especially in sec. D.3.4) are only valid in the Breit frame. Assuming center-of-mass kinematics (3.70)-(3.73), would greatly complicate many of the performed steps. For instance, if no further approximations are made, the two full dimer propagators in the loop contribution in fig. D.8 would have poles in the loop-momentum on two shifted but intersecting spheres in $\mathbb{R}^3$. An analytic calculation of this integral analogue to the Breit frame approach appears very involved. On the other hand, an alternative numerical evaluation seems to be very expensive in terms of computation time, since in the relatively large $(\bar{P}, \bar{K})$-parameter space each sampling point would require a point by point evaluation. Therefore, we will from now on drop all contributions with c-n FSI and only consider the first term $i\bar{M}^{(\mathrm{a})}$.

Dipole matrix elements: In a real scattering experiment, often the so-called *dipole strength* B(E1) is measured, which is the modulus squared of the dipole contribution to the photodisintegration matrix element. In a quantum mechanical calculation such a contribution can be obtained by inserting an electric dipole operator between the considered initial and final states (see e.g. ref. [113, 114]). In our kinematics, the dipole operator has the form $|\hat{\mathbf{r}}|Y_{10}(\hat{\mathbf{e_r}})$, where the spherical harmonic reads $Y_{10}(\mathbf{e_r}) = \sqrt{3/(4\pi)}\cos\theta_r$. In order to extract the dipole contribution within our quantum field theoretical framework, we follow a method that was recently used in ref. [84] for the determination of the B(E1) strength for the photodisintegration of the one-neutron halo nucleus ^{11}Be. Our calculation represents a generalization of the used method to two-neutron halo nuclei. Thereby, the dipole matrix element can effectively can be calculated from the full matrix element as $\sqrt{3/(4\pi)}$ times the coefficient in front of the term that is linear in Q. The additional factor is required in order to match with the mentioned dipole operator definition. Thus, the dipole matrix element reads:

$$\bar{M}^{(\mathrm{a})}_{E1}(E_\Sigma, \mathbf{k}_0, \mathbf{k}_1) \;=\; \sqrt{3/(4\pi)} \cdot (\partial_Q \bar{M}^{(\mathrm{a})})(E_\Sigma, 0, \mathbf{k}_0, \mathbf{k}_1) \quad . \tag{3.74}$$

Performing an integration over the remaining final state momenta then yields the corresponding dipole strength distribution:

$$\begin{aligned} \frac{\mathrm{dB(E1)}}{\mathrm{d}E_\Sigma} \;=\; & \int \frac{\mathrm{d}^3\mathbf{k}_0}{(2\pi)^3} \int \frac{\mathrm{d}^3\mathbf{k}_1}{(2\pi)^3} \left|\bar{M}^{(\mathrm{a})}_{E1}(E_\Sigma, \mathbf{k}_0, \mathbf{k}_1)\right|^2 \\ & \times\; \delta\Big(\frac{\mathbf{k}_0^2}{2m_0} + \frac{\mathbf{k}_1^2}{2m_1} + \frac{(\mathbf{k}_0+\mathbf{k}_1)^2}{2m_1} - E_\Sigma\Big) \quad . \end{aligned} \tag{3.75}$$

In terms of kinematic variables, $\mathrm{dB(E1)}/\mathrm{d}E_\Sigma$ only depends on the total energy E_Σ. An explicit formula is given in eq. (D.84) in sec. D.3.5 in the appendix. The required extraction of the linear term and the momentum integration of final state can be found in secs. D.3.5.1 and D.3.5.2, respectively. With regard to the numerical determination of $\mathrm{dB(E1)}/\mathrm{d}E_\Sigma$, the integral kernel in eq. (D.84) has adverse properties. In sec. B we explain how the resulting numerical problems can be controlled within our calculation.

3.2.4.2 First results

We are now in the position to calculate the dipole contribution to the photodisintegration of concrete two-neutron halo nuclei, where all *c*-*n* FSI are neglected. Again, we apply our model to the isotopes ^{11}Li, ^{14}Be and ^{22}C that were already discussed in sec. 3.2.2.2 in the context of form factors and charge radii. We transfer the discussion of the dominant errors in these systems from this analysis. Required input parameters are again taken from tab. 3.1.

In fig. 3.17, dipole strength distributions calculated from eq. (3.75) are depicted as functions of the total energy E_Σ. For ^{11}Li and ^{14}Be, the estimated errors from higher orders in the effective theory expansion dominate and are given by the shaded bands. For ^{22}C, the shaded region originates from varying the binding energies within their errors, where, due

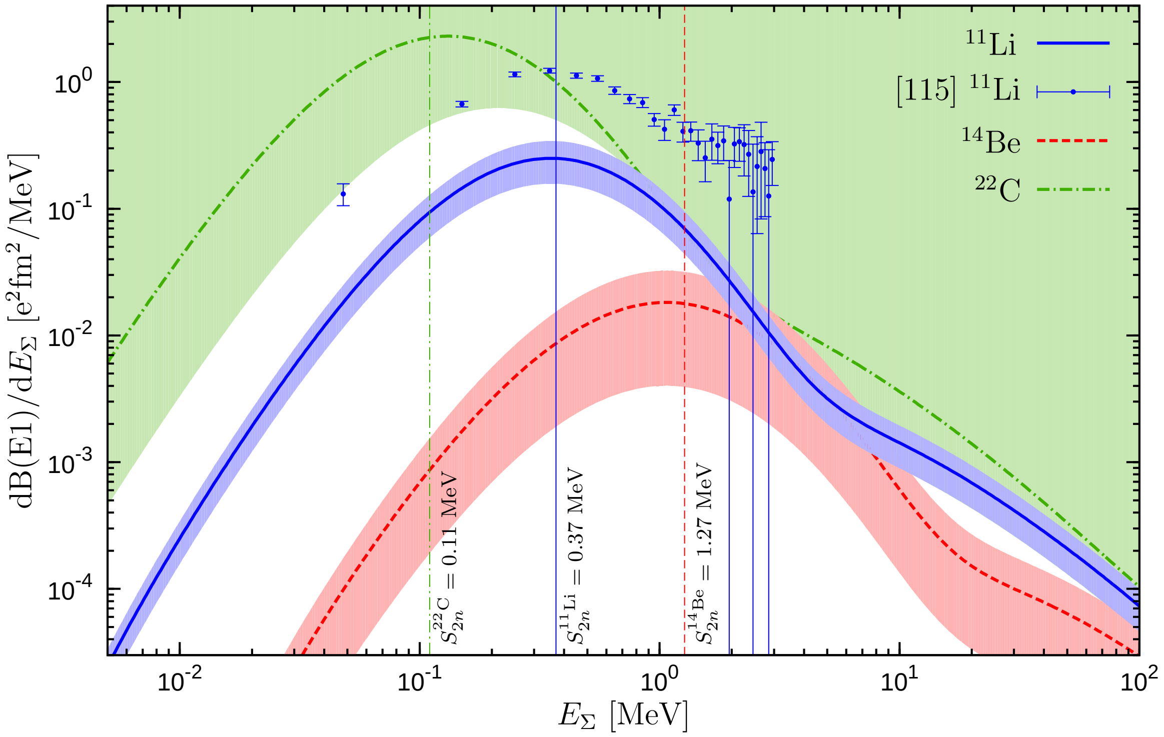

Figure 3.17: The dipole strength distribution $\mathrm{dB(E1)}/\mathrm{d}E_\Sigma$ as function of the total energy E_Σ for the halo nuclei ^{11}Li, ^{14}Be and ^{22}C (blue solid line, red long-dashed line and green dash dotted line). The data points for ^{11}Li are extracted from ref. [115]. Shaded bands are the errors. For ^{11}Li and ^{14}Be, they are the estimated theory errors from higher order contributions. For ^{22}C, the band originates from varying the experimentally determined separation energies within their uncertainties. The vertical lines represent the two-neutron separation energies.

to the large uncertainties, also $S_{1n}^{cn} \to S_{2n}^{cnn}$ can not be excluded. In this limit, $\mathrm{dB(E1)}/\mathrm{d}E_\Sigma$ diverges. For $E_\Sigma \to 0^+$ or $E_\Sigma \to \infty$, the dipole strength distribution formally vanishes. However, we have to keep in mind that our model with three structureless particles can only be valid in low-energy regime. For all three isotopes, $\mathrm{dB(E1)}/\mathrm{d}E_\Sigma$ peaks near the corresponding two-neutron separation energy. However, the exact functional dependency seems to be nontrivial.

The dipole strength of ^{11}Li has been measured at the RIPS [116] facility at RIKEN. Thereby, the required ^{11}Li beam was produced from the fragmentation of a ^{18}O primary beam with 100 MeV/nucleon. We extracted the corresponding data for the dipole strength in ^{11}Li from ref. [115]. The resultant data points are also given in fig. 3.17. The analysis in ref. [115] is based on the assumption that the two-neutron separation energy of the halo system is $S_{2n}^{^{11}\mathrm{Li}} = 0.3$ MeV, which is $\sim 20\%$ smaller than our value 0.37 MeV. However, the author of ref. [115] states that, for the latter case, the dipole strength is enhanced by only 6%, which can be neglected compared to our error estimate of $\sim 40\%$ from the expansion parameter. Although the peak position and the shape of our curve and the data set are compatible, our EFT result clearly underestimates the measured data points by roughly a factor of 5. Since previous studies [113–115] indicated that neglecting parts of the FSI typically leads to an underestimation of the dipole strength, we expect a full calculation that includes the second contribution in fig. 3.16 to describe the data better. A calculation of the corresponding matrix element $i\bar{M}^{(\mathrm{b})}$ remains future work [117]. A summary of the presented results can be found in chapter 4.

Chapter 4

Summary and outlook

In this thesis, we applied non-relativistic EFT with large scattering length to halo nuclei. We investigated phenomena and calculated observables in the strong as well as in the electromagnetic sector.

In chapter 2, we investigated the possibility of discrete scale invariance and the Efimov effect in a three-body system with resonant two-particle P-wave interactions. We started our analysis on the Lagrangian level in eq. (2.18) and demonstrated, how such a theory can equivalently be rewritten via the introduction of P-wave auxiliary dimer fields. The two-body problem can be renormalized using low-energy parameters from the effective range expansion (see eq. (2.26)). Thereby, negative effective ranges can only be obtained by introducing non-normalizable ghost fields. The structure of the resulting full dimer propagator was analyzed with a method that can also be extended to higher partial waves. For P-wave interactions, a physical shallow dimer only appears for $r < 0$ and $1/a \in (0, |r|^2/58)$. However, in this case also an unphysical deep dimer with negative residue emerges, limiting the region of applicability in the two-body sector to energies $E \gg -|r^2|/(18\mu)$.

With respect to the three-body problem in our P-wave model, we considered a system of two identical particles ψ_1 resonantly interacting with a third one ψ_0. We set up a matrix integral equation for the T-matrix of dimer-particle scattering, where the coupling of spin and orbital angular momenta lead to a decoupling of different J^P channels. A semi-analytic approach using Mellin transforms identified all channels exhibiting discrete scale invariance. For ψ_1 being fermions, those are $J^P \in \{0^+, 1^+, 1^-, 2^+\}$. For bosonic ψ_1 fields, $J^P = 1^+$ is the only such channel. In all five cases, we calculated the discrete scaling factor λ_0 as function of the mass ratio $A = m_0/m_1$ (see fig. 2.8). These channels require renormalization, e.g. by adding appropriate cut-off dependent three-body coupling term to the Lagrangian. Numerically solving the three-body bound-state equation yielded an approximate Efimov spectrum, which in the unitary limit is exact. The occurrence of the Efimov effect in the P-wave sector might also add insight into a general classification of all three-body systems that display the Efimov effect. The results from the semi-analytic approach were confirmed, providing a positive consistency check. The used methodology can also be transferred to other configurations.

Unfortunately, the discovered Efimov effect seems to be of purely mathematical nature.

First of all, causality bounds exclude the realization of the unitary limit by imposing $r < 0$. For a negative effective range, however, trimer energies always lie below the mentioned unphysical deep dimer state. A corresponding bound-state spectrum is depicted in fig. 2.10. The physical shallow dimer only exists for $1/a \in (0, |r|^2/58)$. Thus, our theory is only suited to describe dimer-particle scattering in this parameter region and only for energies $E \gg -|r^2|/(18\mu)$ around threshold. Consequently, a Lagrangian of type (2.18) with two-particle P-wave interactions can not generate physical three-body bound states in our formalism. This, in addition, also prevents a proper renormalization of those channels in the three-body sector that exhibit discrete scale invariance. We discussed several possible remedies to this problem. A promising one might be that the stable Efimov trimers below the unphysical deep dimer survive as unstable resonances in the region between the deep and the shallow dimer. However, such resonances probably will not display discrete scale invariance, but, in principle, they could be used for the renormalization of the three-body sector. The required generalization of our formalism to complex binding energies implies major extensions of the applied numerical methods and is left for future work. Since the spurious deep dimer state completely originates from the structure of the full dimer propagator in the two-body problem, another reasonable approach would be to modify the form of this propagator in a suitable way. Obviously, simply including interaction terms and effective range parameters of higher orders would only increase the number of spurious poles and thus compound the problem. However, one can argue that for small binding momenta, the unitary cubic term can be neglected. While the resulting trimer spectrum is free of spurious dimers, there are severe drawbacks of this approach. First of all, unitarity is lost. Furthermore, the trimer spectrum does not display discrete scale invariance or an Efimov effect anymore, since the modified asymptotic behavior of the full P-wave dimer propagator significantly changes the structure of the T-matrix equation. Consequently, without further modifications, the Efimov effect seems to be impossible for P-wave interactions. This was also recently predicted by Nishida and Son in a different formalism using scale dimension arguments for local operators [118]. Moreover, our P-wave Lagrangian combined with the applied power counting scheme can not generate physical three-body bound states. Our results hold for general bosonic three-body systems as well as halo nuclei such as ^{6}He.

In chapter 3, we then set up an EFT framework for two-neutron halo nuclei with resonant S-wave interactions, meaning that the cn and nn S-wave scattering lengths are much larger than the range of the interaction. We introduced auxiliary dimer and trimer fields in the Lagrangian (3.1) and calculated the two- and three-body problem in the strong sector. Thereby, the renormalization of the trimer propagator and the extraction of the trimer wave function renormalization were discussed in detail. Performing minimal coupling, we extended our formalism to the electromagnetic sector in order to describe the electromagnetic structure of two-neutron halo nuclei.

With regard to physical observables, we chose Breit frame kinematics and first calculated the charge form factor and the electric charge radius of such halo systems to leading order in the expansion in $R_{\text{core}}/R_{\text{halo}}$. The charge form factor receives contributions from three different classes of diagrams. They are illustrated in fig. 3.9. In all three contributions, the irreducible trimer-dimer-particle coupling from eq. (3.53) appears naturally. Our calculation provides the correct normalization of the charge form factor at vanishing momentum transfer $\mathcal{F}_{\mathrm{E}}(0) = 1$, as it is required by current conservation. Numerically, we find deviations from unity to be less than 10^{-5}. We then applied our formalism to the known and suspected light halo nuclei ^{11}Li, ^{14}Be and ^{22}C and discussed the dominant error contributions. The resulting charge radii are $\delta\langle r_{\mathrm{E}}^2\rangle_{^{11}\mathrm{Li}} = 1.68(62)$ fm^2, $\delta\langle r_{\mathrm{E}}^2\rangle_{^{14}\mathrm{Be}} = 0.41(32)$ fm^2 and $\delta\langle r_{\mathrm{E}}^2\rangle_{^{22}\mathrm{C}} = 1.66^{+\infty}_{-0.49}$ fm^2. For ^{11}Li, a comparison with the measured value 1.171(120) fm^2 shows good agreement within the $\sim 40\%$ uncertainty originating from the expansion parameter of our leading order calculation. The other charge radii are true predictions that can be compared to future experiments. For a more quantitative comparison with experiment, the extension to higher orders is clearly required. This includes the treatment of effective range effects [80, 93, 95]. An inclusion of P-wave interactions for ^{11}Li and ^{14}Be would require a proper treatment of the above-discussed problems related to three-body systems with resonant P-wave interactions. To date, electron scattering experiments which would give access to the charge form factor have not been carried out. Such experiments are planned at FAIR (ELISe) [119]. However, ELISe is not part of the start version of FAIR and corresponding experiments are far in the future.

Derived formulas in the strong and the electromagnetic sector were then used in order to calculate universal correlations in two-neutron halo systems. First, we analyzed the dependence of the charge radius on the core mass and the separation energies S_{2n}^{cnn} and S_{1n}^{cn}. Our results are summarized in figs. 3.11 and 3.12. As expected, the charge radius decreases with increasing core radius. However, the exact dependence for large core masses deviates from a simple $1/m_c$ dependence. Moreover, the charge radius increases as the energies $S_{2n}^{cnn} - S_{1n}^{cn}$ and S_{2n}^{cnn} decrease. In particular, we found a sudden increase of the charge radius along the line $S_{1n}^{cn} = 0$ where the three-body system becomes Borromean. A better understanding of these characteristics will require further studies. We then investigated universal features of the heavy two-neutron halo candidate ^{62}Ca. Thereby, required values for model input parameters were borrowed from an analysis of ^{60}Ca-n phase shift data generated by coupled-cluster methods. This analysis indicated that the ^{60}Ca-n scattering length is positive and about 6 times larger than the effective range, justifying the applicability of our framework. In fig. 3.13, we gave the ^{61}Ca-n scattering length as a function of the two-neutron separation energy S_{2n}^{cnn}, revealing discrete scale invariance. From considerations based on the corresponding scaling factor of this system and the breakdown scale of our halo EFT, we conclude that two Efimov states are possible in the ^{62}Ca system and that it is unlikely that this system possesses no bound state, i.e. is unbound. In addition, in fig. 3.14, we gave the dependence of the relative charge radius $\delta\langle r_{\mathrm{E}}^2\rangle$ as function of S_{2n}^{cnn}. As expected, $\delta\langle r_{\mathrm{E}}^2\rangle$ diverges (vanishes) for vanishing (diverging) three-body binding energy. Measurements of these observables will clearly pose a significant challenge for experiment. For example, ^{58}Ca is the heaviest Calcium isotope that has been observed experimentally [120]. However, the planned FRIB might provide access to calcium isotopes as heavy as ^{68}Ca and thereby facilitate a test of our results [121].

Finally, we also derived formulas for the dipole strength in the Coulomb dissociation of a two-neutron halo nucleus into its three fragments. The corresponding matrix element is illustrated in fig. 3.16 in terms of Feynman diagrams. It contains contributions from two different classes of diagrams, namely those without and those with c-n final state pair-interactions. A halo EFT calculation of the latter part requires the determination of the irreducible photon-trimer coupling depicted in fig. 3.9 in the center-of-mass frame of the three fragments. Since such a calculation is far from being straightforward, in this work, we only considered the first-mentioned part. Analogue to the form factor calculation, we applied our framework to ^{11}Li, ^{14}Be and ^{22}C using the same input parameters and error estimates. The results for $\mathrm{dB(E1)}/\mathrm{d}E_\Sigma$ as a function of the total energy E_Σ are depicted in fig. 3.17. $\mathrm{dB(E1)}/\mathrm{d}E_\Sigma$ approximately peaks at the two-neutron separation energy of the halo system. In accordance with previous theoretical predictions that neglected some of the FSI, our results for ^{11}Li underestimate experimental data that was measured at the RIPS facility at RIKEN. Thus, a consistent calculation including all final state interactions is clearly needed [117]. Again, an extension to higher order effects such as effective range corrections would contribute to a more quantitative halo EFT analysis of the considered nuclei.

Appendix A

Kernel analytics

A.1 Structure of the full dimer propagator

In this section, we investigate the structure of the full dimer propagator and its singularities. The challenge is to systematically understand the behavior of its poles and residues in dependence of the scattering parameters. We perform our analysis in a rather elaborate and formal approach. In this way, it can be easily applied to a large class of two-particle interactions.

A.1.1 Pole geometry

We start our analysis by assuming that the inverse of the full dimer propagator $D(\mathbf{p})$ with four-momentum $\bar{p}$ is a polynomial in

$$y_i(\bar{p}) = \sqrt{2\mu_i\Big(p^0 - \frac{\mathbf{p}^2}{2M_i} + i\varepsilon\Big)} \quad . \tag{A.1}$$

This requirement is fulfilled for all theories considered in this work (see eq. (2.27) and eq. (3.14)). For ease of notation, from now on, we drop the particle type indices and simply write $y = y_i(\bar{p})$. First, we define a polynomial of degree N with its $N+1$ complex coefficients $\{\alpha_0, \ldots \alpha_N\}$ as

$$\begin{aligned} P_{N,\vec{\alpha}}(y) \ &:= \ \sum_{n=0}^{N} \alpha_n \, y^n \ = \ \alpha_N \prod_{n=0}^{N-1} (y - y_n) \quad , \\ P_{N,\vec{\alpha},0} \ &:= \ \{\, y \in \mathbb{C} \,|\, P_{N,\vec{\alpha}}(y) = 0 \,\} \ = \ \{y_0, \ldots, y_{N-1}\} \ \subset \ \mathbb{C} \quad . \end{aligned} \tag{A.2}$$

The set $P_{N,\vec{\alpha},0}$ is composed of the N complex zeros of the polynomial. Assuming that all these roots are pairwise distinct, a partial fraction decomposition can then be performed according to:

$$\frac{1}{P_{N,\vec{\alpha}}(y)} \ = \ \sum_{n=0}^{N-1} \frac{1/C_n}{y - y_n} \quad , \qquad C_n \ := \ \alpha_N \prod_{n \neq m=0}^{N-1} (y_n - y_m) \ \in \ \mathbb{C} \quad . \tag{A.3}$$

The derivative of the polynomial reads:

$$(\partial_y P_{N,\vec{\alpha}})(y) \;=\; \sum_{n=1}^{N} \alpha_n \, n \, y^{n-1} \;=\; \sum_{n=0}^{N-1} (n+1)\, \alpha_{n+1} \, y^n \;=\; P_{N-1,A\vec{\alpha}}(y) \quad , \tag{A.4}$$

where $A_{nm} := (n+1)\delta_{n+1,m}$. On the other hand, we can also use the product rule in order to determine the derivative:

$$(\partial_y P_{N,\vec{\alpha}})(y) \;=\; \alpha_N \Big[\prod_{n \neq m = 0}^{N-1} (y - y_m) \;+\; (y - y_n)\, \partial_y \prod_{n \neq m = 0}^{N-1} (y - y_m) \Big] \quad . \tag{A.5}$$

This holds for all $n \in \{0, 1, \ldots, N\}$ and leads to the simple relation:

$$(\partial_y P_{N,\vec{\alpha}})(y_n) \;=\; C_n \quad . \tag{A.6}$$

Using the standard branch of the complex root and the formula (A.1), we deduce that $y \in \sqrt{\mathbb{C}} = \{\, z \in \mathbb{C} \,|\, \arg(z) \in (-\pi/2, \pi/2] \,\}$ holds. The poles of the first branch are the physical ones. Poles of the second branch of the complex root $y \in -\sqrt{\mathbb{C}}$ are unphysical. In terms of a complex signum $\operatorname{sgn}(z) := (\operatorname{sgn}(\operatorname{Re}(z)), \operatorname{sgn}(\operatorname{Im}(z))) \in \sigma^2$ with $\sigma := \{-, 0, +\}$, we can also characterize the two areas by

$$\pm\sqrt{\mathbb{C}} \;=\; \pm\{\, z \in \mathbb{C} \,|\, \operatorname{sgn}(z) \in \{(0,0), (0,+), (+,+), (+,0), (+,-)\} \,\} \quad . \tag{A.7}$$

Thus, we divide the set of complex roots into two disjoint subsets $P_{N,\vec{\alpha},0} = P^{(1)}_{N,\vec{\alpha},0} \cup P^{(2)}_{N,\vec{\alpha},0}$ with $P^{(1)}_{N,\vec{\alpha},0} := P_{N,\vec{\alpha},0} \cap \sqrt{\mathbb{C}}$ and $P^{(2)}_{N,\vec{\alpha},0} := P_{N,\vec{\alpha},0} \cap (-\sqrt{\mathbb{C}})$ corresponding to the 2 branches of the complex root. Introducing a Riemann surface, both branches can be connected and the root becomes bijective. The first and second branch then corresponds to the first and second Riemann sheet, respectively. For a four-momentum pole $\bar{p}$ of the full dimer propagator, $\bar{p} \in y^{-1}(y_n)$ has to be fulfilled, where $y^{-1}(y_n) \subset \mathbb{C}^4$ simply denotes the fiber of the polynomial root y_n. If $y_n \in P^{(2)}_{N,\vec{\alpha},0}$ holds, the fiber is empty.

The residue of a pole can be calculated according to:

$$\begin{aligned} Z_n \;&=\; \left[(\partial_{p^0} D^{-1})(\bar{p})\right]^{-1} \;=\; \left[(\partial_y P_{N,\vec{\alpha}})(y(\bar{p})) \cdot (\partial_{p^0} y)(\bar{p})\right]^{-1} \;=\; \frac{1}{\mu} \frac{y_n}{P_{N-1,A\vec{\alpha}}(y_n)} \\ &=\; \frac{1}{\mu} \frac{y_n}{C_n} \;=\; \frac{1}{\mu\, \alpha_N} \frac{y_n}{\prod_{n \neq m=0}^{N-1} (y_n - y_m)} \;=\; \frac{1}{\mu\, \alpha_N} \frac{1}{y_n^{N-2} \prod_{n \neq m=0}^{N-1} (1 - \frac{y_m}{y_n})} \quad . \end{aligned} \tag{A.8}$$

In order for a pole y_n to be physical with positive residue, the conditions $y_n \in P^{(1)}_{N,\vec{\alpha},0}$ and $Z_n > 0$ have to be fulfilled. In the following concrete examples, we will calculate all poles of the polynomial and check whether these two conditions are satisfied. For the applications in this work, values of scattering parameters will always be chosen such that all poles y_n of the full dimer propagator are pairwise distinct and consequently of first order.

The, in general complex, dimer binding energy $E^{(2)}_n$, corresponding to a pole y_n, reads:

$$E^{(2)}_n \;:=\; \frac{y_n^2}{2\mu} \quad . \tag{A.9}$$

A.1.1.1 S-wave interactions

We now investigate the pole-structure of the renormalized full dimer propagator (2.27) that results from two-particle S-wave interactions:

$$\begin{aligned} D(\bar{p}) \;&=\; -\frac{2\pi}{g^2\mu}\,\frac{1}{-\frac{1}{a}\,+\,\frac{r}{2}\,y^2(\bar{p})\,-\,iy(\bar{p})} \\ &=\; \frac{1}{P_{2,\vec{\alpha}}(y(\bar{p}))} \qquad \text{with} \qquad \vec{\alpha} \;=\; -\frac{g^2\mu}{2\pi}\begin{pmatrix} -1/a \\ -i \\ r/2 \end{pmatrix} \quad . \end{aligned} \tag{A.10}$$

In the last line we used the notation of eq. (A.2) with $N = 2$. In order to find the dimer poles, we have to solve

$$-\frac{1}{a}\,+\,\frac{r}{2}\,y^2\,-\,iy \;=\; 0 \quad , \tag{A.11}$$

where the scattering length a and the effective range r are assumed to be real. We distinguish between two cases:

Vanishing effective range: First, we consider $r = 0$. Then the trivial case $1/a = 0$ has a root at zero. This point in parameter space is the unitary limit. For non-vanishing $1/a$, the only solution is:

$$y_0 \;=\; \frac{i}{a} \qquad \Rightarrow \qquad Z_0 \;=\; -\frac{2\pi}{g^2\mu^2}\frac{y_0}{-i} \;=\; \frac{2\pi}{g^2\mu^2}\frac{1}{a} \quad . \tag{A.12}$$

In tabular tab. A.2 we give the positions of the poles y_n, residues Z_n and binding energies $E_n^{(2)} - i\varepsilon$ from eq. (A.9) in the complex plane.

Non-vanishing effective range: In the case of non-vanishing effective range $r \neq 0$, eq. (A.11) is a quadratic equation. In order to find its solutions, we first define $\frac{i}{r}(x+1) := y$, leading to:

$$\begin{aligned} 0 \;&=\; -\frac{1}{a}\,-\,\frac{1}{2r}(x+1)^2\,+\,\frac{1}{r}(x+1) \\ \Leftrightarrow \quad 0 \;&=\; (x+1)^2 - 2(x+1) + \frac{2r}{a} \;=\; x^2 - \kappa \quad , \quad \kappa \;:=\; 1 - \frac{2r}{a} \in \mathbb{R} \quad . \end{aligned} \tag{A.13}$$

Table A.1: Poles of the full S-wave dimer propagator as solutions of eq. (A.13) and eq. (A.11). The solutions depend on the dimensionless parameter $\kappa = 1 - 2r/a$.

$\kappa \in$	x_0 x_1	y_0 y_1
$(-\infty, 0]$	$i\sqrt{\lvert\kappa\rvert}$ $-i\sqrt{\lvert\kappa\rvert}$	$\frac{1}{r}\big(-\sqrt{\lvert\kappa\rvert} + i\big)$ $\frac{1}{r}\big(\sqrt{\lvert\kappa\rvert} + i\big)$
$[0, \infty)$	$-\sqrt{\kappa}$ $\sqrt{\kappa}$	$\frac{i}{r}\big(-\sqrt{\kappa} + 1\big)$ $\frac{i}{r}\big(\sqrt{\kappa} + 1\big)$

The explicit solutions of eq. (A.13) and eq. (A.11) are collected in tab. A.1, where we also gave values for the corresponding pole positions $y_n = \frac{i}{r}(x+1)$ of the full dimer propagator eq. (A.10). From the pole positions, dimer binding energies can then be determined according to eq. (A.9).

In order to extract the residues, we apply eq. (A.8) in the way

$$Z_n \;=\; \frac{1}{\mu}\,\frac{y_n}{P_{1,A\vec{\alpha}}(y_n)} \;=\; -\frac{2\pi}{g^2\mu^2}\,\frac{y_n}{r y_n - i} \;=\; -\frac{2\pi}{g^2\mu^2}\,\frac{1}{r}\,(1 + 1/x_n) \quad . \tag{A.14}$$

We are now able to read off the positions of the complex poles y_n, residues Z_n and binding energies $E_n^{(2)} - i\varepsilon$. They are summarized in tab. A.2. Parameters that would lead to double poles are left out. There are cases where no poles on the physical sheet appear. If $r = 0$ or if $r < 0$ and $1/a \in (1/(2r), \infty)$ holds, all poles on the physical sheet have positive residue.

$\mathrm{sgn}(y_n)$ $\mathrm{sgn}(Z_n)$ $\mathrm{sgn}(E_n^{(2)} - i\varepsilon)$	$r < 0$			$r = 0$		$r > 0$		
$\kappa \ \in$ $1/a \ \in$	$(-\infty, 0)$ $(-\infty, -\frac{1}{2\vert r\vert})$	$(0, 1)$ $(-\frac{1}{2\vert r\vert}, 0)$	$(1, \infty)$ $(0, \infty)$	 $(0, \infty)$	 $(-\infty, 0)$	$(1, \infty)$ $(-\infty, 0)$	$(0, 1)$ $(0, \frac{1}{2\vert r\vert})$	$(-\infty, 0)$ $(\frac{1}{2\vert r\vert}, \infty)$
$n = 0$	$(+,-)$ (1) $(+,-)$ un $(\sigma,-)$ lo	$(0,-)$ (2) $(-,0)$ un $(-,-)$ lo	$(0,+)$ (1) $(+,0)$ ph $(-,-)$ lo	$(0,+)$ (1) $(+,0)$ ph $(-,-)$ lo	$(0,-)$ (2) $(-,0)$ un $(-,-)$ lo	$(0,-)$ (2) $(-,0)$ un $(-,-)$ lo	$(0,+)$ (1) $(+,0)$ ph $(-,-)$ lo	$(-,+)$ (2) $(-,+)$ un $(\sigma,-)$ lo
$n = 1$	$(-,-)$ (2) $(+,+)$ un $(\sigma,+)$ up	$(0,-)$ (2) $(+,0)$ ph $(-,-)$ lo	$(0,-)$ (2) $(+,0)$ ph $(-,-)$ lo	/ / /	/ / /	$(0,+)$ (1) $(-,0)$ un $(-,-)$ lo	$(0,+)$ (1) $(-,0)$ un $(-,-)$ lo	$(+,+)$ (1) $(-,-)$ un $(\sigma,+)$ up

Table A.2: Positions of poles, residues and binding energies in the complex plane given in terms of $\mathrm{sgn}(y_n)$, $\mathrm{sgn}(Z_n)$ and $\mathrm{sgn}(E_n^{(2)} - i\varepsilon)$, respectively. We used $\kappa = 1 - 2r/a$. The number (1) ((2)) denotes that y_n is located on the physical, first (unphysical, second) Riemann sheet and lo (up) means that the corresponding binding energy $E_n^{(2)} - i\varepsilon$ lies in the upper (lower) complex half plane. A pole with physical (unphysical) residue Z_n is labeled by ph (un). $\sigma = \{-, 0, +\}$ is the set of possible signs. Red columns mark regions in parameter space where poles on the physical sheet with binding energy in the upper complex half plane exist, prohibiting the application of the residue theorem in the derivation of the dimer-particle scattering integral equation. The other column-colors represent parameters where all poles on the first sheet have binding energies in the lower complex half plane. Thereby, white (blue) marks the physical (unphysical) case where all first-sheet poles have positive (non-positive) residue. Yellow represents the mixed case where first-sheet poles with both positive and non-positive residues coexists.

A.1.1.2 P-wave interactions

We now investigate the pole-structure of the renormalized full dimer propagator (2.27) resulting from two-particle P-wave interactions:

$$\begin{aligned} D(\bar{p}) &= -\frac{6\pi}{g^2\mu}\,\frac{1}{-\frac{1}{a}+\frac{r}{2}\,y^2(\bar{p})-iy^3(\bar{p})} \\ &= \frac{1}{P_{3,\vec{\alpha}}(y(\bar{p}))} \qquad \text{with} \qquad \vec{\alpha} = -\frac{g^2\mu}{6\pi}\begin{pmatrix} -1/a \\ 0 \\ r/2 \\ -i \end{pmatrix} \quad . \end{aligned} \tag{A.15}$$

In the last line we used the notation of eq. (A.2) with $N = 3$. In order to find the dimer poles, we have to solve

$$-\frac{1}{a} + \frac{r}{2}y^2 - iy^3 = 0 \quad . \tag{A.16}$$

The scattering volume a and the effective range r are assumed to be real. Again we distinguish between two cases:

Vanishing effective range: First, we consider $r = 0$. Then the trivial case $1/a = 0$ has a triple root at zero. This point in parameter space is the unitary limit. For non-vanishing $1/a$, the solutions are:

$$\begin{aligned} & y_n = \zeta^{-n}\,(-i)\sqrt[3]{1/a} \quad , \quad \zeta := e^{\frac{2\pi i}{3}} \quad , \quad n \in \{0,1,2\} \\ \Rightarrow \quad & Z_n = \frac{1}{\mu\,\alpha_3}\,\frac{1}{y_n\prod_{n\neq m=0}^{2}(1-\frac{y_m}{y_n})} = -\frac{6\pi}{g^2\mu^2}\,\frac{1}{(-i)^2\sqrt[3]{1/a}}\,\frac{\zeta^n}{(1-\zeta)(1-\zeta^*)} \\ & \quad = \frac{6\pi}{g^2\mu^2}\,\frac{\sqrt[3]{a}}{3}\,\zeta^n \quad . \end{aligned} \tag{A.17}$$

In tabular tab. A.4 we give the positions of the poles y_n, residues Z_n and binding energies $E_n^{(2)} - i\varepsilon$ from eq. (A.9) in the complex plane.

Non-vanishing effective range: In the case of non-vanishing effective range $r \neq 0$, the solutions of eq. (A.16) are less obvious. We use the Cardano method in order to find them [122]. Therefore, we first define $i\frac{r}{3}\left(x-\frac{1}{2}\right) := y$, eliminating the quadratic term according to:

$$\begin{aligned} 0 &= -\frac{1}{a} - \left(\frac{r}{3}\right)^3\frac{3}{2}\left(x-\frac{1}{2}\right)^2 - \left(\frac{r}{3}\right)^3\left(x-\frac{1}{2}\right)^3 \\ \Leftrightarrow \quad 0 &= \left(x-\frac{1}{2}\right)^3 + \frac{3}{2}\left(x-\frac{1}{2}\right)^2 + \frac{3^3}{ar^3} = \left(x-\frac{1}{2}\right)^2(x+1) + \frac{27}{ar^3} \\ &= x^3 - \frac{3}{4}x + \frac{1}{4} + \frac{27}{ar^3} = x^3 - \frac{3}{4}x + \frac{\tau}{4} \quad , \quad \tau := 1 + \frac{108}{ar^3} \in \mathbb{R} \quad . \end{aligned} \tag{A.18}$$

Since the coefficients of this polynomial are all real, it follows that if x is a solution, then also x^* is a solution. Consequently, among the at most three different complex solutions

$\vec{x} := (x_0, x_1, x_2)$, at least one has to be real. Another property of the solutions can be derived as follows: Assuming that $x_n(\tau)$ is a solution of eq. (A.18) for τ we deduce

$$(-x_n(\tau))^3 - \frac{3}{4}(-x_n(\tau)) + \frac{1}{4}(-\tau) \;=\; -\left(x_n(\tau)^3 - \frac{3}{4}x_n(\tau) + \frac{1}{4}\tau\right) \;=\; 0 \quad . \tag{A.19}$$

Consequently, $-x_n(\tau)$ is a solution of eq. (A.18) for $-\tau$. Due to this antisymmetry, it suffices to understand the behavior of the poles for $\tau \geq 0$. For $\tau < 0$, we simply use $\vec{x}(\tau) = -\vec{x}(|\tau|)$.

Following the Cardano method, the three concrete solutions of eq. (A.18) can be written in terms of the parametrization:

$$\begin{aligned} \vec{x} \;&=\; \begin{pmatrix} \zeta^0 u_+ + \zeta^0 u_- \\ \zeta^1 u_+ + \zeta^2 u_- \\ \zeta^2 u_+ + \zeta^1 u_- \end{pmatrix} \;=\; \begin{pmatrix} (u_+ + u_-) \\ -\frac{1}{2}(u_+ + u_-) + i\frac{\sqrt{3}}{2}(u_+ - u_-) \\ -\frac{1}{2}(u_+ + u_-) - i\frac{\sqrt{3}}{2}(u_+ - u_-) \end{pmatrix} \\ &\text{with} \quad \zeta \;=\; e^{\frac{2\pi i}{3}} \quad \text{and} \quad u_\pm \;:=\; \frac{1}{2}\sqrt[3]{-\tau \pm \sqrt{\tau^2 - 1}} \\ &\Rightarrow \quad x_0 + x_1 + x_2 \;=\; 0 \quad \text{and} \quad u_+ u_- \;=\; \frac{1}{4} \quad . \end{aligned} \tag{A.20}$$

Thereby, the cube root $\sqrt[3]{z}$ of a complex number z is the unique complex number which is determined by the conditions $(\sqrt[3]{z})^3 = z$ and $\arg(\sqrt[3]{z}) \in [-\pi/6, \pi/6) \cup [5\pi/6, 7\pi/6)$. We now distinguish between two different cases:

- $\tau \in (1, \infty)$: In this case $\chi_\tau := \operatorname{arccosh}(\tau) \in (0, \infty)$ is well-defined and from eq. (A.20) we see that $u_\pm$ is real, since the radicand of the square root is positive. This leads to:

$$\begin{aligned} u_\pm \;&=\; \frac{1}{2}\sqrt[3]{-\cosh\chi_\tau \pm \sqrt{\cosh^2\chi_\tau - 1}} \\ &=\; \frac{1}{2}\sqrt[3]{-(\cosh\chi_\tau \mp \sinh\chi_\tau)} \;=\; \frac{1}{2}\sqrt[3]{-e^{\mp\chi_\tau}} \;=\; -\frac{1}{2}e^{\mp\chi_\tau/3} \\ \Rightarrow\; u_+ \pm u_- \;&=\; -\frac{1}{2}\left(e^{-\chi_\tau/3} \pm e^{\chi_\tau/3}\right) \;=\; \begin{cases} -\cosh(\chi_\tau/3) \\ \sinh(\chi_\tau/3) \end{cases} \\ \Rightarrow\; \vec{x}(\tau) \;&=\; \begin{pmatrix} -\cosh(\chi_\tau/3) \\ \frac{1}{2}\cosh(\chi_\tau/3) + i\frac{\sqrt{3}}{2}\sinh(\chi_\tau/3) \\ \frac{1}{2}\cosh(\chi_\tau/3) - i\frac{\sqrt{3}}{2}\sinh(\chi_\tau/3) \end{pmatrix} \\ \Rightarrow\; \vec{x}(\tau \to \infty) \;&=\; -\sqrt[3]{\frac{\tau}{4}}\begin{pmatrix} 1 \\ \zeta^* \\ \zeta \end{pmatrix} \qquad \text{and} \qquad \vec{x}(\tau \to 1^+) \;=\; \begin{pmatrix} -1 \\ \frac{1}{2} \\ \frac{1}{2} \end{pmatrix} \quad . \end{aligned} \tag{A.21}$$

  Hence, we have a real root $x_0 < 0$ and two complex conjugated roots $x_{1,2}$ in the right half plane. For large values of τ, the 3 roots form an equilateral, centered triangle, which scales with $\sqrt[3]{\tau}$. In the limit $\tau \to 1^+$ the 2 complex conjugated roots meet at the positive real axis.

- $\tau \in (0,1)$: In this case $\phi_\tau := \arccos(\tau) \in (0, \pi/2)$ is well-defined and $u_\pm$ has a non-vanishing imaginary part, since the radicand of the square root in eq. (A.20) is negative. We get:

$$\begin{aligned}
u_\pm &= \frac{1}{2}\sqrt[3]{-(\tau \mp i\sqrt{1-\tau^2})} \;=\; \frac{1}{2}\sqrt[3]{-(\cos\phi_\tau \mp i\sin\phi_\tau)} \\
&= \frac{1}{2}\sqrt[3]{-e^{\mp i\phi_\tau}} \;=\; -\frac{1}{2}e^{\mp i\frac{\phi_\tau}{3}} \\
\Rightarrow\; (u_+ \pm u_-) &= -\frac{1}{2}\left(e^{-i\frac{\phi_\tau}{3}} \pm e^{i\frac{\phi_\tau}{3}}\right) \;=\; \begin{cases} -\cos(\phi_\tau/3) \\ i\sin(\phi_\tau/3) \end{cases} \qquad \text{(A.22)} \\
\Rightarrow\; \vec{x}(\tau) &= \begin{pmatrix} -\cos(\phi_\tau/3) \\ \frac{1}{2}\cos(\phi_\tau/3) - \frac{\sqrt{3}}{2}\sin(\phi_\tau/3) \\ \frac{1}{2}\cos(\phi_\tau/3) + \frac{\sqrt{3}}{2}\sin(\phi_\tau/3) \end{pmatrix} \;=\; \begin{pmatrix} -\cos(\phi_\tau/3) \\ \cos((\pi+\phi_\tau)/3) \\ \cos((\pi-\phi_\tau)/3) \end{pmatrix} \\
\Rightarrow\; \vec{x}(\tau \to 1^-) &= \begin{pmatrix} -1 \\ \frac{1}{2} \\ \frac{1}{2} \end{pmatrix} \quad \text{and} \quad \vec{x}(\tau \to 0^+) \;=\; \begin{pmatrix} -\frac{\sqrt{3}}{2} \\ 0 \\ \frac{\sqrt{3}}{2} \end{pmatrix} \quad ,
\end{aligned}$$

where $\cos(\pi/3) = 1/2$, $\sin(\pi/3) = \sqrt{3}/2$ and standard addition and subtraction theorems for trigonometric functions were used.

$\tau \in$	x_0 x_1 x_2	y_0 y_1 y_2
$(-\infty, -1]$	$-\frac{1}{2}\cosh(\chi_{\lvert\tau\rvert}/3) + i\frac{\sqrt{3}}{2}\sinh(\chi_{\lvert\tau\rvert}/3)$ $-\frac{1}{2}\cosh(\chi_{\lvert\tau\rvert}/3) - i\frac{\sqrt{3}}{2}\sinh(\chi_{\lvert\tau\rvert}/3)$ $\cosh(\chi_{\lvert\tau\rvert}/3)$	$\frac{r}{3}(-\frac{\sqrt{3}}{2}\sinh(\chi_{\lvert\tau\rvert}/3) - \frac{i}{2}(\cosh(\chi_{\lvert\tau\rvert}/3) + 1))$ $\frac{r}{3}(\frac{\sqrt{3}}{2}\sinh(\chi_{\lvert\tau\rvert}/3) - \frac{i}{2}(\cosh(\chi_{\lvert\tau\rvert}/3) + 1))$ $\frac{r}{3}\,i(\cosh(\chi_{\lvert\tau\rvert}/3) - \frac{1}{2})$
$[-1, 0]$	$-\cos((\pi - \phi_{\lvert\tau\rvert})/3)$ $-\cos((\pi + \phi_{\lvert\tau\rvert})/3)$ $\cos(\phi_{\lvert\tau\rvert}/3)$	$\frac{r}{3}\,i(-\cos((\pi - \phi_{\lvert\tau\rvert})/3) - \frac{1}{2})$ $\frac{r}{3}\,i(-\cos((\pi + \phi_{\lvert\tau\rvert})/3) - \frac{1}{2})$ $\frac{r}{3}\,i(\cos(\phi_{\lvert\tau\rvert}/3) - \frac{1}{2})$
$[0, 1]$	$-\cos(\phi_\tau/3)$ $\cos((\pi + \phi_\tau)/3)$ $\cos((\pi - \phi_\tau)/3)$	$\frac{r}{3}\,i(-\cos(\phi_\tau/3) - \frac{1}{2})$ $\frac{r}{3}\,i(\cos((\pi + \phi_\tau)/3) - \frac{1}{2})$ $\frac{r}{3}\,i(\cos((\pi - \phi_\tau)/3) - \frac{1}{2})$
$[1, \infty)$	$-\cosh(\chi_\tau/3)$ $\frac{1}{2}\cosh(\chi_\tau/3) + i\frac{\sqrt{3}}{2}\sinh(\chi_\tau/3)$ $\frac{1}{2}\cosh(\chi_\tau/3) - i\frac{\sqrt{3}}{2}\sinh(\chi_\tau/3)$	$\frac{r}{3}\,i(-\cosh(\chi_\tau/3) - \frac{1}{2})$ $\frac{r}{3}(-\frac{\sqrt{3}}{2}\sinh(\chi_\tau/3) + \frac{i}{2}(\cosh(\chi_\tau/3) - 1))$ $\frac{r}{3}(\frac{\sqrt{3}}{2}\sinh(\chi_\tau/3) + \frac{i}{2}(\cosh(\chi_\tau/3) - 1))$

Table A.3: Solutions of eq. (A.18) and eq. (A.16) depending on the parameter $\tau = 1 + \frac{108}{ar^3}$. The quantities χ and ϕ depend on τ and are given through $\chi_\tau = \operatorname{arccosh}(\tau) \in (0, \infty)$ and $\phi_\tau = \arccos(\tau) \in (0, \pi/2)$.

As expected, the vector $\vec{x}$ of the three complex roots continuously depends on the parameter $\tau \geq 0$. Using the antisymmetry derived in eq. (A.19), we expand this continuity to all $\tau \in \mathbb{R}$ by relabeling $x_0 \leftrightarrow x_2$ for $\tau \leq 0$. In fig. A.1 we illustrate how the roots are traveling through the complex plane dependent on the effective range parameters. Explicit expressions are collected in tab. A.3, where we also gave values for the corresponding pole

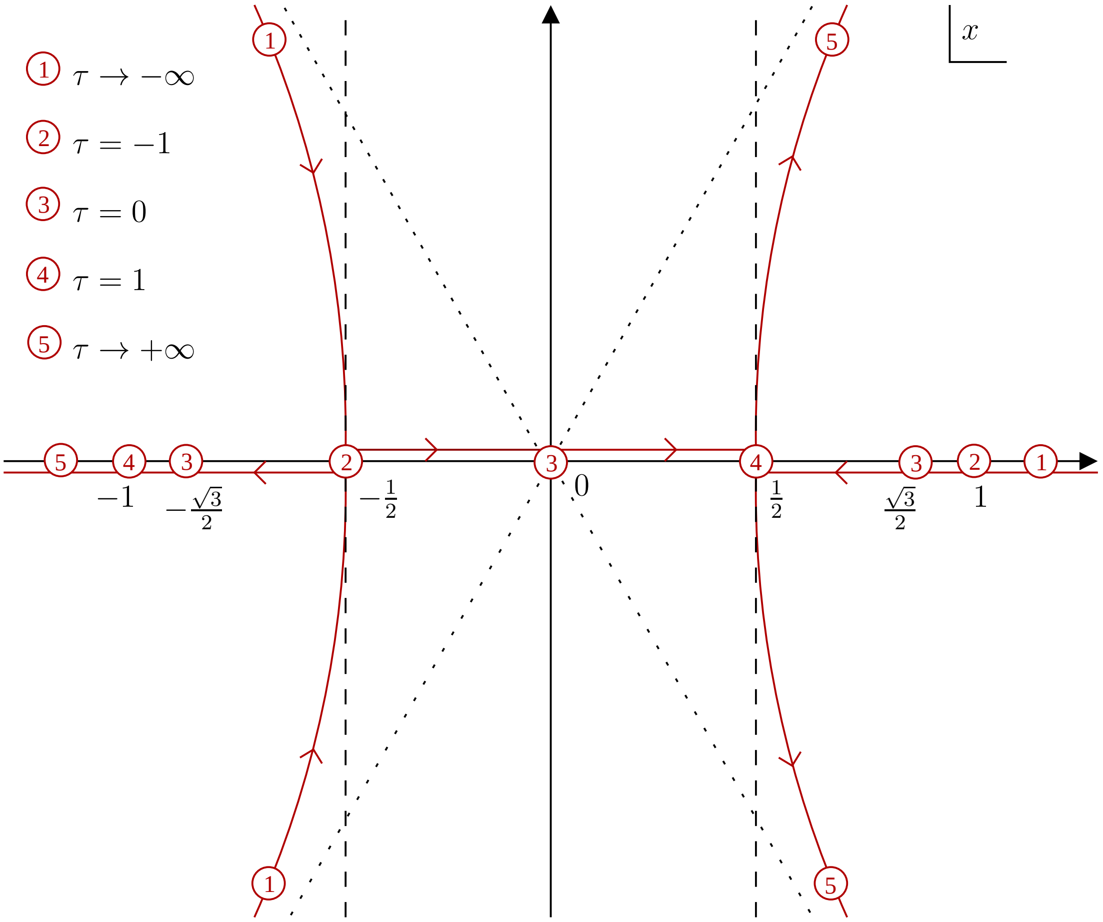

Figure A.1: Positions of the three complex roots of eq. (A.18) as a function of the parameter $\tau = 1 + \frac{108}{ar^3} \in \mathbb{R}$. The dashed lines located at $\mathrm{Re}(x) = \pm 1/2$ are useful in order to determine the positions of the corresponding poles y and their residues Z. The dotted lines at $\mathrm{Im}(x) = \pm\sqrt{3}\mathrm{Re}(x)$ indicate the asymptotic trajectories of the poles for diverging τ.

positions $y_n = i\frac{r}{3}\left(x_n - \frac{1}{2}\right)$ of the full dimer propagator (A.15). From the pole positions, the dimer binding energies are again determined via eq. (A.9).

In order to extract the residues, we apply eq. (A.8) in the way:

$$Z_n = \frac{1}{\mu}\frac{y_n}{P_{2,A\vec{\alpha}}(y_n)} = -\frac{6\pi}{g^2\mu^2}\frac{y_n}{ry_n - i3y_n^2} = -\frac{6\pi}{g^2\mu^2}\frac{1}{r}\frac{1}{x_n + \frac{1}{2}} \quad . \tag{A.23}$$

Using the scheme in fig. A.1, we are now able to read off the positions of the complex poles y_n, residues Z_n and binding energies $E_n^{(2)} - i\varepsilon$. They are summarized in tab. A.4, where, due to double poles at $\tau = \pm 1$, these particular parameter values are left out. A comparison with the S-wave results from tab. A.2 reveals striking differences. Unlike for S-wave interactions, there are always one or two poles on the first Riemann sheet. However, only for parameters $r < 0$ and $1/a \in (0, \frac{|r|^3}{54})$ (yellow column) one of them has positive residue, namely y_1. Nevertheless, in this case there is also a second pole y_0 on the physical sheet, which has negative residue and has a deeper binding energy. Thus, there is no configuration of effective range parameters where all poles on the physical sheet have positive residue.

In the derivation of the integral equation for dimer-particle scattering, the residue theorem was applied in order to perform the energy integral of the loop momentum. Therefore, it is crucial to understand, under which circumstances the binding energies $E_n^{(2)} - i\varepsilon$ of all first-sheet poles lie in the lower complex half plane, no matter what their residues are. Considering the results in tab. A.4, this is exactly the case if the parameters obey $(r = 0) \wedge (1/a < 0)$ or $(r < 0) \wedge (\tau \in (-1, 1) \cup (1, \infty))$ or $(r > 0) \wedge (\tau \in (-\infty, -1) \cup (-1, 1))$ (yellow and blue columns in tab. A.4). In terms of the scattering volume, all these cases can be combined as: $-1/a \in (\max\{0, r^3/54\}, \infty) \setminus \max\{0, r^3/54\}$. The omitted point $\max\{0, r^3/54\}$ represents configurations with unphysical poles of second order. For scattering parameters outside this region, the integral equation for dimer particle scattering is obtained by analytic continuation (red columns in tab. A.4).

$\mathrm{sgn}(y_n)$ $\mathrm{sgn}(Z_n)$ $\mathrm{sgn}(E_n^{(2)}-i\varepsilon)$	$r<0$			$r=0$		$r>0$		
$\tau\ \in$ $-1/a\ \in$	🟥 $(-\infty,-1)$ $(-\infty,-\frac{\lvert r\rvert^3}{54})$	🟨 $(-1,1)$ $(-\frac{\lvert r\rvert^3}{54},0)$	🟦 $(1,\infty)$ $(0,\infty)$	🟦 $(0,\infty)$	🟥 $(-\infty,0)$	🟥 $(1,\infty)$ $(-\infty,0)$	🟦 $(-1,1)$ $(0,\frac{\lvert r\rvert^3}{54})$	🟦 $(-\infty,-1)$ $(\frac{\lvert r\rvert^3}{54},\infty)$
$n=0$	$(+,+)$ (1) $(-,-)$ un $(\sigma,+)$ up	$(0,+)$ (1) $(-,0)$ un $(-,-)$ lo	$(0,+)$ (1) $(-,0)$ un $(-,-)$ lo	$(0,+)$ (1) $(-,0)$ un $(-,-)$ lo	$(0,-)$ (2) $(+,0)$ ph $(-,-)$ lo	$(0,-)$ (2) $(+,0)$ ph $(-,-)$ lo	$(0,-)$ (2) $(+,0)$ ph $(-,-)$ lo	$(-,-)$ (2) $(+,+)$ un $(\sigma,+)$ up
$n=1$	$(-,+)$ (2) $(-,+)$ un $(\sigma,-)$ lo	$(0,+)$ (1) $(+,0)$ ph $(-,-)$ lo	$(+,-)$ (1) $(+,-)$ un $(\sigma,-)$ lo	$(+,-)$ (1) $(+,-)$ un $(\sigma,-)$ lo	$(-,+)$ (2) $(-,+)$ un $(\sigma,-)$ lo	$(-,+)$ (2) $(-,+)$ un $(\sigma,-)$ lo	$(0,-)$ (2) $(-,0)$ un $(-,-)$ lo	$(+,-)$ (1) $(+,-)$ un $(\sigma,-)$ lo
$n=2$	$(0,-)$ (2) $(+,0)$ ph $(-,-)$ lo	$(0,-)$ (2) $(+,0)$ ph $(-,-)$ lo	$(-,-)$ (2) $(+,+)$ un $(\sigma,+)$ up	$(-,-)$ (2) $(+,+)$ un $(\sigma,+)$ up	$(+,+)$ (1) $(-,-)$ un $(\sigma,+)$ up	$(+,+)$ (1) $(-,-)$ un $(\sigma,+)$ up	$(0,+)$ (1) $(-,0)$ un $(-,-)$ lo	$(0,+)$ (1) $(-,0)$ un $(-,-)$ lo

Table A.4: Positions of poles, residues and binding energies in the complex plane given in terms of $\mathrm{sgn}(y_n)$, $\mathrm{sgn}(Z_n)$ and $\mathrm{sgn}(E_n^{(2)}-i\varepsilon)$, respectively. We used $\tau = 1+108/(ar^3)$. The number (1) ((2)) denotes that y_n is located on the physical, first (unphysical, second) Riemann sheet and lo (up) means that the corresponding binding energy $E_n^{(2)}-i\varepsilon$ lies in the upper (lower) complex half plane. A pole with physical (unphysical) residue Z_n is labeled by ph (un). $\sigma = \{-,0,+\}$ is the set of possible signs. Red columns mark regions in parameter space where poles on the physical sheet with binding energy in the upper complex half plane exist, prohibiting the application of the residue theorem in the derivation of the dimer-particle scattering integral equation. The other column-colors represent parameters where all poles on the first sheet have binding energies in the lower complex half plane. Thereby, white (blue) marks the physical (unphysical) case where all first-sheet poles have positive (non-positive) residue. Yellow represents the mixed case where first-sheet poles with both positive and non-positive residues coexists.

A.1.2 Cauchy principal value integrals

In this section, we discuss how loop momentum integrals with full dimer propagators, as they, for instance, appear in the T-matrix integral equations (2.49) and (3.41), can be evaluated in the limit $\varepsilon \to 0^+$. Our method is based on the Cauchy principal value formula $\mathcal{PV}_c \int_a^b \mathrm{d}x := \lim_{\varepsilon\to 0^+}\big\{\int_a^{c-\varepsilon}\mathrm{d}x + \int_{c+\varepsilon}^b \mathrm{d}x\big\}$. As explained in sec. A.1.1 we know that the inverse on-shell dimer propagator has the form of a polynomial (A.3). This yields the partial fraction decomposition:

$$D(E,q) \;=\; \sum_{n=0}^{N-1} \frac{1/C_n}{\sqrt{2\mu\big(E - \frac{q^2}{2\bar{\mu}} + i\varepsilon\big)} - y_n} \quad . \tag{A.24}$$

In order to integrate over such a term, we first use the Sokhatsky–Weierstrass-theorem

$$\begin{aligned}
&\lim_{\varepsilon\to 0^+}\int_a^b \mathrm{d}x\,\frac{f(x)}{x-(y\pm i\varepsilon)} \\
&= \begin{cases} \mathcal{PV}_y \int_a^b \mathrm{d}x \frac{f(x)}{x-y} \pm i\pi f(y) \;=\; \int_a^b \mathrm{d}x\,\frac{f(x)-f(y)}{x-y} + \Big[\ln\frac{b-y}{y-a} \pm i\pi\Big]\, f(y) & : y\in(a,b) \\ \int_a^b \mathrm{d}x\,\frac{f(x)}{x-y} & : y \notin [a,b] \end{cases} \\
&= \int_a^b \mathrm{d}x\,\frac{f(x) - \Theta_{(a,b)}(y) f(y)}{x-y} + \Theta_{(a,b)}(y)\left[\ln\frac{b-y}{y-a} \pm i\pi\right] f(y) \quad .
\end{aligned} \tag{A.25}$$

The generalized Θ-function reads:

$$\Theta_\Omega(x) \;:=\; \begin{cases} 1 & : x \in \Omega \subset \mathbb{C} \\ 0 & : \text{otherwise} \quad . \end{cases} \tag{A.26}$$

Also we added $0 = f(y) - f(y)$ in eq. (A.25) such that the point $x = y$ becomes a removable singularity and the Cauchy principal value transforms into a standard Riemann integral. Assuming $\alpha \in \mathbb{R}$, $\beta > 0$ and $\gamma \in \mathbb{C}$, we define $\rho^2 := (\alpha - \gamma^2)/\beta$ and use eq. (A.25) to derive the formula:

$$\begin{aligned}
&\lim_{\varepsilon\to 0^+}\int_a^b \mathrm{d}x\,\frac{f(x)}{\sqrt{\alpha-\beta x^2+i\varepsilon}-\gamma} \;=\; \lim_{\varepsilon\to 0^+}\int_{a^2}^{b^2}\mathrm{d}z\,\frac{(-\frac{1}{\beta})(\sqrt{\alpha-\beta z+i\varepsilon}+\gamma)\frac{f(\sqrt{z})}{2\sqrt{z}}}{z - \frac{\alpha-\gamma^2}{\beta} - i\varepsilon} \\
&= \lim_{\varepsilon\to 0^+}\int_{a^2}^{b^2}\mathrm{d}z\,\frac{g(z)}{z-(\rho^2+i\varepsilon)} \quad \text{with} \quad g(z) \;:=\; (-\frac{1}{\beta})(\sqrt{\alpha-\beta z+i\varepsilon}+\gamma)\frac{f(\sqrt{z})}{2\sqrt{z}} \\
&= \int_{a^2}^{b^2}\mathrm{d}z\,\frac{g(z) - \Theta_{(a^2,b^2)}(\rho^2)g(\rho^2)}{z-\rho^2} + \Theta_{(a^2,b^2)}(\rho^2)\left[\ln\frac{b^2-\rho^2}{\rho^2-a^2} + i\pi\right] g(\rho^2) \\
&= \int_a^b \mathrm{d}x\left[\frac{f(x)}{\sqrt{\alpha-\beta x^2}-\gamma} \;+\; \Theta_{\sqrt{\mathbb{C}}}(\gamma)\,\Theta_{(a^2,b^2)}(\rho^2)\,\frac{\gamma}{\beta}\,\frac{2x}{x^2-\rho^2}\,\frac{f(\rho)}{\rho}\right] \\
&\quad -\; \Theta_{\sqrt{\mathbb{C}}}(\gamma)\,\Theta_{(a^2,b^2)}\,(\rho^2)\,\frac{\gamma}{\beta}\left[\ln\frac{b^2-\rho^2}{\rho^2-a^2} + i\pi\right]\frac{f(\rho)}{\rho} \quad .
\end{aligned} \tag{A.27}$$

Thereby, we substituted $z := x^2$ and used the identity $g(\rho^2) = \Theta_{\sqrt{\mathbb{C}}}(\gamma)\,(-\gamma/\beta)\,f(\rho)/\rho$. We now apply eq. (A.27) to an integral over a full dimer propagator and a momentum-dependent function f^ε, which itself is well-behaving in the limit $\varepsilon \to 0^+$. Doing so, we end up with:

$$\begin{aligned}\lim_{\varepsilon\to 0^+}\int_0^\Lambda \mathrm{d}q\, D(E,q)\; f^\varepsilon(q) \;&=\; \sum_{n=0}^{N-1}\frac{1}{C_n}\lim_{\varepsilon\to 0^+}\int_0^\Lambda \frac{f^\varepsilon(q)}{\sqrt{2\mu E-\frac{\mu}{\bar{\mu}}q^2+i\varepsilon}-y_n}\\ =\int_0^\Lambda \mathrm{d}q\,&\left[D(E,q)\;f^0(q)\;-\;\sum_{n=0}^{N-1}\Theta_{\sqrt{\mathbb{C}}}(y_n)\,\Theta_{(0^2,\Lambda^2)}(q_n^2)\;\frac{\bar{\mu}}{\mu}\,\frac{y_n}{C_n}\,\frac{2q}{q^2-q_n^2}\,\frac{f^0(q_n)}{q_n}\right]\\ +\;\sum_{n=0}^{N-1}\Theta_{\sqrt{\mathbb{C}}}(y_n)\,\Theta_{(0,\Lambda^2)}(q_n^2)\;&\frac{\bar{\mu}}{\mu}\,\frac{y_n}{C_n}\left[\ln\frac{\Lambda^2-q_n^2}{q_n^2}+i\pi\right]\frac{f^0(q_n)}{q_n}\qquad,\end{aligned}\tag{A.28}$$

where $q_n^2 = q_n^2(E) := 2\bar{\mu}(E - E_n^{(2)})$. Consequently, $\Theta_{(0,\Lambda^2)}(q_n^2) = \Theta_{(E_n^{(2)},E_n^{(2)}+\Lambda^2/(2\bar{\mu}))}(E)$ holds, implying that the dimer energy $E_n^{(2)} = y_n^2/(2\mu)$ has to be real. Thus, in general $y_n \in \mathbb{R}\cup i\mathbb{R}$ is required. However, in all cases considered in sec. A.1.1.2 no real poles y_n were found. Consequently, extra contributions in eq. (A.28) can only appear if a pole y_n is purely imaginary, leading to a negative dimer binding energy $E_n^{(2)} = -|y_n|^2/(2\mu)$, as it should. From that, we directly see that the energy E has to be larger than $E_n^{(2)}$ in order for $\Theta_{(E_n^{(2)},E_n^{(2)}+\Lambda^2/(2\bar{\mu}))}(E)$ to be non-vanishing. In addition, also the cut-off Λ has to be chosen sufficiently large. In terms of the numerical evaluation of such dimer integrals, each extra contribution in eq. (A.28), in the end, effectively simply corresponds to one additional sampling point with complex weight-factor in the integral sum.

A.2 Legendre functions of second kind

In this section, we analyze the mathematical features of the analytically continued Legendre functions of second kind $\{Q_\ell : \mathbb{C}\setminus\{-1,1\}\to\mathbb{C}\,|\,\ell\in\mathbb{N}_0\}$. They are defined through:

$$Q_\ell(c) \;:=\; \frac{1}{2}\int_{-1}^{1}\mathrm{d}x\;\frac{P_\ell(x)}{c-x}\qquad. \tag{A.29}$$

We know that the appearing Legendre functions of first kind $\{P_\ell : [-1,1]\to\mathbb{R}\,|\,\ell\in\mathbb{N}_0\}$ build an orthogonal basis on the interval $[-1,1]$ and obey the symmetry:

$$P_\ell(-x) \;=\; (-1)^\ell P_\ell(x)\qquad. \tag{A.30}$$

Thus, we directly deduce the symmetry of the Q_ℓ functions:

$$Q_\ell(-c) \;=\; \frac{1}{2}\int_{-1}^{1}\mathrm{d}x\;\frac{P_\ell(x)}{-c-x} \;=\; -\frac{1}{2}\int_{-1}^{1}\mathrm{d}x\;\frac{P_\ell(-x)}{c-x} \;=\; (-1)^{\ell+1}Q_\ell(c)\qquad. \tag{A.31}$$

A.2.1 Recursion formula

The Legendre functions of first kind fulfill the orthogonality relation

$$\int_{-1}^{1} \mathrm{d}x\, P_\ell(x)\, P_{\ell'}(x) \;=\; \frac{2}{2\ell+1}\,\delta_{\ell\ell'} \quad . \tag{A.32}$$

They can be defined recursively through:

$$\begin{aligned} P_0(x) &= 1 \quad , \qquad P_1(x) \;=\; x \quad , \\ \forall \ell \geq 2: \quad \ell\, P_\ell(x) &= (2\ell-1)\, x\, P_{\ell-1}(x) \;-\; (\ell-1)\, P_{\ell-2}(x) \quad . \end{aligned} \tag{A.33}$$

Applying these formulas for the Q_ℓ functions, yields:

$$\begin{aligned} Q_0(c) &= \frac{1}{2}\int_{-1}^{1} \mathrm{d}x\, \frac{1}{c-x} \;=\; \frac{1}{2}\left[\ln(c+1) - \ln(c-1)\right] \\ &= \frac{1}{2}\left[\ln|c+1| + i\arg(c+1) - \ln|c-1| - i\arg(c-1)\right] \\ &= \frac{1}{2}\ln\left|\frac{c+1}{c-1}\right| + \frac{i}{2}\left[\arg(c+1) - \arg(c-1)\right] \quad , \\ Q_1(c) &= \frac{1}{2}\int_{-1}^{1} \mathrm{d}x\, \frac{x}{c-x} \;=\; \frac{1}{2}\int_{-1}^{1} \mathrm{d}x\, \left[c\,\frac{1}{c-x} - 1\right] \;=\; c\, Q_\ell(c) - 1 \quad , \end{aligned} \tag{A.34}$$

and the very same recursion relation:

$$\begin{aligned} \ell\, Q_\ell(c) &= \frac{1}{2}\int_{-1}^{1} \mathrm{d}x\, \frac{\ell\, P_\ell(x)}{c-x} \;=\; \frac{1}{2}\int_{-1}^{1} \mathrm{d}x\, \frac{(2\ell-1)\, x\, P_{\ell-1}(x) - (\ell-1)\, P_{\ell-2}(x)}{c-x} \\ &= (2\ell-1)\,\frac{1}{2}\int_{-1}^{1} \mathrm{d}x\, \left[c\,\frac{1}{c-x} - 1\right] P_{\ell-1}(x) \;-\; (\ell-1)\,\frac{1}{2}\int_{-1}^{1} \mathrm{d}x\, \frac{P_{\ell-2}(x)}{c-x} \\ &= (2\ell-1)\left[c\,\frac{1}{2}\int_{-1}^{1} \mathrm{d}x \frac{P_{\ell-1}(x)}{c-x} - \frac{1}{2}\int_{-1}^{1} \mathrm{d}x P_{\ell-1}(x)\right] \;-\; (\ell-1)\, Q_{\ell-2}(c) \\ &= (2\ell-1)\, c\, Q_{\ell-1}(c) \;-\; (2\ell-1)\delta_{\ell 0}\frac{1}{2\ell+1} \;-\; (\ell-1)\, Q_{\ell-2}(c) \\ &= (2\ell-1)\, c\, Q_{\ell-1}(c) \;-\; (\ell-1)\, Q_{\ell-2}(c)\;, \quad \forall \ell \geq 2 \quad . \end{aligned} \tag{A.35}$$

Applying eqs. (A.34) and (A.35), all Q_ℓ functions can be reconstructed from Q_0, yielding the convenient formula (see e.g. [122] p. 530):

$$Q_\ell \;=\; P_\ell\, Q_0 - \sum_{k=1}^{\ell} \frac{1}{k}\, P_{k-1}\, P_{\ell-k} \quad . \tag{A.36}$$

In this equation, the terms P_ℓ are the analytically continued Legendre functions of the first kind.

A.2.2 Analytic structure

Eq. (A.36) implicates that the analytic structures of Q_ℓ and Q_0 the same. Since the complex logarithm is analytic on $\mathbb{C} \setminus (-\infty, 0]$, eq. (A.34) implies the analyticity of Q_0 on $\mathbb{C} \setminus (-\infty, 1]$. Considering only real arguments $c \in \mathbb{R} \setminus \{\pm 1\}$, yields:

$$\begin{aligned}
\lim_{\varepsilon\to 0^+} Q_\ell(c \pm i\varepsilon) &= P_\ell(c) \lim_{\varepsilon\to 0^+} Q_0(c \pm i\varepsilon) - \sum_{k=1}^{\ell} \frac{1}{k} P_{k-1}(c)\, P_{\ell-k}(c) \quad , \\
\lim_{\varepsilon\to 0^+} Q_0(c \pm i\varepsilon) &= \frac{1}{2} \ln \left| \frac{c+1}{c-1} \right| + \frac{i}{2} \lim_{\varepsilon\to 0^+} \left[\arg(c+1 \pm i\varepsilon) - \arg(c-1 \pm i\varepsilon)\right] \qquad \text{(A.37)} \\
&= \begin{cases} \frac{1}{2}\ln\frac{c+1}{c-1} + \frac{i}{2}[0-0] & : -1 < 1 < c \\ \frac{1}{2}\ln\frac{c+1}{1-c} + \frac{i}{2}[0-\pm\pi] & : -1 < c < 1 \\ \frac{1}{2}\ln\frac{c+1}{c-1} + \frac{i}{2}[\pm\pi-\pm\pi] & : c < -1 < 1 \end{cases} = \begin{cases} \operatorname{arctanh}\left(\frac{1}{c}\right) & : |c| > 1 \\ \operatorname{arctanh}(c) \ \mp \ i\frac{\pi}{2} & : |c| < 1 \ , \end{cases}
\end{aligned}$$

where we used

$$\forall z \in \mathbb{R} \ : \quad \lim_{\epsilon\to 0^+} \arg(z \pm i\varepsilon) = \begin{cases} 0 & : \ z \geq 0 \\ \pm\pi & : \ z < 0 \quad . \end{cases} \tag{A.38}$$

Therefore, Q_0 is also analytic on $(-\infty, -1]$. Consequently, all Q_ℓ are analytic on $\mathbb{C} \setminus [-1, 1]$. At the interval $[-1, 1]$ they have a cut with logarithmic singularities at the boundaries ± 1.

For the on-shell kinematics that are consider in this work, the argument of Q_0 always has the form $c_{ij}(E, p, k) - i\varepsilon$, where the energy- and momentum-dependent quantity

$$c_{ij}(E, p, k) = \frac{m_{ij}}{p\, k} \Big(\frac{p^2}{2\mu_j} + \frac{k^2}{2\mu_i} - E \Big) \tag{A.39}$$

is real. Thus, in the physical limit of our theory $\varepsilon \to 0^+$, we always have to take the lower case of eq. (A.37)

$$\lim_{\varepsilon\to 0^+} Q_0(c - i\varepsilon) = \begin{cases} \operatorname{arctanh}(1/c) & : |c| > 1 \\ \operatorname{arctanh}(c) \ + \ i\frac{\pi}{2} & : |c| < 1 \end{cases} \tag{A.40}$$

as proper building block for the integral kernel.

A.2.2.1 Geometry of singularities

As we have seen, the Q_ℓ functions have logarithmic singularities at ± 1. In order to understand their position in the momentum plane, we have to solve:

$$c_{ij}(E, p, k) = \frac{m_{ij}}{p\, k} \Big(\frac{p^2}{2\mu_j} + \frac{k^2}{2\mu_i} - E \Big) = \kappa \qquad \text{with} \qquad \kappa \in \{\pm 1\} \quad . \tag{A.41}$$

Defining the momentum vector $\vec{x}_0 := (p, k)^{\mathrm{T}}$, we first rescale it with the diagonal matrix $D_1^{ij}(E) := \operatorname{diag}(\sqrt{2\mu_j |E|}, \sqrt{2\mu_i |E|}$ via $\vec{x}_0 =: D_1^{ij}(E) \cdot \vec{x}_1$. In this way, eq. (A.41) transforms into the quadratic form

$$\vec{x}_1^{\mathrm{T}} \cdot N(\kappa \sin\phi_{ij}) \cdot \vec{x}_1 - \operatorname{sgn}(E) = 0 \quad , \tag{A.42}$$

where the symmetric 2×2 matrix $N(a) := \left(\begin{smallmatrix}1 & a\\ a & 1\end{smallmatrix}\right)$ has eigenvalues $1\pm a$. It can be diagonalized according to $R^{\mathrm{T}}N(a)R = D_2(a)$ with $D_2(a) := \mathrm{diag}(1+a, 1-a)$ and a $\pi/2$-rotation matrix $R = 1/\sqrt{2}\left(\begin{smallmatrix}1 & -1\\ 1 & 1\end{smallmatrix}\right) \in SO(2)$. Since $\sin\phi_{ij} \in (0,1)$ holds, both eigenvalues are positive. Using $\vec{x}_1 =: R\cdot D_2(\kappa\sin\phi_{ij})^{-1/2}\cdot\vec{x}_2$ then yields:

$$(\vec{x}_2)_1^2 \;+\; (\vec{x}_2)_2^2 \;-\; \mathrm{sgn}(E) \;=\; 0 \quad . \tag{A.43}$$

For negative energies, eq. (A.43) has no solution. If $E > 0$ holds, it represents a circle of radius 1. This circle is transformed into centered ellipses under $D_2(\kappa\sin\phi_{ij})^{-1/2}$ and that afterwards are rotated by R. Within the $\vec{x}_1$ plane, the major and minor semiaxes of these centered ellipses end at the points $1/\sqrt{2(1\mp\sin\phi_{ij})}(1,1)^{\mathrm{T}}$, respectively. Under $D_1^{ij}(E)$, these points are mapped to $1/\sqrt{1\mp\sin\phi_{ij}}(\sqrt{\mu_j|E|}, \sqrt{\mu_i|E|})^{\mathrm{T}}$ in the p-k momentum plane. Considering all channels, the length

$$\bar{\Lambda}(E) \;:=\; \max_{i\neq j}\left\{\sqrt{\frac{(\mu_i+\mu_j)}{1\mp\sin\phi_{ij}}|E|}\right\} \tag{A.44}$$

of the largest such semiaxes then determines a square $[0,\bar{\Lambda}(E)]^2$ that always surrounds the area of logarithmic singularities. Note that the composed mapping $A_\kappa^{ij}(E) := D_1^{ij}(E)\cdot R\cdot D_2(\kappa\sin\phi_{ij})^{-1/2}$, has the channel- and κ-independent determinant:

$$\begin{aligned}\det[A_\kappa^{ij}(E)] \;&=\; (2\sqrt{\mu_i\mu_j}|E|)\cdot 1\cdot(1+\kappa\sin\phi_{ij})^{-1/2}(1-\kappa\sin\phi_{ij})^{-1/2}\\ &=\; 2m_{ij}\sin\phi_{ij}(1-\sin^2\phi_{ij})^{-1/2}|E| \;=\; 2m_{ij}\tan\phi_{ij}\,|E| \;=\; 2\bar{M}|E| \quad .\end{aligned} \tag{A.45}$$

A.2.3 Hypergeometric series

For real arguments c with $|c| > 1$, the Q_ℓ-functions from eq. (A.40) can also be expressed in terms of hypergeometric series [122]:

$$\begin{aligned}Q_\ell(c) \;&=\; \frac{\sqrt{\pi}\,\Gamma(\ell+1)}{2^{\ell+1}\Gamma(\ell+\frac{3}{2})}\,\frac{1}{c^{\ell+1}}\,{}_2F_1\left[\frac{\ell}{2}+1,\,\frac{\ell}{2}+\frac{1}{2};\,\ell+\frac{3}{2};\,\frac{1}{c^2}\right] \;=\; \frac{\sqrt{\pi}\,\Gamma(\ell+1)}{2^{\ell+1}\Gamma(\ell+\frac{3}{2})}\,\frac{1}{c^{\ell+1}}\\ &\qquad\times\sum_{m=0}^{\infty}\frac{\Gamma(m+\frac{\ell}{2}+1)}{\Gamma(\frac{\ell}{2}+1)}\,\frac{\Gamma(m+\frac{\ell}{2}+\frac{1}{2})}{\Gamma(\frac{\ell}{2}+\frac{1}{2})}\,\frac{\Gamma(\ell+\frac{3}{2})}{\Gamma(m+\ell+\frac{3}{2})}\frac{\frac{1}{c^{2m}}}{\Gamma(m+1)}\\ &=\; \frac{\sqrt{\pi}\,\Gamma(\ell+1)}{2^{\ell+1}\,\Gamma(\frac{\ell+1}{2})\,\Gamma(\frac{\ell+1}{2}+\frac{1}{2})}\,\frac{1}{c^{\ell+1}}\sum_{m=0}^{\infty}\frac{\Gamma(\frac{2m+\ell+1}{2})\,\Gamma(\frac{2m+\ell+1}{2}+\frac{1}{2})}{\Gamma(m+\ell+\frac{3}{2})}\,\frac{\frac{1}{c^{2m}}}{\Gamma(m+1)}\\ &=\; \frac{\sqrt{\pi}\,\Gamma(\ell+1)}{2^{\ell+1}\,\sqrt{\pi}\,2^{1-(\ell+1)}\,\Gamma(\ell+1)}\sum_{m=0}^{\infty}\frac{\sqrt{\pi}\,2^{1-(2m+\ell+1)}\,\Gamma(2m+\ell+1)}{\Gamma(m+\ell+\frac{3}{2})}\,\frac{c^{-(2m+\ell+1)}}{\Gamma(m+1)}\\ &=\; \frac{\sqrt{\pi}}{2^{\ell+1}}\,\frac{1}{c^{\ell+1}}\sum_{m=0}^{\infty}\frac{\Gamma(2m+\ell+1)}{2^{2m}\,\Gamma(m+\ell+\frac{3}{2})\,\Gamma(m+1)}\,\frac{1}{c^{2m}} \quad .\end{aligned} \tag{A.46}$$

For the gamma function we used the known relations:

$$\Gamma(z+1) \;=\; z\,\Gamma(z) \quad , \qquad \Gamma(z)\,\Gamma(z+1/2) \;=\; 2^{1-2z}\,\sqrt{\pi}\,\Gamma(2z) \quad . \tag{A.47}$$

A.2.3.1 Approximative expansion

For higher angular momentum numbers ℓ, the calculation of Q_ℓ with the help of eq. (A.36) becomes numerically unstable for large $|c|$. This is due to the fact that Q_0 vanishes, whereas all P_ℓ diverge. Since $|c| \to \infty$ holds for $|E| \to \infty$ or $p, k \to \{0, \infty\}$, the case of large $|c|$ often occurs within a numerical calculation and therefore is worthy to by analyzed in more detail.

In order to deal with the numerical problems, we first interpret the series (A.46) as a Taylor expansion in $1/c$ and rewrite it in the way:

$$\begin{aligned} Q_\ell \;&=\; \sum_{m=0}^{\infty} Q_\ell^m \quad , \qquad Q_\ell^m(c) \;:=\; \frac{\sqrt{\pi}}{2^{\ell+1}} \frac{1}{c^{\ell+1}} \, d_\ell^m \, \frac{1}{c^{2m}} \quad , \\ d_\ell^m \;&:=\; \frac{\Gamma(2m+\ell+1)}{2^{2m}\,\Gamma(m+\ell+\frac{3}{2})\,\Gamma(m+1)} \quad . \end{aligned} \tag{A.48}$$

In this form, the Q_ℓ-functions are numerically stable for large $|c|$. Moreover, for a given accuracy it suffices to only keep the lowest order terms of this series, saving computation time.

In the following, we quantify the error of the aborting series (A.48). First, for all $m \geq 1$, we define the ratio of two succeeding coefficients:

$$\begin{aligned} \rho_\ell^m \;:=\; \frac{d_\ell^m}{d_\ell^{m-1}} \;&=\; \frac{(2m+l)(2m+\ell-1)}{2^2\,(m+\ell+\frac{1}{2})m} \;=\; \underbrace{\left(1+\frac{\ell}{2m}\right)}_{\in\,(1,\infty)} \underbrace{\left(1-\frac{\ell+2}{2\ell+2m+1}\right)}_{\in\,(0,1)} \\ \Rightarrow \quad 0 \;< 1-\frac{\ell+2}{2\ell+3} \;&\leq\; 1-\frac{\ell+2}{2\ell+2m+1} \;<\; \rho_\ell^m \;<\; 1+\frac{\ell}{2m} \;\leq\; 1+\frac{\ell}{2} \quad . \end{aligned} \tag{A.49}$$

Comparing the full function Q_ℓ with the aborting series, we narrow down their relative deviation $r_\ell^n := (Q_\ell - Q_\ell^{n-1})/Q_\ell$ by using $d_\ell^{m+n} = d_\ell^m \prod_{i=m+1}^{m+n} \rho_\ell^i$ and eq. (A.49) via:

$$\begin{aligned} c^{2n}\, r_\ell^n(c) \;&=\; \frac{\sum_{m=n}^{\infty} d_\ell^m \, \frac{1}{c^{2(m-n)}}}{\sum_{m=0}^{\infty} d_\ell^m \, \frac{1}{c^{2m}}} \;=\; \frac{\sum_{m=0}^{\infty} d_\ell^{m+n} \, \frac{1}{c^{2m}}}{\sum_{m=0}^{\infty} d_\ell^m \, \frac{1}{c^{2m}}} \\ &=\; \frac{\sum_{m=0}^{\infty} d_\ell^m \, \frac{1}{c^{2m}} \left(\prod_{i=m+1}^{m+n} \rho_\ell^i\right)}{\sum_{m=0}^{\infty} d_\ell^m \, \frac{1}{c^{2m}}} \\ &\begin{cases} < \;\; \dfrac{\sum_{m=0}^{\infty} d_\ell^m \frac{1}{c^{2m}} \left(\prod_{i=m+1}^{m+n} (1+\ell/2)\right)}{\sum_{m=0}^{\infty} d_\ell^m \frac{1}{c^{2m}}} \;=\; \left(1+\frac{\ell}{2}\right)^n \\ > \;\; \dfrac{\sum_{m=0}^{\infty} d_\ell^m \frac{1}{c^{2m}} \left(\prod_{i=m+1}^{m+n} (1-(\ell+2)/(2\ell+3))\right)}{\sum_{m=0}^{\infty} d_\ell^m \frac{1}{c^{2m}}} \;=\; \left(1-\frac{\ell+2}{2\ell+3}\right)^n \quad . \end{cases} \end{aligned} \tag{A.50}$$

The last two inequalities can only be performed for real arguments c. For such $c \in \mathbb{R}$, the relative deviation lies within the boundaries $0 \leq r_{\min} < r_\ell^n(c) < r_{\max} < 1$ as long as

$$\frac{\sqrt[n]{r_{\min}}}{1-\frac{\ell+2}{2\ell+3}} \;<\; \frac{1}{c^2} \;<\; \frac{\sqrt[n]{r_{\max}}}{1+\frac{\ell}{2}} \tag{A.51}$$

holds. Thus, for $|c| > \sqrt{(1+\ell/2)/\sqrt[n]{r_{\max}}}$, the relative error reads $r_\ell^n(c) < r_{\max} < 1$. If, as an example, we demand the relative error to be smaller than $r_{\max} = 1\%$, for $|c| \gtrsim 3.163\sqrt{1+\ell/2}$ already the first order approximation $Q_\ell \approx Q_\ell^1$ suffices to achieve this accuracy.

A.2.4 Mellin transform

In our analysis of the scaling behavior and the three-body spectrum, we need the functions $\mathcal{Q}_\ell$, which are the Mellin transforms of Legendre functions of second kind. Assuming that their argument reads $c(x) = (x + x^{-1})/(2\sin\phi)$, we now present two equivalent formulas for $\mathcal{Q}_\ell(s) := \mathcal{M}[Q_\ell \circ c](s)$.

Hypergeometric form: First, we derive an expression based on the hypergeometric representation (A.46), yielding:

$$\begin{aligned}
\mathcal{Q}_\ell(s) &:= \mathcal{M}[Q_\ell \circ c](s) = \int_0^\infty \mathrm{d}x\, x^{s-1}(Q_\ell \circ c)(x) \\
&= \sqrt{\pi} \sum_{m=0}^{\infty} \frac{\Gamma(2m+\ell+1)}{\Gamma(m+\ell+\frac{3}{2})\,\Gamma(m+1)} \int_0^\infty \mathrm{d}x\, x^{s-1}(2c(x))^{-(2m+\ell+1)} \\
&= \sin^{\ell+1}\phi\, \frac{\sqrt{\pi}}{2} \sum_{m=0}^{\infty} \frac{\Gamma(2m+\ell+1)}{\Gamma(m+\ell+\frac{3}{2})\,\Gamma(m+1)} \sin^{2m}\phi \\
&\quad \times \int_0^\infty \mathrm{d}x\, 2\, x^{s-1} \left(x + x^{-1}\right)^{-(2m+\ell+1)} \quad .
\end{aligned} \tag{A.52}$$

The last integral can be evaluated according to

$$\begin{aligned}
\int_0^\infty \mathrm{d}x\, 2\, x^{s-1} \left(x + x^{-1}\right)^{-(2m+\ell+1)} &= \int_0^\infty \mathrm{d}x\, 2\, x^{s+2m+\ell} \left(x^2+1\right)^{-(2m+\ell+1)} \\
= \int_0^\infty \frac{\mathrm{d}y}{\sqrt{y}}\, y^{\frac{s+2m+\ell}{2}} (y+1)^{-(2m+\ell+1)} &= \int_0^\infty \mathrm{d}y\, \frac{y^{\alpha-1}}{(1+y)^{\alpha+\beta}} = B(\alpha,\beta) \\
= \frac{\Gamma(\alpha)\,\Gamma(\beta)}{\Gamma(\alpha+\beta)} &= \frac{\Gamma(m+\frac{\ell+1+s}{2})\,\Gamma(m+\frac{l+1-s}{2})}{\Gamma(2m+\ell+1)} \quad ,
\end{aligned} \tag{A.53}$$

with $\alpha := m + (\ell+1+s)/2$ and $\beta := m + (l+1-s)/2$. Thereby, we used an integral representation for the Beta-function B. Its convergence is only given in the parameter region $\mathrm{Re}(\alpha) > 0$ and $\mathrm{Re}(\beta) > 0$. In terms of s, these conditions translate to $s \in \langle -1, 1\rangle$, where $\langle a, b\rangle := \{s \in \mathbb{C} \,|\, a < \mathrm{Re}(s) < b\}$. In this fundamental strip, the Mellin transform

$$\begin{aligned}
\mathcal{Q}_\ell(s) &= \sin^{\ell+1}\phi\, \frac{\sqrt{\pi}}{2} \sum_{m=0}^{\infty} \frac{\Gamma(m+\frac{\ell+1+s}{2})\,\Gamma(m+\frac{\ell+1-s}{2})}{\Gamma(m+\ell+\frac{3}{2})\,\Gamma(m+1)} \sin^{2m}\phi \\
&= \sin^{\ell+1}\phi\, \frac{\sqrt{\pi}}{2}\, \frac{\Gamma(\frac{\ell+1+s}{2})\,\Gamma(\frac{\ell+1-s}{2})}{\Gamma(\ell+\frac{3}{2})}\, {}_2F_1\left[\frac{\ell+1+s}{2}, \frac{\ell+1-s}{2};\, \ell+\frac{3}{2};\, \sin^2\phi\right]
\end{aligned} \tag{A.54}$$

exists. An alternative way to determine this strip is to make use of the asymptotic behavior of the Legendre-functions of second kind (A.46) via:

$$c(x) \;=\; \begin{cases} \mathcal{O}(x^{-1}) & : x \to 0 \\ \mathcal{O}(x) & : x \to \infty \end{cases} \quad \Rightarrow \quad (Q_\ell \circ c)(x) \;=\; \begin{cases} \mathcal{O}(x^{\ell+1}) & : x \to 0 \\ \mathcal{O}(x^{-\ell-1}) & : x \to \infty \end{cases} \quad . \tag{A.55}$$

The integral over $x^{s-1}(Q_\ell \circ c)(x)$ again only converges if $s \in \langle -\ell-1, \ell+1 \rangle$ holds.

Transcendental form: We can also find an analytic expression for the $\mathcal{Q}_\ell$ that omits the hypergeometric series (A.46). Defining a translation operator $\hat{T}_a$ through

$$(\hat{T}_a f)(s) \;:=\; f(s-a) \tag{A.56}$$

it reads:

$$\mathcal{Q}_\ell \;=\; P_\ell(\hat{c})\mathcal{Q}_0 \quad , \qquad \hat{c} \;:=\; \frac{\hat{T}_{-1} + \hat{T}_1}{2\sin\phi} \quad , \qquad \mathcal{Q}_0(s) \;=\; \pi\phi\,\frac{j_0(\phi s)}{\cos(\frac{\pi}{2}s)} \quad . \tag{A.57}$$

P_ℓ are now Legendre polynomials in the operator $\hat{c}$ and $j_0(x) = \sin(x)/x$ is the zeroth spherical Bessel function. We prove eq. (A.57) by mathematical induction over $\ell \in \mathbb{N}_0$:

<u>$\ell = 0$:</u> We begin with the first base case $\ell = 0$. Defining $\phi_\pm := \pi/2 \pm \phi \in (0, \pi)$, we rewrite Q_0 according to:

$$(Q_0 \circ c)(x) \;=\; \frac{1}{2}\ln\left(\frac{1 + \frac{2}{\omega}x + x^2}{1 - \frac{2}{\omega}x + x^2}\right) \;=\; \frac{1}{2}\left[\zeta_{\phi_-}(x) - \zeta_{\phi_+}(x)\right] \tag{A.58}$$

with $\zeta_\phi(x) := \ln(1 + 2\cos\phi\, x + x^2)$. The Mellin transform $\mathcal{M}[\zeta_\phi](s) = \frac{2\pi}{s}\frac{\cos(\phi s)}{\sin(\pi s)}$ can be found in [123]. Applying this to eq. (A.58), yields

$$\begin{aligned} \mathcal{Q}_0(s) \;&=\; \frac{\pi}{s}\,\frac{\cos(\phi_- s) - \cos(\phi_+ s)}{\sin(\pi s)} \;=\; \frac{\pi}{s}\,\frac{2\sin\left(\frac{\phi_+ + \phi_-}{2}s\right)\sin\left(\frac{\phi_+ - \phi_-}{2}\right)}{2\sin\left(\frac{\pi}{2}s\right)\cos\left(\frac{\pi}{2}s\right)} \\ &=\; \frac{\pi}{s}\,\frac{\sin(\phi s)}{\cos(\frac{\pi}{2}s)} \;=\; \pi\phi\,\frac{j_0(\phi s)}{\cos(\frac{\pi}{2}s)} \end{aligned} \tag{A.59}$$

such that the singularity at the origin $s = 0$ is removable with $\mathcal{Q}_0(0) = \pi\phi$. Thus, $\mathcal{Q}_0$ is analytic in the fundamental strip $s \in \langle -1, 1 \rangle$. More precisely, $\mathcal{Q}_0$ is meromorphic in $\mathbb{C}$ with poles at $\pm(2\mathbb{N}_0 + 1)$. Since $P_0(\hat{c}) = \mathrm{id}$ holds, the case $\ell = 0$ is proven.

$\underline{\ell = 1:}$ From eq. (A.34) we know that $Q_1 \circ c = c \cdot (Q_0 \circ c - c^{-1})$ holds. The Mellin transform of c^{-1} reads:

$$\begin{aligned} \mathcal{M}[c^{-1}](s) \;&=\; 2\sin\phi \int_0^\infty \mathrm{d}x \, \frac{x^{s-1}}{x + x^{-1}} \;=\; 2\sin\phi \int_{-\infty}^\infty \mathrm{d}y \, \frac{e^{(s+1)y}}{e^{2y}+1} \\ = 2\sin\phi \; (2\pi i) \sum_{n=0}^\infty \frac{e^{(s+1)i(n+\frac{1}{2})\pi}}{2\, e^{2i(n+\frac{1}{2})\pi}} \;&=\; \sin\phi \; (2\pi i) \frac{e^{(s-1)i\frac{\pi}{2}}}{1 - e^{(s-1)i\pi}} \;=\; \pi\phi \, \frac{j_0(\phi)}{\cos(\frac{\pi}{2}s)} \quad , \end{aligned} \tag{A.60}$$

where the integral exists in fundamental strip $s \in \langle -1, 1 \rangle$. Thereby, we deformed the contour such that it encloses countably infinitely many poles on the upper imaginary axis and afterwards applied the residue theorem, leading to a geometric series. Combining the results (A.59) and (A.60), yields:

$$\mathcal{M}[Q_0 \circ c - c^{-1}](s) \;=\; \mathcal{Q}_0(s) - \mathcal{M}[c^{-1}](s) \;=\; \pi\phi \, \frac{j_0(\phi s) - j_0(\phi)}{\cos(\frac{\pi}{2}s)} \quad . \tag{A.61}$$

The singularities at $s = \pm 1$ are now removable, such the fundamental strip is enlarged to $\langle -3, 3 \rangle$. Using the translation property

$$(\hat{x}^a f)(x) \;:=\; x^a \cdot f(x) \qquad \Rightarrow \qquad \mathcal{M}[\hat{x}^a f] \;=\; \hat{T}_{-a} \mathcal{M}[f] \tag{A.62}$$

of the Mellin transform and its linearity, we derive

$$\begin{aligned} \mathcal{Q}_1(s) \;&= \mathcal{M}[c \cdot (Q_0 \circ c - c^{-1})](s) \;=\; (\hat{c}\,\mathcal{M}[Q_0 \circ c - c^{-1}])(s) \\ &= \frac{\pi\phi}{2\sin\phi} \left[\frac{j_0(\phi(s+1)) - j_0(\phi)}{\cos(\frac{\pi}{2}(s+1))} + \frac{j_0(\phi(s-1)) - j_0(\phi)}{\cos(\frac{\pi}{2}(s-1))} \right] \\ &= \frac{\pi\phi}{2\sin\phi} \, \frac{j_0(\phi(s-1)) - j_0(\phi(s+1))}{\sin(\frac{\pi}{2}s)} \;=\; (\hat{c}\,\mathcal{Q}_0)(s) \quad , \end{aligned} \tag{A.63}$$

with the intersected fundamental strip $\langle -3-1, 3-1 \rangle \cap \langle -3+1, 3+1 \rangle = \langle -2, 2 \rangle$. Note that again the singularity at $s = 0$ is removable with $\mathcal{Q}_1(0) = 2(1 - \phi \cot\phi)$ such that $\mathcal{Q}_1$ is even meromorphic in $\mathbb{C}$ with poles at $\pm(2\mathbb{N}_0 + 2)$. Since $P_1(\hat{c}) = \hat{c}$ holds, eq. (A.63) proves the second base case.

$\underline{\{\ell - 2, \ell - 1\} \Rightarrow \ell:}$ For $\ell \geq 2$, the inductive step can now be performed using the recursion relation (A.33) and the translation property (A.62). Taking the Mellin transform on both sides of eq. (A.35), yields:

$$\begin{aligned} \mathcal{Q}_\ell \;&=\; \frac{2\ell - 1}{\ell} \, \hat{c}\, \mathcal{Q}_{\ell-1} \;-\; \frac{\ell - 1}{\ell} \, \mathcal{Q}_{\ell-2} \;=\; \frac{2\ell - 1}{\ell} \, \hat{c}\, P_{\ell-1}(\hat{c}) \, \mathcal{Q}_0 \;-\; \frac{\ell - 1}{\ell} \, P_{\ell-2}(\hat{c}) \, \mathcal{Q}_0 \\ &=\; \left[\frac{2\ell - 1}{\ell} \, \hat{c}\, P_{\ell-1}(\hat{c}) \;-\; \frac{\ell - 1}{\ell} \, P_{\ell-2}(\hat{c}) \right] \mathcal{Q}_0 \;=\; P_\ell(\hat{c}) \, \mathcal{Q}_0 \quad , \end{aligned} \tag{A.64}$$

which proves eq. (A.57).

Hence, in terms of analytic properties, $\mathcal{Q}_\ell$ is meromorphic in $\mathbb{C}$ with countably infinitely many poles of first order. They are located on the real axis at $\pm(2\mathbb{N}_0+\ell+1)$. This leads to a fundamental strip $\langle -\ell-1, \ell+1\rangle$. Comparing the expression (A.57) with eq. (A.36), we see that the extra term $(-1)\sum_{k=1}^{\ell}\frac{1}{k}P_{k-1}P_{\ell-k}$ in (A.36) leads to an enlarger fundamental strip, but effectively vanishes after performing a Mellin transformation.

Appendix B

Kernel numerics

In this part of the appendix, we briefly discuss the numerical methods that were applied in order to calculate the presented results. Within this work, all integrals were discretized via the Gauss–Legendre integration method [124]. Calculations of determinants, eigenvalues, eigenvectors and solutions of systems of linear equations as well as the bisection root finding algorithm were all implemented using C^{++} with standard LAPACK routines. The complex root finding in eq. (2.17) and in eq. (2.59) was performed using Mathematica. In the following, we used all functions synonym with their discretized version.

T-matrix: In order to solve a T-matrix integral equation of type (2.49) or (3.41) numerically, we first analytically perform the limit $\varepsilon \to 0^+$. Therefore, the analytically continued Legendre functions of second kind Q_ℓ, appearing in $\bar{R}$, have to be evaluated at $\lim_{\varepsilon\to 0^+} Q_\ell(c - i\varepsilon)$, where c is real. Corresponding analytic expression are derived in appendix A.2.2, especially see eqs. (A.37) and (A.40). For total angular momenta $\ell \geq 1$, these analytic expressions become numerically unstable in the limit $|c| \to \infty$. However, for arguments $|c| > 1$ the Q_ℓ-functions can be expanded in $1/c$, as explained in sec. A.2.3.1. We use such a finite expansion (A.48) in order to omit these instabilities. Thereby, we always require errors to be less than 1% by taking into account appropriately high orders in $1/c$. Furthermore, in the limit $\varepsilon \to 0^+$, potential poles of the full dimer propagator $\bar{D}_i$ can move towards the loop momentum integration contour $[0, \Lambda]$ if the energy lies above the dimer threshold $E > E_i^{(2)}$. In sec. A.1.2, we explain how the corresponding integrals are evaluated with the help of Cauchy principal value methods, leading to one additional contribution for each momentum pole in $\bar{D}_i$. For the loop momentum cut-off Λ we chose values $\Lambda \in [10^5, 10^8]$.

As discussed in sec. A.2.2.1, there are also logarithmic singularities in the Q_ℓ-functions if the energy E is positive. In terms of the loop momentum q, these singularities are integrable and their location is bounded from above by $\bar{\Lambda}(E) < \Lambda$ from eq. (A.44). For such energies, we split up the loop momentum interval according to $[0, \Lambda] = [0, \bar{\Lambda}(E)] \cup [\bar{\Lambda}(E), \Lambda]$. If $E < 0$, we simply set $\bar{\Lambda}(E) = 0$ and drop the first interval. With regard to the second interval $[\bar{\Lambda}(E), \Lambda]$, the substitution $q \mapsto (e^\rho - 1)$ proved very beneficial for the numerical convergence. Choosing $N_q \in \mathbb{N}$ sampling points and weights, the T-matrix integral equation is discretized in the momenta q, p and k, leading to the inhomogeneous linear equation:

$$\bar{T}(E) \;=\; \bar{R}(E) \,+\, \bar{R}(E)\,\bar{D}(E)\,\bar{T}(E) \quad . \tag{B.1}$$

$\bar{R}(E)$, $\bar{D}(E)$ and $\bar{T}(E)$ are the matrix versions of the corresponding functions. They have multichannel indices that specify the scattering channel as well as the momentum sampling point and the additional pole contribution. If $E > 0$ holds, we use $N_q/2$ sampling points for each $[0, \bar{\Lambda}(E)]$ and $[\bar{\Lambda}(E), \Lambda]$. This leads to a denser distribution in the area of logarithmic singularities, improving the numerical convergence. Solving eq. (B.1), the resulting matrix $\bar{T}(E)$ can be reinserted into the T-matrix equation in order to calculate arbitrary off-shell elements $\bar{T}_{ij}(E,p,k)$. These are e.g. used for the determination of the scattering amplitude and the scattering length in eq. (3.42). Furthermore, the matrix $\bar{T}(E)$ appears in the numerical evaluation of the integrals (3.46) and (3.53). For calculations of this type, we typically used $N_q \gtrsim 75$ sampling points.

Bound states and renormalization in the three-body problem: For the numerical solution of the three-body bound-state equations (2.51) and (3.44), we discretize the momenta completely analogous to the procedure that was used for the T-matrix. Since the trimer energies obey $E = E^{(3)} < E^{(2)}_{\text{min}} := \min\{E^{(2)}_i\} \leq 0$, there are no additional dimer poles and no logarithmic singularities in the loop momentum. The problem then appears as a homogeneous system of linear equations:

$$B \;=\; \bar{R}(E^{(3)})\,\bar{D}(E^{(3)})\,B \quad . \tag{B.2}$$

B is the bound-state vector and $\bar{R}(E^{(3)})$ and $\bar{D}(E^{(3)})$ are the kernel matrices. The eigenvalue problem (B.2) has nontrivial solutions at the energy $E^{(3)}$ if and only if

$$f(\Lambda, \bar{H}, E^{(3)}) \;=\; 0 \qquad \text{with} \qquad f(\Lambda, \bar{H}, E) \;:=\; \det\bigl[\,\mathbb{1} \,-\, \bar{R}(\Lambda, \bar{H}, E)\,\bar{D}(E)\,\bigr] \quad , \tag{B.3}$$

where we explicitly wrote out the $\bar{H}$ and Λ dependencies of the kernel matrices. The function f displays an oscillating behavior with logarithmic period until. For energies larger than the cut-off it approaches unity. Its concrete form depends among other thins on the choice of the sampling points and is physically irrelevant. Only the position of its zeros represents a physical observable. We use eq. (B.3) in two ways. For a given Λ and $\bar{H}$, where also the case of vanishing three-body force $\bar{H} = 0$ is not excluded, its roots in the energy variable E give the spectrum of three-body bound states. On the other hand, for prespecified cut-off Λ and binding energy $E = E^{(3)}$ we can interpret it as a function in $\bar{H}$. Searching the roots in $\bar{H}$ then fixes the three-body force, renormalizing the cut-off dependence in the three-body problem. For that purpose, it proved advantageous to rewrite $\bar{H} = (\Lambda^2 \bar{H})/\Lambda^2$ and then search for roots in the dimensionless rescaled three-body force $\Lambda^2 \bar{H}$. For energies below the deepest dimer state $E < E^{(2)}_{\text{min}}$, the values of f are real. In this case, we apply the bisection method as a reliable root-finding algorithm. For calculations in this sector, typically $N_q \gtrsim 30$ sampling points sufficed.

Form factor: From eq. (3.64), we know that the form factor can be written as the sum of three contributions $\mathcal{F}_\mathrm{E} = \mathcal{F}_{\mathrm{E},0} + \mathcal{F}_{\mathrm{E},1} + \mathcal{F}_{\mathrm{E},2}$ which correspond to the parallel-, exchange- and loop-diagrams depicted in figs. D.6, D.7 and D.8, respectively. Their expressions in eqs. (D.38), (D.52) and (D.69) are integrals over the two momenta p and k. A discretization in both momenta leads to the quadratic form

$$\begin{aligned}\mathcal{F}_\mathrm{E}(Q) \;&= |\beta\,\bar{H}|^2 \Big\{ \rho^\mathrm{T} \cdot \big[\, Y_0^\mathrm{M}(Q) \,+\, Y_1^\mathrm{M}(Q) \,+\, Y_2^\mathrm{M}(Q) \,\big] \cdot \rho \\ &\qquad\qquad -\; 2\,\rho^\mathrm{T} \cdot Y_0^\mathrm{V}(Q) \;+\; Y_0^\mathrm{S}(Q) \Big\}\end{aligned} \tag{B.4}$$

in the vector $\rho := |\beta\,\bar{H}|^{-1}\,\bar{D}^{[0]} \cdot \bar{G}$. In all three contributions, the appearing momentum integrals were disrcetized with $N_p, N_k, N_q \gtrsim 75$ sampling points. For the internal angular integrations, $N_x, N_y, N_\phi \gtrsim 10$ points sufficed. Thus, taking into account the overall number of integrations in each form factor contribution, the total number of Υ_i^M-function calls that are required for the calculation of the form factor at one specific momentum transfer Q is of the order $\gtrsim 10^7$.

Dipole strength distribution: Considering formula (D.84) for the dipole strength of the photodisintegration of a two-neutron halo system, we discretize the momentum integration in q and write the appearing matrix element as

$$\begin{aligned}\bar{M}_{E1}^{(\mathrm{a})}(E_\Sigma, k_0, k_1, x_0, x_1) \;&=\; (\mathcal{Z}e)\sqrt{\frac{3}{4\pi}}\,|\beta\bar{H}| \\ \times\; &\Big[\rho^\mathrm{T} \cdot Y_{\mathrm{E1}}^\mathrm{V}(E_\Sigma, k_0, k_1, x_0, x_1) \;-\; Y_{\mathrm{E1}}^\mathrm{S}(E_\Sigma, k_0, k_1, x_0, x_1)\Big] \quad ,\end{aligned} \tag{B.5}$$

where, again, the vector $\rho := |\beta\,\bar{H}|^{-1}\,\bar{D}^{[0]} \cdot \bar{G}$ was used. However, the vector- and scalar-valued functions $Y_{\mathrm{E1}}^\mathrm{V}(E_\Sigma, q, k_0, k_1, x_0, x_1)$ and $Y_{\mathrm{E1}}^\mathrm{S}(E_\Sigma, q, k_0, k_1, x_0, x_1)$ in the integral kernel contain the term $(\partial Q)(c) = 1/(1-c^2)$, which has poles in the limit $\varepsilon \to 0^+$. These poles depend on E_Σ, $E^{(3)}$ and on the integral variables q, k_0, k_1, x_0, x_1 in a rather intricate way. Hence, an analytic calculation of the limit $\varepsilon \to 0^+$ would be very elaborate if not even impossible. Furthermore, there are poles in the terms $1/(E^{(3)} - E_\Sigma + i\varepsilon)$ and $1/(E^{(3)} - E_\Sigma + i\varepsilon)^2$. We thus calculate the integral for $\mathrm{d}B(E1)/\mathrm{d}E_\Sigma$ for finite values $\varepsilon > 0$ and numerically perform the limit $\varepsilon \to 0^+$. Thereby, one method is to simply take only one very small value $\varepsilon \lesssim 0.008$, which requires a relatively large number of sampling points $N_q \gtrsim 400$. Since the algorithmic efficiency of some of the used routines is $\mathcal{O}(n^3)$, one run typically takes $(400/75)^3 \approx 150$ times longer than for the form factor case. Another method is to calculate $\mathrm{d}B(E1)/\mathrm{d}E_\Sigma$ for about 10 different ε-values in the interval $[0.001, 0.2]$, identify the linear part of the curve and then extrapolate this part to $\varepsilon = 0$. A test revealed that both methods give identical results if for the first method N_q is sufficiently large. However, the advantage of the latter one is that, for total energies around $E_\Sigma \approx S_{2n}^{cnn}$, numerical stability is already achieved for only $N_q \gtrsim 100$. In comparison to a typical form factor calculation this implies an only about $10 \times (100/75)^3 \approx 50$ times longer computation time. Therefore, in practice we applied the latter method. For the remaining four angular integrals, $N_{x_0}, N_{x_1}, N_y, N_\phi \gtrsim 10$ sampling points sufficed.

Appendix C

Angular momentum coupling

In this section, we perform the projection of the integral kernel R onto states with definite J^P quantum numbers, where J is the total angular momentum and P is the parity. Following the steps that are explained in sec. 2.3.3.3, we calculate the corresponding expressions in detail. Since formulas pertaining to Clebsch–Gordan-coefficients $C^{JM}_{j_1 s_1; j_2 s_2}$ and spherical harmonics $Y_{\ell m}$ will be frequently used, we first repeat some of their basic properties. For a comprehensive overview, see e.g. ref. [75].

C.1 Clebsch–Gordan-coefficients

Completeness and symmetry: Since CGCs are the coefficients of a unitary matrix, they fulfill the completeness relations

$$\sum_{J=|j_1-j_2|}^{j_1+j_2} \sum_{M=-J}^{J} C^{JM}_{j_1 m_1; j_2 m_2}\, C^{JM}_{j_1 m_3; j_2 m_4} \;=\; \delta^{m_1 m_3}\, \delta^{m_2 m_4} \tag{C.1}$$

and

$$\sum_{m_1} \sum_{m_2} C^{J_3 M_3}_{j_1 m_1; j_2 m_2} C^{J_4 M_4}_{j_1 m_1; j_2 m_2} \;=\; \delta^{J_3 J_4}\, \delta^{M_3 M_4} \qquad . \tag{C.2}$$

Furthermore, they obey the symmetry properties:

$$\begin{aligned}
C^{j_3 m_3}_{j_1 m_1; j_2 m_2} &= (-1)^{j_1+j_2-j_3} C^{j_3,-m_3}_{j_1,-m_1; j_2,-m_2} \;=\; (-1)^{j_1+j_2-j_3} C^{j_3 m_3}_{j_2 m_2; j_1 m_1} \\
&= (-1)^{j_2+m_2} \sqrt{(2j_3+1)/(2j_1+1)}\, C^{j_1,-m_1}_{j_3,-m_3; j_2 m_2} \\
&= (-1)^{j_1-m_1} \sqrt{(2j_3+1)/(2j_2+1)}\, C^{j_2,-m_2}_{j_1 m_1; j_3,-m_3} \\
&= (-1)^{j_2+m_2} \sqrt{(2j_3+1)/(2j_1+1)}\, C^{j_1 m_1}_{j_2,-m_2; j_3 m_3} \\
&= (-1)^{j_1-m_1} \sqrt{(2j_3+1)/(2j_2+1)}\, C^{j_2 m_2}_{j_3 m_3; j_1,-m_1} \qquad .
\end{aligned} \tag{C.3}$$

Coupling of angular momenta: With the help of CGCs, matrix elements can be coupled to quantities with definite total angular momentum. Therefore, we assume that we have several of such quantities $\{X_1, X_2, \dots\}$ with upper angular momentum indies $[j_1m_1; j_2m_2|j_3m_3; j_4m_4]$. The coupling to total angular momentum is the performed according to:

$$X_i^{[J_1M_1;j_1;j_2|J_2M_2;j_3;j_4]} \;:=\; \sum_{n=1}^{4}\sum_{m_n} C^{J_1M_1}_{j_1m_1;j_2m_2} X_i^{[j_1m_1;j_2m_2|j_3m_3;j_4m_4]} C^{J_2M_2}_{j_3m_3;j_3m_4} \quad . \tag{C.4}$$

With the help of eq. (C.1), the product of such objects is coupled via:

$$\begin{aligned}
&\sum_{n=1}^{6}\sum_{m_n} C^{J_1M_1}_{j_1m_1;j_2m_2} X_i^{[j_1m_1;j_2m_2|j_5m_5;j_6m_6]} X_j^{[j_5m_5;j_6m_6|j_3m_3;j_4m_4]} C^{J_2M_2}_{j_3m_3;j_3m_4} \\
&= \sum_{j_7,j_8}\sum_{n=1}^{8}\sum_{m_n} C^{J_1M_1}_{j_1m_1;j_2m_2} X_i^{[j_1m_1;j_2m_2|j_5m_5;j_6m_6]} \,\delta^{m_5m_7}\delta^{m_6m_8}\,\delta^{j_5j_7}\delta^{j_6j_8} \\
&\quad \times\; X_j^{[j_7m_7;j_8m_8|j_3m_3;j_4m_4]} \, C^{J_2M_2}_{j_3m_3;j_3m_4} \\
&= \sum_{J_3=|j_5-j_6|}^{j_5+j_6}\;\sum_{M_3=-J_3}^{J_3}\;\sum_{j_7,j_8}\delta^{j_5j_7}\delta^{j_6j_8}\sum_{n=1}^{8}\sum_{m_n} \\
&\quad \times\; C^{J_1M_1}_{j_1m_1;j_2m_2}\, X_i^{[j_1m_1;j_2m_2|j_5m_5;j_6m_6]}\, C^{J_3M_3}_{j_5m_5;j_6m_6} \\
&\quad \times\; C^{J_3M_3}_{j_7m_7;j_8m_8}\, X_j^{[j_7m_7;j_8m_8|j_3m_3;j_4m_4]}\, C^{J_2M_2}_{j_3m_3;j_3m_4} \\
&= \sum_{J_3=|j_5-j_6|}^{j_5+j_6}\;\sum_{M_3=-J_3}^{J_3} X_i^{[J_1M_1;j_1;j_2|J_3M_3;j_5;j_6]}\; X_j^{[J_3M_3;j_5;j_6|J_2M_2;j_3;j_4]} \quad .
\end{aligned} \tag{C.5}$$

C.2 Spherical harmonics

The spherical harmonics $Y_{\ell m}$ are eigenfunctions of the angular momentum operator and form a complete and orthonormal set of functions on the 2-sphere. We use a normalization where the constant zeroth function reads $Y_{00}(\mathbf{e_p}) = 1/\sqrt{4\pi}$. The spherical harmonics fulfill the orthogonality relations:

$$\int \mathrm{d}\Omega_{\mathbf{q}}\, Y_{\ell_1 m_1}(\mathbf{e_p})\, Y^*_{\ell_2 m_2}(\mathbf{e_p}) \;=\; \delta^{\ell_1\ell_2}\delta^{m_1m_2} \quad\Rightarrow\quad \int \mathrm{d}\Omega_{\mathbf{q}}\, Y_{\ell m}(\mathbf{e_p}) \;=\; \delta^{0\ell}\delta^{0m}\sqrt{4\pi} \quad . \tag{C.6}$$

Furthermore, they are related to Legendre functions of first kind P_ℓ according to:

$$(2\ell+1)\, P_\ell(\mathbf{e_p}\cdot\mathbf{e_k}) \;=\; 4\pi \sum_m Y^*_{\ell m}(\mathbf{e_p})\, Y_{\ell m}(\mathbf{e_k}) \quad . \tag{C.7}$$

In combination with the formula for the conjugate of a spherical harmonic

$$Y^*_{\ell m} \;=\; (-1)^m\, Y_{\ell,-m} \tag{C.8}$$

the symmetry relations (C.3) of CGCs can be used in order to rewrite the known product-formula for spherical harmonics:

$$\begin{aligned}
Y_{\ell_1 m_1}\, Y_{\ell_2 m_2} \;&=\; \sqrt{(2\ell_1+1)(2\ell_2+1)/(4\pi)}\sum_{\ell_3,m_3} \frac{C^{\ell_3 0}_{\ell_1 0;\ell_2 0} C^{\ell_3 m_3}_{\ell_1 s_1;\ell_2 s_2}}{\sqrt{2\ell_3+1}}\; Y_{\ell_3 m_3} \\
&=\; \sqrt{(2\ell_1+1)/(4\pi)}(-1)^{\ell_1}\sum_{\ell_3,m_3} C^{\ell_2 0}_{\ell_1 0;\ell_3 0} C^{\ell_3 m_3}_{\ell_1 s_1;\ell_2 s_2}\; Y_{\ell_3 m_3} \\
&=\; \sqrt{(2\ell_1+1)/(4\pi)}(-1)^{\ell_1 - m_1}\sum_{\ell_3,m_3} C^{\ell_3 0}_{\ell_1 0;\ell_2 0} C^{\ell_2,-m_2}_{\ell_1 M_1;\ell_3,-m_3}\; Y_{\ell_3 m_3} \quad .
\end{aligned} \tag{C.9}$$

C.3 Angular decomposition of the interaction kernel

With regard to angular momentum coupling in the case of two-particle P-wave interactions, we first transform the on-shell integral kernel (2.35) with the help of relation (2.39), giving the intrinsic dimer spin-singlet components:

$$\begin{aligned}
&R^{[1|1]}_{ij}(E,\mathbf{p},\mathbf{k}) \\
&\quad = -\Big[\nu\,\kappa_{ij}\;(g_i g_j)\;\frac{\big(k\,A\mathbf{e_k} + \frac{m_j}{M_i} p\,A\mathbf{e_p}\big)\big(p\,A\mathbf{e_p} + \frac{m_i}{M_j} k\,A\mathbf{e_k}\big)^\dagger}{E - \frac{p^2}{2\mu_j} - \frac{k^2}{2\mu_i} - \frac{pk\,\mathbf{e_p}\,\mathbf{e_k}}{m_{ij}} + i\varepsilon} \;+\; \delta_{1i}\delta_{1j}\,\mathbb{1}\,H\Big] \quad .
\end{aligned} \tag{C.10}$$

The kernel function $R^{[1|1]}$ can be expanded in terms of orbital angular momentum contributions according to eq. (2.41). For the constant three-particle interaction $-\delta_{1i}\delta_{1j}\mathbb{1}H$, this decomposition into spherical harmonics is trivial. It is based on the identity:

$$1 \;=\; 4\pi \sum_{\ell_1,m_1}\sum_{\ell_2,m_2} Y^*_{\ell_1 m_1}(\mathbf{e_p})\;\delta^{0\ell_1}\,\delta^{0\ell_2}\;\delta^{0m_1}\,\delta^{0m_2}\;Y_{\ell_2 m_2}(\mathbf{e_k}) \quad . \tag{C.11}$$

The remaining part, originating from two-particle interactions, has a complicated angular dependence. Consequently, its decomposition is more tricky. We begin with rewriting the denominator:

$$\begin{aligned}
\frac{1}{E - \frac{p^2}{2\mu_j} - \frac{k^2}{2\mu_i} - \frac{pk\,\mathbf{e_p}\,\mathbf{e_k}}{m_{ij}} + i\varepsilon} \;&=:\; \sum_\ell (2\ell+1) f^{[\ell]}(E,p,k)\, P_\ell(\mathbf{e_p}\,\mathbf{e_k}) \quad \Rightarrow \\
f^{[\ell]}(E,p,k) \;&=\; \frac{1}{2}\int_{-1}^{1} \mathrm{d}x \frac{P_\ell(x)}{E - \frac{p^2}{2\mu_j} - \frac{k^2}{2\mu_i} + i\varepsilon - \frac{pk\,x}{m_{ij}}} \\
&=\; \frac{m_{ij}}{pk}\,\frac{1}{2}\int_{-1}^{1} \mathrm{d}x \frac{P_\ell(x)}{-c_{ij}(E,p,k) - x} \;=\; \frac{m_{ij}}{pk}\,Q_\ell(-c_{ij}(E,p,k)) \\
&=\; \frac{m_{ij}}{pk}(-1)^{\ell+1}\,Q_\ell(c_{ij}(E,p,k)) \quad , \quad c_{ij}(E,p,k) \;:=\; \frac{m_{ij}}{pk}\Big(\frac{p^2}{2\mu_j} + \frac{k^2}{2\mu_i} - E - i\varepsilon\Big) \;.
\end{aligned} \tag{C.12}$$

The appearing Legendre functions of first and second kind P_ℓ and Q_ℓ and their properties and symmetries are discussed in detail in sec. A.2. Here, we simply applied the formulas (A.29) and (A.32). Using the known relation (C.7) yields a preliminary decomposition of the denominator:

$$\begin{aligned} \frac{1}{E-\frac{p^2}{2\mu_j}-\frac{k^2}{2\mu_i}-\frac{pk\,\mathbf{e_p}\,\mathbf{e_k}}{m_{ij}}+i\varepsilon} \;&=\; (-4\pi)\,\frac{m_{ij}}{pk}\sum_{\ell,m}(-1)^\ell Q_\ell(c_{ij}(E,p,k)) \\ &\qquad\times\; Y^*_{\ell m}(\mathbf{e_p})\,Y_{\ell m}(\mathbf{e_k}) \quad . \end{aligned} \tag{C.13}$$

Its angular entanglement with the numerator will be resolved in the following. Therefore, we write:

$$\begin{aligned} &\left(k\,A\mathbf{e_k}+\frac{m_j}{M_i}p\,A\mathbf{e_p}\right)\cdot\left(p\,A\mathbf{e_p}+\frac{m_i}{M_j}k\,A\mathbf{e_k}\right)^\dagger \;=\; \sqrt{\mu_i\mu_j}\,\frac{pk}{m_{ij}}\,\Bigg[\frac{1}{\omega_{ij}}\,\underbrace{(A\mathbf{e_p})(A\mathbf{e_k})^\dagger}_{(i)} \\ &+\sqrt{\frac{\mu_i}{\mu_j}}\frac{p}{k}\,\underbrace{(A\mathbf{e_p})(A\mathbf{e_p})^\dagger}_{(ii)}+\sqrt{\frac{\mu_j}{\mu_i}}\frac{k}{p}\,\underbrace{(A\mathbf{e_k})(A\mathbf{e_k})^\dagger}_{(iii)}+\omega_{ij}\,\underbrace{(A\mathbf{e_k})(A\mathbf{e_p})^\dagger}_{(iv)}\Bigg] \quad . \end{aligned} \tag{C.14}$$

Using the definition (2.39), the appearing products of the matrix A with unit vectors in spherical coordinates can be written as:

$$\begin{aligned} A\mathbf{e_p} \;&=\; \begin{pmatrix} \frac{-1}{\sqrt{2}} & \frac{-i}{\sqrt{2}} & 0 \\ 0 & 0 & 1 \\ \frac{1}{\sqrt{2}} & \frac{-i}{\sqrt{2}} & 0 \end{pmatrix}\begin{pmatrix} \sin\theta_p\cos\phi_p \\ \sin\theta_p\sin\phi_p \\ \cos\theta_p \end{pmatrix} \;=\; \begin{pmatrix} -\frac{1}{\sqrt{2}}\sin\theta_p e^{i\phi_p} \\ \cos\theta_p \\ \frac{1}{\sqrt{2}}\sin\theta_p e^{-i\phi_p} \end{pmatrix} \;=\; \sqrt{\frac{4\pi}{3}}\begin{pmatrix} Y_{11}(\mathbf{e_p}) \\ Y_{10}(\mathbf{e_p}) \\ Y_{1,-1}(\mathbf{e_p}) \end{pmatrix} \\ \Rightarrow\;\; \left[(A\mathbf{e_k})(A\mathbf{e_p})^\dagger\right]_{s_1s_2} \;&=\; \frac{4\pi}{3}Y^*_{1s_2}(\mathbf{e_p})\,Y_{1s_1}(\mathbf{e_k}) \quad . \end{aligned} \tag{C.15}$$

Inserting eqs. (C.14), (C.15) and (C.12) into eq. (C.10), we see that, after an appropriate relabeling of the summation indices, four different products of spherical harmonics appear. They correspond to the terms (*i*), (*ii*), (*iii*) and (*iv*) in eq. (C.14). In the following, we rewrite and calculate all four parts separately. Thereby, we make use of the symmetry properties of spherical harmonics and CGCs. Note that in our case all angular momentum quantum numbers are integers such that for the CGC-symmetries (C.3), the signs of the quantum numbers in the exponents of the (-1) factors do not matter.

(i): We use eqs. (C.15), (C.8) and (C.9) to calculate:

$$\begin{aligned}
&Y^*_{\ell_3 m_3}(\mathbf{e_p})\,Y_{\ell_3 m_3}(\mathbf{e_k})\ \left[(A\mathbf{e_p})(A\mathbf{e_k})^\dagger\right]^{s_1 s_2}\\
&= \frac{4\pi}{3}\,(-1)^{s_1+s_2}[Y_{1,-s_1}(\mathbf{e_p})\,Y_{\ell_3 m_3}(\mathbf{e_p})]^*\ Y_{1,-s_2}(\mathbf{e_k})\,Y_{\ell_3 m_3}(\mathbf{e_k})\\
&= \frac{4\pi}{3}\,(-1)^{s_1+s_2}\left[\sqrt{\frac{3}{4\pi}}(-1)^{1-(-s_1)}\sum_{\ell_1,m_1} C^{\ell_1 0}_{10;\ell 0} C^{\ell_3,-m_3}_{1,-s_1;\ell_1,-m_1}\ Y_{\ell_1 m_1}(\mathbf{e_p})\right]^*\\
&\qquad\qquad \times\ \sqrt{\frac{3}{4\pi}}(-1)^{1-(-s_2)}\sum_{\ell_2,m_2} C^{\ell_2 0}_{10;\ell_3 0} C^{\ell_3,-m_3}_{1,-s_2;\ell_2,-m_2}\ Y_{\ell_2 m_2}(\mathbf{e_k})\\
&= \sum_{\ell_1,m_1}\sum_{\ell_2,m_2} C^{\ell_1 0}_{10;\ell_3 0} C^{\ell_2 0}_{10;\ell_3 0} C^{\ell_3,-m_3}_{1,-s_1;\ell_1,-m_1} C^{\ell_3,-m_3}_{1,-s_2;\ell_2,-m_2}\ Y^*_{\ell_1 m_1}(\mathbf{e_p})\,Y_{\ell_2 m_2}(\mathbf{e_k})\\
&= \sum_{\ell_1,m_1}\sum_{\ell_2,m_2} C^{\ell_1 0}_{\ell_3 0;10} C^{\ell_2 0}_{\ell_3 0;10} C^{\ell_3 m_3}_{1s_1;\ell_1 m_1} C^{\ell_3 m_3}_{1s_2;\ell_2 m_2}\ Y^*_{\ell_1 m_1}(\mathbf{e_p})\,Y_{\ell_2 m_2}(\mathbf{e_k}) \quad .
\end{aligned} \tag{C.16}$$

(ii): Again, eqs. (C.15), (C.8) and (C.9) imply:

$$\begin{aligned}
&Y^*_{\ell_2 m_2}(\mathbf{e_p})\,Y_{\ell_2 m_2}(\mathbf{e_k})\ \left[(A\mathbf{e_p})(A\mathbf{e_p})^\dagger\right]^{s_1 s_2}\\
&= \frac{4\pi}{3}\,(-1)^{s_1}[Y_{1,-s_1}(\mathbf{e_p})\,Y_{1s_2}(\mathbf{e_p})\,Y_{\ell_2 m_2}(\mathbf{e_p})]^*\,Y_{\ell_2 m_2}(\mathbf{e_k})\\
&= \frac{4\pi}{3}\,(-1)^{s_1}[Y_{1,-s_1}(\mathbf{e_p})\\
&\qquad \times\ \sqrt{\frac{3}{4\pi}}(-1)^1\sum_{\ell_3,m_3} C^{\ell_2 0}_{10;\ell_3 0} C^{\ell_3 m_3}_{1s_2;\ell_2 m_2}\ Y_{\ell_3 m_3}(\mathbf{e_p})]^*\,Y_{\ell_2 m_2}(\mathbf{e_k})\\
&= \frac{4\pi}{3}\,(-1)^{1+s_1}\sqrt{\frac{3}{4\pi}}\sum_{\ell_3,m_3} C^{\ell_2 0}_{10;\ell_3 0} C^{\ell_3 m_3}_{1s_2;\ell_2 m_2}\\
&\qquad \times\ \sqrt{\frac{3}{4\pi}}\,(-1)^{1-(-s_1)}\sum_{\ell_1,m_1} C^{\ell_1 0}_{10;\ell_3 0} C^{\ell_3,-m_3}_{1,-s_1;\ell_1,-m_1} Y^*_{\ell_1 m_1}(\mathbf{e_p})\,Y_{\ell_2 m_2}(\mathbf{e_k})\\
&= (-1)^{1+\ell_2-\ell_3}\sum_{\ell_3,m_3}\sum_{\ell_1,m_1} C^{\ell_1 0}_{\ell_3 0;10} C^{\ell_2 0}_{\ell_3 0;10} C^{\ell_3 m_3}_{1s_1;\ell_1 m_1} C^{\ell_3 m_3}_{1s_2;\ell_2 m_2}\ Y^*_{\ell_1 m_1}(\mathbf{e_p}) Y_{\ell_2 m_2}(\mathbf{e_k})\ .
\end{aligned} \tag{C.17}$$

(iii): We use eq. (C.17) from part (ii) in order to derive:

$$\begin{aligned}
&Y^*_{\ell_1 m_1}(\mathbf{e_p})\,Y_{\ell_1 m_1}(\mathbf{e_k})\ \left[(A\mathbf{e_k})(A\mathbf{e_k})^\dagger\right]^{s_1 s_2}\\
&= \left[Y^*_{\ell_1 m_1}(\mathbf{e_k})\,Y_{\ell_1 m_1}(\mathbf{e_p})\ \left[(A\mathbf{e_k})(A\mathbf{e_k})^\dagger\right]^{s_2 s_1}\right]^*\\
&= (-1)^{1+\ell_1-\ell_3}\sum_{\ell_3,m_3}\sum_{\ell_2,m_2} C^{\ell_1 0}_{\ell_3 0;10} C^{\ell_2 0}_{\ell_3 0;10} C^{\ell_3 m_3}_{1s_1;\ell_1 m_1} C^{\ell_3 m_3}_{1s_2;\ell_2 m_2}\ Y^*_{\ell_1 m_1}(\mathbf{e_p}) Y_{\ell_2 m_2}(\mathbf{e_k})\ .
\end{aligned} \tag{C.18}$$

(*iv*): This part can be calculated from part (*i*). According to eq. (C.16), we write:

$$\begin{aligned}
& Y^*_{\ell_3 m_3}(\mathbf{e_p})\, Y_{\ell_3 m_3}(\mathbf{e_k})\ \left[(A\mathbf{e_k})(A\mathbf{e_p})^\dagger\right]^{s_1 s_2} \\
&= (-1)^{m_3+m_3}\left[Y^*_{\ell_3,-m_3}(\mathbf{e_p})\, Y_{\ell_3,-m_3}(\mathbf{e_k})\ \left[(A\mathbf{e_p})(A\mathbf{e_k})^\dagger\right]^{s_2 s_1}\right]^* \\
&= \sum_{\ell_1,m_1}\sum_{\ell_2,m_2} C^{\ell_1 0}_{\ell_3 0;10} C^{\ell_2 0}_{\ell_3 0;10} C^{\ell_3,-m_3}_{1s_2;\ell_1 m_1} C^{\ell_3,-m_3}_{1s_1;\ell_2 m_2}\, Y_{\ell_1 m_1}(\mathbf{e_p}) Y^*_{\ell_2 m_2}(\mathbf{e_k}) \qquad \text{(C.19)} \\
&= \sum_{\ell_1,m_1}\sum_{\ell_2,m_2} C^{\ell_1 0}_{\ell_3 0;10} C^{\ell_2 0}_{\ell_3 0;10} C^{\ell_3,-m_3}_{1s_2;\ell_1,-m_1} C^{\ell_3,-m_3}_{1s_1;\ell_2,-m_2} (-1)^{m_1+m_2} Y^*_{\ell_1 m_1}(\mathbf{e_p}) Y_{\ell_2 m_2}(\mathbf{e_k}).
\end{aligned}$$

Result: As we see, the parts (*i*)-(*iii*) have the same structure in terms of CGCs. Collecting all parts and using the short notation $Q_\ell = Q_\ell(c_{ij}(E,p,k))$, we end up with:

$$\begin{aligned}
& R^{[1s_1;\ell_1 m_1|1s_2;\ell_2 m_2]}(E,p,k) \;=\; \int \frac{\mathrm{d}\Omega_\mathbf{p}}{4\pi} \int \frac{\mathrm{d}\Omega_\mathbf{k}}{4\pi}\, Y_{\ell_2 m_2}(\mathbf{e_p})\, R^{[1s_1|1s_2]}(E,\mathbf{p},\mathbf{k})\, Y^*_{\ell_2 m_2}(\mathbf{e_k}) \\
&= -\Big[\nu\kappa_{ij}\,(g_i g_j)\,\sqrt{\mu_i\mu_j}\,(-1) \sum_{\ell_3,m_3} (-1)^{\ell_3} C^{\ell_1 0}_{\ell_3 0;10} C^{\ell_2 0}_{\ell_3 0;10} \qquad \text{(C.20)} \\
&\quad \times \Big(\Big[\frac{1}{\omega_{ij}} Q_{\ell_3} - \sqrt{\frac{\mu_i}{\mu_j}}\frac{p}{k} Q_{\ell_2} - \sqrt{\frac{\mu_j}{\mu_i}}\frac{k}{p} Q_{\ell_1}\Big] C^{\ell_3 m_3}_{1s_1;\ell_1 m_1} C^{\ell_3 m_3}_{1s_2;\ell_2 m_2} \\
&\quad + \ \omega_{ij} Q_{\ell_3}\, C^{\ell_3,-m_3}_{1s_2;\ell_1,-m_1} C^{\ell_3,-m_3}_{1s_1;\ell_2,-m_2} (-1)^{m_1+m_2}\Big) + \delta_{1i}\delta_{1j}\,\delta^{s_1 s_2}\delta^{0\ell_1}\delta^{0\ell_2}\delta^{0m_1}\delta^{0m_2} H\Big] \quad .
\end{aligned}$$

C.4 Eigenstates of total angular momentum

In order to project onto eigenstates of the total angular momentum operator, we couple the intrinsic dimer spin with the orbital angular momentum of the dimer-particle system according to eq. (C.4). That way, eq. (C.20) transforms to:

$$\begin{aligned}
&R^{[J_1M_1;1;\ell_1|J_2M_2;1;\ell_2]}(E,p,k)\\
&= \sum_{s_1,s_2}\sum_{m_1,m_2} C^{J_1M_1}_{1s_1;\ell_1m_1}\, R^{[1s_1;\ell_1;m_1|1s_2;\ell_2;m_2]}(E,p,k)\, C^{J_2M_2}_{1s_2;\ell_2m_2}\\
&= -\Big[\nu\kappa_{ij}\,(g_ig_j)\,\sqrt{\mu_i\mu_j}\,(-1)\sum_{\ell_3}(-1)^{\ell_3}C^{\ell_10}_{\ell_30;10}\,C^{\ell_20}_{\ell_30;10}\\
&\quad\times\Big(\Big[\frac{1}{\omega_{ij}}Q_{\ell_3}-\sqrt{\frac{\mu_i}{\mu_j}}\frac{p}{k}Q_{\ell_2}-\sqrt{\frac{\mu_j}{\mu_i}}\frac{k}{p}Q_{\ell_1}\Big]\\
&\quad\times\overbrace{\sum_{s_1,s_2}\sum_{m_1,m_2,m_3} C^{J_1M_1}_{1s_1;\ell_1m_1}C^{\ell_3m_3}_{1s_1;\ell_1m_1}C^{\ell_3m_3}_{1s_2;\ell_2m_2}C^{J_2M_2}_{1s_2;\ell_2m_2}}^{=:\ C^{(a)}}\\
&\quad+\omega_{ij}Q_{\ell_3}\overbrace{\sum_{s_1,s_2}\sum_{m_1,m_2,m_3} C^{J_1M_1}_{1s_1;\ell_1m_1}C^{\ell_3,-m_3}_{1s_2;\ell_1,-m_1}C^{\ell_3,-m_3}_{1s_1;\ell_2,-m_2}C^{J_2M_2}_{1s_2;\ell_2m_2}(-1)^{m_1+m_2}}^{=:\ C^{(b)}}\Big)\\
&\quad+\ \delta_{1i}\delta_{1j}\,H\,\overbrace{\delta^{0\ell_1}\delta^{0\ell_2}\sum_{s_1,s_2}\sum_{m_1,m_2} C^{J_1M_1}_{1s_1;\ell_1m_1}\,\delta^{s_1s_2}\,\delta^{0m_1}\delta^{0m_2}C^{J_2M_2}_{1s_2;\ell_2m_2}}^{=:\ C^{(c)}}\Big]\quad .
\end{aligned}\tag{C.21}$$

The three appearing sums over magnetic quantum numbers $C^{(a)}$, $C^{(b)}$ and $C^{(c)}$ can be simplified to a great extend. Using the orthogonality relation (C.2) and the symmetries (C.3), we separate the sums according to:

$$\begin{aligned}
C^{(a)} &= \sum_{m_3}\Big(\sum_{s_1}\sum_{m_1}C^{J_1M_1}_{1s_1;\ell_1m_1}C^{\ell_3m_3}_{1s_1;\ell_1m_1}\Big)\Big(\sum_{s_2}\sum_{m_2}C^{J_2M_2}_{1s_2;\ell_2m_2}C^{\ell_3m_3}_{1s_2;\ell_2m_2}\Big)\\
&= \sum_{m_3}\delta^{J_1\ell_3}\,\delta^{M_1m_3}\ \delta^{J_2\ell_3}\,\delta^{M_2m_3}\ =\ \delta^{J_1\ell_3}\,\delta^{J_1J_2}\,\delta^{M_1M_2}\quad .
\end{aligned}\tag{C.22}$$

The term $C^{(b)}$ is a little bit more involved to compute, since, in contrast to the prior cases, summations over magnet quantum numbers are now entangled and can not be separated into two parts. In order to simplify the expressions treatment, we use Wigner-6j-symbols (W6J) (see again [75] for further details). They obey the identity:

$$\begin{aligned}
&\sum_{n=1}^{5}\sum_{m_n}C^{j_6m_6}_{j_1m_1;j_3m_3}C^{j_1m_1}_{j_4m_4;j_5m_5}C^{j_2m_2}_{j_5m_5;j_3m_3}C^{j_7m_7}_{j_4m_4;j_2m_2}\\
&\qquad= \delta^{j_6j_7}\delta^{m_6m_7}\ \sqrt{(2j_1+1)(2j_2+1)}\begin{Bmatrix} j_1 & j_6 & j_3\\ j_2 & j_5 & j_4\end{Bmatrix}\quad .
\end{aligned}\tag{C.23}$$

Using the CGC-symmetries (C.3), we conclude:

$$
\begin{aligned}
C^{(b)} &= \sum_{s_1,s_2}\sum_{m_1,m_2,m_3} (-1)^{m_1+m_2} C^{J_1M_1}_{1s_1;\ell_1m_1} C^{\ell_3,-m_3}_{1s_1;\ell_2,-m_2} C^{\ell_3,-m_3}_{1s_2;\ell_1,-m_1} C^{J_2M_2}_{1s_2;\ell_2m_2} \\
&= \sum_{s_1,s_2}\sum_{m_1,m_2,m_3} (-1)^{m_1+m_2} C^{J_1M_1}_{1s_1;\ell_1m_1} (-1)^{\ell_2+(-m_2)} \sqrt{\frac{2\ell_3+1}{3}}\, C^{1s_1}_{\ell_2m_2;\ell_3,-m_3} \\
&\times\ (-1)^{\ell_1-(-m_1)} \sqrt{\frac{2\ell_3+1}{3}}\, C^{1,-s_2}_{\ell_3m_3;\ell_1,-m_1} (-1)^{1+\ell_2-J_2} C^{J_2M_2}_{\ell_2m_2;1s_2} \\
&= (-1)^{1+\ell_1-J_2}\frac{2\ell_3+1}{3} \sum_{s_1,s_2}\sum_{m_1,m_2,m_3} C^{J_1M_1}_{1s_1;\ell_1m_1} C^{1s_1}_{\ell_2m_2;\ell_3,-m_3} C^{1,-s_2}_{\ell_3m_3;\ell_1,-m_1} C^{J_2M_2}_{\ell_2m_2;1s_2} \\
&= (-1)^{\ell_3-J_2}\frac{2\ell_3+1}{3} \sum_{s_1,s_2}\sum_{m_1,m_2,m_3} C^{J_1M_1}_{1s_1;\ell_1m_1} C^{1s_1}_{\ell_2m_2;\ell_3m_3} C^{1s_2}_{\ell_3m_3;\ell_1m_1} C^{J_2M_2}_{\ell_2m_2;1s_2} \\
&= \delta^{J_1J_2}\,\delta^{M_1M_2}\ (-1)^{\ell_3-J_2}(2\ell_3+1) \begin{Bmatrix} 1 & J_1 & \ell_1 \\ 1 & \ell_3 & \ell_2 \end{Bmatrix} \quad .
\end{aligned}
\tag{C.24}
$$

The remaining contribution is trivial:

$$
\begin{aligned}
C^{(c)} &= \delta^{0\ell_1}\delta^{0\ell_2} \sum_{s_1} C^{J_1M_1}_{1s_1;00} C^{J_2M_2}_{1s_1;00} \ = \ \delta^{0\ell_1}\delta^{0\ell_2} \sum_{s_1} \delta^{1J_1}\delta^{M_1s_1}\,\delta^{1J_2}\delta^{M_2s_1} \\
&= \delta^{0\ell_1}\delta^{0\ell_2}\,\delta^{1J_1}\delta^{J_1J_2}\,\delta^{M_1M_2} \quad .
\end{aligned}
\tag{C.25}
$$

Inserting eqs. (C.23)-(C.25) into eq. (C.21), the term $\delta^{J_1J_2}\delta^{M_1M_2}$ factors out, yielding:

$$
\begin{aligned}
R^{[J_1M_1;1;\ell_1|J_2M_2;1;\ell_2]}(E,p,k) \ &= \ \sum_{s_1,s_2}\sum_{m_1,m_2} C^{J_1M_1}_{1s_1;\ell_1m_1}\, R^{[1s_1;\ell_1m_1|1s_2;\ell_2m_2]}(E,p,k)\, C^{J_2M_2}_{1s_2;\ell_2m_2} \\
= \ -\delta^{J_1J_2}\delta^{M_1M_2} &\Bigg[\nu\kappa_{ij}\,(g_ig_j)\,\sqrt{\mu_i\mu_j}\,(-1) \sum_{\ell_3} (-1)^{\ell_3} C^{\ell_10}_{\ell_30;10}\, C^{\ell_20}_{\ell_30;10} \\
\times\ &\Bigg\{ \Big[\frac{1}{\omega_{ij}} Q_{\ell_3} - \sqrt{\frac{\mu_i}{\mu_j}}\frac{p}{k} Q_{\ell_2} - \sqrt{\frac{\mu_j}{\mu_i}}\frac{k}{p} Q_{\ell_1} \Big] \delta^{J_1\ell_3} \\
&+\ \omega_{ij} Q_{\ell_3} (-1)^{\ell_3-J_1}(2\ell_3+1) \begin{Bmatrix} 1 & J_1 & \ell_1 \\ 1 & \ell_3 & \ell_2 \end{Bmatrix} \Bigg\} \ +\ \delta_{1i}\delta_{1j}\,\delta^{0\ell_1}\delta^{0\ell_2}\delta^{1J_1}\,H \Bigg] \\
=:\ \delta^{J_1J_2}\delta^{M_1M_2}\, &R^{[J_1][\ell_1|\ell_2]}(E,p,k) \quad .
\end{aligned}
\tag{C.26}
$$

Hence, channels with different total angular momenta are decoupled and the structure of the interaction kernel reads $R^{[J_1M_1;1;\ell_1|J_2M_2;1;\ell_2]} = \delta^{J_1J_2}\delta^{M_1M_2}R^{[J_1][\ell_1|\ell_2]}$. This behavior is a consequence of the Wigner–Eckhardt theorem. However, channels with different orbital angular momenta in the dimer-particle system are still coupled.

C.5 Parity decoupling

Considering eq. (C.26), the remaining part of the interaction kernel

$$
\begin{aligned}
R^{[J][\ell_1|\ell_2]}(E,p,k) \;&=\; -\Big[\nu\kappa_{ij}\,(g_i g_j)\,\sqrt{\mu_i\mu_j}\,(-1)^{J+1} \\
&\times\;\Big(C^{\ell_1 0}_{J0;10}\,C^{\ell_2 0}_{J0;10}\Big[\frac{1}{\omega_{ij}}Q_J-\sqrt{\frac{\mu_i}{\mu_j}}\frac{p}{k}Q_{\ell_2}-\sqrt{\frac{\mu_j}{\mu_i}}\frac{k}{p}Q_{\ell_1}\Big] \\
&+\;\omega_{ij}\sum_\ell C^{\ell_1 0}_{\ell 0;10}\,C^{\ell_2 0}_{\ell 0;10}(2\ell+1)\begin{Bmatrix}1 & J & \ell_1\\ 1 & \ell & \ell_2\end{Bmatrix}Q_\ell\Big)\;+\;\delta_{1i}\delta_{1j}\,\delta^{1J}\,\delta^{0\ell_1}\delta^{0\ell_2}\,H\Big]
\end{aligned}
\tag{C.27}
$$

still looks relatively difficult to handle. However, using features of special CGCs and W6Js, it can be simplified to a great extend. With respect to the remaining CGCs in eq. (C.26), we first note that they have the form:

$$
\begin{aligned}
C^{\ell_1 0}_{\ell 0;10} \;&=\; -\frac{\Theta_{\ell-1}}{2\ell(2\ell+1)}\left[\ell^2(\ell-\ell_1)(\ell-\ell_1+1)(\ell+\ell_1+1)(\ell+\ell_1+2)\right]^{\frac{1}{2}}\,C^{\ell_1 0}_{\ell-1,0;00} \\
&+\frac{1}{2(\ell+1)(2\ell+1)}\left[(\ell+1)^2(-\ell+\ell_1)(-\ell+\ell_1+1)(\ell+\ell_1)(\ell+\ell_1+1)\right]^{\frac{1}{2}}\,C^{\ell_1 0}_{\ell+1,0;00} \\
&=\;-\sqrt{\frac{\ell}{2\ell+1}}\,\Theta_{\ell-1}\,\delta^{\ell_1\ell-1}+\sqrt{\frac{\ell+1}{2\ell+1}}\,\delta^{\ell_1\ell+1}\quad .
\end{aligned}
\tag{C.28}
$$

Thereby, we used a formula for specific CGCs (see [75] p.256 eq.(26) for more details) and the relation $C^{j_1 0}_{j_2 0;00}=\Theta_{j_2}\delta^{j_1 j_2}$. The discrete Heaviside function $\Theta:\mathbb{Z}\to\{0,1\}$ vanishes for negative integers and otherwise is unity. Hence, the product of two such CGCs can be written as the matrix element:

$$
\begin{aligned}
C^{\ell_1 0}_{\ell 0;10}C^{\ell_2 0}_{\ell 0;10} \;&=\frac{1}{2\ell+1}\Big[\Theta_{\ell-1}\,\ell\,\delta^{\ell_1\ell-1}\,\delta^{\ell_2\ell-1}\;-\;\Theta_{\ell-1}\sqrt{\ell(\ell+1)}\,\delta^{\ell_1\ell-1}\,\delta^{\ell_2\ell+1} \\
&\qquad-\;\Theta_{\ell-1}\sqrt{\ell(\ell+1)}\,\delta^{\ell_1\ell+1}\,\delta^{\ell_2\ell-1}\;+\;(\ell+1)\,\delta^{\ell_1\ell+1}\,\delta^{\ell_2\ell+1}\Big] \\
&=\frac{1}{2\ell+1}\begin{pmatrix}\Theta_{\ell-1}\,\ell & 0 & -\Theta_{\ell-1}\sqrt{\ell(\ell+1)}\\ 0 & 0 & 0\\ -\Theta_{\ell-1}\sqrt{\ell(\ell+1)} & 0 & \ell+1\end{pmatrix}^{\ell_1\ell_2}\quad .
\end{aligned}
\tag{C.29}
$$

For $\ell=0$, only the component $\ell_1=\ell_2=\ell+1=1$ is non-vanishing such that the general 3×3-matrix effectively reduces to its lower right component. With the help of relation (C.29), we rearrange the sum over W6Js in eq. (C.27) according to:

$$
\begin{aligned}
&\sum_\ell C^{\ell_1 0}_{10;\ell 0}C^{\ell_2 0}_{10;\ell 0}(2\ell+1)\begin{Bmatrix}1 & J & \ell_1\\ 1 & \ell & \ell_2\end{Bmatrix}Q_\ell \;=\;\sum_\ell\Big[\ell\begin{Bmatrix}1 & J & \ell-1\\ 1 & \ell & \ell-1\end{Bmatrix}\delta^{\ell_1\ell-1}\,\delta^{\ell_2\ell-1} \\
&-\sqrt{\ell(\ell+1)}\begin{Bmatrix}1 & J & \ell-1\\ 1 & \ell & \ell+1\end{Bmatrix}\delta^{\ell_1\ell-1}\delta^{\ell_2\ell+1}\;-\;\sqrt{\ell(\ell+1)}\begin{Bmatrix}1 & J & \ell+1\\ 1 & \ell & \ell-1\end{Bmatrix}\delta^{\ell_1\ell+1}\delta^{\ell_2\ell-1} \\
&+(\ell+1)\begin{Bmatrix}1 & J & \ell+1\\ 1 & \ell & \ell+1\end{Bmatrix}\delta^{\ell_1\ell+1}\,\delta^{\ell_2\ell+1}\Big]Q_\ell\quad .
\end{aligned}
\tag{C.30}
$$

Thereby, the Θ-functions were dropped, since, de facto, they are already included in the corresponding W6Js due to the following properties: W6Js are invariant under permutations of columns and under interchanges of upper and lower components in any two columns. Furthermore, the upper row of a non-vanishing W6J fulfills the triangle condition. Combining both arguments leads to:

$$\begin{aligned}
&\begin{Bmatrix} a & b & c \\ d & e & f \end{Bmatrix} = \Delta(a,b,c)\Delta(d,e,c)\Delta(d,b,f)\Delta(a,e,f) \begin{Bmatrix} a & b & c \\ d & e & f \end{Bmatrix} \quad , \\
&\Delta : \mathbb{Z}^3 \longrightarrow \{0,1\} \quad , \quad \Delta(a,b,c) := \begin{cases} 1 & : \ |a-c| \le b \le a+c \\ 0 & : \ \text{otherwise} \quad . \end{cases}
\end{aligned} \tag{C.31}$$

Using these symmetry arguments, all W6Js in eq. (C.30) can be reordered according to:

$$\begin{aligned}
\begin{Bmatrix} 1 & a & 1+a \\ 1 & b & c \end{Bmatrix} &= \Delta(1,b,1+a)\Delta(1,a,c)\Delta(1,b,c) \cdot (-1)^{a+b} \left[\frac{2(2a)!(a+b+3)!}{(2a+3)!(b-a)!} \right. \\
&\times \left. \frac{(a+b)!(a-b+2)!(b+c-1)!(c-a+1)!}{(b-c+1)!(c-b+1)!(b+c+2)!(a-c+1)!(a+c-1)!(a+c+2)!} \right]^{\frac{1}{2}} \quad ,
\end{aligned} \tag{C.32}$$

where we made use of a special formula (see [75] p.300 eq.(3)). Applying (C.32), the first W6J in eq. (C.30) reads:

$$\begin{aligned}
&\begin{Bmatrix} 1 & J & \ell-1 \\ 1 & \ell & \ell-1 \end{Bmatrix} = \begin{Bmatrix} 1 & \ell-1 & \ell \\ 1 & \ell-1 & J \end{Bmatrix} = \Delta(1,\ell-1,J)\,(-1)^{\ell-1+\ell-1} \\
&\quad \times \left[\frac{2(2\ell-2)!(2\ell+1)!(2\ell-2)!2(\ell+J-2)!(J-\ell+2)!}{(2\ell+1)!(\ell-J)!(J-\ell+2)!(\ell+J+1)!(\ell-J)!(\ell+J-2)!(\ell+J+1)!} \right]^{\frac{1}{2}} \\
&= \Delta(1,\ell-1,J) \frac{2(2\ell-2)!}{(\ell-J)!(\ell+J+1)!} \\
&= \frac{\Theta_{J-1}\,\delta^{\ell J}}{(2J+1)J(2J-1)} + \frac{\Theta_{J-1}\,\delta^{\ell,J+1}}{(J+1)(2J+1)} + \frac{\delta^{\ell,J+2}}{2J+3} \quad .
\end{aligned} \tag{C.33}$$

Similarly, we treat the second and third W6J

$$\begin{aligned}
&\begin{Bmatrix} 1 & J & \ell-1 \\ 1 & \ell & \ell+1 \end{Bmatrix} = \begin{Bmatrix} 1 & J & \ell+1 \\ 1 & \ell & \ell-1 \end{Bmatrix} = \begin{Bmatrix} 1 & \ell & \ell+1 \\ 1 & J & \ell-1 \end{Bmatrix} \\
&= \Delta(1,J,1+\ell)\Delta(1,J,\ell-1)\ (-1)^{\ell+J} \\
&\quad \times \left[\frac{2(2\ell)!(\ell+J+3)!(\ell+J)!(\ell-J+2)!(J+\ell-2)!}{(2\ell+3)!(J-\ell)!(J-\ell+2)!(\ell-J)!(J+\ell+1)!2(2\ell-2)!(2\ell+1)!} \right]^{\frac{1}{2}} \\
&= \frac{\Theta_{J-1}\,\delta^{\ell J}}{2J+1}
\end{aligned} \tag{C.34}$$

and the forth by writing:

$$
\begin{aligned}
\begin{Bmatrix} 1 & J & \ell+1 \\ 1 & \ell & \ell+1 \end{Bmatrix} &= \begin{Bmatrix} 1 & \ell & \ell+1 \\ 1 & J & \ell+1 \end{Bmatrix} = \Delta(1,J,1+\ell)\,(-1)^{\ell+J} \\
&\times \left[\frac{2(2\ell)!(\ell+J+3)!(\ell+J)!(\ell-J+2)!(J+\ell)!2}{(2\ell+3)!(J-\ell)!(J-\ell)!(\ell-J+2)!(J+\ell+3)!(2\ell)!(2\ell+3)!}\right]^{\frac{1}{2}} \\
&= \Delta(1,J,1+\ell)\,(-1)^{\ell+J}\frac{2(\ell+J)!}{(2\ell+3)!(J-\ell)!} \\
&= \frac{\Theta_{J-2}\,\delta^{\ell,J-2}}{2J-1} - \frac{\Theta_{J-1}\,\delta^{\ell,J-1}}{(2J+1)J} + \frac{\delta^{\ell J}}{(2J+3)(J+1)(2J+1)} \quad .
\end{aligned}
\tag{C.35}
$$

Inserting the relations (C.33)-(C.35) into eq. (C.30), we end up with:

$$
\begin{aligned}
&\sum_\ell (2\ell+1) C^{\ell_1 0}_{10;\ell 0} C^{\ell_2 0}_{10;\ell 0} \begin{Bmatrix} 1 & J & \ell_1 \\ 1 & \ell & \ell_2 \end{Bmatrix} Q_\ell \\
&= \frac{\Theta_{J-1}J}{(2J+1)J(2J-1)}\,\delta^{\ell_1 J-1}\delta^{\ell_2 J-1}\,Q_J + \frac{\Theta_{J-1}(J+1)}{(J+1)(2J+1)}\,\delta^{\ell_1 J}\delta^{\ell_2 J}\,Q_{J+1} \\
&+ \frac{(J+2)}{2J+3}\,\delta^{\ell_1 J+1}\delta^{\ell_2 J+1}\,Q_{J+2} - \frac{\Theta_{J-1}\sqrt{J(J+1)}}{2J+1}\,\delta^{\ell_1 J-1}\delta^{\ell_2 J+1}\,Q_J \\
&- \frac{\Theta_{J-1}\sqrt{J(J+1)}}{2J+1}\,\delta^{\ell_1 J+1}\delta^{\ell_2 J-1}\,Q_J + \frac{\Theta_{J-2}(J-1)}{2J-1}\,\delta^{\ell_1 J-1}\delta^{\ell_2 J-1}\,Q_{J-2} \\
&- \frac{\Theta_{J-1}J}{(2J+1)J}\,\delta^{\ell_1 J}\delta^{\ell_2 J}\,Q_{J-1} + \frac{(J+1)}{(2J+3)(J+1)(2J+1)}\,\delta^{\ell_1 J+1}\delta^{\ell_2 J+1}\,Q_J \\
&= \frac{1}{2J+1}\begin{pmatrix} \frac{\Theta_{J-2}(J-1)(2J+1)Q_{J-2}}{2J-1}+\frac{\Theta_{J-1}Q_J}{2J-1} & 0 & -\Theta_{J-1}\sqrt{J(J+1)}Q_J \\ 0 & \Theta_{J-1}(Q_{J+1}-Q_{J-1}) & 0 \\ -\Theta_{J-1}\sqrt{J(J+1)}Q_J & 0 & \frac{Q_J}{2J+3}+\frac{(J+2)(2J+1)Q_{J+2}}{2J+3} \end{pmatrix}^{\ell_1\ell_2} \quad .
\end{aligned}
\tag{C.36}
$$

Inserting both analytic expressions (C.29) and (C.36) into eq. (C.27), we see that the (3×3)-matrix $R^{[J]}$ decomposes into two blocks $R^{[J]} = R^{[J^+]} \oplus R^{[J^-]}$: The four corners of $R^{[J]}$ have positive parity and are the components of the (2×2)-matrix:

$$
\begin{aligned}
R^{[J^+]}_{ij} &= \nu\kappa_{ij}\,(g_i g_j)\,\sqrt{\mu_i\mu_j}\,\frac{(-1)^J}{2J+1}\begin{pmatrix} \Theta_{J-1} & 0 \\ 0 & 1 \end{pmatrix} \\
&\times \begin{pmatrix} \omega_{ij}\frac{(J-1)(2J+1)}{2J-1}Q_{J-2} - J\left(\sqrt{\frac{\mu_i}{\mu_j}}\frac{p}{k}+\sqrt{\frac{\mu_j}{\mu_i}}\frac{k}{p}\right)Q_{J-1} + \left(\frac{\omega_{ij}}{2J-1}+\frac{J}{\omega_{ij}}\right)Q_J & \sqrt{J(J+1)}\left[\sqrt{\frac{\mu_j}{\mu_i}}\frac{k}{p}Q_{J-1} - \left(\omega_{ij}+\frac{1}{\omega_{ij}}\right)Q_J + \sqrt{\frac{\mu_i}{\mu_j}}\frac{p}{k}Q_{J+1}\right] \\ \sqrt{J(J+1)}\left[\sqrt{\frac{\mu_i}{\mu_j}}\frac{p}{k}Q_{J-1} - \left(\omega_{ij}+\frac{1}{\omega_{ij}}\right)Q_J + \sqrt{\frac{\mu_j}{\mu_i}}\frac{k}{p}Q_{J+1}\right] & \left(\frac{\omega_{ij}}{2J+3}+\frac{J+1}{\omega_{ij}}\right)Q_J - (J+1)\left(\sqrt{\frac{\mu_i}{\mu_j}}\frac{p}{k}+\sqrt{\frac{\mu_j}{\mu_i}}\frac{k}{p}\right)Q_{J+1} + \omega_{ij}\frac{(J+2)(2J+1)}{2J+3}Q_{J+2} \end{pmatrix}\begin{pmatrix} \Theta_{J-1} & 0 \\ 0 & 1 \end{pmatrix} \\
&- \delta_{1i}\delta_{1j}\,\delta^{1J}\,\begin{pmatrix} H & 0 \\ 0 & 0 \end{pmatrix} \quad .
\end{aligned}
\tag{C.37}
$$

The center of $R^{[J]}$ has negative parity and is a scalar in terms of angular momenta:

$$
R^{[J^-]}_{ij} = \nu\kappa_{ij}\,(g_i g_j)\,\sqrt{\mu_i\mu_j}\,\frac{(-1)^J}{2J+1}\,\Theta_{J-1}\,(Q_{J+1}-Q_{J-1}) \quad . \tag{C.38}
$$

Appendix D

Feynman diagrams

D.1 Feynman rules

In this chapter, we calculate amplitudes of Feynman diagrams based on the Lagrangians (2.18), (3.1) and (3.62). Thereby, in our field theoretical approach, each diagram corresponds to an expression of the form $\text{con}\,\langle\ldots\rangle$, which symbolizes that we implicitly sum over all contractions of field operators that appear within the angle brackets. Using Feynman rules in momentum space, every appearing loop with four-momentum $\bar{q}$ leads to an additional integration over $\int \mathrm{d}^4q/(2\pi)^4$.

D.2 P-wave interactions

In this section, we calculate amplitudes of Feynman diagrams that based on the Lagrangian (2.18), which describes a three-body system with two-particle P-wave interactions.

D.2.1 Dimer self-energy

Figure D.1: Dimer self-energy term $-i\Sigma_{ij}^{ab}$, contributing to the full P-wave dimer propagator.

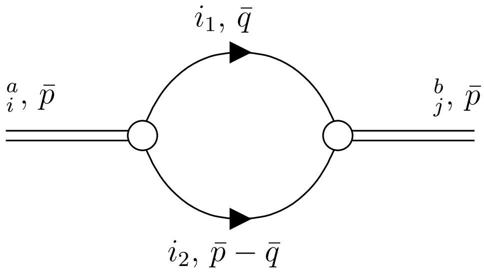

First, we calculate the self-energy $-i\Sigma_{ij}^{ab}$. The corresponding bubble-diagram is depicted in fig. D.1. The matrix element reads:

$$\begin{aligned}
-\, i\Sigma^{ab}_{ij}(\bar{p}) \;&=\; \frac{1}{2!}\,\mathrm{con}\Big\langle\, d^b_j \,\Big|\, (i\mathcal{L}^{(2)})^2 \,\Big|\, d^a_i \,\Big\rangle \\
&= \frac{1}{2!}\,\mathrm{con}\Big\langle\, d^b_j \,\Big|\, \Big[i \sum_{k\in I_2} \sum_{c=1}^{3} \big(-g_k\mu_k\, d^{c\,\dagger}_k \big(\psi_{k_1}\Big(\frac{\overleftrightarrow{i\nabla}}{\hat{m}}\Big)\psi_{k_2}\big)^c \;+\; \mathrm{h.\,c.}\big)\Big]^2 \,\Big|\, d^a_i \,\Big\rangle \\
&= (-i\mu_j g_j)(-i\mu_i g_i)\;\mathrm{con}\Big\langle\, 0 \,\Big|\, \big(\psi_{j_1}\Big(\frac{\overleftrightarrow{i\nabla}}{\hat{m}}\Big)\psi_{j_2}\big)^b \big(\psi_{i_1}\Big(\frac{\overleftrightarrow{i\nabla}}{\hat{m}}\Big)\psi_{i_2}\big)^{\dagger a} \,\Big|\, 0 \,\Big\rangle \\
&= \delta_{ij}(-g_i^2)\;\int \frac{\mathrm{d}^4\bar{q}}{(2\pi)^4} \frac{i\left(\mathbf{q}-\frac{m_{i_1}}{M_i}\mathbf{p}\right)^b}{q^0 - \frac{\mathbf{q}^2}{2m_{i_1}} + i\varepsilon}\; \frac{i\left(\mathbf{q}-\frac{m_{i_1}}{M_i}\mathbf{p}\right)^a}{p^0 - q^0 - \frac{(\mathbf{p}-\mathbf{q})^2}{2m_{i_2}} + i\varepsilon} \quad .
\end{aligned} \tag{D.1}$$

Introducing a three-momentum cut-off Λ_i in the i-channel, we split up the integral according to $\int \mathrm{d}^4\bar{q} = \int_{|\mathbf{q}|<\Lambda_i} \mathrm{d}^3\mathbf{q} \int_{-\infty}^{\infty} \mathrm{d}q^0$. The q^0 contour integration on the real axis can be closed by a lower arc. Since the only pole in the lower complex q^0-plane is located at $\mathbf{q}^2/(2m_{i_1}) - i\varepsilon$, the residue theorem yields:

$$\begin{aligned}
-\,\Sigma^{ab}_{ij}(\bar{p}) \;&=\; (-i)\,\delta_{ij}\,(-\mu_i^2 g_i^2)\, i^2\,(-2\pi i) \int_{|\mathbf{q}|<\Lambda_i} \frac{\mathrm{d}^3\mathbf{q}}{(2\pi)^4} \frac{\left(\mathbf{q}-\frac{m_{i_1}}{M_i}\mathbf{p}\right)^b \left(\mathbf{q}-\frac{m_{i_1}}{M_i}\mathbf{p}\right)^a}{p^0 - \frac{\mathbf{q}^2}{m_{i_1}} - \frac{(\mathbf{p}-\mathbf{q})^2}{2m_{i_2}} + i2\varepsilon} \\
&= -\delta_{ij}\, g_i^2 \int\limits_{|\mathbf{q}|<\Lambda_i} \frac{\mathrm{d}^3 q}{(2\pi)^3} \frac{(\mathbf{q})^b(\mathbf{q})^a}{p^0 - \frac{\mathbf{q}^2}{2\mu_i} - \frac{\mathbf{p}^2}{2M_i} + 2i\varepsilon} \\
&= \delta_{ij}\delta^{ab}\, \frac{g_i^2}{(2\pi)^3} \int_0^{\Lambda_i} \mathrm{d}q\, q^2 \int_0^{2\pi} \mathrm{d}\phi \int_{-1}^{1} \mathrm{d}\cos\theta \frac{(q\cos\theta)^2}{\frac{q^2}{2\mu_i} - p^0 + \frac{\mathbf{p}^2}{2M_i} - 2i\varepsilon} \\
&= \delta_{ij}\delta^{ab}\, \frac{g_i^2\mu_i}{3\pi^2} \int_0^{\Lambda_i} \mathrm{d}q\, \frac{q^4}{q^2 - y_i^2} \quad \text{with} \quad y_i(\bar{p}) \;:=\; \sqrt{2\mu_i\left(p^0 - \frac{\mathbf{p}^2}{2M_i} + i\varepsilon\right)} \\
&= \delta_{ij}\delta^{ab}\, \frac{g_i^2\mu_i}{3\pi^2} \int_0^{\Lambda_i} \mathrm{d}q\, \left[q^2 + y_i^2 - \frac{y_i^3}{2}\left(\frac{1}{q+y_i} - \frac{1}{q-y_i}\right)\right] \\
&= \delta_{ij}\delta^{ab}\, \frac{g_i^2\mu_i}{3\pi^2} \left[\frac{q^3}{3} + y_i^2 q - \frac{y_i^3}{2}\left(\ln(q+y_i) - \ln(q-y_i)\right)\right]_0^{\Lambda_i} \\
&= \delta_{ij}\delta^{ab}\, \frac{g_i^2\mu_i}{3\pi^2} \left[\frac{\Lambda_i^3}{3} + y_i^2\Lambda_i + \frac{y_i^3}{2}\,(i\pi)\right] \;=\; \delta_{ij}\delta^{ab}\, \frac{g_i^2\mu_i}{3\pi^2} \left[\frac{\Lambda_i^3}{3} + \Lambda_i y_i^2(\bar{p}) + \frac{\pi}{2}\, i y_i^3(\bar{p})\right] \quad .
\end{aligned} \tag{D.2}$$

Thereby, we shifted the loop momentum $\mathbf{q} \mapsto \mathbf{q} + \frac{m_{i_1}}{M_i}\mathbf{p}$, chose spherical coordinates for the $\mathrm{d}^3\mathbf{q}$ integration with the z-axis in the a-direction and assumed that the three-momentum cut-off Λ_i is much bigger than all other energy scales. Furthermore, we used the standard definition for the root of a complex number z with $\sqrt{z}^2 = z$ and $\arg(\sqrt{z}) \in (-\pi/2, \pi/2]$. Thus, the real part of the square root is always non-negative. In addition, we took the principal branch of the complex logarithm. We note that the self-energy Σ_{ij}^{ab} is diagonal and constant in the spatial indices a and b.

D.2.2 Dimer-particle interaction

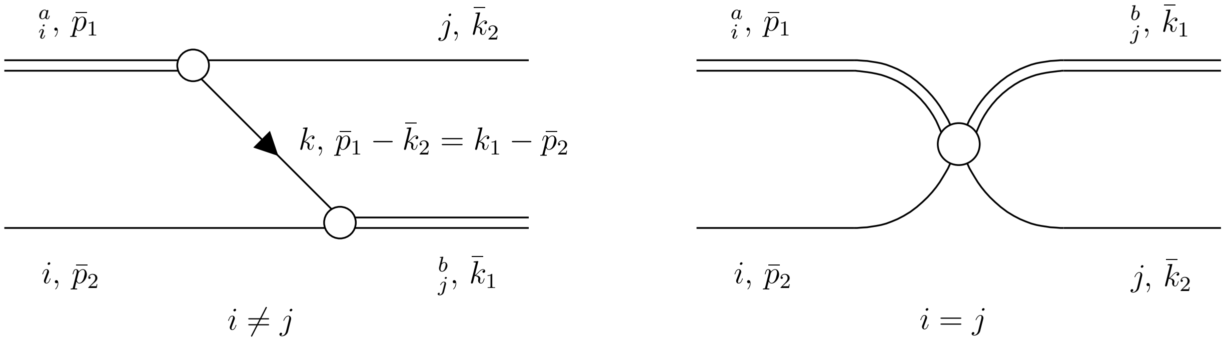

Figure D.2: Dimer particle interaction diagrams. $iR_{ij,\neq}^{ab}$ is constructed out of two two-particle P-wave couplings. $iR_{ij,=}^{ab}$ is the three-particle interaction.

Using center-of-mass kinematics according to eqs. (2.29) and (2.30), we now calculate the amplitude $iR_{ij}^{ab} = iR_{ij,\neq}^{ab} + iR_{ij,=}^{ab}$ of the dimer-particle interaction graph depicted in fig. D.2. Since $\mathbf{P} = 0$ holds, for the first diagram $iR_{ij,\neq}^{ab}$, which is composed of two two-particle couplings and a single-particle propagator, we get:

$$\begin{aligned}
iR_{ij,\neq}^{ab}(\bar{P},\bar{p},\bar{k}) &= \frac{1}{2!}\,\mathrm{con}\Big\langle\, d_j^b\,\psi_j \,\Big|\, (i\mathcal{L}^{(2)})^2 \,\Big|\, d_i^a\,\psi_i \Big\rangle \\
&= \frac{1}{2!}\,\mathrm{con}\Big\langle\, d_j^b \,\Big|\, \Big[i\sum_{k\in I_2}\sum_{c=1}^{3}\big(-g_k\mu_k\, d_{kc}^{\dagger}\big(\psi_{k_1}\Big(\frac{i\overleftrightarrow{\nabla}}{\hat{m}}\Big)\psi_{k_2}\big)^c \;+\; \mathrm{h.\,c.}\big)\Big]^2 \,\Big|\, d_i^a\, \Big\rangle \\
&= (-i\mu_j g_j)(-i\mu_i g_i)\;\mathrm{con}\Big\langle\, \psi_j \,\Big|\, \big(\psi_{j_1}\Big(\frac{i\overleftrightarrow{\nabla}}{\hat{m}}\Big)\psi_{j_2}\big)^b\,\big(\psi_{i_1}\Big(\frac{i\overleftrightarrow{\nabla}}{\hat{m}}\Big)\psi_{i_2}\big)^{\dagger a} \,\Big|\, \psi_i\, \Big\rangle \\
&= (-i)\,\nu\,\kappa_{ij}\;(g_i g_j)\;\frac{\big(\mathbf{k} - \frac{m_j}{M_i}(\mathbf{P}-\mathbf{p})\big)^a\big(\mathbf{p} - \frac{m_i}{M_j}(\mathbf{P}-\mathbf{k})\big)^b}{((E-p^0)-k^0) - \frac{((\mathbf{P}-\mathbf{p})-\mathbf{k})^2}{2m_{ij}} + i\varepsilon} \\
&= (-i)\,\nu\,\kappa_{ij}\;(g_i g_j)\;\frac{\big(\mathbf{k} + \frac{m_j}{M_i}\mathbf{p}\big)^a\big(\mathbf{p} + \frac{m_i}{M_j}\mathbf{k}\big)^b}{E - p^0 + \frac{\mathbf{p}^2}{2m_i} - k^0 + \frac{\mathbf{k}^2}{2m_j} - \frac{\mathbf{p}^2}{2\mu_j} - \frac{\mathbf{k}^2}{2\mu_i} - \frac{\mathbf{p}\cdot\mathbf{k}}{m_{ij}} + i\varepsilon}\quad .
\end{aligned} \tag{D.3}$$

The obtained prefactors are defined as

$$\nu \;:=\; \begin{cases} +1 & : \;\#\text{fermions} \leq 1 \\ -1 & : \;\#\text{fermions} > 1 \end{cases}\quad , \quad \kappa_{ij} \;:=\; \begin{cases} 1 & : \;2 \text{ types} \\ (1-\delta_{ij}) & : \;3 \text{ types} \end{cases}\quad , \tag{D.4}$$

where ν accounts for possible anticommutations of the fields if at least two of them are fermions. κ distinguishes between the cases of two and three different particle types.

Combining this result with the trivial momentum-independent three-particle-interaction part

$$iR^{ab}_{ij,=}(\bar{P},\bar{p},\bar{k}) \;=\; (-i)\,\delta_{1i}\delta_{1j}\delta^{ab}\,H \quad , \tag{D.5}$$

we end up with the full P-wave interaction kernel:

$$\begin{aligned} R^{ab}_{ij}(\bar{P},\bar{p},\bar{k}) \;=\; -\Bigg[\nu\,\kappa_{ij}\,(g_i g_j)\,&\frac{\left(\mathbf{k}+\frac{m_j}{M_i}\mathbf{p}\right)^a\left(\mathbf{p}+\frac{m_i}{M_j}\mathbf{k}\right)^b}{E-p^0+\frac{\mathbf{p}^2}{2m_i}-k^0+\frac{\mathbf{k}^2}{2m_j}-\frac{\mathbf{p}^2}{2\mu_j}-\frac{\mathbf{k}^2}{2\mu_i}-\frac{\mathbf{p}\cdot\mathbf{k}}{m_{ij}}+i\varepsilon} \\ &+\;\delta_{1i}\delta_{1j}\delta^{ab}\,H\Bigg] \quad . \end{aligned} \tag{D.6}$$

This result also holds for off-shell center-of-mass kinematics. If the incoming and outgoing single-particle four-momenta are on-shell, the term $-p^0+\frac{\mathbf{p}^2}{2m_i}-k^0+\frac{\mathbf{k}^2}{2m_j}$ in the denominator vanishes.

D.3 Two-neutron halo EFT with external currents

In this section, we calculate amplitudes of Feynman diagrams based on the Lagrangians (3.1) and (3.62) for a two-neutron halo system with external currents and two-particle S-wave interactions.

D.3.1 Dimer self-energy

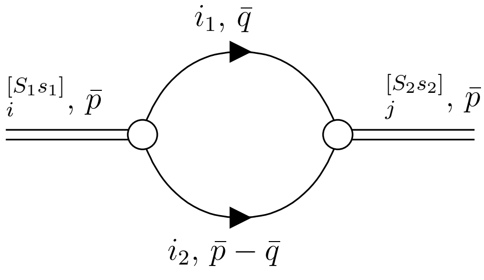

Figure D.3: Dimer self-energy term $-i\Sigma^{[S_1 s_1|S_2 s_2]}_{ij}$, contributing to the full dimer propagator.

We calculate the self-energy $-i\Sigma_{ij}$ corresponding to the bubble-diagram in fig. D.3. First, we denote that $\Sigma^{[S_i s_1|S_j s_2]}_{ij} = \delta_{ij}\delta^{S_i S_j}\delta^{s_1 s_2}\Sigma_i$ is diagonal, where the reduced matrix elements read:

- Σ_0:

$$\begin{aligned} -\,i\Sigma_0(\bar{p}) \;&=\; \frac{1}{2!}\;\mathrm{con}\Big\langle\, d_0 \,\Big|\, (i\mathcal{L}^{(2)})^2 \,\Big|\, d_0 \,\Big\rangle \\ &=\; \frac{1}{2!}\;\mathrm{con}\Big\langle\, d_0 \,\Big|\, \Big(i\frac{g_0}{2}\Big)^2 \Big[d_0^\dagger\,(\vec{\psi}_1^{\,\mathrm{T}} P\,\vec{\psi}_1) + (\vec{\psi}_1^{\,\mathrm{T}} P\,\vec{\psi}_1)^\dagger\, d_0\Big]^2 \,\Big|\, d_0 \,\Big\rangle \\ &=\; -\frac{g_0^2}{4}\,\frac{2}{2!}\sum_{s_1,s_2,s_3,s_4} P^{s_1 s_2}(P^\dagger)^{s_3 s_4}\left[\delta^{s_2 s_3}\delta^{s_1 s_4} - \delta^{s_1 s_3}\delta^{s_2 s_4}\right]\, i\Sigma_0^\circ(\bar{p}) \\ &=\; -\frac{g_0^2}{4}\,2\mathrm{Tr}[PP^\dagger]\; i\Sigma_0^\circ(\bar{p}) \;=\; -\frac{g_0^2}{2}\, i\Sigma_0^\circ(\bar{p}) \quad , \end{aligned} \tag{D.7}$$

- Σ_1:

$$\begin{aligned} -\,i\Sigma_1(\bar{p}) \;&=\; \frac{1}{2!}\;\mathrm{con}\Big\langle\, d_1^s \,\Big|\, (i\mathcal{L}^{(2)})^2 \,\Big|\, d_1^s \,\Big\rangle \\ &=\; \frac{1}{2!}\;\mathrm{con}\Big\langle\, d_1^s \,\Big|\, (ig_1)^2 \Big[\vec{d}_1^\dagger\,\vec{\psi}_1\,\psi_0 \;+\; \psi_0^\dagger\,\vec{\psi}_1^\dagger\,\vec{d}_1\Big]^2 \,\Big|\, d_1^s \,\Big\rangle \\ &=\; -g_1^2\frac{2}{2!}\, i\Sigma_1^\circ(\bar{p}) \;=\; -g_1^2\, i\Sigma_1^\circ(\bar{p}) \quad . \end{aligned} \tag{D.8}$$

The remaining integral $i\Sigma_i^\circ(\bar{p})$ can be evaluated by introducing a three-momentum cut-off Λ_i and applying the residue theorem analogous to eq. (D.2):

$$\begin{aligned} i\Sigma_i^\circ(\bar{p}) \;&=\; \int \frac{\mathrm{d}^4\bar{q}}{(2\pi)^3}\int_{-\infty}^{\infty}\frac{\mathrm{d}q^0}{2\pi}\,\frac{i}{q^0 - \frac{\mathbf{q}^2}{2m_{i_1}} + i\varepsilon}\;\frac{i}{p^0 - q^0 - \frac{(\mathbf{p}-\mathbf{q})^2}{2m_{i_2}} + i\varepsilon} \\ &=\; i\int\limits_{q<\Lambda_i}\frac{\mathrm{d}^3\mathbf{q}}{(2\pi)^3}\,\frac{1}{p^0 - \frac{\mathbf{q}^2}{m_{i_1}} - \frac{(\mathbf{p}-\mathbf{q})^2}{2m_{i_2}} + i2\varepsilon} \;=\; i\int\limits_{q<\Lambda_i}\frac{\mathrm{d}^3\mathbf{q}}{(2\pi)^3}\,\frac{1}{p^0 - \frac{\mathbf{q}^2}{2\mu_i} - \frac{\mathbf{p}^2}{2M_i} + 2i\varepsilon} \\ &=\; -i\frac{4\pi}{(2\pi)^3}(2\mu_i)\int_0^{\Lambda_i}\mathrm{d}q\,\frac{q^2}{q^2 - y_i^2} \quad \text{with} \quad y_i(\bar{p}) \;=\; \sqrt{2\mu_i\Big(p^0 - \frac{\mathbf{p}^2}{2M_i} + i\varepsilon\Big)} \\ &=\; -i\frac{\mu_i}{\pi^2}\int_0^{\Lambda_i}\mathrm{d}q\left[1 - \frac{y_i}{2}\left(\frac{1}{q+y_i} - \frac{1}{q-y_i}\right)\right] \\ &=\; -i\frac{\mu_i}{\pi^2}\left[q - \frac{y_i}{2}\left(\ln(q+y_i) - \ln(q-y_i)\right)\right]_0^{\Lambda_i} \;=\; -i\frac{\mu_i}{\pi^2}\left[\Lambda_i + \frac{y_i(\bar{p})}{2}(i\pi)\right] \quad . \end{aligned} \tag{D.9}$$

Note that the loop momentum was shifted according to $\mathbf{q} \mapsto \mathbf{q} + \frac{m_{i_1}}{M_i}\mathbf{p}$, eliminating the angle $\mathbf{e_p}\cdot\mathbf{e_q}$.

D.3.2 Two particle scattering

We now calculate the full two-particle scattering amplitude it_{ij} that is depicted in fig. D.4. The incoming (outgoing) particles of type i_1 and i_2 (j_1 and j_2) have four-momenta $\bar{p}_1$ and $\bar{p}_2$ ($\bar{k}_1$ and $\bar{k}_2$). Denoting its total four-momentum by $\bar{P} = \bar{p}_1 + \bar{p}_2 = \bar{k}_1 + \bar{k}_2$, the only non-vanishing matrix elements are the diagonal ones:

Figure D.4: Feynman graph for the two-particle scattering matrix element $it_{ij}(\bar{p}_1, \bar{p}_2, \bar{k}_1, \bar{k}_2)$.

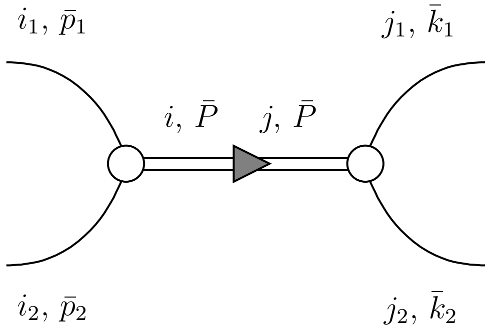

- t_{00}:

$$\begin{aligned}
it_{00}^{[00|00]}(\bar{p}_1, \bar{p}_2, \bar{k}_1, \bar{k}_2) \;&=\; \frac{1}{2!}\,\mathrm{con}\left\langle (\vec{\psi}_1^{\,\mathrm{T}} P\,\vec{\psi}_1) \middle| (i\mathcal{L}^{(2)})^2 \middle| (\vec{\psi}_1^{\,\mathrm{T}} P\,\vec{\psi}_1) \right\rangle \\
=\; \left(-i\frac{g_0}{2}\right)^2 \frac{2}{2!}\,&\mathrm{con}\left\langle (\vec{\psi}_1^{\,\mathrm{T}} P\,\vec{\psi}_1) \middle| \left((\vec{\psi}_1^{\,\mathrm{T}} P\,\vec{\psi}_1)^\dagger d_0\right)\,\left(d_0^\dagger(\vec{\psi}_1^{\,\mathrm{T}} P\,\vec{\psi}_1)\right) \middle| (\vec{\psi}_1^{\,\mathrm{T}} P\,\vec{\psi}_1) \right\rangle \\
=\; -\frac{g_0^2}{4} \sum_{s_1,s_2,s_3,s_4} &P^{s_1 s_2}(P^\dagger)^{s_3 s_4}\left[\delta^{s_2 s_3}\delta^{s_1 s_4} - \delta^{s_1 s_3}\delta^{s_2 s_4}\right] \\
&\times\; P^{s_5 s_6}(P^\dagger)^{s_7 s_8}\left[\delta^{s_6 s_7}\delta^{s_5 s_8} - \delta^{s_5 s_7}\delta^{s_6 s_8}\right]\; D_0(\bar{P}) \\
=\; -\frac{g_0^2}{4}\,&\left(2\mathrm{Tr}\left[PP^\dagger\right]\right)^2 iD_0(\bar{P}) \;=\; -g_0^2\, iD_0(\bar{P}) \quad ,
\end{aligned} \tag{D.10}$$

- t_{11}:

$$\begin{aligned}
it_{11}^{[\frac{1}{2}s_1|\frac{1}{2}s_2]}(\bar{p}_1, \bar{p}_2, \bar{k}_1, \bar{k}_2) \;&=\; \frac{1}{2!}\,\mathrm{con}\left\langle (\psi_1^{s_2}\psi_0) \,\middle|\, (i\mathcal{L}^{(2)})^2 \,\middle|\, (\psi_1^{s_1}\psi_0) \right\rangle \\
=\; -g_1^2\frac{2}{2!}\,&\mathrm{con}\left\langle (\psi_1^{s_2}\psi_0) \,\middle|\, \left(\psi_0^\dagger\,\vec{\psi}_1^\dagger\,\vec{d}_1\right)\,\left(\vec{d}_1^\dagger\,\vec{\psi}_1\,\psi_0\right) \,\middle|\, (\psi_1^{s_1}\psi_0) \right\rangle \\
=\; -g_1^2\,\delta^{s_1 s_2}\, &iD_1(\bar{P}) \quad .
\end{aligned} \tag{D.11}$$

D.3.3 Dimer-particle interaction

Using general kinematics (3.16)-(3.17), we now calculate the amplitude iR_{ij} of the dimer-particle interaction graph depicted in fig. D.5. The expressions for the four possible cases read:

- R_{00}:

$$\begin{aligned}
iR_{00}^{[00;00|00;00]}(\bar{P}, \bar{p}, \bar{k}) \;&=\; \frac{1}{2!}\,\mathrm{con}\left\langle \psi_0\, d_0 | (i\mathcal{L}^{(3)})^2 | \psi_0\, d_0 \right\rangle \\
=\; (-ih)^2\frac{2}{2!}\,&\mathrm{con}\left\langle \psi_0\, d_0 \right| \left((\psi_0\, d_0)^\dagger t\right)\,\left(t^\dagger(\psi_0\, d_0)\right) \left| \psi_0\, d_0 \right\rangle \;=\; -i\frac{h^2}{\Xi} \;=:\; -iH
\end{aligned} \tag{D.12}$$

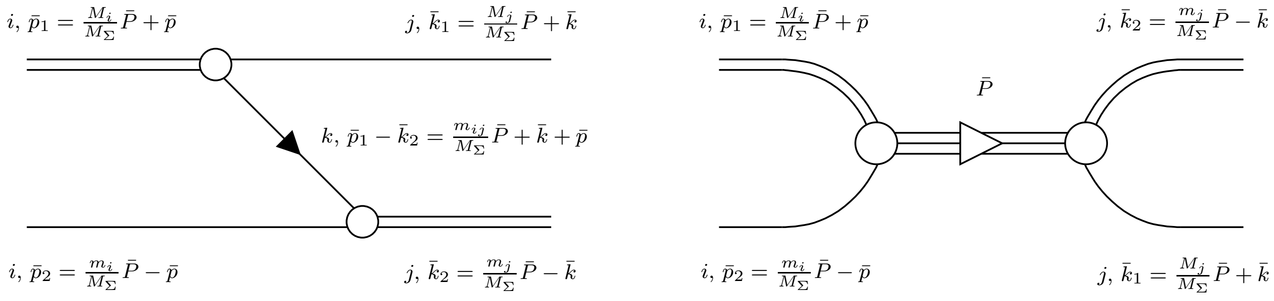

$(i,j) \neq (0,0)$ $(i,j) = (0,0)$

Figure D.5: Dimer particle interaction diagrams iR_{ij}. The part with $(i,j) \neq (0,0)$ is constructed out of two two-particle S-wave couplings. The channel $(i,j) = (0,0)$ includes the three-particle interaction.

- R_{01}:

$$\begin{aligned}
iR_{01}^{[00;00|\frac{1}{2}s_3;\frac{1}{2}s_4]}(\bar{P},\bar{p},\bar{k}) &= \frac{1}{2!}\,\mathrm{con}\left\langle \psi_1^{s_4} d_1^{s_3} \middle| (i\mathcal{L}^{(2)})^2 \middle| \psi_0 d_0 \right\rangle \\
= \left(-\frac{g_0 g_1}{2}\right) &\frac{2}{2!}\mathrm{con}\left\langle \psi_1^{s_4} d_1^{s_3} \middle| \left((\vec{\psi}_1^{\,\mathrm{T}} P \vec{\psi}_1)^\dagger d_0\right) \left((\vec{d}_1^{\,\dagger} \vec{\psi}_1)\psi_0\right) \middle| \psi_0 d_0 \right\rangle \\
= \left(-\frac{g_0 g_1}{2}\right) &\sum_{s_5,s_6,s_7} \delta^{s_4 s_7} (P^\dagger)^{s_5 s_6} \left[\delta^{s_3 s_5}(-\delta^{s_6 s_7}) - \delta^{s_3 s_6}(-\delta^{s_5 s_7})\right] \\
\times &\frac{i}{\frac{m_{01}}{M_\Sigma}P^0 + p^0 + k^0 - \frac{\left(\frac{m_{01}}{M_\Sigma}\mathbf{P}+\mathbf{p}+\mathbf{k}\right)^2}{2m_{01}} + i\varepsilon} \\
= &\frac{-i(g_0 g_1)\, C^{00}_{\frac{1}{2}s_3;\frac{1}{2}s_4}}{\frac{m_{01}}{M_\Sigma}P^0 + p^0 + k^0 - \frac{\left(\frac{m_{01}}{M_\Sigma}\mathbf{P}+\mathbf{p}+\mathbf{k}\right)^2}{2m_{01}} + i\varepsilon}\,,
\end{aligned} \tag{D.13}$$

where we used

$$\begin{aligned}
&\frac{1}{2}\sum_{s_5,s_6,s_7} \delta^{s_4 s_7} (P^\dagger)^{s_5 s_6} \left[\delta^{s_3 s_5}(-\delta^{s_6 s_7}) - \delta^{s_3 s_6}(-\delta^{s_5 s_7})\right] \\
&= \frac{1}{2}\left[(P^\dagger)^{s_4 s_3} - (P^\dagger)^{s_3 s_4}\right] = P^{s_3 s_4} = C^{00}_{\frac{1}{2}s_3;\frac{1}{2}s_4}\,.
\end{aligned} \tag{D.14}$$

- R_{10}: Due to symmetry, we know that the following identity holds:

$$\begin{aligned}
iR_{10}^{[\frac{1}{2}s_1;\frac{1}{2}s_2|00;00]}(\bar{P},\bar{p},\bar{k}) &= iR_{01}^{[00;00|\frac{1}{2}s_1;\frac{1}{2}s_1]}(\bar{P},\bar{k},\bar{p}) \\
= &\frac{-i(g_1 g_0)\, C^{00}_{\frac{1}{2}s_1;\frac{1}{2}s_2}}{\frac{m_{10}}{M_\Sigma}P^0 + p^0 + k^0 - \frac{\left(\frac{m_{10}}{M_\Sigma}\mathbf{P}+\mathbf{p}+\mathbf{k}\right)^2}{2m_{10}} + i\varepsilon}\,.
\end{aligned} \tag{D.15}$$

- R_{11}:

$$\begin{aligned}
i\, R_{11}^{[\frac{1}{2}s_1;\frac{1}{2}s_2|\frac{1}{2}s_3;\frac{1}{2}s_4]}(\bar{P},\bar{p},\bar{k}) \;&=\; \frac{1}{2!}\,\mathrm{con}\left\langle \psi_1^{s_4} d_1^{s_3} \right| (i\mathcal{L}^{(2)})^2 \left| \psi_1^{s_2} d_1^{s_1} \right\rangle \\
=\; (-g_1^2)\,\frac{2}{2!}\,\mathrm{con}&\left\langle \psi_1^{s_4} d_1^{s_3} \right| \left((\vec{d}_1^{\dagger}\, \vec{\psi}_1)\psi_0 \right) \left(\psi_0^{\dagger} (\vec{\psi}_1^{\dagger}\, \vec{d}_1) \right) \left| \psi_1^{s_2} d_1^{s_1} \right\rangle \\
=\; (-g_1^2)\; \sum_{s_5,s_6} & \delta^{s_3 s_5}\delta^{s_6 s_1}\; (-\delta^{s_4 s_6})\delta^{s_5 s_2} \\
\times\; & \frac{i}{\frac{m_{11}}{M_\Sigma}P^0 + p^0 + k^0 - \frac{\left(\frac{m_{11}}{M_\Sigma}\mathbf{P}+\mathbf{p}+\mathbf{k}\right)^2}{2m_{11}} + i\varepsilon} \\
=\; & \frac{-i(g_1^2)\;(-\delta^{s_2 s_3}\delta^{s_4 s_1})}{\frac{m_{11}}{M_\Sigma}P^0 + p^0 + k^0 - \frac{\left(\frac{m_{11}}{M_\Sigma}\mathbf{P}+\mathbf{p}+\mathbf{k}\right)^2}{2m_{11}} + i\varepsilon} \quad .
\end{aligned} \tag{D.16}$$

- R_{ij}: Using the relation for the real part of the denominator

$$\frac{m_{ij}}{M_\Sigma}P^0 + \epsilon_{i,\mathbf{p}} + \epsilon_{j,\mathbf{k}} - \frac{\left(\frac{m_{ij}}{M_\Sigma}\mathbf{P}+\mathbf{p}+\mathbf{k}\right)^2}{2m_{ij}} = E - \frac{\mathbf{p}^2}{2\mu_j} - \frac{\mathbf{k}^2}{2\mu_i} - \frac{\mathbf{p}\cdot\mathbf{k}}{m_{ij}} \tag{D.17}$$

and defining out the spin factors

$$\begin{pmatrix} \sigma_{00}^{[00;00|00;00]} & \sigma_{01}^{[00;00|\frac{1}{2}s_3;\frac{1}{2}s_4]} \\ \sigma_{10}^{[\frac{1}{2}s_1;\frac{1}{2}s_2|00;00]} & \sigma_{11}^{[\frac{1}{2}s_1;\frac{1}{2}s_2|\frac{1}{2}s_3;\frac{1}{2}s_4]} \end{pmatrix} := \begin{pmatrix} 0 & C^{00}_{\frac{1}{2}s_3;\frac{1}{2}s_4} \\ C^{00}_{\frac{1}{2}s_1;\frac{1}{2}s_2} & -\delta^{s_2 s_3}\delta^{s_4 s_1} \end{pmatrix} \quad , \tag{D.18}$$

we summarize the results (D.12)-(D.16) through the compact formula:

$$\begin{aligned}
&R_{ij}^{[S_i s_1;S_i s_2|S_j s_3;S_j s_4]}(\bar{P},\bar{p},\bar{k}) \\
&\quad = -\left[\frac{\sigma_{ij}^{[S_i s_1;S_i s_2|S_j s_3;S_j s_4]}\; g_i g_j}{E + p^0 - \epsilon_{i,\mathbf{p}} + k^0 - \epsilon_{j,\mathbf{k}} - \frac{\mathbf{p}^2}{2\mu_j} - \frac{\mathbf{k}^2}{2\mu_i} - \frac{\mathbf{p}\cdot\mathbf{k}}{m_{ij}} + i\varepsilon} \;+\; \delta_{i0}\,\delta_{j0}\,H \right] \quad .
\end{aligned} \tag{D.19}$$

D.3.4 Form factor contributions

We now calculate all three parts $\mathcal{F}_{\mathrm{E},0}$, $\mathcal{F}_{\mathrm{E},1}$ and $\mathcal{F}_{\mathrm{E},2}$, which contribute to the electric form factor $\mathcal{F}_{\mathrm{E}} = \sum_{i=0}^{2} \mathcal{F}_{\mathrm{E},i}$, individually. In fig. 3.9, the corresponding equation (3.64) is represented in terms of Feynman graphs. The total four-momenta of the incoming and outgoing trimer bound states are $\bar{P}$ and $\bar{K}$, respectively. The four-momentum transfer then reads $\bar{Q} = \bar{K} - \bar{P}$. Energy conservation implies:

$$E(\bar{K}) + \frac{\mathbf{K}^2}{2M_\Sigma} \;=\; K^0 \;=\; P^0 + Q^0 \;=\; E(\bar{P}) + \frac{\mathbf{P}^2}{2M_\Sigma} + Q^0 \quad . \tag{D.20}$$

For intermediate dimer-particle states that occur in Feynman diagrams, we always use the shifted kinematics (3.17) in order to incorporate the matrix elements derived in sec. 3.1.4. Furthermore, throughout the form factor calculations, we will use the linear combinations

$$\bar{J}_{\pm} := \frac{\bar{K} \pm \bar{P}}{2} \quad . \tag{D.21}$$

The four-momentum transfer then reads $\bar{Q} = 2\bar{J}_{-}$.

D.3.4.1 Breit frame

We perform our calculations in the Breit frame where no energy is transferred, i.e. $Q^0 = 0$. Since the process is assumed to be elastic, the binding energies are equal $E(\bar{P}) = E(\bar{K}) = E = E^{(3)} < 0$. In combination with eqs. (D.20) and (D.21), this implies the conditions:

$$J_{-}^{0} = 0 \quad , \qquad \mathbf{P}^2 = \mathbf{K}^2 \;\Rightarrow\; \mathbf{J}_{+} \cdot \mathbf{J}_{-} = 0 \quad . \tag{D.22}$$

Thus, only the orientation of the trimer three-momentum can change. Using the relation (D.22) will significantly simplify many expressions in the below calculations.

D.3.4.2 Parallel term

Figure D.6: The $i\Gamma_0$ contribution to the form factor matrix element. The photon couples to a core field propagating parallel to the nn-dimer. It corresponds to the first term in the sum on the right-hand side of the lower equation in fig. 3.9.

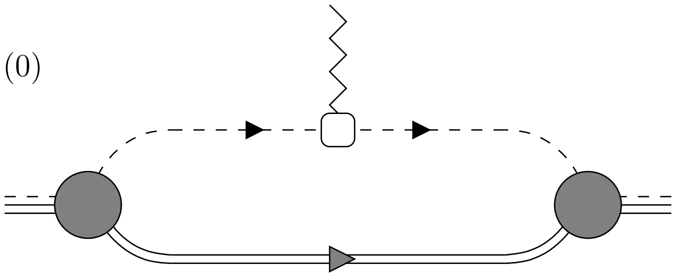

We begin with the calculation of $\mathcal{F}_{\mathrm{E},0}$, represented in fig. D.6. The charged core propagates parallel to the nn-dimer. The corresponding reduced matrix element $i\Gamma_0^{\mathrm{red}}$ is the first summand on the right-hand side of the lower equation in fig. 3.9. Using eq. (3.65), its renormalized version reads:

$$\begin{aligned} i\bar{\Gamma}_0^{\mathrm{red}}(\bar{P},\bar{K},\bar{p},\bar{k}) \;&=\; (\mathcal{Z}e)^{-1}\,|Z_0|^{-\frac{1}{2}}\;\frac{i}{\epsilon_0(\bar{P},\mathbf{p}) - p^0 + i\varepsilon}\;(-i\mathcal{Z}e)\;\frac{i}{\epsilon_0(\bar{K},\mathbf{k}) - k^0 + i\varepsilon} \\ &\quad\times\; iD_0(\bar{P},\bar{p})\;(2\pi)^4\delta^{(4)}\Big(\big(\frac{M_0}{M_\Sigma}\bar{P} + \bar{p}\big) - \big(\frac{M_0}{M_\Sigma}\bar{K} + \bar{k}\big)\Big)\;|Z_0|^{-\frac{1}{2}} \\ &=\; i\frac{i\bar{D}_0(\bar{P},\bar{p})}{(\epsilon_0(\bar{P},\mathbf{p}) - p^0 + i\varepsilon)(\epsilon_0(\bar{K},\mathbf{k}) - k^0 + i\varepsilon)}\;(2\pi)^4\delta^{(4)}\Big(\bar{k} - \big(\bar{p} - \frac{M_0}{M_\Sigma}\bar{Q}\big)\Big) \quad . \end{aligned} \tag{D.23}$$

Inserting eq. (D.23) into eq. (3.9), the $\delta^{(4)}$-function eliminates the $\mathrm{d}^4\bar{k}$ intergral:

$$\begin{aligned}\mathcal{F}_{\mathrm{E},0}(\bar{P},\bar{K}) &= \int\limits_{p<\Lambda} \frac{\mathrm{d}^4\bar{p}}{(2\pi)^4}\, \frac{i\,\bar{G}_0(\bar{P},\bar{p})\;\bar{D}_0(\bar{P},\bar{p})\;\bar{G}_0(\bar{K},\bar{p}-\frac{M_0}{M_\Sigma}\bar{Q})}{(\epsilon_0(\bar{P},\mathbf{p})-p^0+i\varepsilon)(\epsilon_0(\bar{K},\mathbf{p}-\frac{M_0}{M_\Sigma}\mathbf{Q})-p^0+i\varepsilon)} \\ &= \int\limits_{q<\Lambda} \frac{\mathrm{d}^4\bar{q}}{(2\pi)^4}\, \frac{i\,\bar{G}_0(\bar{P},\bar{q}+\bar{r})\;\bar{D}_0(\bar{J}_-,\bar{q})\;\bar{G}_0(\bar{K},\bar{q}-\bar{r})}{(\epsilon_0(\bar{P},\mathbf{q}+\mathbf{r})-q^0+i\varepsilon)(\epsilon_0(\bar{K},\mathbf{q}-\mathbf{r})-q^0+i\varepsilon)} \quad .\end{aligned} \tag{D.24}$$

In the last step we shifted the loop integration via the substitution $\bar{q} := \bar{p} - \bar{r}$ with

$$\bar{r} \;:=\; \frac{M_0}{M_\Sigma}\,\bar{J}_- \;=\; \frac{M_0}{M_\Sigma}\frac{\bar{Q}}{2} \;=\; \frac{m_1}{M_\Sigma}\bar{Q} \qquad \Rightarrow \qquad r^0 \;=\; 0 \quad , \qquad r \ll \Lambda \quad . \tag{D.25}$$

In addition, we used the identity

$$\frac{M_0}{M_\Sigma}\bar{P} + \bar{p} \;=\; \frac{M_0}{M_\Sigma}\bar{J}_+ + \bar{q} \qquad \Rightarrow \qquad \bar{D}_0(\bar{P},\bar{p}) \;=\; \bar{D}_0(\bar{J}_+,\bar{q}) \tag{D.26}$$

in order to rewrite the full dimer propagator. Inserting eq. (3.22) and the integral equation (3.54) for the irreducible trimer-dimer-particle coupling, the interim result (D.24) assumes the form:

$$\begin{aligned}\mathcal{F}_{\mathrm{E},0}(\bar{P},\bar{K}) &= \int\limits_{q<\Lambda} \frac{\mathrm{d}^3\mathbf{q}}{(2\pi)^3} \int_{-\infty}^{\infty} \frac{\mathrm{d}q^0}{2\pi} \\ &\times \Big(\sum_{i=0}^{1} \int_0^\Lambda \mathrm{d}p\, \bar{G}_i(p)\, \bar{D}_i^{[0]}(p)\, {}^{\bullet}\bar{R}_{i0}^{[0]}(E^{(3)}+q^0-\epsilon_0(\bar{P},\mathbf{q}+\mathbf{r}),p,|\mathbf{q}+\mathbf{r}|) \;-\; |\beta\bar{H}|\Big) \\ &\times \frac{i\,\bar{D}_0(E^{(3)}+q^0-\epsilon_0(\bar{J}_+,\mathbf{q}),q)}{(\epsilon_0(\bar{P},\mathbf{q}+\mathbf{r})-q^0+i\varepsilon)(\epsilon_0(\bar{K},\mathbf{q}-\mathbf{r})-q^0+i\varepsilon)} \\ &\times \Big(\sum_{j=0}^{1} \int_0^\Lambda \mathrm{d}k\, {}^{\bullet}\bar{R}_{0j}^{[0]}(E^{(3)}+q^0-\epsilon_0(\bar{K},\mathbf{q}-\mathbf{r}),|\mathbf{q}-\mathbf{r}|,k)\, \bar{D}_j^{[0]}(k)\, \bar{G}_j(k) \;-\; |\beta\bar{H}|\Big) \quad .\end{aligned} \tag{D.27}$$

Note that we used the convention (1.21).

Symmetrization: In order to symmetrize and evaluate the integral (D.27), we define linear combinations of the appearing off-shell energies via: $\epsilon_\pm := \frac{1}{2}[\epsilon_0(\bar{K},\mathbf{q}-\mathbf{r}) \pm \epsilon_0(\bar{P},\mathbf{q}+\mathbf{r})]$. Using the identity

$$\frac{1}{2}\left\{(\mathbf{a}-\mathbf{q})^2 \pm (\mathbf{b}-\mathbf{q})^2\right\} \;=\; \begin{cases} \left(\frac{\mathbf{a}+\mathbf{b}}{2}-\mathbf{q}\right)^2 + \left(\frac{\mathbf{a}-\mathbf{b}}{2}\right)^2 \\ \left(\frac{\mathbf{a}+\mathbf{b}}{2}-\mathbf{q}\right)(\mathbf{a}-\mathbf{b}) \end{cases} \tag{D.28}$$

for arbitrary vector $\mathbf{a}, \mathbf{b}, \mathbf{q} \in \mathbb{R}^3$, we can express $\epsilon_\pm$ through:

$$\begin{aligned}
\epsilon_+ &= \frac{1}{2}\left[\frac{m_0}{M_\Sigma}K^0 - \frac{\left(\frac{m_0}{M_\Sigma}\mathbf{K} - (\mathbf{q}-\mathbf{r})\right)^2}{2m_0} + \frac{m_0}{M_\Sigma}P^0 - \frac{\left(\frac{m_0}{M_\Sigma}\mathbf{P} - (\mathbf{q}+\mathbf{r})\right)^2}{2m_0}\right] \\
&= \frac{m_0}{M_\Sigma}J_+^0 - \frac{1}{2m_0}\frac{1}{2}\left[\left((\frac{m_0}{M_\Sigma}\mathbf{K} + \mathbf{r}) - \mathbf{q}\right)^2 + \left((\frac{m_0}{M_\Sigma}\mathbf{P} - \mathbf{r}) - \mathbf{q}\right)^2\right] \\
&= \frac{m_0}{M_\Sigma}J_+^0 - \frac{1}{2m_0}\left[\left(\frac{(\frac{m_0}{M_\Sigma}\mathbf{K} + \mathbf{r}) + (\frac{m_0}{M_\Sigma}\mathbf{P} - \mathbf{r})}{2} - \mathbf{q}\right)^2\right. \\
&\qquad\qquad\qquad\qquad\left. + \left(\frac{(\frac{m_0}{M_\Sigma}\mathbf{K} + \mathbf{r}) - (\frac{m_0}{M_\Sigma}\mathbf{P} - \mathbf{r})}{2}\right)^2\right] \\
&= \frac{m_0}{M_\Sigma}J_+^0 - \frac{\left(\frac{m_0}{M_\Sigma}\mathbf{J}_+ - \mathbf{q}\right)^2}{2m_0} - \frac{\mathbf{J}_-^2}{2m_0} = \epsilon_0(\bar{J}_+, \mathbf{q}) - \frac{m_0\,\mathbf{r}^2}{2\bar{\mu}_0^2} \quad ,
\end{aligned} \tag{D.29}$$

$$\begin{aligned}
\epsilon_- &= \frac{1}{2}\left[\frac{m_0}{M_\Sigma}K^0 - \frac{\left(\frac{m_0}{M_\Sigma}\mathbf{K} - (\mathbf{q}-\mathbf{r})\right)^2}{2m_0} - \frac{m_0}{M_\Sigma}P^0 + \frac{\left(\frac{m_0}{M_\Sigma}\mathbf{P} - (\mathbf{q}+\mathbf{r})\right)^2}{2m_0}\right] \\
&= \frac{m_0}{M_\Sigma}J_-^0 - \frac{1}{2m_0}\frac{1}{2}\left[\left((\frac{m_0}{M_\Sigma}\mathbf{K} + \mathbf{r}) - \mathbf{q}\right)^2 - \left((\frac{m_0}{M_\Sigma}\mathbf{P} - \mathbf{r}) - \mathbf{q}\right)^2\right] \\
&= \frac{m_0}{M_\Sigma}J_-^0 - \frac{1}{2m_0}\left(\frac{\left(\frac{m_0}{M_\Sigma}\mathbf{P} - \mathbf{r}\right) + \left(\frac{m_0}{M_\Sigma}\mathbf{K} + \mathbf{r}\right)}{2} - \mathbf{q}\right) \\
&\qquad\qquad\qquad\qquad \times \left(\left(\frac{m_0}{M_\Sigma}\mathbf{K} + \mathbf{r}\right) - \left(\frac{m_0}{M_\Sigma}\mathbf{P} - \mathbf{r}\right)\right) \\
&= \frac{m_0}{M_\Sigma}J_-^0 - \frac{\left(\frac{m_0}{M_\Sigma}\mathbf{J}_+ - \mathbf{q}\right)\cdot 2\mathbf{J}_-}{2m_0} = \frac{\mathbf{q}\cdot\mathbf{r}}{\bar{\mu}_0} \quad .
\end{aligned} \tag{D.30}$$

For the last equation, the Breit frame conditions (D.22) were crucial. From eqs. (D.29) and (D.30) one can directly deduce:

$$\begin{aligned}
\epsilon_+ - \epsilon_0(\bar{J}_+, \mathbf{q}) &= -\frac{m_0\,\mathbf{r}^2}{2\bar{\mu}_0^2} \quad , \\
\epsilon_+ \pm \epsilon_- &= \begin{cases} \epsilon_0(\bar{K}, \mathbf{q}-\mathbf{r}) \\ \epsilon_0(\bar{P}, \mathbf{q}+\mathbf{r}) \end{cases} \quad \Rightarrow \quad \pm\frac{\mathbf{q}\cdot\mathbf{r}}{\bar{\mu}_0} = \begin{cases} \epsilon_0(\bar{K}, \mathbf{q}-\mathbf{r}) - \epsilon_+ \\ \epsilon_0(\bar{P}, \mathbf{q}+\mathbf{r}) - \epsilon_+ \end{cases} \quad .
\end{aligned} \tag{D.31}$$

Using these relations, we can shift the energy integration over q^0 in eq. (D.27) according to $q^0 \mapsto q^0 + \epsilon_+$, yielding:

$$
\begin{aligned}
\mathcal{F}_{\mathrm{E},0}(\bar{P},\bar{K}) \;=\; & \int\limits_{q<\Lambda} \frac{\mathrm{d}^3\mathbf{q}}{(2\pi)^3} \int_{-\infty}^{\infty} \frac{\mathrm{d}q^0}{2\pi} \\
& \times \Big(\int_0^\Lambda \mathrm{d}p\; \bar{G}(p)^{\mathrm{T}}\, \bar{D}^{[0]}(p)\, {}^{\bullet}\!\bar{R}^{[0]}(E^{(3)} + q^0 + \frac{\mathbf{q}\cdot\mathbf{r}}{\bar{\mu}_0}, p, |\mathbf{q}+\mathbf{r}|) \;-\; |\beta\bar{H}|\,\mathbf{e}_0^{\mathrm{T}}\Big) \\
& \times (\mathbf{e}_0\cdot\mathbf{e}_0^{\mathrm{T}})\; \frac{i\,\bar{D}(E^{(3)} + q^0 - \frac{m_0\,\mathbf{r}^2}{2\bar{\mu}_0^2}, q)}{(-\frac{\mathbf{q}\cdot\mathbf{r}}{\bar{\mu}_0} - q^0 + i\varepsilon)(\frac{\mathbf{q}\cdot\mathbf{r}}{\bar{\mu}_0} - q^0 + i\varepsilon)}\; (\mathbf{e}_0\cdot\mathbf{e}_0^{\mathrm{T}}) \\
& \times \Big(\int_0^\Lambda \mathrm{d}k\, {}^{\bullet}\!\bar{R}^{[0]}(E^{(3)} + q^0 - \frac{\mathbf{q}\cdot\mathbf{r}}{\bar{\mu}_0}, |\mathbf{q}-\mathbf{r}|, k)\, \bar{D}^{[0]}(k)\, \bar{G}(k) \;-\; |\beta\bar{H}|\,\mathbf{e}_0\Big) \quad .
\end{aligned}
\tag{D.32}
$$

Note that we wrote the equation in its (2 × 2)-matrix form. The appearing projection matrix $(\mathbf{e}_0\cdot\mathbf{e}_0^{\mathrm{T}})$ has components $(\mathbf{e}_0\cdot\mathbf{e}_0^{\mathrm{T}})_{ij} = \delta_{i0}\delta_{j0}$. Consequently, $(\mathbf{e}_0\cdot\mathbf{e}_0^{\mathrm{T}})^2 = (\mathbf{e}_0\cdot\mathbf{e}_0^{\mathrm{T}})$ holds. Combining this with the fact that $(\mathbf{e}_0\cdot\mathbf{e}_0^{\mathrm{T}})$ commutes with the diagonal dimer matrix $\bar{D}$, one of the two projectors in eq. (D.32) is redundant can can be dropped. We now apply the residue theorem in order to eliminate the energy integral in eq. (D.32). The integrand, as a function of complex q^0, has a root cut in the lower half plane and is analytic in the upper plane except for the two poles $q^0 = \pm\mathbf{q}\cdot\mathbf{r}/_0 + i\varepsilon$ We therefore apply the following formula for $c \in \mathbb{R}$:

$$
\begin{aligned}
& \lim_{\varepsilon\to 0^+} \int_{-\infty}^{\infty} \frac{\mathrm{d}q^0}{2\pi}\, \frac{f(q^0)}{(c + i\varepsilon - q^0)(-c + i\varepsilon - q^0)} \\
&= \lim_{\varepsilon\to 0^+} \frac{2\pi i}{2\pi} \left[\frac{f(c+i\varepsilon)}{(-1)(-c+i\varepsilon-(c+i\varepsilon))} + \frac{f(-c+i\varepsilon)}{(c+i\varepsilon-(-c+i\varepsilon))(-1)}\right] \\
&= \lim_{\varepsilon\to 0^+} i\,\frac{f(c+i\varepsilon) - f(-c+i\varepsilon)}{(c+i\varepsilon) - (-c+i\varepsilon)} \;=\; \begin{cases} i\,\frac{f(c)-f(-c)}{(c)-(-c)} = \frac{i}{2c}\{f(c) - f(-c)\} & : c \neq 0 \\ i\,(\partial f)(0) & : c = 0 \;. \end{cases}
\end{aligned}
\tag{D.33}
$$

This expression is continuous in c, whereas its contributions $if(c)/(2c)$ and $-if(-c)/(2c)$ are singular at $c \to 0$. Applying eq. (D.33) with $c = -\mathbf{q}\cdot\mathbf{r}/_0$ to the form factor integral (D.32), yields:

$$
\begin{aligned}
\mathcal{F}_{\mathrm{E},0}(\bar{P},\bar{K}) \;=\; & \int\limits_{q<\Lambda} \frac{\mathrm{d}^3\mathbf{q}}{(2\pi)^3}\, \frac{i^2}{2\left(-\frac{\mathbf{q}\cdot\mathbf{r}}{\bar{\mu}_0}\right)}\,\Big(-\frac{(2\pi)^3}{4\pi}\,\frac{1}{q^2}\Big) \\
& \times \Bigg\{ \Big(\int_0^\Lambda \mathrm{d}p\; \bar{G}(p)^{\mathrm{T}}\,\bar{D}^{[0]}(p)\,{}^{\bullet}\bar{R}^{[0]}(p,|\mathbf{q}+\mathbf{r}|) \,-\, |\beta\bar{H}|\,\mathbf{e}_0^{\mathrm{T}}\Big) \\
& \quad \times\; (\mathbf{e}_0\cdot\mathbf{e}_0^{\mathrm{T}})\;\bar{D}^{[0]}(E^{(3)} - \frac{\mathbf{q}\cdot\mathbf{r}}{\bar{\mu}_0} - \frac{m_0\,\mathbf{r}^2}{2\bar{\mu}_0^2}, q) \\
& \quad \times\; \Big(\int_0^\Lambda \mathrm{d}k\,{}^{\bullet}\bar{R}^{[0]}(E^{(3)} - 2\frac{\mathbf{q}\cdot\mathbf{r}}{\bar{\mu}_0}, |\mathbf{q}-\mathbf{r}|, k)\,\bar{D}^{[0]}(k)\,\bar{G}(k) \,-\, |\beta\bar{H}|\,\mathbf{e}_0\Big) \\
& - \;\Big(\int_0^\Lambda \mathrm{d}p\; \bar{G}(p)^{\mathrm{T}}\,\bar{D}^{[0]}(p)\,{}^{\bullet}\bar{R}^{[0]}(E^{(3)} + 2\frac{\mathbf{q}\cdot\mathbf{r}}{\bar{\mu}_0}, p, |\mathbf{q}+\mathbf{r}|) \,-\, |\beta\bar{H}|\,\mathbf{e}_0^{\mathrm{T}}\Big) \\
& \quad \times\; \bar{D}^{[0]}(E^{(3)} + \frac{\mathbf{q}\cdot\mathbf{r}}{\bar{\mu}_0} - \frac{m_0\,\mathbf{r}^2}{2\bar{\mu}_0^2}, q)\;(\mathbf{e}_0\cdot\mathbf{e}_0^{\mathrm{T}}) \\
& \quad \times\; \Big(\int_0^\Lambda \mathrm{d}k\,{}^{\bullet}\bar{R}^{[0]}(|\mathbf{q}-\mathbf{r}|, k)\,\bar{D}^{[0]}(k)\,\bar{G}(k) \,-\, |\beta\bar{H}|\,\mathbf{e}_0\Big)\Bigg\} \quad .
\end{aligned}
\tag{D.34}
$$

Thereby, the use of the redefined dimer function (2.43) led to an additional prefactor of $-(2\pi)^3/(4\pi\, q^2)$.

Angular integration: Considering the remaining integral over $\mathbf{q}$ in eq. (D.34), without loss of generality, we assume that $\mathbf{Q}$ and consequently also $\mathbf{r}$ points in 3-direction. Thus, $\mathbf{r} = r\cdot\mathbf{e}_{\mathbf{r}}$ with $\mathbf{e}_{\mathbf{r}} = \mathbf{e}_3$ holds. Choosing spherical coordinates

$$
\mathbf{q} = q\cdot\mathbf{e}_{\mathbf{q}} \quad , \qquad \mathbf{e}_{\mathbf{q}} \;=\; \left(\begin{smallmatrix} \sin\theta\cos\phi \\ \sin\theta\sin\phi \\ \cos\theta \end{smallmatrix}\right) \quad , \tag{D.35}
$$

we see that the integrand in eq. (D.32), in terms of the three-momenta $\mathbf{q}$ and $\mathbf{r}$, only depends on the lengths q, r and the angle $x := \mathbf{e}_{\mathbf{q}}\cdot\mathbf{e}_{\mathbf{r}} = \cos\theta$. The appearing scalar products simply read $\mathbf{q}\cdot\mathbf{r} = qrx$, leading to $|\mathbf{q}\pm\mathbf{r}| = \sqrt{\mathbf{q}^2 \pm 2\mathbf{q}\cdot\mathbf{r} + \mathbf{r}^2} = d(q,r,\pm x)$ with

$$
\forall\, a,b \,\in\, [0,\infty)\,,\; x \,\in\, (-1,1)\;: \qquad d(a,b,x) \;:=\; \sqrt{a^2 + 2abx + b^2} \quad . \tag{D.36}
$$

The integration over ϕ is trivial, and results in an additional factor of 2π such that the integral can be simplified according to:

$$
\int\limits_{q<\Lambda} \frac{\mathrm{d}^3\mathbf{q}}{(2\pi)^3}\, \frac{i^2}{2\left(-\frac{\mathbf{q}\cdot\mathbf{r}}{\bar{\mu}_0}\right)}\,\Big(-\frac{(2\pi)^3}{4\pi}\,\frac{1}{q^2}\Big)\,(\dots) \;=\; \frac{\bar{\mu}_0}{4}\int_0^\Lambda \frac{\mathrm{d}q}{q}\int_{-1}^{1}\frac{\mathrm{d}x}{x}\,(-1)\,(\dots) \quad . \tag{D.37}
$$

In addition, multiplying out the brackets in eq. (D.34), we can interpret the resulting integrands as matrix-, vector- and scalar-valued functions $Y_0^{\mathrm{M}}(Q,p,k)$, $Y_0^{\mathrm{V}}(Q,p)$ and $Y_0^{\mathrm{S}}(Q)$, resulting in:

$$\boxed{\begin{aligned}
&\mathcal{F}_{\mathrm{E},0}(Q) \;=\; \int_0^\Lambda \mathrm{d}p \int_0^\Lambda \mathrm{d}k \; \bar{G}(p)^{\mathrm{T}} \; \bar{D}^{[0]}(p) \; Y_0^{\mathrm{M}}(Q,p,k) \; \bar{D}^{[0]}(k) \; \bar{G}(k)^{\mathrm{T}} \\
&\quad - \; 2|\beta \bar{H}| \int_0^\Lambda \mathrm{d}p \; \bar{G}(p)^{\mathrm{T}} \; \bar{D}^{[0]}(p) \; Y_0^{\mathrm{V}}(Q,p) \; + \; |\beta \bar{H}|^2 \, Y_0^{\mathrm{S}}(Q) \; , \\[2ex]
&Y_0^{\mathrm{X}}(Q\ldots) \;=\; \frac{\bar{\mu}_0}{4} \int_0^\Lambda \frac{\mathrm{d}q}{q} \int_{-1}^1 \frac{\mathrm{d}x}{x} \; \Upsilon_0^{\mathrm{X}}\Big(\frac{M_0}{M_\Sigma}\frac{Q}{2}, q, x\ldots\Big) \quad , \quad \mathrm{X} \in \{\mathrm{M},\mathrm{V},\mathrm{S}\} \; , \\[2ex]
&\Upsilon_0^{\mathrm{M}}(r,q,x,p,k) \\
&\quad = \; \frac{1}{r}\Big\{ {}^{\bullet}\!\bar{R}^{[0]}\Big(E^{(3)} + 2\frac{qrx}{\bar{\mu}_0}, p, d(r,q,x)\Big) \; \bar{D}^{[0]}\Big(E^{(3)} + \frac{qrx}{\bar{\mu}_0} - \frac{m_0\, r^2}{2\bar{\mu}_0^2}, q\Big) \\
&\qquad \times \; (\mathbf{e}_0 \cdot \mathbf{e}_0^{\mathrm{T}}) \; {}^{\bullet}\!\bar{R}^{[0]}(d(r,q,-x),k) \; - \; {}^{\bullet}\!\bar{R}^{[0]}(p,d(r,q,x)) \; (\mathbf{e}_0 \cdot \mathbf{e}_0^{\mathrm{T}}) \\
&\qquad \times \; \bar{D}^{[0]}\Big(E^{(3)} - \frac{qrx}{\bar{\mu}_0} - \frac{m_0\, r^2}{2\bar{\mu}_0^2}, q\Big) \; {}^{\bullet}\!\bar{R}^{[0]}\Big(E^{(3)} - 2\frac{qrx}{\bar{\mu}_0}, d(r,q,-x), k\Big)\Big\} \; , \\
&\Upsilon_0^{\mathrm{V}}(r,q,x,p) \\
&\quad = \; \frac{1}{r}\Big\{ {}^{\bullet}\!\bar{R}^{[0]}\Big(E^{(3)} + 2\frac{qrx}{\bar{\mu}_0}, p, d(r,q,x)\Big) \; \bar{D}^{[0]}\Big(E^{(3)} + \frac{qrx}{\bar{\mu}_0} - \frac{m_0\, r^2}{2\bar{\mu}_0^2}, q\Big) \\
&\qquad\qquad\qquad - \; {}^{\bullet}\!\bar{R}^{[0]}(p,d(r,q,x)) \; \bar{D}^{[0]}\Big(E^{(3)} - \frac{qrx}{\bar{\mu}_0} - \frac{m_0\, r^2}{2\bar{\mu}_0^2}, q\Big)\Big\} \; \mathbf{e}_0 \; , \\
&\Upsilon_0^{\mathrm{S}}(r,q,x) \\
&\quad = \; \frac{1}{r}\, \mathbf{e}_0^{\mathrm{T}} \Big\{ \bar{D}^{[0]}\Big(E^{(3)} + \frac{qrx}{\bar{\mu}_0} - \frac{m_0\, r^2}{2\bar{\mu}_0^2}, q\Big) - \bar{D}^{[0]}\Big(E^{(3)} - \frac{qrx}{\bar{\mu}_0} - \frac{m_0\, r^2}{2\bar{\mu}_0^2}, q\Big)\Big\} \mathbf{e}_0 \; .
\end{aligned}} \tag{D.38}$$

Properties: In order to determine $\mathcal{F}_{\mathrm{E},0}(Q)$, we have to evaluate 4 integrals, namely those over the 3 momenta $p,k,q \in [0,\Lambda]$ and 1 over the angle $x \in [-1,1]$. One can easily check that $\Upsilon_0^{\mathrm{M}}(r,q,x,p,k)/x = \Upsilon_0^{\mathrm{M}}(r,q,-x,k,p)^{\mathrm{T}}/(-x)$, after substituting $x \mapsto -x$, yields the symmetry $Y_0^{\mathrm{M}}(Q,p,k) = Y_0^{\mathrm{M}}(Q,k,p)^{\mathrm{T}}$, as required. Furthermore, the inequality

$$\Big(E^{(3)} - \frac{m_0\, r^2}{2\bar{\mu}_0^2} \pm \frac{qrx}{\bar{\mu}_0}\Big) - \frac{q^2}{2\bar{\mu}_0} \;=\; E^{(3)} - \frac{q^2 \mp 2qrx + \frac{M_\Sigma}{M_0} r^2}{2\bar{\mu}_0} \;<\; -\frac{(q-r)^2}{2\bar{\mu}_0} \;\leq\; 0 \tag{D.39}$$

implies that all appearing dimer propagators $\bar{D}_0^{[0]}$ are uncritical. Since the nn scattering length $a_0 < 0$ is negative, furthermore, they are also real in the limit $\varepsilon \to 0^+$. Moreover, the identity:

$$\lim_{\varepsilon\to 0^+}(-i)y_0\Big(E^{(3)}-\frac{m_0\,r^2}{2\bar{\mu}_0^2}\pm\frac{qrx}{\bar{\mu}_0},q\Big) \;=\; \sqrt{2\mu_0\Big|\Big(E^{(3)}-\frac{m_0\,r^2}{2\bar{\mu}_0^2}\pm\frac{qrx}{\bar{\mu}_0}\Big)-\frac{q^2}{2\bar{\mu}_0}\Big|}\quad . \tag{D.40}$$

holds. Similar considerations hold for the trimer-irreducible dimer-particle interaction functions ${}^{\bullet}\bar{R}_{i0}^{[0]}$ such that the terms $Y_0^{\mathrm{X}}(Q\dots)$ are all real. Thus, $\mathcal{F}_{\mathrm{E},0}(Q)$ is real, as it should. The additional symmetry $\Upsilon_0^{\mathrm{X}}(-r,q,x\dots)/x = \Upsilon_0^{\mathrm{X}}(r,q,-x\dots)/(-x)$, after substituting $x\mapsto -x$, leads to $Y_0^{\mathrm{X}}(-Q\dots) = Y_0^{\mathrm{X}}(Q\dots)$. Consequently, also the form factor contribution $\mathcal{F}_{\mathrm{E},0}(Q)$ is an even function in Q and be written in the usual way $\mathcal{F}_{\mathrm{E},0}(Q^2)$. Note that due to eq. (D.33), the limit $Q\to 0$ in eq. (D.38) exists, but prefactors $\propto 1/Q$ cause numerical instabilities for very small momentum transfer. A discussion of the numerical implementation is given in sec. B.

D.3.4.3 Exchange term

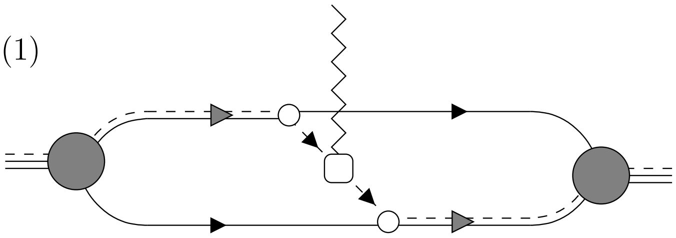

Figure D.7: The $i\Gamma_1$ contribution to the form factor matrix element. The photon couples to a core field that is exchanged between cn-dimers. It corresponds to the second term in the sum on the right-hand side of the lower equation in fig. 3.9.

We proceed with the calculation of $\mathcal{F}_{\mathrm{E},1}$, represented in fig. D.7. The charged core is exchanged between cn-dimers. The corresponding reduced matrix element $i\Gamma_1^{\mathrm{red}}$ is the second summand on the right-hand side of the lower equation in fig. 3.9. Its spin structure is completely analogous to the corresponding dimer-particle interaction in fig. D.5. Projecting onto the spin-singlet state and using eq. (3.65), its renormalized version reads:

$$\begin{aligned}
i\bar{\Gamma}_1^{\mathrm{red}}(\bar{P},\bar{K},\bar{p},\bar{k}) \;=\;& (\mathcal{Z}e)^{-1}|Z_1|^{-\frac{1}{2}}\; iD_1(\bar{P},\bar{p})\;(-ig_1)\;\frac{i}{\epsilon_1(\bar{P},\mathbf{p})-p^0+i\varepsilon}\\
\times\;& \frac{i}{\big(\frac{M_1}{M_\Sigma}P^0+p^0\big)-\big(\frac{m_1}{M_\Sigma}K^0-k^0\big)-\frac{\big((\frac{M_1}{M_\Sigma}\mathbf{P}+\mathbf{p})-(\frac{m_1}{M_\Sigma}\mathbf{K}-\mathbf{k})\big)^2}{2m_0}+i\varepsilon}\\
\times\;& (-i\mathcal{Z}e)\\
\times\;& \frac{i}{\big(\frac{M_1}{M_\Sigma}K^0+k^0\big)-\big(\frac{m_1}{M_\Sigma}P^0-p^0\big)-\frac{\big((\frac{M_1}{M_\Sigma}\mathbf{K}+\mathbf{k})-(\frac{m_1}{M_\Sigma}\mathbf{P}-\mathbf{p})\big)^2}{2m_0}+i\varepsilon}\\
\times\;& \frac{i}{\epsilon_1(\bar{K},\mathbf{k})+i\varepsilon-k^0}\;(-ig_1)\;iD_1(\bar{P},\bar{p})\;|Z_1|^{-\frac{1}{2}}\quad .
\end{aligned} \tag{D.41}$$

Again, we use the rescaled four-momentum $\bar{r} = m_1/M_\Sigma \bar{Q}$ from (D.25) in order to rewrite the two factor appearing denominators. The first one reads:

$$\begin{aligned}
&\Big(\frac{M_1}{M_\Sigma}P^0 + p^0\Big) - \Big(\frac{m_1}{M_\Sigma}K^0 - k^0\Big) - \frac{\big((\frac{M_1}{M_\Sigma}\mathbf{P} + \mathbf{p}) - (\frac{m_1}{M_\Sigma}\mathbf{K} - \mathbf{k})\big)^2}{2m_0} \\
&\quad = P^0 + \big[p^0 - \epsilon_1(\bar{P}, \mathbf{p}) \,+\, k^0 - \epsilon_1(\bar{K}, \mathbf{k})\big] \\
&\qquad - \frac{\big(\frac{m_1}{M_\Sigma}\mathbf{P} - \mathbf{p}\big)^2}{2m_1} - \frac{\big(\frac{m_1}{M_\Sigma}\mathbf{K} - \mathbf{k}\big)^2}{2m_1} - \frac{\big(\frac{M_1}{M_\Sigma}\mathbf{P} - \frac{m_1}{M_\Sigma}\mathbf{K} + \mathbf{p} + \mathbf{k}\big)^2}{2m_0} \\
&\quad = E(\bar{P}) + \frac{\mathbf{P}^2}{2M_\Sigma} + \big[p^0 - \epsilon_1(\bar{P}, \mathbf{p}) \,+\, k^0 - \epsilon_1(\bar{K}, \mathbf{k})\big] \\
&\qquad - \frac{\big(\frac{m_1}{M_\Sigma}\mathbf{P} - \mathbf{p}\big)^2}{2m_1} - \frac{\big(\frac{m_1}{M_\Sigma}\mathbf{P} + (\mathbf{r} - \mathbf{k})\big)^2}{2m_1} - \frac{\big(\frac{m_0}{M_\Sigma}\mathbf{P} - (\mathbf{r} - \mathbf{k}) + \mathbf{p}\big)^2}{2m_0} \\
&\quad = E(\bar{P}) + \big[p^0 - \epsilon_1(\bar{P}, \mathbf{p}) \,+\, k^0 - \epsilon_1(\bar{K}, \mathbf{k})\big] \\
&\qquad + \frac{\mathbf{P}^2}{2M_\Sigma} - \frac{m_1\mathbf{P}^2}{2M_\Sigma^2} + \frac{\mathbf{P}\mathbf{p}}{M_\Sigma} - \frac{\mathbf{p}^2}{2m_1} - \frac{m_1\mathbf{P}^2}{2M_\Sigma^2} - \frac{\mathbf{P}\,(\mathbf{r} - \mathbf{k})}{M_\Sigma} - \frac{(\mathbf{r} - \mathbf{k})^2}{2m_1} \\
&\qquad - \frac{m_0\mathbf{P}^2}{2M_\Sigma^2} - \frac{(\mathbf{r} - \mathbf{k})^2}{2m_0} - \frac{\mathbf{p}^2}{2m_0} + \frac{\mathbf{P}\,(\mathbf{r} - \mathbf{k})}{M_\Sigma} - \frac{\mathbf{P}\mathbf{p}}{M_\Sigma} + \frac{(\mathbf{r} - \mathbf{k})\,\mathbf{p}}{m_0} \\
&\quad = E^{(3)} + \big[p^0 - \epsilon_1(\bar{P}, \mathbf{p}) \,+\, k^0 - \epsilon_1(\bar{K}, \mathbf{k})\big] - \frac{\mathbf{p}^2}{2\mu_1} - \frac{(\mathbf{k} - \mathbf{r})^2}{2\mu_1} - \frac{(\mathbf{k} - \mathbf{r})\,\mathbf{p}}{m_0} \quad .
\end{aligned} \tag{D.42}$$

From that, the second one can be determined via the transformation rules $\bar{p} \leftrightarrow \bar{k}$ and $\bar{P} \leftrightarrow \bar{K} \Rightarrow \bar{r} \mapsto -\bar{r}$, leading to:

$$\begin{aligned}
&\Big(\frac{M_1}{M_\Sigma}K^0 + k^0\Big) - \Big(\frac{m_1}{M_\Sigma}P^0 - p^0\Big) - \frac{\big((\frac{M_1}{M_\Sigma}\mathbf{K} + \mathbf{k}) - (\frac{m_1}{M_\Sigma}\mathbf{P} - \mathbf{p})\big)^2}{2m_0} \\
&\quad = E^{(3)} + \big[k^0 - \epsilon_1(\bar{K}, \mathbf{k}) \,+\, p^0 - \epsilon_1(\bar{P}, \mathbf{p})\big] - \frac{\mathbf{k}^2}{2\mu_1} - \frac{(\mathbf{p} + \mathbf{r})^2}{2\mu_1} - \frac{(\mathbf{p} + \mathbf{r})\,\mathbf{k}}{m_0} \quad .
\end{aligned} \tag{D.43}$$

Inserting eqs. (D.42) and (D.43) into eq. (D.41) and collecting all the factors, the form factor contribution $\mathcal{F}_{\mathrm{E},1}$ from eq. (3.64) assumes the form:

$$\begin{aligned}
\mathcal{F}_{\mathrm{E},1}(\bar{P},\bar{K}) \;=\; & |Z_1|\, g_1^2 \int\limits_{p<\Lambda} \frac{\mathrm{d}^3\mathbf{p}}{(2\pi)^3} \int\limits_{k<\Lambda} \frac{\mathrm{d}^3\mathbf{k}}{(2\pi)^3} \int_{-\infty}^{\infty} \frac{\mathrm{d}p^0}{(2\pi)} \int_{-\infty}^{\infty} \frac{\mathrm{d}k^0}{(2\pi)} \\
\times\; & \frac{i\,\bar{G}_1(\bar{P},\bar{p})\,\bar{D}_1(\bar{P},\bar{p})}{\epsilon_1(\bar{P},\mathbf{p}) - p^0 + i\varepsilon} \\
\times\; & \frac{1}{E^{(3)} + \left[p^0 - \epsilon_1(\bar{P},\mathbf{p}) \,+\, k^0 - \epsilon_1(\bar{K},\mathbf{k})\right] - \frac{\mathbf{p}^2}{2\mu_1} - \frac{(\mathbf{k}-\mathbf{r})^2}{2\mu_1} - \frac{(\mathbf{k}-\mathbf{r})\mathbf{p}}{m_0} + i\varepsilon} \\
\times\; & \frac{1}{E^{(3)} + \left[k^0 - \epsilon_1(\bar{K},\mathbf{k}) \,+\, p^0 - \epsilon_1(\bar{P},\mathbf{p})\right] - \frac{\mathbf{k}^2}{2\mu_1} - \frac{(\mathbf{p}+\mathbf{r})^2}{2\mu_1} - \frac{(\mathbf{p}+\mathbf{r})\mathbf{k}}{m_0} + i\varepsilon} \\
\times\; & \frac{i\,\bar{D}_1(\bar{K},\bar{k})\,\bar{G}_1(\bar{K},\bar{k})}{\epsilon_1(\bar{K},\mathbf{k}) + i\varepsilon - k^0} \quad .
\end{aligned} \tag{D.44}$$

The p^0- and k^0-integral contours can be closed by an upper arc with infinite radius, since the two core propagators connected to the photon coupling have no additional poles in the upper complex half plane. Applying the residue theorem eq. (3.26), leads to:

$$\begin{aligned}
\mathcal{F}_{\mathrm{E},1}(\bar{P},\bar{K}) \;=\; & (2\mu_1)^2\, z_1 \int\limits_{p<\Lambda} \frac{\mathrm{d}^3\mathbf{p}}{(2\pi)^3} \int\limits_{k<\Lambda} \frac{\mathrm{d}^3\mathbf{k}}{(2\pi)^3} \left(-\frac{(2\pi)^3}{4\pi}\frac{1}{p^2}\right)\left(-\frac{(2\pi)^3}{4\pi}\frac{1}{k^2}\right) \\
\times\; & \frac{\bar{G}_1(p)\,\bar{D}_1^{[0]}(p)}{\mathbf{p}^2 + (\mathbf{k}-\mathbf{r})^2 + 2\frac{m_1}{M_1}(\mathbf{k}-\mathbf{r})\mathbf{p} - 2\mu_1 E^{(3)} - i\varepsilon} \\
\times\; & \frac{\bar{D}_1^{[0]}(k)\,\bar{G}_1(k)}{\mathbf{k}^2 + (\mathbf{p}+\mathbf{r})^2 + 2\frac{m_1}{M_1}(\mathbf{p}+\mathbf{r})\mathbf{k} - 2\mu_1 E^{(3)} - i\varepsilon} \quad .
\end{aligned} \tag{D.45}$$

Note that we used redefined dimer functions (2.43) leading to the additional prefactors $-(2\pi)^3/(4\pi\, p^2)$ and $-(2\pi)^3/(4\pi\, k^2)$. The two sums in the denominator can be written as quadratic forms:

$$\mathbf{x}^2 + \mathbf{y}^2 + 2\frac{m_1}{M_1}\mathbf{x}^{\mathrm{T}}\mathbf{y} - 2\mu_1 E^{(3)} - i\varepsilon \;=\; (\mathbf{x}^{\mathrm{T}},\mathbf{y}^{\mathrm{T}}) \begin{pmatrix} 1 & \frac{m_1}{M_1} \\ \frac{m_1}{M_1} & 1 \end{pmatrix} \begin{pmatrix} \mathbf{x} \\ \mathbf{y} \end{pmatrix} - 2\mu_1 E^{(3)} - i\varepsilon \tag{D.46}$$

with some vectors $\mathbf{x},\mathbf{y} \in \mathbb{R}^3$. The appearing matrix is positive definite, since $1 > 0$ and

$$\det \begin{pmatrix} 1 & \frac{m_1}{M_1} \\ \frac{m_1}{M_1} & 1 \end{pmatrix} \;=\; 1 - \left(\frac{m_1}{m_0 + m_1}\right)^2 \;>\; 0 \tag{D.47}$$

holds. In addition, the three-body binding energy $E^{(3)}$ is negative. Consequently, the real part in eq. (D.46) is always positive and does not vanish. Therefore, the limit $\varepsilon \to 0^+$, for the two denominators in eq. (D.45), is uncritical such that we can set $\varepsilon = 0$ in those terms.

Angular integration: Considering the remaining integrals over $\mathbf{p}$ and $\mathbf{k}$ in eq. (D.45), without loss of generality, we can assume that $\mathbf{Q}$ and consequently also $\mathbf{r}$ points in 3-direction. Thus, again $\mathbf{r} = r \cdot \mathbf{e_r}$ with $\mathbf{e_r} = \mathbf{e}_3$ holds. Choosing spherical coordinates

$$\mathbf{p} = p \cdot \mathbf{e_p} \quad , \quad \mathbf{e_p} = \begin{pmatrix} \sin\theta_p \cos\phi_p \\ \sin\theta_p \sin\phi_p \\ \cos\theta_p \end{pmatrix} \quad , \quad \mathbf{k} = k \cdot \mathbf{e_k} \quad , \quad \mathbf{e_k} = \begin{pmatrix} \sin\theta_k \cos\phi_k \\ \sin\theta_k \sin\phi_k \\ \cos\theta_k \end{pmatrix} \quad , \tag{D.48}$$

we see that the integrand in eq. (D.45), in terms of the three-momenta $\mathbf{p}$, $\mathbf{k}$ and $\mathbf{r}$, only depends on their lengths p, k and r and their relative angles

$$\begin{aligned} x := \mathbf{e_p} \cdot \mathbf{e_r} &= \cos\theta_p \quad , \qquad y := \mathbf{e_k} \cdot \mathbf{e_r} = \cos\theta_k \quad , \\ \mathbf{e_p} \cdot \mathbf{e_k} &= \sin\theta_p \cos\phi_p \sin\theta_k \cos\phi_k + \sin\theta_p \sin\phi_p \sin\theta_k \sin\phi_k + \cos\theta_p \cos\theta_k \\ &= \sin\theta_p \sin\theta_k \cos(\phi_p - \phi_k) + \cos\theta_p \cos\theta_k \\ &= \sqrt{1-x^2}\sqrt{1-y^2}\cos(\phi_p - \phi_k) + xy \quad . \end{aligned} \tag{D.49}$$

Compared to the determination of $\mathcal{F}_{\mathrm{E},0}$ in sec. D.3.4.2, the angular integration, this time, is more involved. However, we note that the integrand, in terms of ϕ_p and ϕ_k, effectively only depends on $\cos(\phi_p - \phi_k)$. For an integrable function $f : \mathbb{R} \to \mathbb{C}$, such a dependency implies:

$$\int_0^{2\pi} \mathrm{d}\phi_p \int_0^{2\pi} \mathrm{d}\phi_k \, f(\cos(\phi_p - \phi_k)) = 2\pi \int_0^{2\pi} \mathrm{d}\phi_k \, f(\cos\phi_k) = 4\pi \int_0^{\pi} \mathrm{d}\phi f(\cos\phi) \quad , \tag{D.50}$$

where we substituted $\phi_k \mapsto \phi_k + \phi_p$ and used $\cos(\phi) = \cos(-\phi) = \cos(2\pi - \phi)$. Therefore, the integrals in eq. (D.45) can be simplified according to:

$$\begin{aligned} &(2\mu_1)^2 z_1 \int\limits_{p<\Lambda} \frac{\mathrm{d}^3\mathbf{p}}{(2\pi)^3} \int\limits_{k<\Lambda} \frac{\mathrm{d}^3\mathbf{k}}{(2\pi)^3} \left(-\frac{(2\pi)^3}{4\pi}\frac{1}{p^2}\right)\left(-\frac{(2\pi)^3}{4\pi}\frac{1}{k^2}\right)(\dots) \\ &= \frac{2}{|a_1|} \int_0^\Lambda \mathrm{d}p \int_0^\Lambda \mathrm{d}k \int_{-1}^1 \mathrm{d}x \int_{-1}^1 \mathrm{d}y \int_0^\pi \mathrm{d}\phi \, (\dots) \quad . \end{aligned} \tag{D.51}$$

Applying these relations, the remaining integrand in eq. (D.45) can be interpreted as a matrix-valued function $Y_1^{\mathrm{M}}(Q, p, k)$ yielding:

$$\boxed{\begin{aligned}
\mathcal{F}_{\mathrm{E},1}(Q) \;&=\; \int_0^\Lambda \mathrm{d}p \int_0^\Lambda \mathrm{d}k\ \bar{G}(p)^{\mathrm{T}}\ \bar{D}^{[0]}(p)\ Y_1^{\mathrm{M}}(Q,p,k)\ \bar{D}^{[0]}(k)\ \bar{G}(k) \quad , \\[2ex]
Y_1^{\mathrm{M}}(Q,p,k) \;&=\; \frac{2}{|a_1|} \int_{-1}^{1} \mathrm{d}x \int_{-1}^{1} \mathrm{d}y \int_0^\pi \mathrm{d}\phi\ \Upsilon_1^{\mathrm{M}}\Big(\frac{m_1}{M_\Sigma}Q, x, y, \phi, p, k\Big) \\
\Upsilon_1^{\mathrm{M}}(r,x,y,\phi,p,k) \;&=\; \Upsilon_1^{\mathrm{S}}(r,x,y,\phi,p,k)\ (\mathbf{e}_1 \cdot \mathbf{e}_1^{\mathrm{T}}) \\
\Upsilon_1^{\mathrm{S}}(r,x,y,\phi,p,k) \;&=\; \qquad\qquad\qquad\qquad\qquad\qquad\qquad\qquad\qquad\qquad (\mathrm{D.52}) \\
&\big[p^2 + k^2 + r^2 - 2\big(ky + \frac{m_1}{M_1}px\big)r \\
&\quad + \frac{m_1}{M_1}\,2pk\big[\sqrt{1-x^2}\sqrt{1-y^2}\cos\phi + xy\big] - 2\mu_1 E^{(3)}\big]^{-1} \\
\times\ &\big[p^2 + k^2 + r^2 + 2\big(px + \frac{m_1}{M_1}ky\big)r \\
&\quad + \frac{m_1}{M_1}\,2pk\big[\sqrt{1-x^2}\sqrt{1-y^2}\cos\phi + xy\big] - 2\mu_1 E^{(3)}\big]^{-1}
\end{aligned}}$$

Properties: In order to determine $\mathcal{F}_{\mathrm{E},1}(Q)$, we have to evaluate 5 integrals, namely those over the 2 momenta $p, k \in [0,\Lambda]$ and 3 over the angles $x, y \in [-1,1]$, $\phi \in [0,\pi]$. The matrix structure of $Y_1^{\mathrm{M}}(Q,p,k)$ completely originates from the projector $(\mathbf{e}_1 \cdot \mathbf{e}_1^{\mathrm{T}})$. The scalar function Υ_1^{S} fulfills $\Upsilon_1^{\mathrm{S}}(r,x,y,\phi,p,k) = \Upsilon_1^{\mathrm{S}}(r,-y,-x,\phi,k,p)$ such that substituting $(x,y) \mapsto (-y,-x)$ yields the symmetry $Y_1^{\mathrm{M}}(Q,p,k) = Y_1^{\mathrm{M}}(Q,k,p)^{\mathrm{T}}$, as required. All appearing functions are real. Consequently, $\mathcal{F}_{\mathrm{E},1}(Q)$ is real, as it should. The additional symmetry $\Upsilon_1^{\mathrm{S}}(-r,x,y,\phi,p,k) = \Upsilon_1^{\mathrm{S}}(r,-x,-y,\phi,p,k)$, after substituting $(x,y) \mapsto (-x,-y)$, leads to $Y_1^{\mathrm{M}}(-Q,p,k) = Y_1^{\mathrm{M}}(Q,p,k)$. Consequently also the contribution to the form factor $\mathcal{F}_{\mathrm{E},1}(Q)$ is an even function in Q and can effectively only depend on Q^2. The limit $Q \to 0$ is uncritical for $\mathcal{F}_{\mathrm{E},1}(Q^2)$. A discussion of the numerical implementation is given in sec. B.

D.3.4.4 Loop term

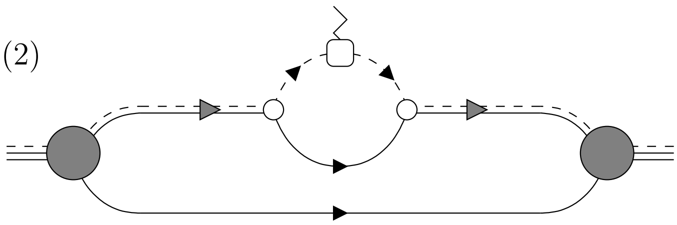

Figure D.8: The $i\Gamma_2$ contribution to the form factor matrix element. The photon couples to a core field inside a *cn*-bubble. It corresponds to the third term in the sum on the right-hand side of the lower equation in fig. 3.9.

We complete our form factor derivation by calculating $\mathcal{F}_{\mathrm{E},2}$, which is represented in fig. D.8. The charged core couples to the photon inside a *cn*-bubble. The corresponding reduced matrix element $i\Gamma_2^{\mathrm{red}}$ is the third summand on the right-hand side of the lower equation in fig. 3.9. Using the definition (3.65), its renormalized version reads:

$$\begin{aligned} i\bar{\Gamma}_2^{\mathrm{red}}(\bar{P},\bar{K},\bar{p},\bar{k}) &= (\mathcal{Z}e)^{-1}\,|Z_1|^{-\frac{1}{2}}\;iD_1(\bar{P},\bar{p})\,\frac{i}{\epsilon_1(\bar{P},\mathbf{p})+i\varepsilon-p^0} \\ &\times\;(-i)\Sigma^\gamma\Big(\frac{M_1}{M_\Sigma}\bar{P}+\bar{p},\,\frac{M_1}{M_\Sigma}\bar{K}+\bar{k}\Big) \\ &\times\;(2\pi)^4\delta^{(4)}\Big(\big(\frac{m_1}{M_\Sigma}\bar{P}-\bar{p}\big)-\big(\frac{m_1}{M_\Sigma}\bar{K}-\bar{k}\big)\Big)\;iD_1(\bar{K},\bar{k})\;|Z_1|^{-\frac{1}{2}} \quad . \end{aligned} \tag{D.53}$$

The matrix element $(-i\Sigma^\gamma)$ represents the bubble diagram depicted in fig. D.9, which we will calculate separately. Analogue to eq. (3.65) we define

$$\bar{\Sigma}^\gamma \;:=\; (\mathcal{Z}e)^{-1}\,|Z_1|^{\frac{1}{2}}\;\Sigma^\gamma\;|Z_1|^{\frac{1}{2}} \quad . \tag{D.54}$$

Symmetrization: Using again the rescaled four-momentum $\bar{r}=m_1/M_\Sigma\bar{Q}$ from (D.25), we insert eq. (D.53) into eq. (3.64) for $\mathcal{F}_{\mathrm{E},2}$. The $\delta^{(4)}$-function imposes $\bar{k}=\bar{p}+\bar{r}$. Collecting all factors, yields:

$$\begin{aligned} \mathcal{F}_{\mathrm{E},2}(\bar{P},\bar{K}) \;&=\; \int\limits_{p<\Lambda}\frac{\mathrm{d}^4\bar{p}}{(2\pi)^4}\;\bar{G}_1(\bar{P},\bar{p})\,\bar{D}_1(\bar{P},\bar{p}) \\ &\quad\times\;\frac{i\,\bar{\Sigma}^\gamma\big(\frac{M_1}{M_\Sigma}\bar{P}+\bar{p},\,\frac{M_1}{M_\Sigma}\bar{K}+\bar{p}+\bar{r}\big)}{\epsilon_1(\bar{P},\mathbf{p})-p^0+i\varepsilon}\;\bar{D}_1(\bar{K},\bar{p}+\bar{r})\;\bar{G}_1(\bar{K},\bar{p}+\bar{r}) \\ &=\; \int\limits_{q<\Lambda}\frac{\mathrm{d}^3\mathbf{q}}{(2\pi)^3}\int_{-\infty}^{\infty}\frac{\mathrm{d}q^0}{(2\pi)}\;\bar{G}_1(\bar{P},\bar{q}-\bar{s})\,\bar{D}_1(\bar{P},\bar{q}-\bar{s}) \\ &\quad\times\;\frac{i\,\bar{\Sigma}^\gamma\big(\frac{M_1}{M_\Sigma}\bar{P}+\bar{q}-\bar{s},\,\frac{M_1}{M_\Sigma}\bar{K}+\bar{q}+\bar{s}\big)}{\epsilon_1(\bar{P},\mathbf{q}-\mathbf{s})-p^0+i\varepsilon}\;\bar{D}_1(\bar{K},\bar{q}+\bar{s})\;\bar{G}_1(\bar{K},\bar{q}+\bar{s}) \quad . \end{aligned} \tag{D.55}$$

In the last step we shifted the loop momentum according to $\bar{q}\mapsto\bar{p}+\bar{s}$ with $\bar{s}:=\bar{r}/2\;\Rightarrow\;s^0=0$. For the shifted momenta, the relation

$$\begin{aligned} \epsilon_1(\bar{P},\mathbf{q}-\mathbf{s}) &= \frac{m_1}{M_\Sigma}P^0-\frac{\big(\frac{m_1}{M_\Sigma}\mathbf{P}-(\mathbf{q}-\mathbf{s})\big)^2}{2m_1} \;=\; \frac{m_1}{M_\Sigma}K^0-\frac{\big(\frac{m_1}{M_\Sigma}\mathbf{K}-(\mathbf{q}+\mathbf{s})\big)^2}{2m_1} \\ &= \epsilon_1(\bar{K},\mathbf{q}+\mathbf{s}) \end{aligned} \tag{D.56}$$

implies that closing the q^0-integration with an upper arc, imposes on-shell conditions for both four momenta $\bar{q}-\bar{s}$ and $\bar{q}+\bar{s}$. This is also what we would have expected, since in the Feynman diagram in fig. D.8 there is only one single-particle propagator, whom we artificially assigned two equal four-momenta in order to enable the inclusion of both

$\bar{G}_1$-functions. The equation then reads:

$$
\begin{aligned}
\mathcal{F}_{\mathrm{E},2}(\bar{P},\bar{K}) \;=\; & \int\limits_{q<\Lambda} \frac{\mathrm{d}^3\mathbf{q}}{(2\pi)^3}\; \bar{G}_1(|\mathbf{q}-\mathbf{s}|)\, \bar{D}_1(|\mathbf{q}-\mathbf{s}|) \\
& \times\, \bar{\Sigma}^\gamma\Big(\frac{M_1}{M_\Sigma}\bar{P}+\bar{q}-\bar{s},\, \frac{M_1}{M_\Sigma}\bar{K}+\bar{q}+\bar{s}\Big)\Big|_{q^0=\epsilon_1(\bar{P},\mathbf{q}-\mathbf{s})+i\varepsilon} \\
& \times\; \bar{D}_1(|\mathbf{q}+\mathbf{s}|)\; \bar{G}_1(|\mathbf{q}+\mathbf{s}|) \\
=\; & \int\limits_{q<\Lambda} \frac{\mathrm{d}^3\mathbf{q}}{(2\pi)^3}\; \Big(\sum_{i=0}^{1}\int_0^\Lambda \mathrm{d}p\, \bar{G}_i(p)\, \bar{D}_i^{[0]}(p)\, {}^\bullet\bar{R}_{i1}^{[0]}(p,|\mathbf{q}-\mathbf{s}|)\Big) \\
& \times\; \bar{D}_1(|\mathbf{q}-\mathbf{s}|)\; \bar{\Sigma}^\gamma\Big(\frac{M_1}{M_\Sigma}\bar{P}+\bar{q}-\bar{s},\, \frac{M_1}{M_\Sigma}\bar{K}+\bar{q}+\bar{s}\Big)\Big|_{q^0=\epsilon_1(\bar{P},\mathbf{q}-\mathbf{s})+i\varepsilon} \\
& \times\; \bar{D}_1(|\mathbf{q}+\mathbf{s}|)\; \Big(\sum_{j=0}^{1}\int_0^\Lambda \mathrm{d}k\, {}^\bullet\bar{R}_{1j}^{[0]}(|\mathbf{q}+\mathbf{s}|,k)\, \bar{D}_j^{[0]}(k)\, \bar{G}_j(k)\Big) \quad .
\end{aligned}
\tag{D.57}
$$

The last line follows from the integral equation (3.54) for the irreducible trimer-dimer-particle coupling.

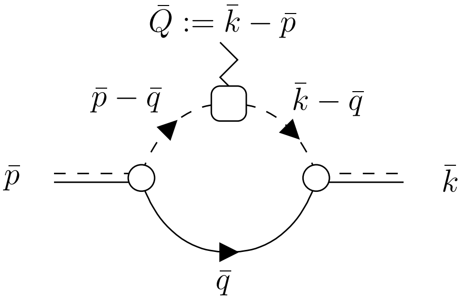

Figure D.9: Diagram for the matrix element $-i\Sigma^\gamma$. The photon couples to a core field inside a cn-bubble. It is contained in the $i\Gamma_2$ contribution to the form factor matrix element as it is depicted in fig. D.8.

Bubble graph: We now analytically calculate the matrix element $-i\Sigma^\gamma(\bar{p},\bar{k})$ for the bubble diagram, depicted in fig. D.9. Its spin-structure is identical with the one from the self-energy graph in fig. D.3 that was calculated in sec. D.3.1. For general incoming and outgoing four-momenta $\bar{p}$ and $\bar{k}$, its redefined matrix element $-i\bar{\Sigma}^\gamma$ from eq. (D.54) is given through:

$$\begin{aligned}
-\,i\bar{\Sigma}^{\gamma}(\bar{p},\bar{k}) \;&=\; (\mathcal{Z}e)^{-1}\,|Z_1|^{\frac{1}{2}}\,(-ig_1)\int\limits_{q<\Lambda}\frac{\mathrm{d}^3\mathbf{q}}{(2\pi)^3}\int_{-\infty}^{\infty}\frac{\mathrm{d}q^0}{2\pi}\,\frac{i}{q^0-\frac{\mathbf{q}^2}{2m_1}+i\varepsilon}\\
&\times\;\frac{i}{p^0-q^0-\frac{(\mathbf{p}-\mathbf{q})^2}{2m_0}+i\varepsilon}\,(-i\mathcal{Z}e)\,\frac{i}{k^0-q^0-\frac{(\mathbf{k}-\mathbf{q})^2}{2m_0}+i\varepsilon}\,(-ig_1)\,|Z_1|^{\frac{1}{2}}\\
&=\;-iz_1\int\frac{\mathrm{d}^3\mathbf{q}}{(2\pi)^3}\,\frac{1}{\frac{\mathbf{q}^2}{2m_1}+\frac{(\mathbf{q}-\mathbf{p})^2}{2m_0}-p^0-i\varepsilon}\,\frac{1}{\frac{\mathbf{q}^2}{2m_1}+\frac{(\mathbf{q}-\mathbf{k})^2}{2m_0}-k^0-i\varepsilon}\\
&=\;-iz_1\,(2\mu_1)^2\int\frac{\mathrm{d}^3\mathbf{q}}{(2\pi)^3}\int_0^1\mathrm{d}x\,\frac{1}{\big[x\,a(\bar{p},\mathbf{q})\;+\;(1-x)\,a(\bar{k},\mathbf{q})\big]^2}\quad.
\end{aligned}\tag{D.58}$$

Thereby, in the last step we used the identity

$$\frac{\mathbf{q}^2}{2m_1}+\frac{(\mathbf{q}-\mathbf{p})^2}{2m_0}-p^0-i\varepsilon \;=\; \frac{\big(\mathbf{q}-\frac{\mu_1}{m_0}\mathbf{p}\big)^2-y_1^2(\bar{p})}{2\mu_1}\;=:\;\frac{a(\bar{p},\mathbf{q})}{2\mu_1}\quad, \tag{D.59}$$

where the function y_1 is given in eq. (3.7). Furthermore, the Feynman integral trick $1/(a_1a_2)=\int_0^1\mathrm{d}x/[xa_1+(1-x)a_2]^2$. was applied. We now assume that $Q\neq 0$. The case of vanishing three-momentum transfer, can be approximated with arbitrary small Q. Defining the translated and rescaled loop momentum $\mathbf{b}:=(\mathbf{q}-\frac{\mu_1}{m_0}[\,x\,\mathbf{p}+(1-x)\,\mathbf{k}\,])/(\frac{\mu_1}{m_0}Q)$, we collect those contributions in the denominator in eq. (D.58) that depend on $\mathbf{q}$ according to:

$$\begin{aligned}
&x\Big(\mathbf{q}-\frac{\mu_1}{m_0}\mathbf{p}\Big)^2\;+\;(1-x)\Big(\mathbf{q}-\frac{\mu_1}{m_0}\mathbf{k}\Big)^2\\
&\quad=\;x\Big(\frac{\mu_1}{m_0}Q\,\mathbf{b}+\frac{\mu_1}{m_0}\Big((x-1)\,\mathbf{p}\;+\;(1-x)\,\mathbf{k}\Big)\Big)^2\\
&\qquad+\;(1-x)\Big(\frac{\mu_1}{m_0}Q\,\mathbf{b}+\frac{\mu_1}{m_0}\Big(x\,\mathbf{p}\;+\;(-x)\,\mathbf{k}\Big)\Big)^2\\
&\quad=\;x\,\Big(\frac{\mu_1}{m_0}Q\,\mathbf{b}+(1-x)\frac{\mu_1}{m_0}\mathbf{Q}\Big)^2\;+\;(1-x)\Big(\frac{\mu_1}{m_0}Q\,\mathbf{b}-x\frac{\mu_1}{m_0}\mathbf{Q}\Big)^2\\
&\quad=\;[x+(1-x)]\,\Big(\frac{\mu_1}{m_0}Q\,\mathbf{b}\Big)^2\;+\;0\;+\;[x(1-x)^2+(1-x)x^2]\Big(\frac{\mu_1}{m_0}\mathbf{Q}\Big)^2\\
&\quad=\;\Big(\frac{\mu_1}{m_0}Q\Big)^2\big(\mathbf{b}^2\;-\;[\,x^2\;-\;x\,]\big)\quad.
\end{aligned}\tag{D.60}$$

Defining $C_{\bar{p}}:=-y_1^2(\bar{p})/(\frac{\mu_1}{m_0}Q)^2$, this leads to:

$$\begin{aligned}
&x\,a(\bar{p},\mathbf{q})\;+\;(1-x)\,a(\bar{k},\mathbf{q})\\
&\quad=\;\Big(\frac{\mu_1}{m_0}Q\Big)^2\big(\mathbf{b}^2\;-\;[\,x^2\;-\;x\,]\big)\;-\;x\,y_1^2(\bar{p})-(1-x)\,y_1^2(\bar{k})\\
&\quad=\;\Big(\frac{\mu_1}{m_0}Q\Big)^2\big(\mathbf{b}^2\;-\;A_{\bar{p},\bar{k}}(x)\big)\quad,\quad A_{\bar{p},\bar{k}}(x)\;:=\;x^2\;-\;(1+C_{\bar{p}}-C_{\bar{k}})\,x\;-\;C_{\bar{k}}\quad.
\end{aligned}\tag{D.61}$$

Thus, we choose spherical coordinates for **b**, and the integral (D.58) assumes the form:

$$
\begin{aligned}
\bar{\Sigma}^{\gamma}(\bar{p},\bar{k}) \;&=\; z_1\, 4\mu_1^2 \int \frac{\mathrm{d}^3\mathbf{b}}{(2\pi)^3} \left|\frac{\mu_1}{m_0}Q\right|^3 \int_0^1 \mathrm{d}x \, \frac{1}{\left[\left(\frac{\mu_1}{m_0}Q\right)^2 \left(\mathbf{b}^2 \,-\, A_{\bar{p},\bar{k}}(x)\right)\right]^2} \\
&= \frac{4\pi}{(2\pi)^3}\,\frac{2\pi}{\mu_1^2}\frac{1}{|a_1|}\,\frac{\mu_1^2}{|\frac{\mu_1}{m_0}Q|}\int_0^1 \mathrm{d}x\Big(\int_0^\infty \mathrm{d}b\frac{4r^2}{\left[b^2 - A_{\bar{p},\bar{k}}(x)\right]^2}\Big) \\
&= \frac{i}{|a_1|\,|\frac{\mu_1}{m_0}Q|}\int_0^1 \mathrm{d}x\,\frac{1}{\sqrt{A_{\bar{p},\bar{k}}(x)}} \\
&= \frac{1}{|a_1|\,|\frac{\mu_1}{m_0}Q|}\left[\arctan\left(\frac{1+(C_{\bar{k}}-C_{\bar{p}})}{2\sqrt{C_{\bar{p}}}}\right) + \arctan\left(\frac{1-(C_{\bar{k}}-C_{\bar{p}})}{2\sqrt{C_{\bar{k}}}}\right)\right] \quad .
\end{aligned}
\tag{D.62}
$$

Thereby, $\mathrm{Im}(-C_{\bar{p}}) = \varepsilon > 0$ implies $\mathrm{Im}(\sqrt{A_{\bar{p},\bar{k}}(x)}) > 0$ such that the integral formula

$$
\begin{aligned}
&\int_0^\infty \mathrm{d}r\frac{4r^2}{\left(r^2 - A\right)^2} \\
&= \int_0^\infty \mathrm{d}r\left[\frac{1}{\sqrt{A}}\left(\frac{1}{r-\sqrt{A}} - \frac{1}{r+\sqrt{A}}\right) + \frac{1}{(r+\sqrt{A})^2} + \frac{1}{(r-\sqrt{A})^2}\right] \\
&= \left[\frac{1}{\sqrt{A}}\Big(\ln(r-\sqrt{A}) - \ln(r+\sqrt{A})\Big) - \frac{1}{r+\sqrt{A}} - \frac{1}{r-\sqrt{A}}\right]_0^\infty \\
&= 0 - \left[\frac{1}{\sqrt{A}}\Big(\ln(-\sqrt{A}) - \ln(\sqrt{A})\Big) - \frac{1}{\sqrt{A}} - \frac{1}{-\sqrt{A}}\right] \\
&= \frac{1}{\sqrt{A}}\Big(\ln|\sqrt{A}| + i\arg(\sqrt{A}) - \ln|-\sqrt{A}| - i\arg(-\sqrt{A})\Big) \\
&= \frac{i}{\sqrt{A}}\Big(\arg(\sqrt{A}) - \arg(-\sqrt{A})\Big) \;=\; \frac{i}{\sqrt{A}}\,\mathrm{sgn}(\arg(\sqrt{A}))\pi \;=\; \frac{i\pi}{\sqrt{A}}
\end{aligned}
\tag{D.63}
$$

that was used in eq. (D.62), is applicable. In addition, we assumed that $\mathrm{Re}(C_{\bar p})$ and $\mathrm{Re}(C_{\bar k})$ are positive, implying:

$$\begin{aligned}
\int_0^1 \mathrm{d}x\,\frac{1}{\sqrt{A_{\bar p,\bar k}}} \;&=\; \int_0^1 \mathrm{d}x\,\frac{1}{\sqrt{x^2-(1+C_{\bar p}-C_{\bar k})x-C_{\bar k}}}\\
&= \left[\ln\left(2\sqrt{x^2-(1+C_{\bar p}-C_{\bar k})x-C_{\bar k}}+2x-(1+C_{\bar p}-C_{\bar k})\right)\right]_0^1\\
&= \ln\left((C_{\bar k}-C_{\bar p})+1\,+\,i2\sqrt{C_{\bar p}}\right)\;-\;\ln\left((C_{\bar k}-C_{\bar p})-1\,+\,i2\sqrt{C_{\bar k}}\right)\\
&= \ln\left|(C_{\bar k}-C_{\bar p})+1\,+\,i2\sqrt{C_{\bar p}}\right|\;-\;\ln\left|(C_{\bar k}-C_{\bar p})-1\,+\,i2\sqrt{C_{\bar k}}\right|\\
&\quad +i\left\{\arg\left((C_{\bar k}-C_{\bar p})+1\,+\,i2\sqrt{C_{\bar p}}\right)\;-\;\arg\left((C_{\bar k}-C_{\bar p})-1\,+\,i2\sqrt{C_{\bar k}}\right)\right\}\\
&\qquad\qquad \text{use:}\quad \forall\, x\in\mathbb{R},\, y>0:\ \arg(x+iy)\;=\;\frac{\pi}{2}-\arctan\left(\frac{x}{y}\right)\\
&= \ln\left(\sqrt{C_{\bar k}^2+C_{\bar p}^2+1-2C_{\bar k}C_{\bar p}+2C_{\bar k}-2C_{\bar p}+4C_{\bar p}}\right)\\
&\qquad -\;\ln\left(\sqrt{C_{\bar k}^2+C_{\bar p}^2+1-2C_{\bar k}C_{\bar p}-2C_{\bar k}+2C_{\bar p}+4C_{\bar k}}\right)\\
&\quad +i\left[\frac{\pi}{2}-\arctan\left(\frac{(C_{\bar k}-C_{\bar p})+1}{2\sqrt{C_{\bar p}}}\right)-\frac{\pi}{2}+\arctan\left(\frac{(C_{\bar k}-C_{\bar p})-1}{2\sqrt{C_{\bar k}}}\right)\right]\\
&= -i\left[\arctan\left(\frac{1+(C_{\bar k}-C_{\bar p})}{2\sqrt{C_{\bar p}}}\right)+\arctan\left(\frac{1-(C_{\bar k}-C_{\bar p})}{2\sqrt{C_{\bar k}}}\right)\right]\quad .
\end{aligned}\tag{D.64}$$

Eq. (D.64) proves the last line in eq. (D.62). This result for the matrix element $\bar\Sigma^\gamma(\bar p,\bar k)$ of the bubble diagram is also consistent with the formula given in ref. [84] for the charge form factor of the one-neutron halo state ^{11}Be. In our kinematics, we have to replace $\bar p\mapsto\frac{M_1}{M_\Sigma}\bar P+(\bar q-\bar s)$ and $\bar k\mapsto\frac{M_1}{M_\Sigma}\bar K+(\bar q+\bar s)$, leading to:

$$\begin{aligned}
C_{\bar p} \;&=\; -\frac{y_1^2(\bar P,\bar q-\bar s)}{(\frac{\mu_1}{m_0}Q)^2}\bigg|_{q^0=\epsilon_1(\bar P,\mathbf{q}-\mathbf{s})+i\varepsilon} \;=\; -\frac{y_1^2(|\mathbf{q}-\mathbf{s}|)}{(2\frac{M_\Sigma}{M_1}s)^2}\quad ,\\
C_{\bar k} \;&=\; -\frac{y_1^2(\bar K,\bar q+\bar s)}{(\frac{\mu_1}{m_0}Q)^2}\bigg|_{q^0=\epsilon_1(\bar K,\mathbf{q}+\mathbf{s})+i\varepsilon} \;=\; -\frac{y_1^2(|\mathbf{q}+\mathbf{s}|)}{(2\frac{M_\Sigma}{M_1}s)^2}\\
\Rightarrow\quad \frac{1\pm(C_{\bar k}-C_{\bar p})}{2} \;&=\; \frac{1}{2}\left[1\pm\frac{\frac{\mu_1}{\bar\mu_1}\left[(\mathbf{q}+\mathbf{s})^2-(\mathbf{q}-\mathbf{s})^2\right]}{\left(2\frac{M_\Sigma}{M_1}|\mathbf{s}|\right)^2}\right] \;=\; \frac{1}{2}\left[1\pm\frac{m_0}{M_\Sigma}\frac{\mathbf{q}\cdot\mathbf{s}}{s^2}\right]\quad .
\end{aligned}\tag{D.65}$$

Inserting eq. (D.65) into eq. (D.62) and using the anti-symmetry $\arctan(-x) = -\arctan(c)$ we end up with:

$$\begin{aligned}
&\bar{\Sigma}^{\gamma}\left(\frac{M_1}{M_\Sigma}\bar{P} + \bar{q} - \bar{s}, \frac{M_1}{M_\Sigma}\bar{K} + \bar{q} + \bar{s}\right)\Bigg|_{q^0=\epsilon_1(\bar{P},\mathbf{q}-\mathbf{s})+i\varepsilon} \\
&= \frac{1}{|a_1|}\frac{m_0 m_1}{2\mu_1 M_\Sigma}\frac{1}{s}\left[\arctan\left(\frac{\frac{m_0}{M_1}\frac{\mathbf{q}\cdot\mathbf{s}}{s} + \frac{M_\Sigma}{M_1}s}{\sqrt{-y_1^2(|\mathbf{q}-\mathbf{s}|)}}\right) - \arctan\left(\frac{\frac{m_0}{M_1}\frac{\mathbf{q}\cdot\mathbf{s}}{s} - \frac{M_\Sigma}{M_1}s}{\sqrt{-y_1^2(|\mathbf{q}+\mathbf{s}|)}}\right)\right] \quad .
\end{aligned} \tag{D.66}$$

Angular integration: Considering the remaining integral over $\mathbf{q}$ in eq. (D.57) with the bubble contribution (D.66), without loss of generality, we can assume that $\mathbf{Q}$ and consequently also $\mathbf{s}$ points in 3-direction. Thus, again $\mathbf{s} = s \cdot \mathbf{e_s}$ with $\mathbf{e_s} = \mathbf{e}_3$ holds. Choosing spherical coordinates

$$\mathbf{q} = q \cdot \mathbf{e_q} \quad , \qquad \mathbf{e_q} = \begin{pmatrix} \sin\theta\cos\phi \\ \sin\theta\sin\phi \\ \cos\theta \end{pmatrix} \quad , \tag{D.67}$$

we see that the integrand in eq. (D.57), in terms of the three-momenta $\mathbf{q}$ and $\mathbf{s}$, only depends on the lengths q, s and the angle $x := \mathbf{e_q}\cdot\mathbf{e_s} = \cos\theta$. The appearing scalar products simply read $\mathbf{q}\cdot\mathbf{s} = qsx$, leading to $|\mathbf{q} \pm \mathbf{r}| = d(q, r, \pm x)$, where the definition (D.36) is used. The integration over ϕ is trivial. It results in an additional factor of 2π such that the integral can be simplified according to:

$$\int\limits_{q<\Lambda} \frac{\mathrm{d}^3\mathbf{q}}{(2\pi)^3}\frac{1}{|a_1|}\frac{m_0 m_1}{2\mu_1 M_\Sigma}(\dots) \;=\; \frac{1}{(2\pi)^2}\frac{M_1}{M_\Sigma}\frac{1}{2|a_1|}\int_0^\Lambda \mathrm{d}q\, q^2 \int_{-1}^1 \mathrm{d}x\, (\dots) \quad . \tag{D.68}$$

In addition, we can interpret the resulting integrand in eq. (D.57) as a matrix-valued function $Y_2^{\mathrm{M}}(Q, p, k)$, yielding:

$$\boxed{\begin{aligned}
\mathcal{F}_{\mathrm{E},2}(Q) \;&=\; \int_0^\Lambda \mathrm{d}p \int_0^\Lambda \mathrm{d}k\; \bar{G}(p)^{\mathrm{T}}\; \bar{D}^{[0]}(p)\; Y_2^{\mathrm{M}}(Q,p,k)\; \bar{D}^{[0]}(k)\; \bar{G}(k) \\[2ex]
Y_2^{\mathrm{M}}(Q,p,k) \;&=\; \frac{1}{(2\pi)^2}\frac{M_1}{M_\Sigma}\frac{1}{2|a_1|}\int_0^\Lambda \mathrm{d}q\, q^2 \int_{-1}^1 \mathrm{d}x\; \Upsilon_2^{\mathrm{M}}\Big(\frac{m_1}{M_\Sigma}\frac{Q}{2}, q, x, p, k\Big) \\
\Upsilon_2^{\mathrm{M}}(s,q,x,p,k) \;&=\; \Upsilon_2^{\mathrm{S}}(s,q,x)\; {}^{\bullet}\bar{R}^{[0]}(p, d(s,q,-x))\; \bar{D}(d(s,q,-x)) \\
&\qquad \times\; (\mathbf{e}_1 \cdot \mathbf{e}_1^{\mathrm{T}})\; \bar{D}(d(s,q,x))\; {}^{\bullet}\bar{R}^{[0]}(d(s,q,x), k) \\
\Upsilon_2^{\mathrm{S}}&(s,q,x) \\
&= \frac{1}{s}\left[\arctan\left(\frac{\frac{m_0}{M_1}qx + \frac{M_\Sigma}{M_1}s}{\sqrt{-y_1^2(d(s,q,-x))}}\right) \;-\; \arctan\left(\frac{\frac{m_0}{M_1}qx - \frac{M_\Sigma}{M_1}s}{\sqrt{-y_1^2(d(s,q,x))}}\right)\right]
\end{aligned}} \tag{D.69}$$

Properties: In order to determine $\mathcal{F}_{\mathrm{E},2}(Q)$, we have to evaluate 4 integrals, namely those over the 3 momenta $p, k, q \in [0, \Lambda]$ and 1 over the angle $x \in [-1, 1]$. One can easily check that $\Upsilon_2^{\mathrm{S}}(s, q, -x) = \Upsilon_0^{\mathrm{M}}(s, q, x)$ and $\Upsilon_2^{\mathrm{M}}(s, q, x, p, k) = \Upsilon_0^{\mathrm{M}}(s, q, -x, k, p)^{\mathrm{T}}$ hold such that, after substituting $x \mapsto -x$, the symmetry $Y_2^{\mathrm{M}}(Q, p, k) = Y_2^{\mathrm{M}}(Q, k, p)^{\mathrm{T}}$ follows, as required. Since $E^{(3)} < 0$ holds, all appearing functions are uncritical and real in the limit $\varepsilon \to 0^+$. Thus, $\mathcal{F}_{\mathrm{E},2}(Q)$ is real, as it should. The additional symmetries $\Upsilon_2^{\mathrm{S}}(-s, q, x) = \Upsilon_2^{\mathrm{M}}(s, q, x)$ and $\Upsilon_2^{\mathrm{M}}(-s, q, x, p, k) = \Upsilon_2^{\mathrm{M}}(s, q, -x, p, k)$, after substituting $x \mapsto -x$, lead to $Y_2^{\mathrm{M}}(-Q) = Y_2^{\mathrm{M}}(Q)$. Consequently, also the contribution $\mathcal{F}_{\mathrm{E},2}(Q)$ to the form factor is an even function in Q and can be written in the usual way $\mathcal{F}_{\mathrm{E},0}(Q^2)$. Note that the limit $Q \to 0$ in eq. (D.69) exists, but prefactors $\propto 1/Q$ cause numerical instabilities for very small momentum transfer. A discussion of the numerical implementation is given in sec. B.

D.3.5 Photodisintegration

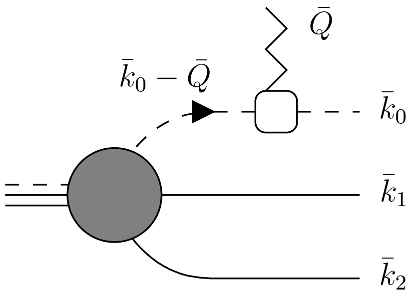

Figure D.10: Feynman diagram for the matrix element $i\bar{M}^{(\mathrm{a})}$ of the photodisintegration of a *cnn*-trimer. All *c*-*n* FSI are neglected. A diagrammatic equation for the appearing irreducible trimer-three-particle coupling is given fig. 3.6

For a two-neutron halo system, we now calculate the matrix element $i\bar{M}^{(\mathrm{a})}$ for the photodisintegration without *c*-*n* FSI. Its Feynman diagram is depicted in fig. D.10 and appears as the first contribution in fig. 3.16. Using the center-of-mass kinematics (3.70)-(3.73), the appearing intermediate core propagator has four-momentum $\bar{k}_0 - \bar{Q}$. Its offset from the on-shell condition reads:

$$\begin{aligned} k_0^0 - Q^0 - \frac{(\mathbf{k}_0 - \mathbf{Q})^2}{2m_0} &= \frac{\mathbf{k}_0^2}{2m_0} - \left(E_\Sigma - E^{(3)} - \frac{\mathbf{Q}^2}{2M_\Sigma}\right) - \frac{(\mathbf{k}_0 - \mathbf{Q})^2}{2m_0} \\ &= E^{(3)} - \left[E_\Sigma - \frac{Q^2}{2M_\Sigma} + \frac{Q(Q - 2\mathbf{e}_3 \cdot \mathbf{k}_0)}{2m_0}\right] \;=:\; E^{(3)} - \bar{E}(E_\Sigma, Q, \mathbf{k}_0) \quad . \end{aligned} \tag{D.70}$$

Using the irreducible trimer-three-particle coupling from eqs. (3.58)-(3.60) and fig. 3.6, we replace the kinematic variables

$$\begin{aligned} E + \frac{\mathbf{p}_i^2}{2m_i} - p_i^0 &\mapsto \delta_{i0}\left[E^{(3)} - (E^{(3)} - \bar{E}(E_\Sigma, Q, \mathbf{k}_0))\right] + (1 - \delta_{i0})\left[E^{(3)} - 0\right] \\ &\quad = \delta_{i0}\,\bar{E}(E_\Sigma, Q, \mathbf{k}_0) \,+\, (1 - \delta_{i0})\,E^{(3)} \;=:\; \bar{E}_i(E_\Sigma, Q, \mathbf{k}_0) \quad , \\ \left|\frac{m_i}{M_\Sigma}\mathbf{P} - \mathbf{p}_i\right| &\mapsto \begin{cases} \left| -\frac{m_0}{M_\Sigma}\mathbf{Q} - (\mathbf{k}_0 - \mathbf{Q})\right| = \left|\frac{M_0}{M_\Sigma}Q\mathbf{e}_3 - \mathbf{k}_0\right| & : i = 0 \\ \left| -\frac{m_1}{M_\Sigma}\mathbf{Q} - \mathbf{k}_1\right| = \left|\frac{m_1}{M_\Sigma}Q\mathbf{e}_3 + \mathbf{k}_1\right| & : i = 1 \\ \left| -\frac{m_1}{M_\Sigma}\mathbf{Q} + (\mathbf{k}_0 + \mathbf{k}_1)\right| = \left|\frac{m_1}{M_\Sigma}Q\mathbf{e}_3 - (\mathbf{k}_0 + \mathbf{k}_1)\right| & : i = 2 \end{cases} \\ &\quad =: \bar{d}_i(Q, \mathbf{k}_0, \mathbf{k}_1) \quad , \end{aligned} \tag{D.71}$$

yielding the result:

$$\begin{aligned}
\bar{M}^{(\mathrm{a})}(E_\Sigma, Q, \mathbf{k}_0, \mathbf{k}_1) \;&=\; (\mathcal{Z}e) \sum_{i=0}^{2} \Big[\sum_{j=0}^{1} \int_0^\Lambda \mathrm{d}q\, \bar{G}_j(q)\, \bar{D}_j^{[0]}(q) \\
&\times\; {}^\bullet\bar{R}_{ji}^{[0]}\big(\bar{E}_i(E_\Sigma, Q, \mathbf{k}_0), q, \bar{d}_i(Q, \mathbf{k}_0, \mathbf{k}_1)\big) \;-\; |\beta \bar{H}|\, \delta_{0i} \Big] \\
&\times\; \sqrt{\frac{z_i}{\tau_i}}\, \frac{\bar{D}_i\big(\bar{E}_i(E_\Sigma, Q, \mathbf{k}_0), \bar{d}_i(Q, \mathbf{k}_0, \mathbf{k}_1)\big)}{E^{(3)} - \bar{E}_0(E_\Sigma, Q, \mathbf{k}_0) + i\varepsilon} \quad .
\end{aligned} \tag{D.72}$$

D.3.5.1 Dipole matrix element

In order to extract the dipole matrix element $\bar{M}_{E1}^{(\mathrm{a})}(E_\Sigma, \mathbf{k}_0, \mathbf{k}_1)$, we apply eq. (3.74) to our result (D.72). The differentiation with respect to Q is rather elaborate but can be performed straightforwardly by applying standard rules of derivation. Using the formulas (3.41), the result can be summarized as:

$$
\boxed{
\begin{aligned}
\bar{M}^{(\mathrm{a})}_{E1}(E_\Sigma,\mathbf{k}_0,\mathbf{k}_1) \;&=\; (\mathcal{Z}e)\,\sqrt{\frac{3}{4\pi}}\,\Big[\int_0^\Lambda \mathrm{d}q\,\bar{G}^{\mathrm{T}}(q)\,\bar{D}^{[0]}(q)\,Y^{\mathrm{V}}_{\mathrm{E1}}(E_\Sigma,q,\mathbf{k}_0,\mathbf{k}_1)\\
&\qquad\qquad\qquad -\;|\beta\bar{H}|\,Y^{\mathrm{S}}_{\mathrm{E1}}(E_\Sigma,\mathbf{k}_0,\mathbf{k}_1)\Big] \quad ,\\
Y^{\mathrm{S}}_{\mathrm{E1}} \;&=\; \bar{\chi}_0 \quad , \qquad (Y^{\mathrm{V}}_{\mathrm{E1}})_i \;=\; \sum_{j=0}^{2}\Big[{}^{\bullet}\bar{R}^{[0]}_{ij}(E_j,q,d_j)\,\Big(\bar{\chi}_j-\frac{\lambda_j}{d_j^2}\,\chi_j\Big)\\
&\qquad -\;(\partial_E{}^{\bullet}\bar{R}^{[0]}_{ij})(E_j,q,d_j)\,\Big(\bar{c}_{ij}(E_j,q,d_j)-\delta_{j0}\frac{d_0^2}{\bar{\mu}_0}\Big)\,\frac{\lambda_j}{d_j^2}\,\chi_j\Big] \quad ,\\[2ex]
(\partial_E{}^{\bullet}\bar{R}^{[0]}_{ij})(E,p,k) \;&=\; (1-\delta_{i0}\delta_{j0})\,\sqrt{\frac{z_iz_j}{\tau_i\tau_j}}\,(-1)\Big(\frac{m_{ij}}{pk}\Big)^2\,(\partial Q_0)(c_{ij}(E,p,k))\\
(\partial Q_0)(c) \;&=\; (1-c^2)^{-1} \quad , \quad \bar{c}_{ij}(E,p,k) \;=\; -\Big(\frac{p^2}{2\mu_j}-\frac{k^2}{2\mu_i}-E-i\varepsilon\Big) \quad ,\\
\chi_i \;&=\; \sqrt{\frac{z_i}{\tau_i}}\,\frac{\bar{D}_i(E_i,d_i)}{E^{(3)}-E_\Sigma+i\varepsilon} \quad ,\\
\bar{\chi}_i \;&=\; -\sqrt{\frac{z_i}{\tau_i}}\Big[\frac{\lambda_0}{\bar{\mu}_0}\,\frac{\bar{D}_i(E_i,d_i)}{(E^{(3)}-E_\Sigma+i\varepsilon)^2}\;+\;(1-\delta_{i0})\,\frac{\lambda_i}{\bar{\mu}_i}\,\frac{(\partial_E\bar{D}_i)(E_i,d_i)}{E^{(3)}-E_\Sigma+i\varepsilon}\Big] \quad ,\\
\bar{D}_i(E,q) \;&=\; -\frac{2\pi}{z_i\mu_i}\,\frac{1}{-\frac{1}{a_i}-iy_i(E,q)} \quad ,\\
(\partial_E\bar{D}_i)(E,q) \;&=\; \frac{2\pi}{z_i}\,\frac{1}{iy_i(E,q)(-\frac{1}{a_i}-iy_i(E,q))^2} \quad ,\\[2ex]
d_i \;:=\; \bar{d}_i(0,\mathbf{k}_0,\mathbf{k}_1) \;&=\; \begin{cases} |\mathbf{k}_0| & : i=0\\ |\mathbf{k}_1| & : i=1\\ |\mathbf{k}_0+\mathbf{k}_1| & : i=2 \quad ,\end{cases}\\
\lambda_i \;:=\; \bar{d}_i(0,\mathbf{k}_0,\mathbf{k}_1)\,(\partial_Q\bar{d}_i)(0,\mathbf{k}_0,\mathbf{k}_1) \;&=\; \begin{cases} -\frac{M_0}{M_\Sigma}\,(\mathbf{k}_0)_3 & : i=0\\ \frac{m_1}{M_\Sigma}\,(\mathbf{k}_1)_3 & : i=1\\ -\frac{m_1}{M_\Sigma}\,(\mathbf{k}_0+\mathbf{k}_1)_3 & : i=2 \quad ,\end{cases}\\
E_i \;:=\; \bar{E}_i(E_\Sigma,0,\mathbf{k}_0) \;&=\; \delta_{i0}E_\Sigma\;-\;(1-\delta_{i0})E^{(3)} \quad .
\end{aligned}
}
\tag{D.73}
$$

For reasons of readability, at some points, we dropped the arguments of d_i, λ_i, E_i, χ_i and $\bar{\chi}_i$.

D.3.5.2 Dipole strength distribution

In order to calculate the dipole strength distribution, we now perform the remaining momentum integrations in eq. (3.75). Analogous to eqs. (D.48) and (D.49), we first choose spherical coordinates for $\mathbf{k}_0$ and $\mathbf{k}_1$ according to:

$$\mathbf{k}_i = k_i \cdot \mathbf{e}_{\mathbf{k}_i} \quad , \quad \mathbf{e}_{\mathbf{k}_i} \; = \; \begin{pmatrix} \sin\theta_i \cos\phi_i \\ \sin\theta_i \sin\phi_i \\ \cos\theta_i \end{pmatrix} \quad . \tag{D.74}$$

We see that $\bar{M}^{(\mathrm{a})}_{E1}$ in eq. (D.73), in terms of the three-momenta $\mathbf{k}_0$ and $\mathbf{k}_1$, effectively only depends on their lengths k_0 and k_1 and polar angles

$$x_i \; := \; \mathbf{e}_{\mathbf{Q}} \cdot \mathbf{e}_{\mathbf{k}_i} \; = \; \cos\theta_i \; = \; (\mathbf{e}_{\mathbf{k}_i})_3 \quad . \tag{D.75}$$

In addition, the δ-function in eq. (3.75) depends on the relative angle

$$\mathbf{e}_{\mathbf{k}_0} \cdot \mathbf{e}_{\mathbf{k}_1} \; = \sqrt{1-x_0^2}\sqrt{1-x_1^2}\cos(\phi_0-\phi_1) + x_0 x_1 \; =: \; x_{01}(x_0, x_1, \cos(\phi_0-\phi_1)) \tag{D.76}$$

and can only contribute if the total energy is positive. Applying formula (D.50), we get:

$$\begin{aligned} \frac{\mathrm{dB(E1)}}{\mathrm{d}E_\Sigma} \; &= \frac{4\pi}{(2\pi)^6}\,\Theta(E_\Sigma) \int_{-1}^{1} \mathrm{d}x_0 \int_{-1}^{1} \mathrm{d}x_1 \int_0^{\pi} \mathrm{d}\phi \int_0^{\infty} \mathrm{d}k_0 \int_0^{\infty} \mathrm{d}k_1 \\ &\quad \times \; k_0^2\, k_1^2 \; |\bar{M}^{(\mathrm{a})}_{E1}(E_\Sigma, k_0, k_1, x_0, x_1)|^2 \\ &\quad \times \; \delta\Big(\frac{k_0^2}{2\mu_1} + \frac{k_1^2}{2\mu_0} + \frac{k_0 k_1 x_{01}(x_0, x_1, \cos\phi)}{m_1} - E_\Sigma\Big) \quad . \end{aligned} \tag{D.77}$$

The δ-function only allows for specific momentum configurations in the k_0-k_1-plane. The allowed values form a centered and rotated ellipse. The two semi-axes of this ellipse depend on the masses, the total energy E_Σ and the angle x_{01}, which itself is a function of x_0, x_1 and ϕ. We proceed stepwise in order to transform the ellipse into its circular form, in which the momentum-integration is trivial. Therefore, we first define $\vec{k} := (k_0, k_1)$ and $F(\vec{k}) := \; k_0^2\, k_1^2 \; |\bar{M}^{(\mathrm{a})}_{E1}(E_\Sigma, k_0, k_1, x_0, x_1)|^2$ such that the integral assumes the form:

$$I \; := \; \int_{[0,\infty)^2} \mathrm{d}^2\vec{k}\, F(\vec{k}) \; \delta\Big(\frac{k_0^2}{2\mu_1} + \frac{k_1^2}{2\mu_0} + \frac{k_0 k_1 x_{01}}{m_1} - E_\Sigma\Big) \quad . \tag{D.78}$$

Substituting $\vec{k} \; =: \; M\vec{l}$ with $M \; := \; \mathrm{diag}(\sqrt{E_\Sigma/\mu_0}, \sqrt{E_\Sigma/\mu_1})$ and defining the quantity $\kappa := \frac{\sqrt{\mu_0\mu_1}}{m_1} x_{01} = \sin(\phi_{01})\, x_{01}$, the argument of the δ-delta function becomes a symmetric quadratic form:

$$\begin{aligned} I \; &= \int_{M^{-1}[0,\infty)^2} \mathrm{d}^2\vec{l}\, \Big|\frac{E_\Sigma}{\sqrt{\mu_0\mu_1}}\Big|\, F(M\vec{l}) \; \delta\Big(\frac{E_\Sigma}{2\mu_0\mu_1}(l_0^2 + l_1^2 + 2\kappa\, l_0 l_1 - 2\mu_0\mu_1)\Big) \\ &= \int_{[0,\infty)^2} \mathrm{d}^2\vec{l}(2\sqrt{\mu_0\mu_1})\, F(M\vec{l}) \; \delta\big(\vec{l}^{\mathrm{T}} \left(\begin{smallmatrix} 1 & \kappa \\ \kappa & 1 \end{smallmatrix}\right) \vec{l} - 2\mu_0\mu_1\big) \quad . \end{aligned} \tag{D.79}$$

Since $|\kappa| < 1$ holds, we transform the ellipse into its circular form using $\vec{l} =: SN\vec{y}$ with $N = \mathrm{diag}(\sqrt{2\mu_0\mu_1/(1+\kappa)}, \sqrt{2\mu_0\mu_1/(1-\kappa)}) \in \mathbb{R}^{2\times 2}$ and $S := \frac{1}{\sqrt{2}}\left(\begin{smallmatrix} 1 & -1 \\ 1 & 1 \end{smallmatrix}\right) \in SO(2)$. This yields:

$$\begin{aligned} I \;&=\; \int_{N^{-1}S^{-1}[0,\infty)^2} \mathrm{d}^2\vec{y}\; \left|\sqrt{\frac{2\mu_0\mu_1}{1+\kappa}}\sqrt{\frac{2\mu_0\mu_1}{1-\kappa}}\right| \cdot |1| \\ &\qquad \times\; (2\sqrt{\mu_0\mu_1})\, F(MSN\vec{y}\,)\; \delta\left(2\mu_0\mu_1(\vec{y}^2 - 1)\right) \\ &=\; \int_{N^{-1}S^{\mathrm{T}}[0,\infty)^2} \mathrm{d}^2\vec{y}\; 2\sqrt{\frac{\mu_0\mu_1}{1-\kappa^2}}\, F\left(MSN\vec{y}\right)\; \delta\left(\vec{y}^2 - 1\right) \quad . \end{aligned} \tag{D.80}$$

We now use spherical coordinates $\vec{y} = r(\cos\alpha, \sin\alpha)^{\mathrm{T}}$. Since S^{T} is a rotation of $-\pi/4$ and N^{-1} simply stretches the $y_{0,1}$ axis by a factors of $\sqrt{(1\pm\kappa)/(2\mu_0\mu_1)}$, the area of integration is given through $(r, \alpha) \in [0,\infty) \times [-\bar{\alpha}, \bar{\alpha}]$ with:

$$\begin{aligned} \bar{\alpha} \;&=\; \arctan\left(\sqrt{\frac{1-\kappa}{2\mu_0\mu_1}}\Big/\sqrt{\frac{1+\kappa}{2\mu_0\mu_1}}\right) \;=\; \arctan\sqrt{\frac{1-\kappa}{1+\kappa}} \;=\; \frac{\arccos\kappa}{2} \;\in\; \left[\frac{\pi}{8}, \frac{3\pi}{8}\right] \\ \Rightarrow \quad \kappa \;&=\; \cos(2\bar{\alpha}) \quad , \qquad 1 \pm \kappa \;=\; 2\begin{cases} \cos^2\bar{\alpha} \\ \sin^2\bar{\alpha} \quad . \end{cases} \end{aligned} \tag{D.81}$$

Consequently, we get:

$$\begin{aligned} I \;&=\; \int_0^\infty \mathrm{d}r\; \int_{-\bar{\alpha}}^{\bar{\alpha}} \mathrm{d}\alpha\; \sqrt{\frac{\mu_0\mu_1}{1-\kappa^2}}\; F\left(MQNr\left(\begin{smallmatrix} \cos\alpha \\ \sin\alpha \end{smallmatrix}\right)\right)\; (2r)\delta\left(r^2 - 1\right) \\ &= \sqrt{\frac{\mu_0\mu_1}{1-\kappa^2}}\; \int_{-\bar{\alpha}}^{\bar{\alpha}} \mathrm{d}\alpha \\ &\qquad \times\; F\Big(\sqrt{\mu_1 E_\Sigma}\Big[\frac{\cos\alpha}{\sqrt{1+\kappa}} - \frac{\sin\alpha}{\sqrt{1-\kappa}}\Big], \sqrt{\mu_0 E_\Sigma}\Big[\frac{\cos\alpha}{\sqrt{1+\kappa}} + \frac{\sin\alpha}{\sqrt{1-\kappa}}\Big]\Big) \\ &= \sqrt{\mu_0\mu_1}\,\frac{\bar{\alpha}}{\sin(2\bar{\alpha})}\; \int_{-1}^{1} \mathrm{d}y \\ &\qquad \times\; F\Big(\sqrt{\frac{\mu_1 E_\Sigma}{2}}\Big[\frac{\cos(\bar{\alpha}y)}{\cos\bar{\alpha}} - \frac{\sin(\bar{\alpha}y)}{\sin\bar{\alpha}}\Big], \sqrt{\frac{\mu_0 E_\Sigma}{2}}\Big[\frac{\cos(\bar{\alpha}y)}{\cos\bar{\alpha}} + \frac{\sin(\bar{\alpha}y)}{\sin\bar{\alpha}}\Big]\Big) \\ &= \frac{\sqrt{\mu_0\mu_1}}{2}\,\frac{\beta}{\sin\beta}\; \int_{-1}^{1} \mathrm{d}y\; F\Big(\sqrt{2\mu_1 E_\Sigma}\,\frac{\sin(\frac{1-y}{2}\beta)}{\sin\beta}, \sqrt{2\mu_0 E_\Sigma}\,\frac{\sin(\frac{1+y}{2}\beta)}{\sin\beta}\Big) \quad , \end{aligned} \tag{D.82}$$

where in the last line we used:

$$\begin{aligned} \frac{\cos(\bar{\alpha}y)}{\cos\bar{\alpha}} \pm \frac{\sin(\bar{\alpha}y)}{\sin\bar{\alpha}} \;&=\; \frac{\sin\bar{\alpha}\cos(\bar{\alpha}y) \pm \sin(\bar{\alpha}y)\cos\bar{\alpha}}{\sin\bar{\alpha}\cos\bar{\alpha}} \;=\; 2\frac{\sin((1\pm y)\bar{\alpha})}{\sin(2\bar{\alpha})} \\ &=\; 2\frac{\sin(\frac{1\pm y}{2}\beta\alpha)}{\sin(\beta)} \quad , \qquad \beta \;:=\; 2\bar{\alpha} \;=\; \arccos\kappa \quad . \end{aligned} \tag{D.83}$$

Inserting this expression and using the formulas from eq. (3.41), leads to the final result:

$$
\boxed{
\begin{aligned}
\frac{\mathrm{dB(E1)}}{\mathrm{d}E_\Sigma} \;&=\; \frac{4\pi}{(2\pi)^6}\, 2(\mu_0\mu_1)^{\frac{3}{2}}\;\Theta(E_\Sigma)\,E_\Sigma^2 \int_{-1}^{1}\mathrm{d}x_0 \int_{-1}^{1}\mathrm{d}x_1 \int_0^\pi \mathrm{d}\phi\, \frac{\beta}{\sin^5\beta} \\
&\times \int_{-1}^{1}\mathrm{d}y\;\sin^2\!\Big(\frac{1-y}{2}\beta\Big)\sin^2\!\Big(\frac{1+y}{2}\beta\Big) \\
&\times \left|\bar{M}^{(\mathrm{a})}_{E1}\Big(E_\Sigma, \sqrt{2\mu_1 E_\Sigma}\,\frac{\sin(\frac{1-y}{2}\beta)}{\sin\beta}, \sqrt{2\mu_0 E_\Sigma}\,\frac{\sin(\frac{1+y}{2}\beta)}{\sin\beta}, x_0, x_1\Big)\right|^2 \\
\beta(x_0,x_1,\cos\phi) \;&=\; \arccos\Big(\frac{\sqrt{\mu_0\mu_1}}{m_1}\,\big[\sqrt{1-x_0^2}\sqrt{1-x_1^2}\cos\phi + x_0x_1\big]\Big) \\[2ex]
\bar{M}^{(\mathrm{a})}_{E1}(E_\Sigma,k_0,k_1,x_0,x_1) \;&=\; (\mathcal{Z}e)\sqrt{\frac{3}{4\pi}}\,\Big[\int_0^\Lambda \mathrm{d}q\,\bar{G}^{\,\mathrm{T}}(q)\,\bar{D}^{[0]}(q) \\
&\quad\times\; Y^{\mathrm{V}}_{\mathrm{E1}}(E_\Sigma,q,k_0,k_1,x_0,x_1) \;-\; |\beta\bar{H}|\,Y^{\mathrm{S}}_{\mathrm{E1}}(E_\Sigma,k_0,k_1,x_0,x_1)\Big] \quad, \\
Y^{\mathrm{S}}_{\mathrm{E1}} \;&=\; \bar{\chi}_0 \quad,\qquad (Y^{\mathrm{V}}_{\mathrm{E1}})_i \;=\; \sum_{j=0}^{2}\Big[{}^{\bullet}\bar{R}^{[0]}_{ij}(E_j,q,d_j)\,\Big(\bar{\chi}_j - \frac{\lambda_j}{d_j^2}\,\chi_j\Big) \\
&\qquad -\;(\partial_E{}^{\bullet}\bar{R}^{[0]}_{ij})(E_j,q,d_j)\,\Big(\bar{c}_{ij}(E_j,q,d_j) - \delta_{j0}\frac{d_0^2}{\bar{\mu}_0}\Big)\,\frac{\lambda_j}{d_j^2}\,\chi_j\Big] \quad, \\[2ex]
(\partial_E{}^{\bullet}\bar{R}^{[0]}_{ij})(E,p,k) \;&=\; (1-\delta_{i0}\delta_{j0})\,\sqrt{\frac{z_iz_j}{\tau_i\tau_j}}\,(-1)\Big(\frac{m_{ij}}{pk}\Big)^2(\partial Q_0)(c_{ij}(E,p,k)) \\
(\partial Q_0)(c) \;&=\; (1-c^2)^{-1} \quad,\quad \bar{c}_{ij}(E,p,k) \;=\; -\Big(\frac{p^2}{2\mu_j} - \frac{k^2}{2\mu_i} - E - i\varepsilon\Big) \quad, \\
\chi_i \;&=\; \sqrt{\frac{z_i}{\tau_i}}\,\frac{\bar{D}_i(E_i,d_i)}{E^{(3)}-E_\Sigma+i\varepsilon} \quad, \\
\bar{\chi}_i \;&=\; -\sqrt{\frac{z_i}{\tau_i}}\left[\frac{\lambda_0}{\bar{\mu}_0}\,\frac{\bar{D}_i(E_i,d_i)}{(E^{(3)}-E_\Sigma+i\varepsilon)^2} \;+\; (1-\delta_{i0})\,\frac{\lambda_i}{\bar{\mu}_i}\,\frac{(\partial_E\bar{D}_i)(E_i,d_i)}{E^{(3)}-E_\Sigma+i\varepsilon}\right] \quad, \\
\bar{D}_i(E,q) \;&=\; -\frac{2\pi}{z_i\mu_i}\,\frac{1}{-\frac{1}{a_i} - iy_i(E,q)} \quad, \\
(\partial_E\bar{D}_i)(E,q) \;&=\; \frac{2\pi}{z_i}\,\frac{1}{iy_i(E,q)(-\frac{1}{a_i}-iy_i(E,q))^2} \quad, \\[2ex]
d_i \;&=\; \begin{cases} k_0 \\ k_1 \\ \big[2m_1\big(E_\Sigma - \frac{k_0^2}{2m_0} - \frac{k_1^2}{2m_1}\big)\big]^{\frac{1}{2}} \end{cases} ,\; \lambda_i \;=\; \begin{cases} -\frac{M_0}{M_\Sigma}\,k_0x_0 & : i=0 \\ \frac{m_1}{M_\Sigma}\,k_1x_1 & : i=1 \\ -\frac{m_1}{M_\Sigma}\,(k_0x_0+k_1x_1) & : i=2 \end{cases} , \\
E_i \;&=\; \delta_{i0}E_\Sigma \;-\; (1-\delta_{i0})E^{(3)} \quad .
\end{aligned}
}
\tag{D.84}
$$

Thereby, $Y^{\mathrm{V}}_{\mathrm{E1}}(E_\Sigma, q, k_0, k_1, x_0, x_1) \in \mathbb{C}^2$ and $Y^{\mathrm{S}}_{\mathrm{E1}}(E_\Sigma, k_0, k_1, x_0, x_1) \in \mathbb{C}$ hold. Hence, we end up with 1 momentum integral $q \in [0, \Lambda]$ and 4 angular integrals $x_0, x_1, y \in [-1, 1]$, $\phi \in [0, \pi]$. There seems to be no reasonable chance to perform the limit $\varepsilon \to 0^+$ in eq. (D.84) analytically. A discussion of the numerical implementation is given in sec. B.

Bibliography

[1] P. W. Higgs. Broken symmetries, massless particles and gauge fields. *Phys. Lett.*, **12**:132–133, (1964).

[2] P. W. Higgs. Broken symmetries, massless particles and gauge fields. *Phys. Lett.*, **13**:508–509, (1964).

[3] F. Englert and R. Brout. Broken Symmetry and the Mass of Gauge Vector Mesons. *Phys. Rev. Lett.*, **13**:321–323, (1964).

[4] D. J. Gross and F. Wilczek. Ultraviolet Behavior of Nonabelian Gauge Theories. *Phys. Rev. Lett.*, **30**:1343–1346, (1973).

[5] H. D. Politzer. Reliable Perturbative Results for Strong Interactions? *Phys. Rev. Lett.*, **30**:1346–1349, (1973).

[6] K. G. Wilson. Confinement of quarks. *Phys. Rev. D*, **10**:2445–2459, (1974).

[7] A. Bazavov et al. Full nonperturbative QCD simulations with 2+1 flavors of improved staggered quarks. *Rev. Mod. Phys.*, **82**:1349–1417, (2010), arXiv:0903.3598v2 [hep-lat].

[8] G. Ecker. Chiral perturbation theory. *Prog. Part. Nucl. Phys.*, **35**:1–80, (1995), arXiv:hep-ph/9501357.

[9] S. Scherer. Introduction to chiral perturbation theory . *Adv. Nucl. Phys.*, **27**:277, (2003), arXiv:hep-ph/0210398.

[10] V. Bernard and U.-G. Meissner. Chiral perturbation theory. *Ann. Rev. Nucl. Part. Sci.*, **57**:33–60, (2007), arXiv:hep-ph/0611231.

[11] J. J. Sakurai. *Modern Quantum Mechanics.* Addison-Wesley Publishing Company, Inc., (1985).

[12] J. R. Taylor. *Scattering Theory.* Dover Publications, Inc., (1972).

[13] R. G. Newton. *Scattering Theory of Waves and Particles.* Springer-Verlag New York, Inc., 2nd edition, (1966).

[14] D. E. Gonzales Trotter et al. New Measurement of the $^1S_0$ Neutron-Neutron Scattering Length Using the Neutron-Proton Scattering Length as a Standard. *Phys. Rev. Lett.*, **83**:3788–3791, (1999), arXiv:nucl-ex/9904011v2.

[15] G. A. Miller, B. M. K. Nefkens and I. Slaus. Charge symmetry, quarks and mesons. *Phys. Rept.*, **194**:1–116, (1990).

[16] S. K. Choi et al. [Belle Collaboration]. Observation of a narrow charmonium-like state in exclusive $B^+ \to K^+\pi^+\pi^- J/\psi$ decays. *Phys. Rev. Lett.*, **91**:262001, (2003), arXiv:hep-ex/0309032.

[17] X. L. Wang et al. [Belle Collaboration]. Observation of Two Resonant Structures in $e^+e^- \to \pi^+\pi^-\psi(2S)$ via Initial State Radiation at Belle. *Phys. Rev. Lett.*, **99**:142002, (2007), arXiv:0707.3699v2 [hep-ex].

[18] D. L. Canham, H.-W. Hammer and R. P. Springer. On the scattering of D and D^* mesons off the $X(3872)$. *Phys. Rev. D*, **80**:014009, (2009), arXiv:0906.1263 [hep-ph].

[19] P. Hagen, H.-W. Hammer, C. Hanhart. Two and three-body structure of the $Y(4660)$. *Phys. Lett. B*, **696**:103–108, (2011), arXiv:1007.1126v2 [hep-ph].

[20] H. Feshbach. A Unified Theory of Nuclear Reactions. II. *Ann. Phys.*, **19**:287–313, (1962).

[21] S. Inouye et al. Observation of Feshbach resonances in a Bose–Einstein condensate. *Nature*, **392**:151–154, (1998).

[22] J. L. Roberts et al. Resonant Magnetic Field Control of Elastic Scattering in Cold ^{85}Rb. *Phys. Rev. Lett.*, **81**:5109–5112, (1998), arXiv:physics/9808018 [physics.atom-ph].

[23] E. Braaten and H.-W. Hammer. Universality in few-body systems with large scattering length. *Phys. Rept.*, **428**:259–390, (2006), arXiv:cond-mat/0410417v3 [cond-mat.other].

[24] K. G. Wilson. Renormalization Group and Strong Interactions. *Phys. Rev. D*, **3**:1818–1846, (1971).

[25] V. Efimov. Energy levels arising from resonant two-body forces in a three-body system. *Phys. Lett. B*, **33**:563–564, (1970).

[26] F. Ferlaino and R. Grimm. Forty years of Efimov physics: How a bizarre prediction turned into a hot topic. *Physics*, **3**:9, (2010).

[27] H. W. Hammer and L. Platter. Efimov physics from a renormalization group perspective. *Phil. Trans. Roy. Soc. Lond. A*, **369**:2679–2700, (2011), arXiv:1102.3789 [nucl-th].

[28] T. Kraemer. Evidence for Efimov quantum states in an ultracold gas of cesium atoms. *Nature*, **440**:315–318, (2006), arXiv:cond-mat/0512394v2 [cond-mat.other].

[29] M. Zaccanti et al. Observation of an Efimov spectrum in an atomic system. *Nature Physics*, **5**:586–591, (2009), arXiv:0904.4453 [cond-mat.quant-gas].

[30] N. Gross, Z. Shotan, S. Kokkelmans, L. Khaykovich. Observation of universality in ultracold ^{7}Li three-body recombination. *Phys. Rev. Lett.*, **103**:163202, (2009), arXiv:0906.4731v2 [cond-mat.other].

[31] G. Barontini et al. Observation of heteronuclear atomic Efimov resonances. *Phys. Rev. Lett.*, **103**:043201, (2009), arXiv:0901.4584 [cond-mat.other].

[32] K. Helfrich, H.-W. Hammer and D. S. Petrov. Three-body problem in heteronuclear mixtures with resonant interspecies interaction. *Phys. Rev. A*, **81**:042715, (2010), arXiv:1001.4371v2 [cond-mat.quant-gas].

[33] K. Riisager. Nuclear halo states. *Rev. Mod. Phys.*, **66**:1105–1116, (1994).

[34] M. V. Zhukov et al. Bound state properties of Borromean halo nuclei: ^{6}He and ^{11}Li. *Phys. Rep.*, **231**:151–199, (1993).

[35] P.G. Hansen, A.S. Jensen and B. Jonson. Nuclear Halos. *Ann. Rev. Nucl. Part. Sci.*, **45**:591–634, (1995).

[36] A.S. Jensen, K. Riisager, D.V. Fedorov and E. Garrido. Structure and reactions of quantum halos. *Rev. Mod. Phys.*, **76**:215–261, (2004).

[37] C. A. Bertulani, H.-W. Hammer and U. Van Kolck. Effective Field Theory for Halo Nuclei: Shallow p-Wave States. *Nucl. Phys. A*, **712**:37–58, (2002), arXiv:nucl-th/0205063v2.

[38] P.F. Bedaque, H.-W. Hammer and U. van Kolck. Narrow resonances in effective field theory. *Phys. Lett. B*, **569**:159–167, (2003), arXiv:nucl-th/0304007.

[39] L. Platter. Low-Energy Universality in Atomic and Nuclear Physics. *Few-Body Syst.*, **46**:1139–171, (2009), arXiv:0904.2227 [nucl-th].

[40] H.-W. Hammer and L. Platter. Efimov States in Nuclear and Particle Physics. *Ann. Rev. Nucl. Part. Sci.*, **60**:207–236, (2010), arXiv:1001.1981 [nucl-th].

[41] J. Erler et al. The limits of the nuclear landscape. *Nature*, **486**:509–512, (2012).

[42] C. Fahlander and B. Jonson. Nobel Symposium 152: Physics with Radioactive Beams. *Phys. Scr.*, **T152**:010301, (2013).

[43] K. Blaum, J. Dilling and W. Nörtershäuser. Precision Atomic Physics Techniques for Nuclear Physics with Radioactive Beams. *Phys. Scripta*, **T152**:014017, (2013), arXiv:1210.4045 [physics.atom-ph].

[44] K. Tanaka et al. Observation of a Large Reaction Cross Section in the Drip-Line Nucleus ^{22}C. *Phys. Rev. Lett.*, **104**:062701, (2010).

[45] W. Horiuchi and Y. Suzuki. ^{22}C: An S-wave two-neutron halo nucleus. *Phys. Rev. C*, **74**:034311, (2006), arXiv:nucl-th/0605055v2.

[46] D. L. Canham and H.-W. Hammer. Universal properties and structure of halo nuclei. *Eur. Phys. J. A*, **37**:367–380, (2008), arXiv:0807.3258 [nucl-th].

[47] D. L. Canham and H.-W. Hammer. Range corrections for two-neutron halo nuclei in effective theory. *Nucl. Phys. A*, **836**:275–292, (2010), arXiv:0911.3238v2 [nucl-th].

[48] B. Acharya, C. Ji and D. R. Phillips. Implications of a matter-radius measurement for the structure of Carbon-22. *Phys. Lett. B*, **723**:196–200, (2013), arXiv:1303.6720v2 [nucl-th].

[49] D. V. Fedorov, A. S. Jensen and K. Riisager. Efimov states in halo nuclei. *Phys. Rev. Lett.*, **73**:2817–2820, (1994), arXiv:nucl-th/9409018.

[50] A. E. A. Amorim, T. Frederico and L. Tomio. Universal aspects of Efimov states and light halo nuclei. *Phys. Rev. C*, **56**:R2378–R2381, (1997), arXiv:nucl-th/9708023.

[51] I. Mazumdar, V. Arora and V. S. Bhasin. Three-body analysis of the occurrence of Efimov states in $2n$ halo nuclei such as ^{19}B, ^{22}C, and ^{20}C. *Phys. Rev. C*, **61**:051303(R), (2000).

[52] M. T. Yamashita, L. Tomio and T. Frederico. Radii in weakly-bound light halo nuclei. *Nucl. Phys. A*, **735**:40–54, (2004), arXiv:nucl-th/0401063v2.

[53] T. Frederico, A. Delfino, L. Tomio and M. T. Yamashita. Universal aspects of light halo nuclei. *Prog. Part. Nucl. Phys.*, **67**:939–994, (2012).

[54] T.-L. Ho and R.B. Diener. Fermion Superfluids of Non-Zero Orbital Angular Momentum near Resonance. *Phys. Rev. Lett.*, **94**:090402, (2005), arXiv:cond-mat/0408468 [cond-mat.other].

[55] Y. Ohashi. BCS-BEC crossover in a gas of Fermi atoms with a P-wave Feshbach resonance. *Phys. Rev. Lett.*, **94**:050403, (2005), arXiv:cond-mat/0410516 [cond-mat.other].

[56] V. Gurarie, L. Radzihovsky and A.V. Andreev. Quantum phase transitions across P-wave Feshbach resonance. *Phys. Rev. Lett.*, **94**:230403, (2005), arXiv:cond-mat/0410620v3 [cond-mat.supr-con].

[57] C.-H. Cheng and S.-K. Yip. Anisotropic Fermi Superfluid via P-wave Feshbach Resonance. *Phys. Rev. Lett.*, **95**:070404, (2005), arXiv:cond-mat/0504278 [cond-mat.other].

[58] V. Gurarie and L. Radzihovsky. Resonantly-paired fermionic superfluids. *Ann. Phys.*, **322**:2–119, (2007), arXiv:cond-mat/0611022 [cond-mat.supr-con].

[59] J. Levinsen, N. Cooper and V. Gurarie. Strongly-resonant P-wave superfluids. *Phys. Rev. Lett.*, **99**:210402, (2007), arXiv:0705.4460 [cond-mat.supr-con].

[60] C. A. Regal, C. Ticknor, J. L. Bohn and D. S. Jin. Tuning p-wave interactions in an ultracold Fermi gas of atoms. *Phys. Rev. Lett.*, **90**:053201, (2003), arXiv:cond-mat/0209071.

[61] J. Zhang et al. P-wave Feshbach resonances of ultra-cold ^{6}Li. *Phys. Rev. A*, **70**:030702, (2004), arXiv:quant-ph/0406085v2.

[62] C. H. Schunck et al. Feshbach Resonances in Fermionic ^{6}Li. *Phys. Rev. A*, **71**:045601, (2005), arXiv:cond-mat/0407373 [cond-mat.soft].

[63] F. Ferlaino et al. Feshbach spectroscopy of a K-Rb atomic mixture. *Phys. Rev. A*, **73**:040702(R), (2006), arXiv:cond-mat/0510630v2 [cond-mat.other].

[64] J. Fuchs et al. Binding Energies of ^{6}Li p-wave Feshbach Molecules. *Phys. Rev. A*, **77**:053616, (2008), arXiv:0802.3262v2 [cond-mat.other].

[65] Y. Inada et al. Collisional Properties of p-Wave Feshbach Molecules. *Phys. Rev. Lett.*, **101**:100401, (2008), arXiv:0803.1405v3 [cond-mat.other].

[66] E. M. Loebl. *Group Theory and Its Applications, Volume II.* Academic Press, Inc., (1971).

[67] L. Platter, H.-W. Hammer and U.-G. Meissner. The Four boson system with short range interactions. *Phys. Rev. A*, **70**:052101, (2004), arXiv:cond-mat/0404313v2 [cond-mat.other].

[68] P. Hagen. $Y(4660)$ in effektiver Feldtheorie, Diplomarbeit in Physik, (2010).

[69] E. Nielsen, D. V. Fedorov, A. S. Jensen and E. Garrido. The three-body problem with short-range interactions. *Phys. Rep.*, **347**:373–459, (2001).

[70] J. H. Macek and J. Sternberg. Properties of Pseudopotentials for Higher Partial Waves. *Phys. Rev. Lett.*, **97**:023201, (2006).

[71] J. H. Macek. Efimov states of fermionic species. *Nucl. Phys. A*, **790**:747–751, (2007).

[72] E. Braaten, P. Hagen, H.-W. Hammer and L. Platter. Renormalization in the Three-body Problem with Resonant P-wave Interactions. *Phys. Rev. A*, **86**:012711, (2012), arXiv:1110.6829v4 [cond-mat.quant-gas].

[73] Peng Zhang, Pascal Naidon, Masahito Ueda. The scattering amplitude of ultracold atoms near the p-wave magnetic Feshbach Resonance. *Phys. Rev. A*, **82**:062712, (2010), arXiv:1010.0293v1 [physics.atom-ph].

[74] Y. Nishida. Impossibility of the Efimov effect for P-wave interactions. *Phys. Rev. A*, **86**:012710, (2012), arXiv:1111.6961v2 [cond-mat.quant-gas].

[75] D. A. Varshalovich. *Quantum Theory of Angular Momentum.* World Scientific, (1988).

[76] G. V. Skorniakov and K. A. Ter-Martirosian. *Sov. Phys. JETP*, **4**:648, (1957).

[77] M. E. Peskin and D. V. Schroeder. *An Introduction To Quantum Field Theory.* Westview Press, (1995).

[78] P. M. Morse and H. Feshbach. *Methods of Theoretical Physics, Part I.* McGraw-Hill Science/Engineering/Math, (1953).

[79] H.-W. Hammer and D. Lee. Causality and the effective range expansion . *Ann. Phys.*, **325**:2212–2233, (2010), arXiv:1002.4603v2 [nucl-th].

[80] C. Ji, D. R. Phillips and L. Platter. The three-boson system at next-to-leading order in an effective field theory for systems with a large scattering length. *Ann. Phys.*, **327**:1803–1824, (2012), arXiv:1106.3837v2 [nucl-th].

[81] C. Ji and D. R. Phillips. Effective Field Threory Analysis of Three-Boson Systems at Next-To-Next-To-Leading Order. *Few-Body Syst.*, (2013), arXiv:1212.1845v2 [nucl-th].

[82] C. Ji, C. Elster and D. R. Phillips. contributed talk at the Fall Meeting of the APS Division of Nuclear Physics, East Lansing, Oct. 26–29. (2011), http://meetings.aps.org/Meeting/DNP11/Event/151071.

[83] R. Higa, H.-W. Hammer and U. van Kolck. alpha-alpha Scattering in Halo Effective Field Theory. *Nucl. Phys. A*, **809**:171–188, (2008), arXiv:0802.3426v2 [nucl-th].

[84] H.-W. Hammer and D. R. Phillips. Electric properties of the Beryllium-11 system in Halo EFT. *Nucl. Phys. A*, **865**:17–42, (2011), arXiv:1103.1087v2 [nucl-th].

[85] G. Rupak and R. Higa. Model-Independent Calculation of Radiative Neutron Capture on Lithium-7. *Phys. Rev. Lett.*, **106**:222501, (2011), arXiv:1101.0207 [nucl-th].

[86] G. Rupak, L. Fernando and A. Vaghani. Radiative Neutron Capture on Carbon-14 in Effective Field Theory. *Phys. Rev. C*, **86**:044608, (2012), arXiv:1204.4408 [nucl-th].

[87] B. Acharya and D. R. Phillips. Carbon-19 in Halo EFT: Effective-range parameters from Coulomb-dissociation experiments. *Nucl. Phys. A*, **913**:103–115, (2013), arXiv:1302.4762v3 [nucl-th].

[88] V. Lensky and M. C. Birse. Coupled-channel effective field theory and proton-^{7}Li scattering. *Eur. Phys. J. A*, **47**:142, (2011), arXiv:1109.2797v2 [nucl-th].

[89] P. Hagen, H.-W. Hammer and L. Platter. Charge form factors of two-neutron halo nuclei in halo EFT. *Eur. Phys. J. A*, **49**:118, (2013), arXiv:1304.6516v2 [nucl-th].

[90] G. Hagen, P. Hagen, H.-W. Hammer and L. Platter. Efimov Physics around the neutron rich Calcium-60 isotope. *Phys. Rev. Lett.*, **111**:132501, (2013), arXiv:1306.3661 [nucl-th].

[91] J. Rotureau and U. van Kolck. Effective Field Theory and the Gamow Shell Model: The ^{6}He Halo Nucleus. *Few-Body Syst.*, **54**:725–735, (2013), arXiv:1201.3351 [nucl-th].

[92] P. F. Bedaque, G. Rupak, H. W. Grießhammer and H.-W. Hammer. Low-energy expansion in the three-body system to all orders and the triton channel. *Nucl. Phys. A*, **714**:589–610, (2003), arXiv:nucl-th/0207034v2.

[93] D. B. Kaplan. More effective field theory for nonrelativistic scattering. *Nucl. Phys. B*, **494**:471–484, (1997), arXiv:nucl-th/9610052.

[94] P. F. Bedaque and U. van Kolck. Nucleon-deuteron scattering from an effective field theory. *Phys. Lett. B*, **428**:221–226, (1998), arXiv:nucl-th/9710073.

[95] H.-W. Hammer and T. Mehen. Range corrections to doublet S-wave neutron-deuteron scattering. *Phys. Lett. B*, **516**:353–361, (2001), arXiv:nucl-th/0105072.

[96] D. B. Kaplan, M. J. Savage and M. B. Wise. Perturbative calculation of the electromagnetic form factors of the deuteron. *Phys. Rev. C*, **59**:617–629, (1999), arXiv:nucl-th/9804032v3.

[97] L. Platter and H.-W. Hammer. Universality in the triton charge form-factor. *Nucl. Phys. A*, **766**:132–141, (2006), arXiv:nucl-th/0509045v2.

[98] H. Sadeghi and J. Nezamdost. Triton Electric Form Factor at Low Energies. *Prog. Theor. Phys.*, **124**:1037–1050, (2009), arXiv:0908.2052 [nucl-th].

[99] S. Kopecky et al. Neutron charge radius determined from the energy dependence of the neutron transmission of liquid ^{208}Pb and ^{209}Bi. *Phys. Rev. C*, **56**:2229–2237, (1997).

[100] R. Sánchez et al. Nuclear Charge Radii of ^{9,11}Li: The Influence of Halo Neutrons. *Phys. Rev. Lett.*, **96**:033002, (2006), arXiv:physics/0509265v2 [physics.atom-ph].

[101] W. Nörtershäuser et al. Nuclear Charge Radii of ^{7,9,10}Be and the One-Neutron Halo Nucleus ^{11}Be. *Phys. Rev. Lett.*, **102**:062503, (2009), arXiv:0809.2607v4 [nucl-ex].

[102] A. Krieger et al. Nuclear Charge Radius of ^{12}Be. *Phys. Rev. Lett.*, **108**:142501, (2012), arXiv:1202.4873v2 [physics.atom-ph].

[103] W. Geithner et al. Masses and Charge Radii of $^{17-22}$Ne and the Two-Proton-Halo Candidate ^{17}Ne. *Phys. Rev. Lett.*, **101**:252502, (2008).

[104] D. T. Yordanov et al. Nuclear Charge Radii of $^{21-32}$Mg. *Phys. Rev. Lett.*, **108**:042504, (2012).

[105] Chart of Nuclides, National Nuclear Data Center, Brookhaven National Laboratory. (2013), http://www.nndc.bnl.gov/chart/.

[106] M. Stanoiu et al. Disappearance of the N=14 shell gap in the carbon isotopic chain. *Phys. Rev. C*, **78**:034315, (2008).

[107] A. Lapierre et al. Penning-Trap Mass Measurements of the Neutron-Rich K and Ca Isotopes: Resurgence of the N = 28 Shell Strength. *Phys. Rev. C*, **85**:024317, (2012), arXiv:1111.1359v2 [nucl-ex].

[108] A. T. Gallant et al. New Precision Mass Measurements of Neutron-Rich Calcium and Potassium Isotopes and Three-Nucleon Forces. *Phys. Rev. Lett.*, **109**:032506, (2012), arXiv:1204.1987 [nucl-ex].

[109] J. D. Holt, T. Otsuka, A. Schwenk and T. Suzuki. Three-body forces and shell structure in calcium isotopes. *J. Phys. G*, **39**:085111, (2012), arXiv:1009.5984v3 [nucl-th].

[110] G. Hagen et al. Evolution of shell structure in neutron-rich calcium isotopes. *Phys. Rev. Lett.*, **109**:032502, (2012), arXiv:1204.3612v2 [nucl-th].

[111] W. Nazarewicz et al. Structure of proton drip-line nuclei around doubly magic ^{48}Ni. *Phys. Rev. C*, **53**:740–751, (1996).

[112] G. Hagen and N. Michel. Elastic proton scattering of medium mass nuclei from coupled-cluster theory. *Phys. Rev. C*, **86**:021602(R), (2012), arXiv:1206.2336 [nucl-th].

[113] G. F. Bertsch and H. Esbensen. Pair Correlations near the Neutron Drip Line. *Ann. Phys.*, **209**:327–362, (1991).

[114] H. Esbensen and G. F. Bertsch. Soft dipole excitations in ^{11}Li. *Nucl. Phys. A*, **542**:310–340, (1992).

[115] T. Nakamura. Soft E1 excitation of neutron-halo nuclei. *Nucl. Phys. A*, **788**:243–250, (2007).

[116] T. Kubo et al. The RIKEN radioactive beam facility. *Nucl. Instrum. and Meth. Phys. Res. B*, **70**:309–319, (1992).

[117] B. Acharya, P. Hagen, H.-W. Hammer and D. R. Phillips. *work in progress.*

[118] Y. Nishida and D. T. Son. Unitary Fermi gas, epsilon expansion, and nonrelativistic conformal field theories. *published online*, (2010), arXiv:1004.3597 [cond-mat.quant-gas].

[119] A. N. Antonov et al. The electron–ion scattering experiment ELISe at the International Facility for Antiproton and Ion Research (FAIR)–A conceptual design study. *Nucl. Instrum. and Meth. Phys. Res. B*, **637**:60–76, (2011).

[120] O. B. Tarasov et al. Evidence for a Change in the Nuclear Mass Surface with the Discovery of the Most Neutron-Rich Nuclei with $17 \leq Z \leq 25$. *Phys. Rev. Lett.*, **102**:142501, (2009), arXiv:0903.1975 [nucl-ex].

[121] B. Sherrill. Science and Status of the Facility for Rare Isotope Beams. *talk give at Conference on Nuclear Structure, Argonne National Laboratory, USA*, (2012).

[122] I. N. Bronstein, K. A. Semendjajew, G. Musiol and H. Mühlig. *Taschenbuch der Mathematik.* Harri Deutsch, 5th edition, (2001).

[123] A. Erdélyi, W. Magnus, F. Oberhettinger and F. G. Tricomi. *Tables of Integral Transforms. Vol. I.* McGraw-Hill Book Comp., Inc., (1954).

[124] W. H. Press, S. A. Teukolsky, W. T. Vetterling and B. P. Flannery. *Numerical Recipes in C, The Art of Scientific Computing.* Cambridge University Press, 2nd edition, (1992).

Danksagung

Ich widme diese Arbeit meinen Eltern, bei denen ich mich für die große Unterstützung, die sie mir in meinem Leben gegeben haben, bedanken möchte. Auch meinem Bruder, meinen Großeltern und dem Rest meiner Familie möchte ich in diesem Zusammenhang danken.

Großer Dank gilt des Weiteren meinen beiden Referenten Prof. Dr. Hans-Werner Hammer und Prof. Dr. Bastian Kubis. Prof. Hammer danke ich insbesondere für die hervorragende Betreuung meiner Doktorarbeit sowie für seine ausgesprochene Hilfsbereitschaft.

Ich danke weiterhin Prof. Lucas Platter, Prof. Eric Braaten, Prof. Daniel Phillips und Bijaya Acharya für die spannende Zusammenarbeit bei verschiedenen wissenschaftlichen Projekten.

Ferner danke ich der gesamten Arbeitsgruppe Hammer für die angenehme Arbeitsatmosphäre, die gegenseitige Hilfsbereitschaft und das kollegiale Miteinander. Dabei möchte ich besonders meinen Bürokollegen Dr. Sebastian König hervorheben, der mir sowohl bei fachlichen Diskussionen als auch bei Problemen computertechnischer Natur stets eine große Hilfe war.

Zuletzt danke ich meinem guten Freund Michael Brockamp für das Korrekturlesen dieser Arbeit.